Antiferromagnetism, Superconductivity, Pseudogap and Their Interplay with the Mott Transition

by

Lorenzo Fratino

Department of Physics

Royal Holloway University of London

Supervisor: Dr. Giovanni Sordi

This thesis is submitted for a degree of Doctor of Philosophy

October 17, 2017

Declaration of Authorship

I, Lorenzo Fratino, hereby declare that this thesis and the work presented in it is entirely my own. Where I have consulted the work of others, this is always clearly stated.

Signed:

Date:

Abstract

After more than thirty years since the discovery of high temperature superconductivity in the cuprates, their properties still lack a complete theoretical understanding. In this work, we will argue that the key role to decipher the phase diagram of these compounds lies in the physics of the Mott transition, combined with the effect of short-range order correlations. By the use of Cellular Dynamical Mean-Field Theory with the Hybridisation Expansion Continuous-Time Quantum Monte Carlo as the impurity solver, we begin examining the two-dimensional Hubbard model. The comparative analysis at half-filling of the properties of the antiferromagnetic and normal state reveals a detectable, sharp crossover in the condensation energy linked to the underlying Mott transition.

Upon doping the system, the study of several parametric regimes in the presence of $d-$wave superconductivity reveals the role of the pseudogap to correlated metal transition, hidden under the superconducting dome. The Widom line is a line of crossovers that emerges at high-temperature from this transition. This supercritical behaviour not only determines the shape of this dome but also the maxima of T_c at optimal doping as well as the driving mechanism that allows the superconductivity to occur. Furthermore, it explains how the condensation energy can change from potential-energy driven to kinetic-energy driven upon a reduction in doping. The first-order transition affects the superconducting properties, providing an organising principle for the whole phase diagram.

Additionally, we investigate a more realistic model for the cuprates that includes three orbitals per unit cell, the Emery model. We compute the finite temperature behaviour of the metal to charge-transfer insulator transition driven by the interaction and of the pseudogap to correlated metal transition driven by increasing the hole carrier concentration. The features of the superconducting and normal states confirm the Hubbard model scenario, despite the large differences in microscopic details, such as the presence of oxygen and the different band structure.

Contents

List of Figures

Chapter 1

Introduction

The discovery of high-temperature superconductivity in the cuprate $La_{2-\delta}Ba_{\delta}CuO_4$ by Bednorz and Müller [1] inaugurated a new field of research, still open after more than thirty years [2–9]. Despite conventional band theory predicting cuprates to be conductors at half-filling, they are insulators due to a charge transfer process. Indeed, these insulating properties emerge as a consequence of the strong electron correlations and the hopping of electrons among anions and cations within the copper oxide unit cell [2–4, 10]. This band-gap is similar to that of the Mott insulator, i.e. a state that is insulating due to the electron-electron interactions. The difference is that the latter arises thanks to the strong electron correlations and the hopping of electrons among atoms of different unit cells, whereas in the first case the electrons hop within atoms of the same unit cell. Introducing hole carriers in the sample leads to superconductivity at a higher temperature than ever before with a d-wave pairing symmetry [11–16]. The electron-electron interactions favour superconductivity instead of suppressing it and so, to explain the exceptional properties of these systems, a different theoretical framework from the one used in conventional superconductors has to be established. This thesis is devoted to studying the effects of such electronic correlations that govern the physics of carrier-doped Mott insulators. The simplest one-band model to study such systems is provided by the two-dimensional Hubbard model [17–19]:

$$H_{HM} = -\sum_{\langle i,j\rangle,\sigma} t_{ij}(c^{\dagger}_{i\sigma}c_{j\sigma} + c^{\dagger}_{j\sigma}c_{i\sigma}) + U\sum_{i} n_{i\uparrow}\, n_{i\downarrow}, \tag{1.1}$$

where $c^{\dagger}_{i\sigma}$, $c_{i\sigma}$ and $n_{i\sigma} = c_{i\sigma}c^{\dagger}_{i\sigma}$ are respectively the creation, annihilation and the number operator for an electron in the site i with spin σ, t_{ij} is the hopping probability from a site i to a site j, and U the Coulomb potential energy. This paradigmatic model represents the natural playground to understand the Mott physics and it is widely believed to capture many of the essential features of strongly correlated materials [20]. Despite its simplicity, it has no known analytical solution and it must be addressed with some numerical approaches. This can be done using the Dynamical Mean-Field Theory [21] and its cluster extension the Cellular Dynamical Mean-Field Theory [22]. The goal of this thesis is to enlarge the understanding of the rich phase diagram of the cuprates. By investigating the behaviour of the physics of the normal state and by comparing it with the antiferromagnetic and superconducting phases for the undoped and hole-doped system, we will demonstrate how the peculiar effects of the Mott physics and the short range order correlations act as organising principle for the physics of the cuprates. The work of this thesis is arranged as follows:

In Chapter 2 the main phenomenological properties of the phase diagram of cuprates are reviewed. In particular, we focus on the d-wave nature of the superconducting phase, the antiferromagnetic properties and the peculiarity of the pseudogap phase. The latter phase is a state characterised by a finite depression in the local density of states at the Fermi energy and its understanding is of primary importance to comprehend the cuprates [23]. This Chapter is devoted to familiarise the reader to the experimental scenario before presenting our theoretical results in the following Chapters.

In Chapter 3, we will introduce the two-dimensional Hubbard and Emery models, adopted in our theoretical work. These systems have no analytical solution and must be addressed with some numerical methods, such as the Dynamical Mean-Field Theory (DMFT) [21] together with its cluster extension Cellular Dynamical Mean Field Theory (CDMFT) [24, 25] that are illustrated in this Chapter. As we will see, the original many-body system is mapped on a local impurity problem, via self-consistency conditions. Then the solution of the impurity problem can be computed with an impurity solver. Among the many possibilities we chose to use the Continuous-Time Quantum Monte Carlo in its hybridisation expansion approach [26, 27], as it will be introduced. The final result is given by iterating this procedure to obtain an approximate solution employed in the next iteration, until reaching the desired convergence of the observables.

In Chapter 4, we study the half-filled two-dimensional Hubbard model using Cellular Dynamical Mean-Field Theory with Continuous-Time Quantum Monte Carlo. The properties of a phase with large correlation length can be strongly influenced by the underlying normal phase. Sharp crossovers in the mechanism that favours antiferromagnetic correlations and in the corresponding local density of states are observed. These non-trivial crossovers occur at values of the interaction and the temperature that are controlled by the underlying normal-state Mott transition [28].

In Chapter 5, we study the two-dimensional Hubbard model with Cellular Dynamical Mean-Field Theory to address the unusual features of the superconductivity in the cuprates and to relate them to other normal-state phenomena, such as the pseudogap. The fate of the underlying Mott transition at half-filling studied in the previous Chapter plays a fundamental role. Moreover, previous studies with the same methodology have found that upon doping the Mott insulator at low temperature a pseudogap phase appears [29–32]. The low-temperature transition between this phase and the correlated metal at higher doping is first-order, culminating in a second-order critical point. Similarly to what happens in the phase diagram of water [33, 34], at higher temperature the supercritical behaviour of this transition is characterised by a series of crossovers in dynamical, thermodynamical and transport quantities that asymptotically merge in a line, called the Widom line [29–32, 35]. We will observe that the shape of superconducting critical temperature T_c^d, the minima of the condensation energy, the normal-state scattering rate, and the change in the driven pairing mechanism are all remnants of the normal state first-order transition and its supercritical behaviour that also govern the superconducting state [36].

In Chapter 6 we show that our findings of the previous Chapter are robust under inter-band interactions by solving the Emery model [3]. This model takes into account, within each unit cell, two oxygen orbitals where there is no electron-electron repulsion and a copper orbital with strong electron-electron repulsion. The insulating phase is a so-called charge-transfer insulator, not a Mott-Hubbard insulator. Using Cellular Dynamical Mean-Field Theory with Continuous-Time Quantum Monte Carlo as an impurity solver and 12 atoms per cluster, we report the normal and superconducting phase diagram of this model as a function of doping, interaction strength, and temperature. As expected, the three-orbital model is consistent with the experimental observation that doped holes are located predominantly on oxygens, a result

that goes beyond the one-orbital model, analysed in Chapters 4 and 5. Nevertheless, the phase boundary between pseudogap and correlated metal, the Widom line, and the origin of the pairing energy (kinetic versus potential) are similar to the one-orbital model, demonstrating that these are emergent phenomena characteristic of doped Mott insulators, independently of many microscopic details [6, 37].

Finally, in Chapter 7 we will summarise our results, highlighting the questions that are still open and tracing the route for prospectives and future works.

Chapter 2

Cuprates: an Overview

2.1 Introduction

One of the most unexpected discoveries of the last century was made by Kamerlingh Onnes in 1911 when he first detected superconductivity in mercury [38]. Upon cooling down a sample of such material, the resistivity has a sudden drop to zero below a certain critical temperature $T_c = 4.2K$, quite close to the absolute zero temperature. This is the first fundamental property that defines superconductivity. From that moment it took several years to identify all the main features of such a phase and to construct a theory able to explain them. Indeed, we had to wait until 1933 for Meissner and Ochsenfeld to discover that a superconductor expels its magnetic flux during its transition to the superconducting state [39]. This is the second fundamental property that defines superconductivity. The first theoretical advance in understanding this scenario was made with the formulation of the London theory in 1935 [41] and the next step was not taken until 1950 with the introduction of Ginzburg-Landau theory [42]. This last theory led finally to a well accepted microscopic theory of the phenomenon thanks to Baarden, Cooper, and Schrieffer, the eponymous BCS theory [43]. For decades afterwards, this topic established itself as a separate field with many subfields and seemed to exhaust all the questions that were initially raised, little by little the scientific community lost its interest in such investigations. Due to Bednorz and Müller in 1986 high-temperature superconductivity was found in cuprates [1]. Using the ceramic $La_{2-\delta}Ba_{\delta}CuO_4$ they suddenly detected a superconducting transition at $T_c \approx 35K$, a new record. Since then the cuprates, which are the topic of this Chapter, inspired

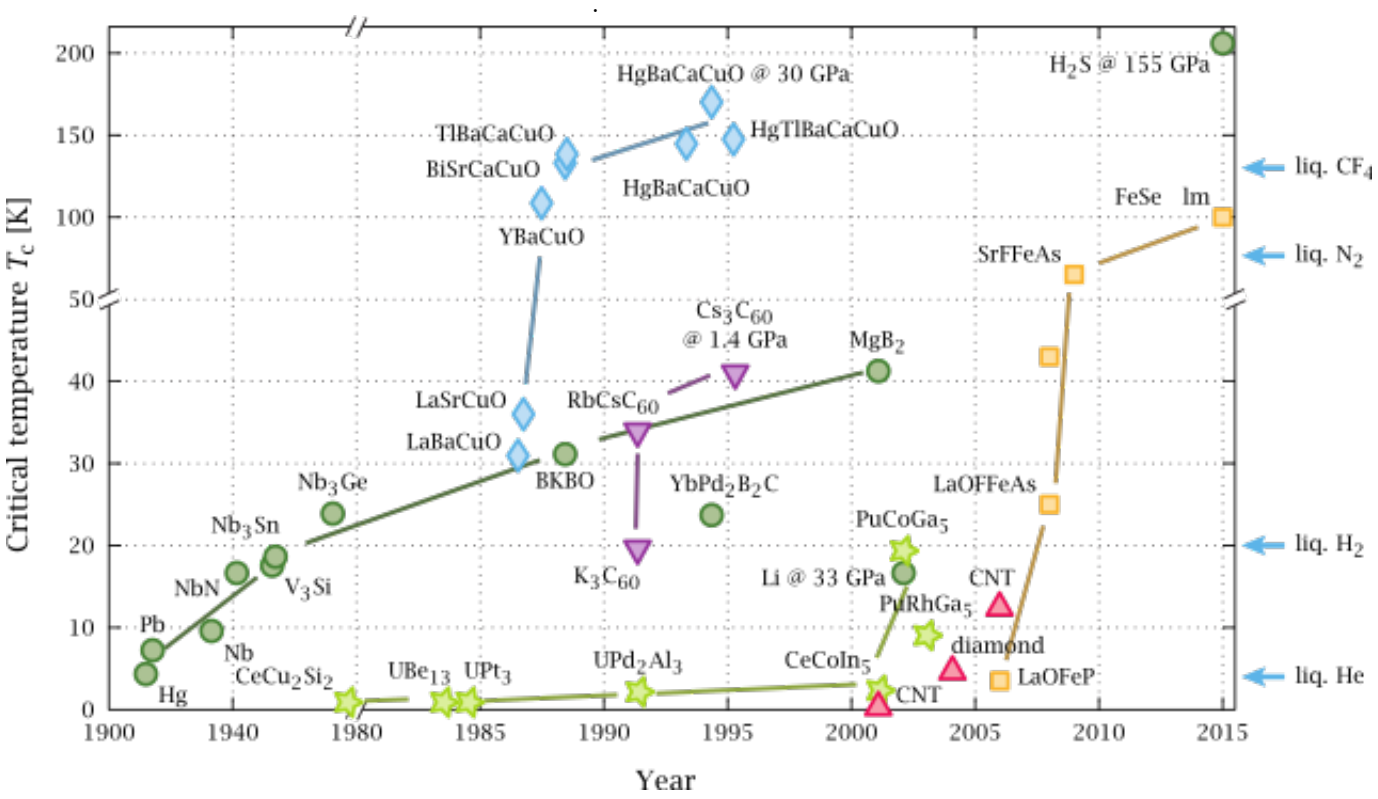

Figure 2.1: Progress in the discovery of superconducting materials. Note in particular that the cuprates are plotted with light blue diamonds, BCS superconductors with green circles, the iron-based superconductors with yellow squares, and the fulleride superconductors with purple triangles. Figure taken from [40]

a new field of investigation namely high-temperature superconductivity. One of the reasons for such a quest is to obtain a superconducting state stable at room temperature so that we can use its unique properties to unveil new technological advances in ways still to be completely understood. The resultant experimental effort allowed for the discovery of other materials accomplishing new records for T_c: already by 1987 a $T_c \approx 90$K was found for $YBa_2Cu_3O_{7-\delta}$ [44] and in 1994 $HgBa_2Ca_2Cu_3O_{8-\delta}$ arrived half way between room temperature and absolute zero, an astonishing value of $T_c \approx 130$K [45, 46]. Fig. 2.1 shows T_c for several compounds as a function of the year of their discovery.

From a theoretical perspective, cuprates are still today very challenging materials to physically describe. Our approach, in the next Chapters, is to begin with the analysis of the properties for the undoped regime, governed by the Mott transition. Then we will see how the physics of Mott has a signature also in the doped region. Before the examination of our theoretical results, it is important to have an overview of the most phenomenological properties

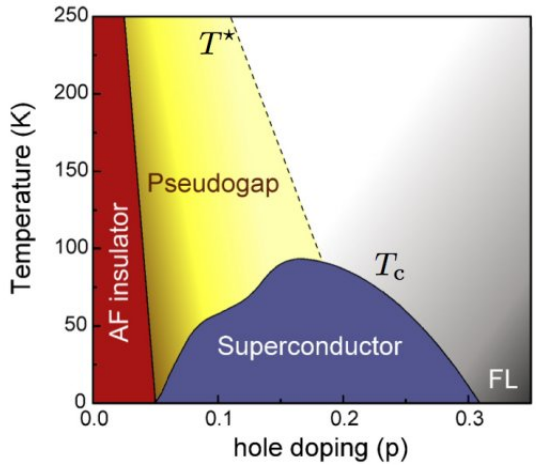

Figure 2.2: Cartoon of the hole doping and temperature phase diagram of cuprates. The parent, i.e. undoped, compounds are in a Mott antiferromagnetic insulating state. Upon doping an antiferromagnetic insulating state (red region), at low temperature a superconducting dome emerges (purple region) leaving then a Fermi liquid state (dark grey). In the under-doped regime, a pseudogap state (yellow region) is also present. It terminates in a crossover line T^* that divides the pseudogap from the correlated metal. Figure taken from [47].

that result from years of intensive experimental inquiries.

In Section 2.2 we will recall the most important features of conventional superconductivity, highlighting some of the differences with cuprates. The nature of their superconductivity is different from the one previously understood, and this appears especially evident in the pairing symmetry that is d-wave, as motivated in Section 2.4.1. Another fundamental feature of cuprates is their quasi-two-dimensional nature that motivates our use of the two-dimensional theoretical models in the next Chapters. Section 2.3 is devoted to introducing the most common crystal structure of the cuprates. Furthermore, their phase diagram keeps puzzling the community due to the richness of phases that are still not well understood. In our theoretical investigations, we focused just on some of the principal phases as sketched in the phase diagram of Fig. 2.2. Here we can appreciate that in the undoped regime cuprates are in a Mott antiferromagnetic state, as outlined in Section 2.4.2. Upon doping the system, a superconducting dome emerges and vanishes in a Fermi liquid state in the over-doped regime, as reviewed in Section 2.4.1. Notably, in the under-doped region, a pseudogap phase is also present, and some of its unusual properties are described in Section 2.4.3. For completeness, in Section 2.4.4 we will also have an overview of other phases that are gaining more and more attention in the last few years and in Section 2.5 we will discuss other families of high temperature

superconductors.

2.2 Conventional Superconductivity: an Overview

Before the discovery of high-temperature superconductivity in cuprates, the theory of superconductivity successfully answered many of the main questions that were posed by experimental results. Here we recall some aspects of conventional superconductors, in order to compare them with those of the unconventional ones. As previously mentioned, there are two essential properties of any superconductor:

- zero resistance below a certain critical temperature T_c,
- expulsion of the magnetic flux, i.e. Meissner effect.

These properties tell us that the electrons are in a macroscopic quantum state, like a Bose-Einstein condensate. This raises the question, how is this possible? Electrons are half-integer spin particles and consequently obey Fermi statistics, but to behave in this fashion we would need to have integer spin particles, namely bosons. Leon Cooper solved this apparently paradoxical situation in 1956 [48]. He showed that in the presence of an attractive interaction, even if arbitrarily small, the electrons tend to pair. They act as effective bosons and as such can form a Bose-Einstein condensate. Despite the screened electric repulsion, in metals at low energy there can be an effective attraction as a result of the electron-phonon interaction. Furthermore, we highlight that such pairs consist of electrons in time-reversed momentum states and consequently have zero center-of-mass momentum, they are not to be thought of as real space objects [49]. Due to the Fermi statistics, the wave function of such pairs is antisymmetric for exchange of one electron with another, so their spin and spatial components must have opposite exchange symmetries. This implies that we can have just two possible scenarios for the pairs:

- spin singlets with an even parity spatial component,
- spin triplets with odd parity.

The first case with an isotropic spatial component (s-wave) turns out to be the one realised in conventional superconductors [43]. In this case, the gluing mechanism is described by

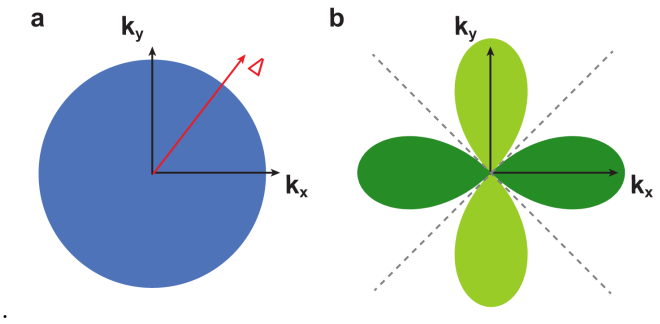

Figure 2.3: Cartoon of the gap amplitude Δ in momentum space. Panel (a): conventional s-wave superconductor: Δ is isotropic in all directions. Panel (b): unconventional ($d_{x^2-y^2}$) superconductor: Δ changes sign assuming null value along the nodes, depicted by the dashed lines. Figure taken from [50].

the following: A metal is made of a crystalline lattice of atoms, the conduction electrons are free to move through it, letting the atoms become positive ions. These electrons then attract the surrounding ions, and once they move away, they leave a positive ionic distortion. This distortion engages a new electron, forming an effective attraction among these particles. This mechanism, electron-phonon interaction, works thanks to the difference in mass between electrons and ions that determine two different dynamics, in other words, the ions are moving slower. The pairing wave function, also known as the order parameter, results in an s-wave state. Fig. 2.3 shows a sketch for the pairing amplitude as a function of the momentum. This quantity is isotropic for an s-wave superconductor (Fig. 2.3 panel (a)), whereas for unconventional superconductors it can change sign and present zero value for certain directions, called nodes, as exemplified for a $d_{x^2-y^2}$ symmetry in Fig. 2.3 panel (b) [14–16]. Thus we can define an "unconventional superconductor" as one that has a non-uniform order parameter in momentum space, namely that is not s-wave. This is the case of the cuprates.

2.3 Crystal Structure

As previously mentioned, cuprates have been well investigated in the constant, ongoing attempt to unveil the secrets of high-temperature superconductivity. Many standard features have been found, and we devote the rest of this Chapter to describe some of them. As revealed by single-crystal X-ray and powder neutron diffraction, the cuprates are layered perovskite oxides [52]. Perovskites are crystal structures combining metals with nonmetals with the particular arrangement, in their ideal form, shown in Fig. 2.4. Their generalised formula

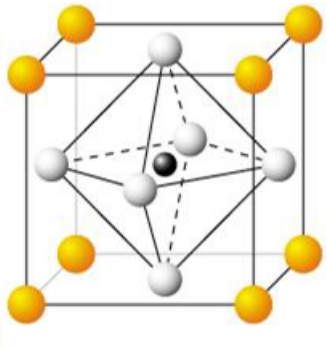

Figure 2.4: The perovskite structure ABX_3. Figure taken from [51].

is ABX_3, where A and B are metallic cations and X atoms are non-metallic anions. They consist of cuboids with the largest of the two metals A lying in the center, the B cations are arranged in all 8 corners and the X anions on the center of the 8 faces. In Fig. 2.5 panel (a)

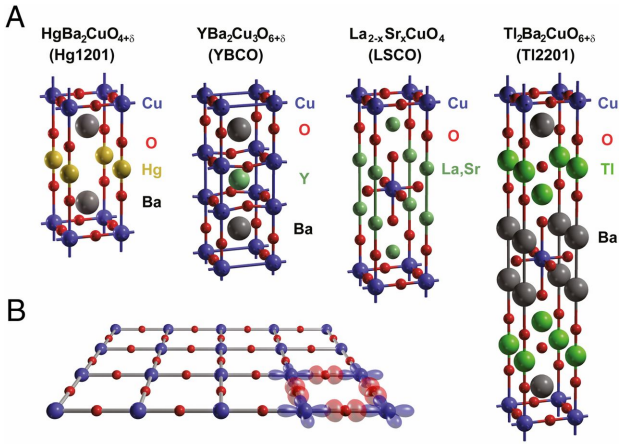

Figure 2.5: Panel (a): Crystal structure of $HgBa_2CuO_{4+\delta}$, $YBa_2Cu_2O_{6+\delta}$, $La_{2-\delta}Sr_2CuO_4$, $Tl_2Ba_2CuO_{6+\delta}$. Panel (b): the CuO_2 planes where in blue is displayed the copper orbital $d_{x^2-y^2}$ and in red the oxygen orbitals p_x, p_y. Figure taken from [53].

we show the crystal structure of some of the most common cuprates. The geometry of the unit cells forms two-dimensional copper oxide layers intertwined via ionic inert layers that supply charge carriers to the first. In Fig. 2.5 panel (b) the CuO_2 plane where superconductivity occurs is displayed. If we take into consideration a "parent" compound, namely a cuprate at zero doping as $LaCuO_4$, we have that the electrons are well localised on the copper plane. We need to pay a high energy price, Hubbard U, to let an electron jump from one site to another.

In this way, the electrons are localised in their lattice sites and such a state without taking into account the spins is a "Mott insulator" or a "Charge transfer insulator" in opposition to classical band theory that would predict a metallic state. Which one of these two insulating

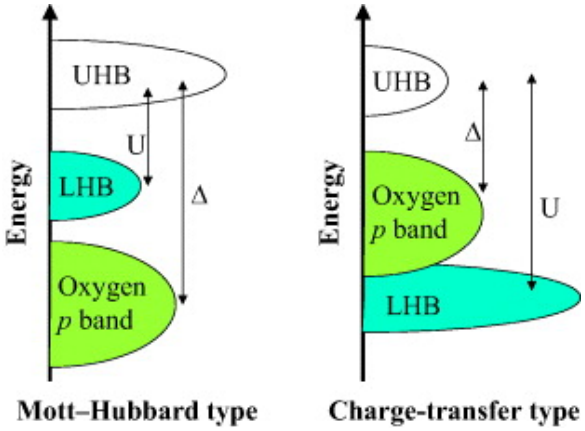

Figure 2.6: Left panel cartoon of the local density of states on the left for the Mott-Hubbard insulator and on the right for a "Charge transfer insulator" and in the right panel for the charge-transfer one for the correlated electrons case at $U > U_{\mathrm{MIT}}$. Depending from the interaction $U > U_{\mathrm{MIT}}$ and the charge-transfer energy $\Delta = |\epsilon_p - \epsilon_d|$ we have two possible insulator states. Figure taken from Ref. [54].

states is present, depends upon the competing energetics of the on site copper interaction U and the charge-transfer energy $\Delta = |\epsilon_p - \epsilon_d|$ with ϵ_p and ϵ_d the energies of the oxygen and copper, respectively, as sketched in Fig. 2.6. In the Mott-Hubbard case the electrons hop between two adjacent unit cells, whereas in the charge-transfer case they jump among atoms within the same unit cell. As we will discuss in Chapter 4, when, within this picture, we also take into consideration the spins, a dynamical degree of freedom, the Pauli principle forces these spins to anti-align, creating an antiferromagnetic state due to the virtual hopping on the oxygens [55, 56]. The electronic configuration of the Cu is a $3d^9$, i.e. the valence is 1^+ with a single hole in $3d$ orbital. This orbital is split into five d-orbitals: four of them are fully occupied xy, xz, yz, and $3z^2 - r^2$ while the highest in energy $x^2 - y^2$ is just half filled [57]. The oxygen ion has a closed shell with configuration $2p^6$ and so, due to the similar energy of such orbitals, we have a strong hybridisation between them, resulting in the topmost energy level that involves both features of Cu $d_{x^2-y^2}$ and O $2p^6$. This strong hybridisation binds a hole in the oxygens with the central ion Cu^{2+} forming a local singlet between the two, called a Zhang-Rice singlet. This electronic structure can be described with two-dimensional models and justifies our usage of the Emery model, where we use a three band structure able to

describe the behaviour of the oxygens and of the copper as outlined in Section 3.48. Furthermore, from the observation that upon doping this compound the holes mainly enter the oxygen [58–60], Zhang and Rice demonstrated that the motion of their eponymous singlet can be described by the Hubbard model [6], that we extensively use in our work.

2.4 Phase Diagram

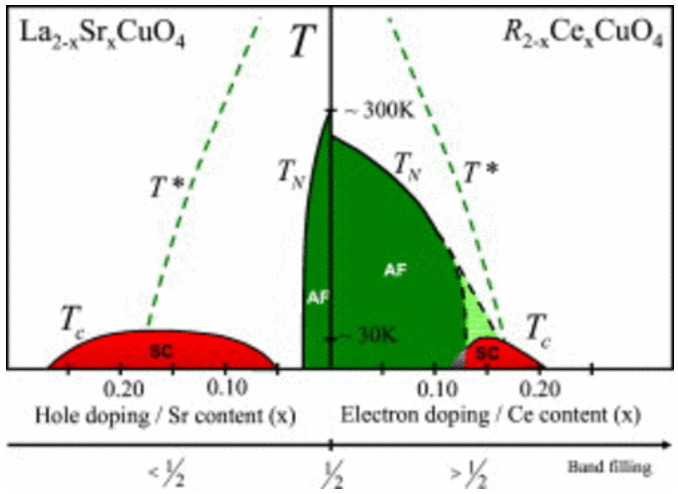

Figure 2.7: Cartoon of the phase diagram of cuprates: for the hole and the electron-doped cuprates on the left and on the right, respectively. In green is indicated the antiferromagnetic region and in red the superconducting dome. The green dashed lines are the crossover lines T^* between the pseudogap and the correlated metal phase. Figure taken from Ref. [61].

By substitution of the metals in the "charge-reservoir" planes, we can dope the system with holes or electrons, as displayed, for example, on the left or right panels of Fig. 2.7 respectively. In this work, the discussion is confined to hole-doped systems. By increasing the hole-doping, the antiferromagnetic state is strongly suppressed, and a d-wave superconducting domain raises up until an optimal doping δ_{opt} upon which T_c reaches its maximum [62, 63]. With further doping, it vanishes into a Fermi liquid state creating a dome-like shape in the phase diagram as shown in Fig. 2.7. It is important to note that for the underdoped regime, i.e. $\delta < \delta_{opt}$, at $T > T_c$ several phases are possibly competing together: charge order, spin-glass and pseudogap states [64].

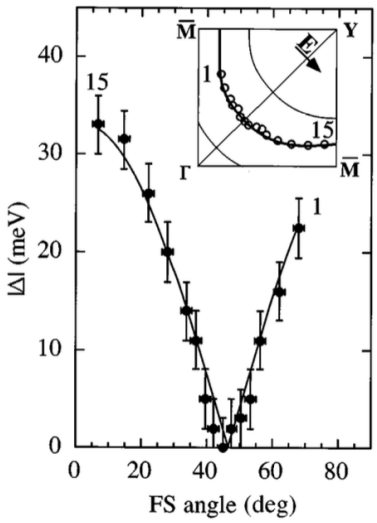

Figure 2.8: ARPES data for $Bi_2Sr_2CaCu_2O_{8+\delta}$ at T=13K for a sample with $T_c = 87$K. The gap is plotted versus the angle on the Fermi surface with filled circles. The solid curve is the fit of the data using a $d_{x^2-y^2}$ order parameter. Figure taken from Ref. [13].

2.4.1 Pairing Symmetry and Superconductivity

The pairing symmetry of the superconducting state in cuprates is of primary importance in order to understand their phase diagram. In Section 2.2 we have already mentioned that cuprates present a d-wave superconductivity, so here we want to recall some experiments that demonstrated it [14, 16].

As shown with measurements of the Knight shift and spin-lattice relaxation by nuclear magnetic resonance (NMR) [11,12,65], carriers in cuprate superconductors form singlet pairing below T_c. In this experimental technique a compound is inserted in a volume in the presence of a magnetic field. This field aligns the spins of the conduction electrons and induces a current in the electronic charge distribution. Due to these effects a magnetic field is also induced on the atoms or molecules of the compound and by measuring this field, the magnetisation of the sample and the magnetic susceptibility we can obtain a measurement of the Knight shift. Indeed, the observed Knight shift is the result of two possible contributions, namely the spin and orbital magnetic contributions. The latter decreases below T_c suggesting that the pairing is a singlet state and the effect of spin-orbit scattering is negligible. Due to Fermi statistics, the parity of the order parameter must be even.

Angular-resolved photoemission spectroscopy (ARPES) can experimentally test the parity

of the Cooper pairs. In this technique a crystal or tiny film is probed with low energy photons in the ultraviolet range that let the conduction electrons of the compound become excited and free to leave via a photoemission process. In this way by resolving the angular distribution of the emitted electrons, we can obtain the dispersion relation between binding energy and momentum distribution of the sample and in this way the band and spectral structure of it. Fig. 2.8 shows some data obtained with ARPES [13]: the angular variation of the gap Δ is in excellent agreement with that expected from a $d_{x^2-y^2}$ order parameter:

$$\Delta_{d_{x^2-y^2}}(k) = \Delta_0 \left(\cos(ak_x) - \cos(ak_y)\right) \tag{2.1}$$

where Δ_0 is the maximum value of the gap and a is the in-plane lattice constant. Moreover, several different techniques such as measurements of the thermal conductivity [66], superconducting quantum interference device SQUID interferometry [67], single-Josephson-junction modulation [68, 69], and tricrystal scanning SQUID magnetometry [70] have confirmed this anisotropy of the pairing potential and the presence of line nodes compatible with a d-wave symmetry. Such symmetry minimises the on-site Coulomb repulsion while retaining 2D confinement in the CuO_2 planes when the interlayer coupling is sufficiently weak.

It is also worth noting that in the heavily over-doped cuprates, $\delta > \delta_{opt}$, significant mixing between s and d-wave order parameter was established. Using Scanning Tunnelling Spectroscopy, where a metal tip is moved over a conducting sample to obtain a topographic map of the surface [71], combined with ARPES [72, 73] and Raman spectroscopy [74, 75] suggests that such s-wave mixing is a general feature of high T_c, except when the crystalline symmetry requires a second superconducting transition as in case of tetragonal crystals [76–78].

These experimental results provide a real proof about the pairing symmetry and justify our theoretical work, in which we restrict our analysis on the d-wave superconductivity in Chapters 5 and 6.

Another unusual property of the superconducting state is the shape of the doping dependence of the superconducting transition temperature T_c. The famous "dome" sketched in Fig. 2.7, whose origin is intertwined with that of the pseudogap, exhibits a strong asymmetry. This asymmetry has been revealed in recent experimental work where the ubiquitous competing charge-density wave, which will be briefly discussed in Section 2.4.4, is removed

by pressure [79]. Also, the condensation energy, i.e. the difference of energy of the ground

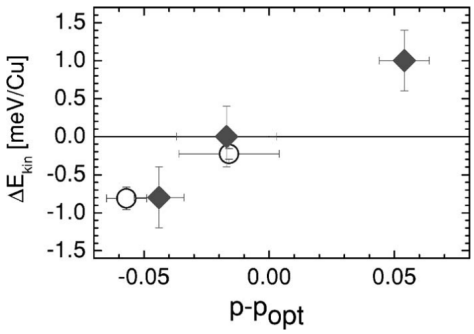

Figure 2.9: Figure taken from [80]. The data with full diamonds and with open circles, respectively taken from Ref. [81] and Ref. [82], represent the difference of the kinetic energy at the ground state between superconducting and normal state $\Delta E_{\rm kin}$ as a function of the difference between the doping p and the optimal doping p_{opt} for samples of $Bi_2Sr_2CaCu_2O_{8+\delta}$.

state in the superconducting and normal state, is a second unusual property. This quantity can be obtained by measuring the reflectivity to explicitly derive the optical conductivity, the integral of which is proportional to the kinetic energy [83]. The normal state contribution is computed by extrapolating the temperature dependence above T_c down to zero temperature. This procedure highlights that differently from the conventional superconductors that have a potential-energy driven pair formation [84], cuprates present a change from kinetic-energy to potential-energy driven mechanism by increasing doping [80, 82, 85–87], as shown in Fig 2.9. A theoretical explanation for such unusual features will be discussed in the Chapters 5 and 6.

2.4.2 Antiferromagnetism

At zero or small doping, the phase diagram of cuprates is characterised by an antiferromagnetic order. This phase appears to be nearby the superconducting dome, as shown in Fig. 2.7. Thus, the study of its properties can reveal valuable information about the nature of the high-temperature superconductivity.

The discovery of the antiferromagnetic phase in La_2CuO_4 was obtained in macroscopic susceptibility measurements [88,89]. However, the spin structure in the Néel state was revealed only with the aid of neutron diffraction [55, 90, 91], by studying the magnetic susceptibility and the magnetisation of the crystals as shown for example in Fig. 2.10 panel (a). Neutron diffraction uses the diffraction pattern of a sample placed in a beam of neutrons to obtain

information about its atomic or magnetic structure. Fig. 2.10 panel (b) shows the behaviour of the Néel temperature as a function of electron doping x for $Pr_{2-x}Ce_xCuO_4$, oxygen doping δ for $La_2CuO_{4+\delta}$ or Zn doping y for $La_2Cu_{1-y}Zn_yO_4$. The antiferromagnetic state is insulating, and upon increasing doping, there is a crossover between commensurate and incommensurate antiferromagnetism. In this second case, there is growing evidence of stripe order formation, with a resulting itinerant antiferromagnetism that can compete with superconductivity or other phases, see Section 2.4.4.

The mechanisms from which the antiferromagnetic state emerges are well identified: at half-filling, although there is a single AF phase, there are qualitative differences between AF at weak and strong coupling. For small Coulomb repulsion U, AF stems from nesting of the Fermi surface, whereas for large U, AF originates from superexchange [28]. This is because in the Mott state the electrons are well localised and thus the local moments tend to order magnetically at low temperature. This change is sometimes referred to as the Slater to Mott crossover, and it will be discussed in Chapter 4, where we will argue that this phase is related to the physics of the normal state, characterised by a metal to insulator transition driven by electron-electron interaction and called the Mott transition.

2.4.3 Pseudogap

As previously mentioned, in the under-doped regime above T_c there is evidence of the existence of a pseudogap phase. Early measurements of the Knight shift and spin-lattice relaxation by nuclear magnetic resonance (NMR) [94, 95], as shown in Fig. 2.11, indicate a strong suppression of spin excitation below a certain temperature $T^* > T_c$ [96]. Such a "spin-gap" is relevant not just for the spin channel but also for the charge one, as can be seen for: specific heat measurement [97], c-axis optical conductivity [98], ARPES [99, 100] and tunnelling spectroscopy [101]. Fig. 2.12 shows some tunnelling spectra measured for several temperatures on under-doped $Bi_2Sr_2CaCu_2O_{8+\delta}$. At low temperature, we can see that the local density of states for the pseudogap is characterised by a finite weight at the Fermi energy, between two peaks just above and below it. Increasing temperature, the peaks broaden and the gap vanishes.

Fig. 2.13 displays the ARPES results for a non-superconducting sample at $\delta = 0.03$ and for superconducting samples at $\delta = 0.08,\ 0.12,\ 0.22$ of $La_{2-\delta}Sr_\delta CuO_4$ [102]. The Fermi surface

of a Fermi liquid determines the boundary between occupied and unoccupied quasiparticle states so that it cannot abruptly end. However, in the pseudogap regime, Fermi arcs appear to be in the nodal region [103]; as shown in Fig. 2.13 panel (a) with the Fermi surface for an under-doped sample with pseudogap. In such a phase the antinodal regions near the Brillouin zone edge are gapped out, giving rise to Fermi arcs. The pseudogap suppression first opens up near $(\pi, 0)$ and progressively removes big portions of the Fermi contour, causing the gapless arcs to shrink with the decreasing of the temperature [104]. Such features disappear with increasing doping in the superconducting state (Fig. 2.13 panels (b), (c), (d)) where a large Fermi surface is observed.

The characteristic suppression of the pseudogap at the Fermi energy has consequences on

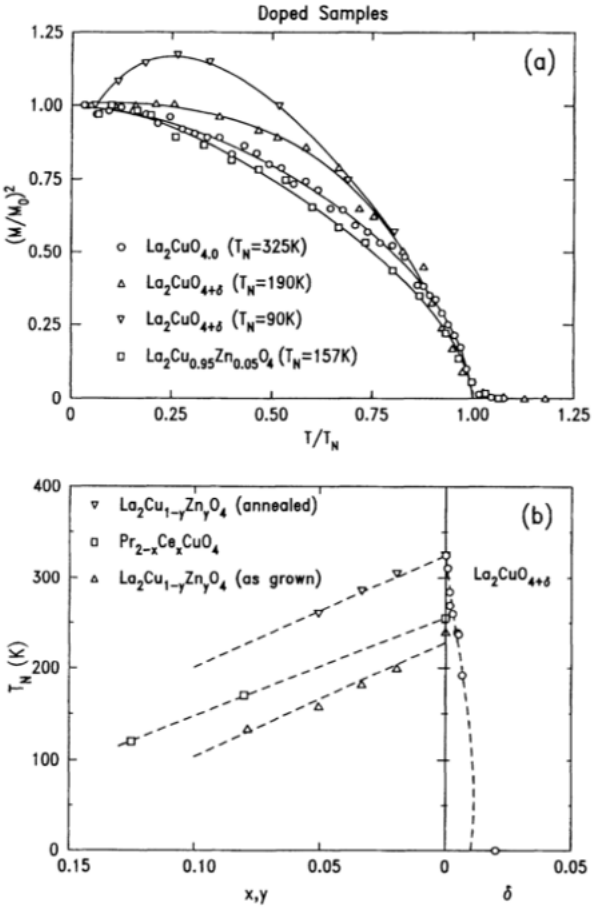

Figure 2.10: Panel (a): magnetisation in reduced units for oxygen- and zinc-doped samples as a function of the ratio of the temperature of the samples and the Néel temperature. Panel (b): Néel temperature for electron doped $Pr_{2-x}Ce_xCuO_4$, oxygen doped $La_2CuO_{4+\delta}$ an Zn doped $La_2Cu_{1-y}Zn_yO_4$ as a function of the doping x, δ, y respectively. Figure taken from Ref. [92].

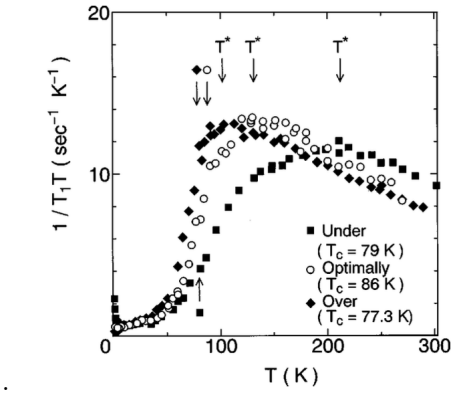

Figure 2.11: NMR spin relaxation rate for $Bi_2Sr_2CaCu_2O_{8+\delta}$ as a function of temperature for different doping. Figure taken from Ref. [93].

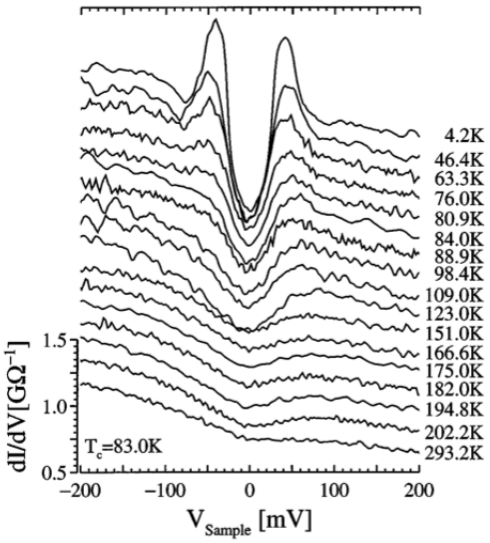

Figure 2.12: Tunnelling spectra measured for several temperatures in under-doped regime for a sample of $Bi_2Sr_2CaCu_2O_{8+\delta}$ with $T_c = 83$ K. Figure taken from Ref. [101].

transport properties, for example in the out-of-plane resistivity $\rho_c(T)$. As shown in Fig. 2.14 this quantity has a non monotonic behaviour in the pseudogap ($x < 0.2$) that becomes linear once we cross the onset temperature T^*. Upon increasing doping ($x > 0.2$), we are in the presence of a "strange metal" state where the resistivity never loses its linear temperature dependence but differs from the one expected in a Fermi liquid, where $\rho_c(T) \approx T^2$ [106].

This unusual behaviour, where the Fermi surface does not present a continuous contour in momentum space, is unprecedented and it occurs in the absence of long-range order. This

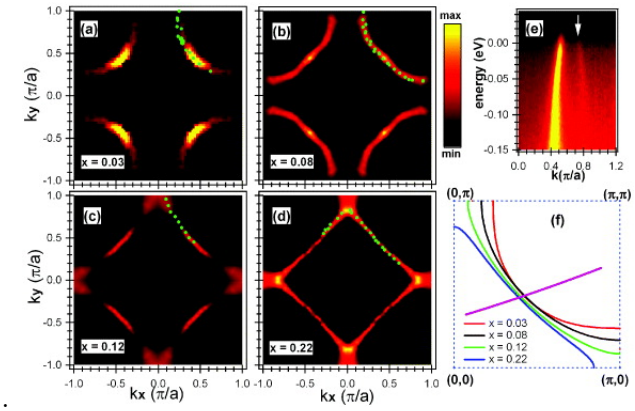

Figure 2.13: Panel (a-d): Fermi surface of $La_{2-\delta}Sr_{\delta}CuO_4$ for several dopings as indicated in the left corner of each panel. Panel (e): ARPES intensity plot, acquired from the $\delta = 0.08$ sample, along the momentum cut indicated in panel (f) by the pink line. Data at $T = 20$K for a non-superconducting sample at $\delta = 0.03$ and at $T = 12$K for all the others superconducting samples. Figure taken from Ref. [102].

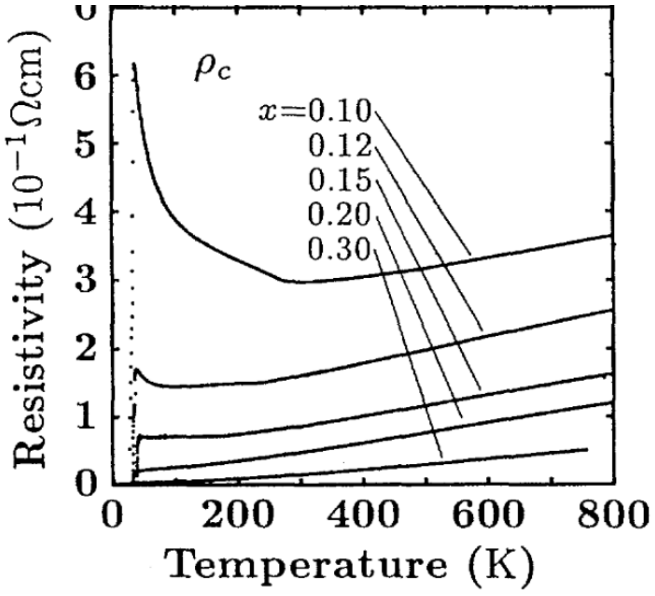

Figure 2.14: Out-of-plane electrical resistivity ρ_c as a function of temperature for samples of $La_{2-x}Sr_xCuO_4$. Figure taken from Ref. [105].

last feature and the other properties of this phase are still puzzling the community and several mechanisms to explain it have been suggested. It could occur because of:

- disorder-broadened long-range ordered phases of Ising-type [107] ;
- fluctuating precursors of a long-range ordered phase limited to T = 0 due to the Bogoliubov-Hohenberg-Mermin-Wagner theorem [108–112];

- Mott physics in two dimensions [32].

In the first two cases, an essential ingredient is the presence of rotational and/or spatial broken-symmetry phases. However, this is not necessary in the last case. This latter mechanism is the one that we will discuss. It only appears if we have a Mott insulating state at zero doping, as observed in hole-doped cuprates, and it is a consequence of the repulsion that causes the strong singlet correlations in two dimensions, left over from the resonating valence bond physics [2,31].

2.4.4 Competing orders

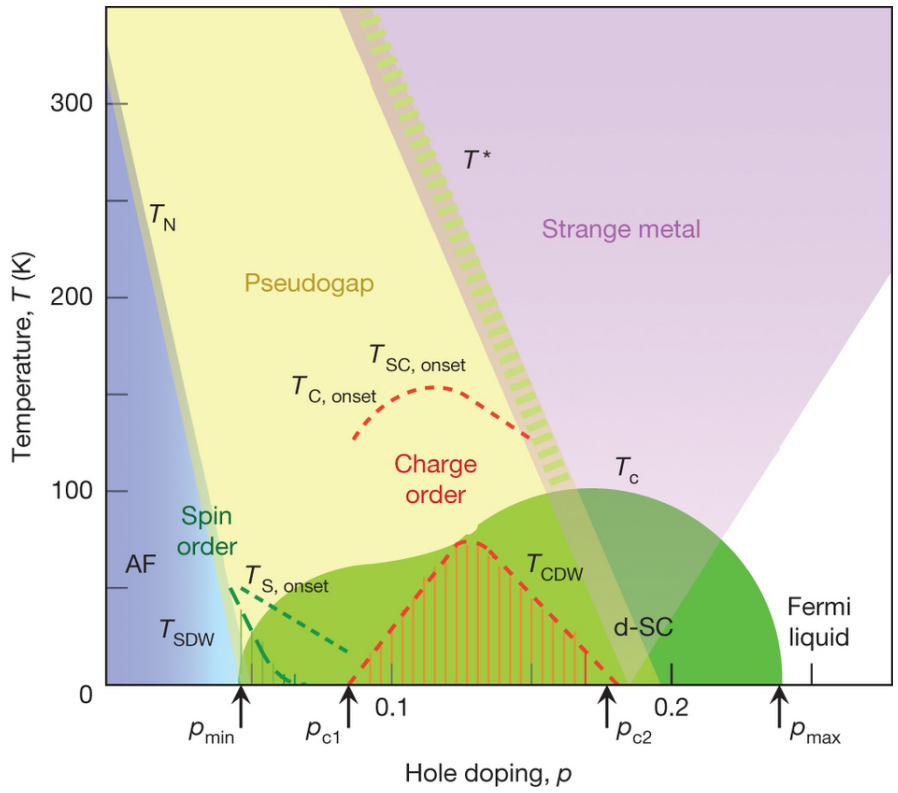

Figure 2.15: Phase diagram temperature versus hole doping for cuprates. The subscript "onset" marks the temperature at which the precursor order or fluctuations become apparent. The dashed green line is the onset temperature for spin order, whereas the dashed red line is the onset temperature for charge order and superconducting fluctuations, and T^* indicates the temperature for the pseudogap crossover. The blue region indicates antiferromagnetic order (AF) and the green one d-wave superconducting order (d-SC). The red striped area indicates charge order. T_{SDW} represents incommensurate spin density wave order. The arrows below the x-axis indicate the quantum critical points for superconductivity and charge order. Figure taken from Ref. [103].

Evidence of new competing phases in the pseudogap region have been found [23], as shown in the more detailed phase diagram of Fig. 2.15. These orders emerge with relatively small

doping of a strongly correlated Mott insulating state [113]. There the electrons organise into collective textures creating new states of matter, such as charge and spin order [114]. Indeed, when a parent compound is doped, a rapid decreasing of the antiferromagnetic correlation length [115] and the appearance of spin order [116, 117] have been observed. This state of matter, characterised by incommensurate antiferromagnetic order and charge segregation, is defined as fluctuating or static stripe order depending on whether these stripes fluctuate over time or not. These appear to be in competition with the superconducting phase [118]. In $La_{2-\delta}Sr_{\delta}CuO_4$ the copper oxide stripes are metallic and superconducting at low temperatures. Evidence has emerged that a charge order is formed in materials with static stripes: in this case the phase reverses from stripe to stripe, but the charge stripes are internally superconducting [113].

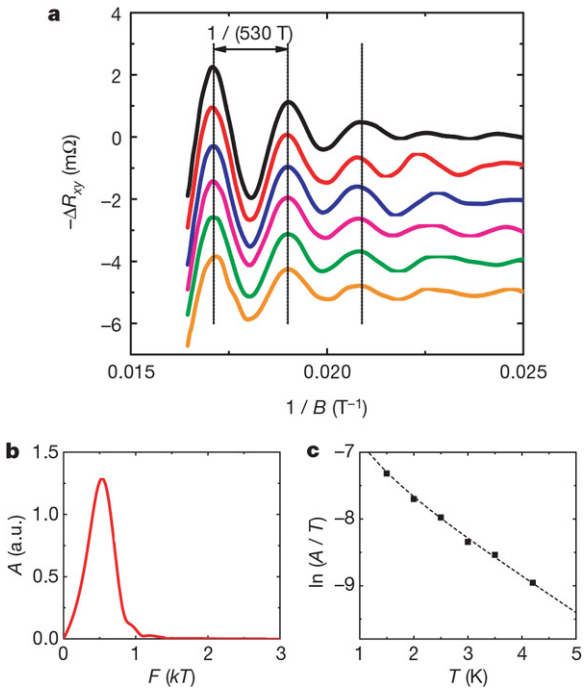

Figure 2.16: Panel (a): the Hall resistance as a function of the inverse magnetic field for a sample of $YBa_2Cu_3O_{6.5}$. Panel (b): power spectrum (Fourier transform) of the oscillatory part. Panel (c): temperature dependence of the oscillation amplitude A, plotted as $\ln(A/T)$ versus T. Figure taken from Ref. [119].

The interest in charge density wave order was originally stimulated by the recent observation of quantum oscillations in the electrical resistance for $YBa_2Cu_3O_{\delta}$ [119]. This demonstrates that the under-doped regime, once superconductivity is suppressed by a magnetic field,

has a well defined Fermi surface in the ground state. This Fermi surface reconstructed in small pockets is widely believed to testify to the presence of charge order [120]. Modulating an external magnetic field, the passage of quantised Landau levels across the Fermi level generates such oscillations, that are considered to be the most robust and direct signature of a coherent Fermi surface. As shown in Fig. 2.16 panel (a), by measuring the electrical resistance of a sample of $YBa_2Cu_3O_6.5$ in presence of an external magnetic field B, quantum oscillations periodic in $1/B$ are clearly visible, as expected from oscillations that arise from Landau quantisation. A Fourier transform yields the power spectrum, displayed in Fig. 2.16 panel (b), which consists of a single frequency, $F = (530 \pm 20)T$. In Fig. 2.16 panel (c) the amplitude of the oscillations are plotted as a function of temperature. This result also suggests a competition between superconductivity and incommensurate spin density wave [23]. All these competing phases are here being taken into consideration to inform the reader about the complexity of the ongoing assessment of the phase diagram of cuprates. It is also important to say that for our theoretical interest we did not take them into account in our calculations even though we have this intention for further studies.

2.5 Other High-Temperature Superconductors

It is worth mentioning that after the discovery of high temperature superconductivity in cuprates, other unconventional superconductor families were found to show this property, as shown in Fig. 2.1.

In 2006 high temperature superconductivity was detected for the first time in iron-based compounds for LaOFeP [121] at 4K and in 2008 for LaOFeAs [122] under pressure up to 43K. Currently iron-based superconductors are the family with the second highest T_c at standard pressure. These compounds have some similarities with the cuprates. They are both strongly correlated electron systems with a layer structure of copper oxide in cuprates and of iron and a pnictogen such as arsenic or phosphorus or a chalcogen for iron-based superconductors. Also the phase diagrams, at first glance, look similar as displayed in Fig. 2.17.

Most undoped iron-based superconductors show a tetragonal-orthorhombic structural phase transition followed at lower temperature by magnetic ordering [124], similar to the cuprate superconductors as shown in Fig 2.17. This magnetic ordering, differently from cuprates, is in

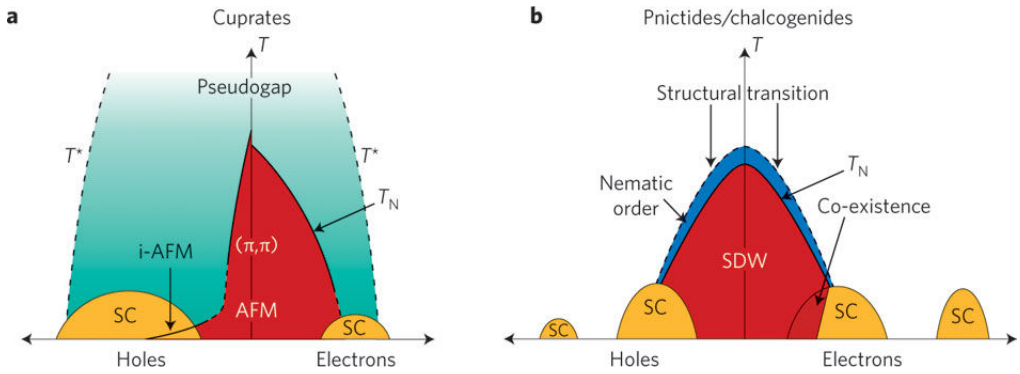

Figure 2.17: Schematic representation of the phase diagram of cuprates on the panel (a) and the iron-based superconductors on the panel (b). In red is coloured the region whit magnetic ordering and in yellow the superconducting one. Peculiar features of each family are the pseudogap for cuprates in light blue and the nematic phase in blue for the iron-based superconductors. Figure taken from Ref. [123].

most of cases antiferromagnetic in one direction and ferromagnetic in the other, namely a stripe order [125]. Another important difference resides in the superconducting order parameter that although still widely debated due to the complex structure of multiple Fermi surfaces [123], appears not to have a d-wave symmetry as shown, for example, in ARPES experiments [126]. Furthermore another striking difference is that the Mott insulating behaviour at half-filling and the pseudogap do not appear at all.

Additionally, fulleride compounds, where alkali-metal atoms are intercalated into C_{60} molecules, show the highest known superconducting critical temperature among molecular superconductors. Indeed, this property was first detected in 1991 [127–129] with a $T_c = 33K$ for Cs_2RbC_{60} [130] and up to $T_c = 38K$ for Cs_3C_{60} [131]. The basic structure, composed of neutral molecules, is insulating with a large Coulomb interaction and by inserting alkaline atoms in the big intermolecular holes, these compounds can show superconducting properties. The interaction responsible for the $s-$wave electron pairing is located on the C_{60} ball and is caused by the vibrational modes of such balls. In other words, as in the BCS model, the Cooper pairs form on this ball due to the vibrations of the mode and then hop from ball to ball. In order to enhance T_c, since these materials are highly compressible, a pressure applied to reduce the distance between fullerenes increases the metal characteristics and changes the critical temperature that for Cs_3C_{60} can arrive up to almost 40 K [131]. Similar results can be obtained at ambient pressure if the alkaline is replaced by another alkaline with a smaller ionic radius, such as Rb with K for instance. These three dimensional materials with partially filled

narrow orbitals are often an example of a Mott transition masked by, or in close proximity to, antiferromagnetism [132–134]. These materials, where conventional phonon-mediated superconductivity and unconventional Mott physics meet together, are superconductors due to the cooperation among the multi-orbital electronic correlations and phonon vibrations [135].

2.6 Conclusion

In this Chapter, we summarised some of the key phenomenological properties of the cuprates. The electronic structure of the cuprates is quasi-two-dimensional and so can be treated with two-dimensional models, vindicating our choice to use the two-dimensional Hubbard model or its three-band extension, the Emery model, as explained in the next Chapter.

The Cooper pair in the superconducting state motivates our choice to confine our investigations on the $d-$wave superconductivity, as we will discuss in Chapters 5 and 6.

The antiferromagnetic phase appears to be ubiquitous in the phase diagram of cuprates, and its properties are discussed in Chapter 4.

The pseudogap phase presents many features that are still enigmatic for the community. Our analysis links it with the Mott transition that takes place at half-filling for the parent compounds, the signature of which survives upon doping a Mott insulator. Indeed in this case, we can observe a new transition, this time between a pseudogap and a correlated metal. The physics of Mott appears to organise the normal, superconducting, and antiferromagnetic states as we will see further in Chapter 4, 5, and 6.

Chapter 3

Model and Methodology

3.1 Introduction

After the previous discussion in which some of the properties that characterise the cuprates were introduced, this chapter is devoted to the model and methodology that was used to obtain the results presented in the rest of the thesis.

The challenge in understanding the high-temperature superconductivity demonstrated in the cuprates arises from the fact that the interactions are too strong [2] to be treated with a simple perturbative approach. Moreover, the predictions of conventional band theory fail in many cases. For example, according to the band theory the parent compound must demonstrate metallic properties, in actual fact they are insulators, as discussed in the previous chapter. Band theory fails because it does not consider electron-electron correlations [136]. The seminal work of Sir Nevill Mott studied the effects of these electronic correlations that drive the so-called Mott transition [137]. He argued that upon considering an array of atoms at half-filling (i.e. one electron per site) with an intra-atomic Coulomb repulsion we can find a paradox in band theory. Indeed, this system is metallic when the atoms are arranged near one another, because the electrons can freely hop from site to site, with hopping amplitude t, and so will delocalise to form a band. Starting from a half-filled band, according to band theory, this system will remain metallic no matter how far apart we pull the atoms. That is to say, in band theory, although we will have to renormalise the hopping parameter, the system will always be metallic no matter how large the lattice constant. Here, we find a contradiction: in-

creasing the lattice separation, we eventually end up with an array of atoms with the electrons localised on each atom, well localised around their nucleus, i.e. an insulator [136]. So why does a metallic state become an insulator upon varying the lattice separation? As pointed out by Mott [138], this insulating state rises thanks to the electron-electron correlations. We have an energy cost U (the intra-atomic Coulomb energy) to let the electrons hop to an occupied state. We can argue, comparing the kinetic energy and the potential energy of this system, that there is a certain critical value of the ratio U/t above which the charge fluctuations are suppressed, leading to an insulator. Thus, Mott stated that increasing lattice spacing or the number of electrons, the conductivity will jump from a finite value to zero, in other words, the system presents a metal to insulator first-order transition. This transition explains the properties of the undoped compounds and its understanding is of primary importance to comprehend the phase diagram of the cuprates of Fig. 2.2, in which the Mott insulator state evolves to a metallic state by passing from an undoped to a strong doping regime.

The Mott transition is well described with the Hubbard model as discussed in Section 3.2. The absence of an analytical solution for it necessitates the development of numerical approaches. Among the many currently being employed, we use the Dynamical Mean-Field Theory as introduced in Section 3.3. This methodology is based on the approximation that the self energy is momentum-independent. In order to address phases such as the $d-$wave superconductivity we need to use a cluster extension called Cellular Dynamical Mean-Field Theory, discussed in Section 3.4. The basic idea of the Dynamical Mean-Field Theory and its extensions is to map the Hubbard model onto an Anderson impurity model that is solved using a numerical approach. Its solution is then used via self-consistency conditions as the solution for the original Hubbard model, reiterating this loop until within the desired accuracy. Among the possible ways to treat the impurity problem we use the Continuous-Time Hybridisation Expansion Algorithm as outlined in Section 3.5. Finally, in Section 3.6 we will discuss a three band extension of the Hubbard model, called the Emery model.

3.2 Two-Dimensional Hubbard Model

The essential physics in cuprates is due to the electronic states of the Cu $d_{x^2?y^2}$ and the O p_x, p_y orbitals. Therefore, a three-band model such as the Emery model of Section 3.6 is a

good starting point to understand the generic features of the cuprates. However a single band

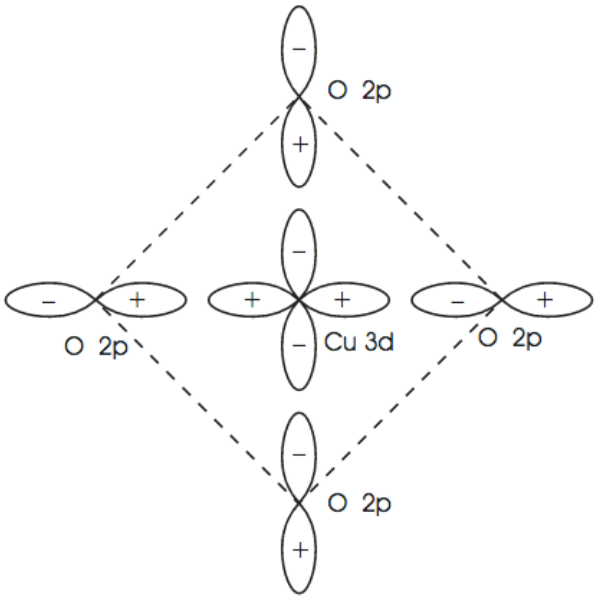

Figure 3.1: Schematic diagram of a CuO_4 cluster. The Cu $3d_{x^2-y^2}$ orbital is surrounded by 2 O $2p_x$, $2p_y$ orbitals; these orbitals hybridise together in a Zhang and Rice singlet. Figure taken from Ref. [139]

model can describe the underling physics of the cuprates, as motivated by the proof of Zhang and Rice that demonstrated how a strong hybridisation between the oxygens and copper forms a local singlet between a hole in the oxygens and a central ion of Cu^{2+} [6] (Fig. 3.1). The resulting Hamiltonian of the Zhang-Rice singlets in the CuO_2 plane reduces to a single-band Hubbard model. In two-dimensions the single-band Hubbard model Hamiltonian is given:

$$H_{HM} = -\sum_{\langle i,j\rangle,\sigma} t_{ij}(c^{\dagger}_{i\sigma}c_{j\sigma} + c^{\dagger}_{j\sigma}c_{i\sigma}) + U\sum_{i} n_{i\uparrow}\, n_{i\downarrow}, \tag{3.1}$$

where $c^{\dagger}_{i\sigma}$, $c_{i\sigma}$ and $n_{i\sigma} = c_{i\sigma}c^{\dagger}_{i\sigma}$ are respectively, the creation, annihilation and the number operator for an electron in the site i with spin σ, t_{ij} is the hopping probability from a site i to a site j, and U the Coulomb potential energy. This Hamiltonian is derived from a single band model expanded in the Wannier basis $w(r - R_i)$ associated with the Bloch states:

$$\psi(r) = \sum_{R_i} w(r - R_i)c_{R_i} := \sum_{i} |i\rangle c_i. \tag{3.2}$$

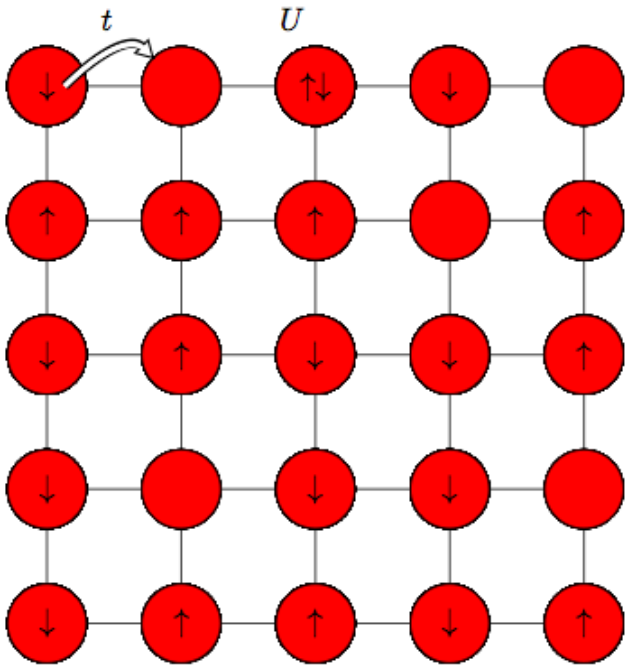

Figure 3.2: Sketch of Hubbard model. The electrons are able to jump from neighbouring sites with hopping probability t meanwhile there is an energy cost U in the case of double occupancy.

The more general Hamiltonian in the presence of the Coulomb interaction V_C can be written as:

$$H = \sum_{\sigma,i,j} c^{\dagger}_{i\sigma} \langle i|T_{kin}|j\rangle c_{j\sigma} + \frac{1}{2} \sum_{\sigma,\sigma',i,j,k,l} \langle i|\langle j|V_C|k\rangle|l\rangle c^{\dagger}_{i\sigma} c^{\dagger}_{j\sigma'} c_{k\sigma} c_{l\sigma'}. \tag{3.3}$$

This model is quite complicated and an important approximation in order to obtain a simplification of it was constructed by Hubbard, Kanamori and Gutzwiller with three almost simultaneous publications in 1963 [17–19]. Assuming that the highest contribution to $\langle i|\langle j|V_C|k\rangle|l\rangle$ arises when all lattice sites are equal and defining $t_{ij} := \langle i|T_{kin}|j\rangle$ and $U := \langle i|\langle i|V_C|i\rangle|i\rangle$ we finally obtain Eq. (3.1). This model encodes two different tendencies for electrons in a lattice:

- The tendency for the electrons to become delocalised, jumping from site to site, leading towards a metallic state.
- The part proportional to U attempts to localise each electron on a single site, leading towards an insulating state.

These two tendencies are quite clear if we analyse the system at half-filling in the two limits $t_{ij} \to 0$ or $U \to 0$. In the former case, the Hamiltonian is diagonal in the localised Wannier

basis, and the electrons are localised. In case of finite hopping and strong coupling, by using standard perturbation theory, the Hubbard model becomes the $t-J$ model:

$$H_{t-J} = -\sum_{\langle i,j\rangle,\sigma} t_{ij}(c^{\dagger}_{i\sigma}c_{j\sigma} + c^{\dagger}_{j\sigma}c_{i\sigma}) + J\sum_{\langle i,j\rangle}\left(\vec{S}_i\vec{S}_j - \frac{n_i\, n_j}{4}\right), \tag{3.4}$$

where $J = 4t^2/U$ is the super-exchange energy and $\vec{S}_i$ the spin of the site i.

In the latter case $U \to 0$, the Hamiltonian 3.1 is diagonal in the momentum basis, and the electrons have delocalised eigenvectors, in other words, they are free to hop without any impediment from the interaction U. So the question that arises from these two limits is: what happens to an intermediate value of the ratio U/t? The answer is the first-order Mott transition. To show this, we need to use a numerical approach such as the Dynamical Mean-Field Theory because, even though this is the simplest model of interacting electrons, it is far from simple to solve.

3.3 Dynamical Mean-Field Theory

In this Section, we will introduce the Dynamical mean-field theory (DMFT) of strongly correlated fermion systems [21,140]. The purpose of this theory is to approximate a lattice problem with many degrees of freedom by a single-site effective system with fewer degrees of freedom. We will take into account local quantum fluctuations, i.e. temporal fluctuations among the possible quantum states at a given site on the lattice. This theory is a natural generalisation for the quantum mechanics of the mean-field theory in classical statistical mechanics, where the interactions of the system on a specific site are approximated by their average and are treated as an external bath. It will be useful to discuss an example of this classical theory in order to make the generalisation to DMFT more clear.

3.3.1 Mean-Field Theory: the Ising Model

A simple model that can be treated with this approach is the Ising model:

$$H_{IM} = -\sum_{\langle i,j\rangle}^{n_s} J_{ij}S_iS_j - h\sum_{i}^{n_s} S_i\ , \tag{3.5}$$

where $\langle i, j \rangle$ denotes the nearest-neighbour, n_s the number of sites in the lattice, $J_{ij} > 0$ is the ferromagnetic coupling, S_i the spin with values 1 and -1, and h is an external magnetic field. This model can be addressed using a mean field theory approach. Practically, this means that we have to choose a site $\bar{k}$ and replace the lattice model by a single-site model embedded in an effective medium. In other words, we are going to map the problem of interacting spins to a problem of non-interacting ones in an effective bath. So we have an effective Hamiltonian:

$$H_{IM}^{(eff)} = -h_{eff} S_{\bar{k}}, \tag{3.6}$$

where we have introduced the effective (Weiss) field h_{eff} that for a lattice with coordinate z is:

$$h_{eff} = h + \sum_i J_{\bar{k}i} \langle S_i \rangle \approx h + Jmz, \tag{3.7}$$

with $m_i = \langle S_i \rangle$ the magnetisation at the site i, and assuming translational invariance ($J_{ij} = J$, $m_i = m$). This one-spin problem can now be solved and the thermal average of this spin is:

$$\langle S_i \rangle = \frac{1}{Z} \sum_{\{S\}} S e^{-S\beta h_{eff}} = \frac{e^{\beta h_{eff}} - e^{-\beta h_{eff}}}{e^{\beta h_{eff}} + e^{-\beta h_{eff}}} = \tanh(\beta h_{eff}). \tag{3.8}$$

$\{S\}$ denotes all the possible spin configurations and $\beta = \frac{1}{KT}$ with K the Boltzmann constant. Now we have to impose the self-consistency relation, i.e. the value of the magnetisation m predicted by single-site model Eq. (3.7) should be equal to the value of m from Eq. (3.8):

$$m = \tanh(\beta h_{eff}) \approx \tanh(\beta h + \beta z J m) \tag{3.9}$$

This is an approximate solution. Indeed these mean-field equations are, in general, an approximation of the exact solution of the Ising model. They become exact in the limit of large lattice coordination: $z \to \infty$. Intuitively, when the number of neighbours of a given site is large enough, they can globally be treated as an external bath. Coupling J must be scaled as J/z to yield a sensible limit $z \to \infty$, i.e. to keep finite the critical temperature T_c.

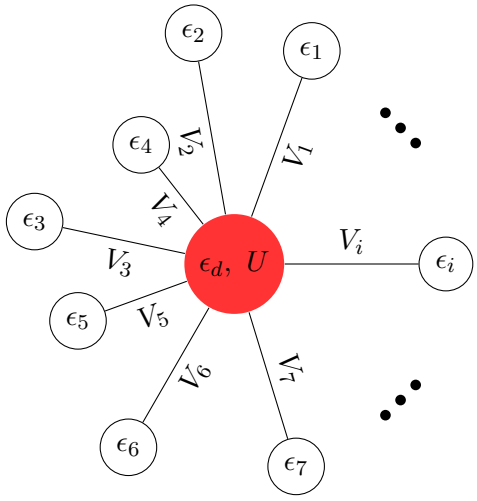

Figure 3.3: Sketch of the Anderson impurity model of Eq. (3.11). An impurity with energy ϵ_d and interaction U coupled with a non interacting bath with energy ϵ_i and coupling constant V_i for each site.

3.3.2 Generalisation to the Quantum Case: Dynamical Mean-Field Theory

The previous approach can be extended to quantum systems. The Dynamical Mean-Field Theory can be used for systems of any dimension and becomes exact in the limit of infinite lattice coordination [140, 141]. Here we present the formulation of the Dynamical Mean-Field Theory [21] for the study of the normal state of the two-dimensional Hubbard model of Eq. (3.1). The size of the Hilbert space for n sites, in the two dimensional case of our interest, is 4^n and an analytical solution for this problem does not exist. The key quantity on which DMFT focuses is the local Green function at a given lattice site:

$$G_{ii}^{(\sigma)}(\tau - \tau') = -\langle T c_{i\sigma}(\tau) c_{i\sigma}^{\dagger}(\tau') \rangle. \tag{3.10}$$

Here T is the time-ordering operator, τ the imaginary time and $\langle \dots \rangle = \int_0^\beta d\tau \dots$ denotes the imaginary time average. In analogy to the mean-field theory for the Ising model, where the local magnetisation m_i is represented as that of a single spin of site i coupled to an effective field h_{eff}, here we introduce the representation of the local Green function as that of a single "atom" coupled to an effective bath. Mathematically, this can be described by the Hamiltonian of the so-called Anderson impurity model (AIM) [142], which describes an impurity embedded

in a bath of electrons:

$$H_{AIM} = \sum_{i,\sigma} \epsilon_i c^\dagger_{i\sigma} c_{i\sigma} + \sum_{i,\sigma} V_i (c^\dagger_{i\sigma} d_\sigma + d^\dagger_\sigma c_{i\sigma}) + \epsilon_d \sum_\sigma n_{d\sigma} + U n_{d\uparrow} n_{d\downarrow}, \tag{3.11}$$

where $c^\dagger_{i\sigma}$, $c_{i\sigma}$ and $d^\dagger_\sigma$, d_σ are respectively, the creation, annihilation operators of the conduction and of the impurity electrons, $\epsilon_i,\ \epsilon_d$ the energies of the electrons and of the impurity, $n_{d\sigma} = d^\dagger_\sigma d_\sigma$ is the number operator of the impurity $d-electrons$. The parameters $\{\epsilon_i\}$ and $\{V_i\}$ must be chosen in such a way that the local Green function of Eq. (3.11) coincides with the one of the original model (3.1) for a given site. Introducing the action formalism for this system, we can demonstrate that these parameters enter only through the so-called *hybridization function*:

$$\Delta(\imath\omega_n) = \sum_i \frac{|V_i|^2}{\imath\omega_n - \epsilon_i}, \tag{3.12}$$

where we have introduced the odd Matsubara frequency:

$$\omega_n \equiv \frac{(2n+1)\pi}{\beta}.$$

In general, the partition function Z is:

$$Z = Tre^{-\beta H}. \tag{3.13}$$

In general, in a system that respects Fermi statistics, the variables $\{\phi_i,\ \phi^*_i\}$ are anti-commuting. Their algebra was first introduced by Hermann Grassmann [143]. For a Fermi system with Grassmann variables $\{\phi_i,\ \phi^*_i\}$ the trace of an operator A is given by:

$$TrA = \int \frac{\prod_i d\phi^*_i d\phi_i}{2\imath\pi} e^{-\sum_i \phi^*_i \phi_i} \langle -\phi | A | \phi \rangle. \tag{3.14}$$

So in our case Eq. (3.13) becomes:

$$Z = \int \mathcal{D}d^\dagger_\sigma \mathcal{D}d_\sigma \prod_i \mathcal{D}c^\dagger_{i\sigma} \mathcal{D}c_{i\sigma} e^{S_0 - \Delta S}, \tag{3.15}$$

with:

$$\int_{x_i,t_i}^{x_f,t_f} \mathcal{D}x(t) = \lim_{M\to\infty} \int \prod_{k=1}^{M-1} \frac{dx_k}{(2\imath\pi)^{\frac{3M}{2}}}.$$

Where we have implicitly divided the interval $\{(x_i,t_i),(x_f,t_f)\}$ into M steps and we have also, divided the total action into two parts. S_0 is the purely local part concerned with the impurity:

$$S_0 = \int_0^\beta d\tau \int_0^\beta d\tau' \sum_\sigma d_\sigma^\dagger(\tau)(\partial_\tau + \epsilon_d) d_\sigma(\tau') + \int_0^\beta d\tau U n_{d\uparrow}(\tau) n_{d\downarrow}(\tau), \tag{3.16}$$

while ΔS includes the rest of the total action:

$$\Delta S = \int_0^\beta d\tau \int_0^\beta d\tau' \sum_{i\sigma} c_{i\sigma}^\dagger(\tau)(\partial_\tau + \epsilon_i) c_{i\sigma}(\tau') + V_i(c_{i\sigma}^\dagger(\tau) d_\sigma(\tau') + d_\sigma^\dagger(\tau) c_{i\sigma}(\tau')). \tag{3.17}$$

The part of Eq. (3.15) that involves the electrons is quadratic in $c_{i\sigma}^\dagger$, $c_{i\sigma}$ and following these substitutions:

- $\eta^*, \eta \to c_{i\sigma}^\dagger, c_{i\sigma}$,
- $\zeta_i, \zeta_i^* \to V_i d_\sigma, V_i d_\sigma^\dagger$,
- $H_0 \to {G^{-1}}_0(\tau) = \partial_\tau + \epsilon_i \xrightarrow{Fourier\ transform} {G^{-1}}_0(\imath\omega_n) = -\imath\omega_n + \epsilon_i$,

it can be computed by using the formula for the Gaussian integral of Grassmann variables:

$$\int \prod_i d\eta^* d\eta e^{-\eta_i^* H_{ij} \eta_j + \zeta_i^* \eta_i + \zeta_i \eta_i^*} = \det(H) e^{\zeta_i^* H_{ij}^{-1} \zeta_j}. \tag{3.18}$$

Finally, the partition function of Eq. (3.15) is:

$$\begin{aligned} Z &= \det(G_0) \int \mathcal{D}d_\sigma^\dagger \mathcal{D}d_\sigma e^{-S_0 - \int_0^\beta d\tau \int_0^\beta d\tau' d_\sigma^\dagger(\tau) \left(\sum_i \frac{|V_i|^2}{\imath\omega_n - \epsilon_i}\right) d_\sigma(\tau')} = \\ &= \det(G_0) \int \mathcal{D}d_\sigma^\dagger \mathcal{D}d_\sigma e^{-S_0 - \int_0^\beta d\tau \int_0^\beta d\tau' d_\sigma^\dagger(\tau) \Delta(\tau,\tau') d_\sigma(\tau')}. \end{aligned} \tag{3.19}$$

In this way, using Eqs. 3.16 and 3.19, we can define an effective action for the impurity that

reads:

$$S_{eff} \equiv const. - \int_0^\beta \int_0^\beta d\tau d\tau' \sum_\sigma d_\sigma^\dagger(\tau) G_{0imp}^{-1}(\tau,\tau') d_\sigma(\tau') + \int_0^\beta d\tau U n_{d\uparrow}(\tau) n_{d\downarrow}(\tau), \quad (3.20)$$

where we have introduced:

$$G_{imp}^{-1}(\tau,\tau') = \frac{1}{-\partial_\tau - \epsilon_d - \Delta(\tau,\tau')} \xrightarrow{Fourier\ transform} G_{0imp}^{-1}(\imath\omega_n) = \frac{1}{\imath\omega_n - \epsilon_d - \Delta(\imath\omega_n)}.$$

$G_{0imp}^{-1}(\imath\omega_n)$ is the non-interacting ($U = 0$) Green function of the single impurity model and it plays the role of an effective field of the Ising model with the difference that here this "field" is a function of the imaginary time instead of a single number. From the above equation we can define a local self-energy from the interacting Green function:

$$G_{imp}(\tau - \tau') = -\langle T d(\tau) d^\dagger(\tau') \rangle_{S_{eff}}. \quad (3.21)$$

Taking $G(k, \imath\omega_n)$ as the momentum dependent lattice Green function, we want to determine the hybridisation function $\Delta(\imath\omega_n)$ such that the impurity Green function $G_{imp}(\imath\omega_n)$ reproduces the local lattice Green function of Eq. (3.10):

$$\sum_k G(k, \imath\omega_n) = G_{imp}(\imath\omega_n). \quad (3.22)$$

Keeping in mind that:

$$G(k, \imath\omega_n) = \frac{1}{\imath\omega_n + \mu - \epsilon_k - \Sigma(k, \imath\omega_n)}, \quad (3.23)$$

Eq. (3.22) is exact only when the lattice self-energy $\Sigma(k, \imath\omega_n)$ has only local terms and it coincides with the impurity self-energy. Otherwise we need the DMFT approximation:

$$\Sigma(k, \imath\omega_n) \approx \Sigma(\imath\omega_n) = \Sigma_{imp}(\imath\omega_n). \quad (3.24)$$

Introducing the Dyson equation for the lattice Green function and for the impurity model:

$$\Sigma(k, \imath\omega_n) = G_0^{-1}(k, \imath\omega_n) - G^{-1}(k, \imath\omega_n), \quad (3.25)$$

$$\Sigma_{imp}(\imath\omega_n) = G_{0imp}^{-1}(\imath\omega_n) - G_{imp}^{-1}(\imath\omega_n), \quad (3.26)$$

the relation of self-consistency, Eq. (3.22), for $\mu = \epsilon_d$ becomes:

$$\sum_k G(k, \imath\omega_n) = \sum_k \frac{1}{\imath\omega_n + \mu - \epsilon_k - \Sigma_{imp}(\imath\omega_n)} = \\ = \sum_k \frac{1}{\Delta(\imath\omega_n) - \epsilon_k - G^{-1}_{imp}(\imath\omega_n)} = G_{imp}(\imath\omega_n). \tag{3.27}$$

In this way, as outlined in Fig. 3.4, we obtain a self-consistency condition for the impurity

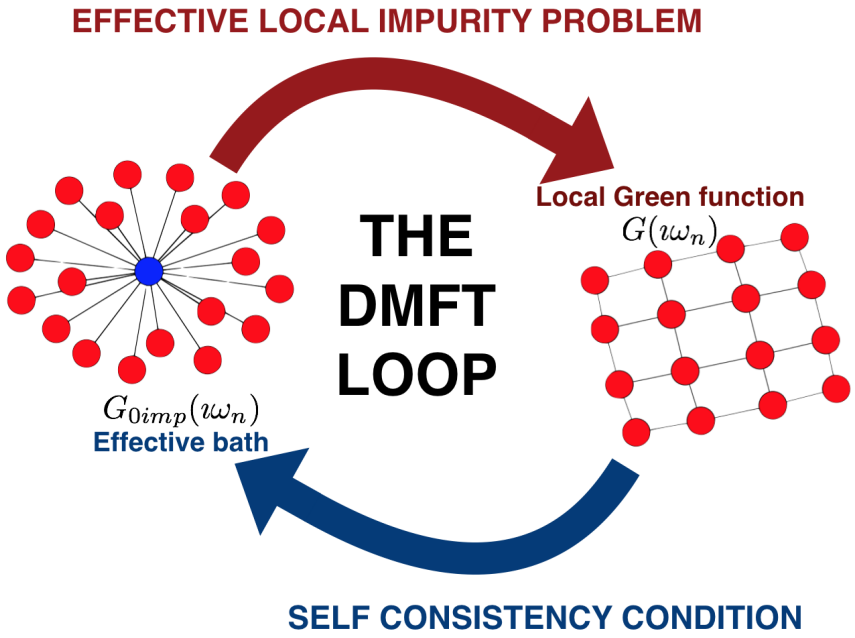

Figure 3.4: Sketch of the Dynamical Mean-Field Theory loop.

model dependent on the hybridisation function $\Delta(\imath\omega_n)$, that plays the role of a dynamical mean field. This procedure is iterative because the solution of the impurity problem must be computed with numerical methods (impurity solvers), such as the Continuous-Time Quantum Monte Carlo discussed in sec. 3.5. Such a solution is then employed to repeat the DMFT loop until convergence of the self energy is reached.

It is interesting to note that the DMFT approximation of Eq. (3.24) becomes exact in two cases:

- *The non interacting limit (U=0)*: from Eq. (3.20) we immediately get that $G(\imath\omega_n) = G_{0imp}(\imath\omega_n)$ and indeed we have $\Sigma_{imp}(\imath\omega_n) = 0 \Longrightarrow G(k, \imath\omega_n) = \frac{1}{\imath\omega_n + \mu - \epsilon_k}$.
- *The atomic limit ($t_{ij} = 0$)*: in this case $\epsilon_k \equiv \sum_{ij} t_{ij} e^{\imath \mathbf{k}(\mathbf{R_i} - \mathbf{R_j})} = 0$,and from Eq.

(3.27) we immediately get $\Delta(\imath\omega_n) = 0 \Longrightarrow V_i = 0 \ \forall \ i$ thus the sites are isolated and $\Sigma_{imp}(k, \imath\omega_n) = \Sigma_{imp}(\imath\omega_n)$.

In contrast with the mean-field approaches, the DMFT gives a full account of the dynamical properties of the model, allowing the study of systems characterised by the presence of many energy scales. Furthermore, there is no bias towards any specific coupling regime allowing a systematic study of these different energy ranges. However, when we use this technique, we also have to be aware of some liabilities. The biggest disadvantage of this method is its local mean-field character. This is the main motivation to generalise it from a single site impurity problem to a cluster one [25, 144]. This is the topic of the next Section.

3.4 Cellular-DMFT

Prior to this section we have considered a single site of the lattice as the impurity of the system, but in doing this we have lost completely any k dependence for the self-energy as made clear by the DMFT approximation of Eq. (3.24). Here we will introduce an extension of this method to include spatial correlations whilst preserving its dynamical character. In this case we will treat as the impurity not just a single site, but a finite size plaquette. The DMFT equations were unambiguously obtained through a systematic expansion around the infinite-dimension limit [140], but this limit cannot define a unique mean-field scheme which selects some spatial degrees of freedom (those of the cluster), treating the others at a mean-field level [25, 144]. In this section, we will discuss one of the possible methods that allows this, the so-called Cellular-DMFT. The cluster has open boundary conditions and the effective action is built without constraint, but the translational symmetry is broken. In this case we need first to define the topology of the cluster. Due to the actual choice that we have made for our calculations, we will treat the case of a two by two square plaquette, the minimum size of a cluster able to encode the d-wave symmetry of the superconducting phase. Such a choice immediately defines the set of arrays for the real space $\mathbf{X}$:

$$\mathbf{X} = \{(0,0), (1,0), (0,1), (1,1)\} \tag{3.28}$$

This set in the momentum space becomes:

$$\mathbf{K} = \{(0,0),(\pi,0),(0,\pi),(\pi,\pi)\} \tag{3.29}$$

It is also useful to introduce the set of arrays that define the superlattice $\tilde{\mathbf{x}}$ and that map the position of any site of the cluster onto the neighbouring ones:

$$\tilde{\mathbf{x}} = \{(0,0),(2,0),(0,2),(-2,0),(0,-2)\} \tag{3.30}$$

The $\tilde{\mathbf{k}}$ vector for any cluster is:

$$\tilde{\mathbf{k}} = (k_x, k_y) \tag{3.31}$$

Similarly to the DMFT case, we can obtain an equation analogous to Eq. (3.20).

$$S^{(c)}_{eff} = -\int_0^\beta d\tau d\tau' \sum_{i,j,\sigma} d^\dagger_{\sigma,i}(\tau)\left[\mathbf{G^{-1}_{0imp}}(\tau-\tau')\right]_{ij} d_{\sigma,j}(\tau') + \int_0^\beta d\tau U n_{\uparrow,i}(\tau) n_{\downarrow,i}(\tau), \tag{3.32}$$

where i and j span the cluster coordinate $\mathbf{X}$. The cluster Green function is then defined as:

$$\mathbf{G_c}(\tau-\tau')_{ij} = -\langle T d_i(\tau) d^\dagger_j(\tau')\rangle_{S^{(c)}_{eff}} \tag{3.33}$$

and then the cluster self-energy in matrix notation after a Fourier transform:

$$\mathbf{\Sigma_c}(\imath\omega_n) = \mathbf{G}^{-1}_{0imp}(\imath\omega_n) - \mathbf{G}^{-1}_c(\imath\omega_n) \tag{3.34}$$

With the exception of $\mathbf{X}$, $\tilde{\mathbf{x}}$, $\mathbf{K}$, $\tilde{\mathbf{k}}$, we denote quantities that are represented with 4 X 4 matrices in bold. Now introducing the following approximation:

$$\mathbf{\Sigma}(\tilde{\mathbf{x}}_\mathbf{i} - \tilde{\mathbf{x}}_\mathbf{j}, \imath\omega_n) \approx \mathbf{\Sigma_c}(\imath\omega_n), \tag{3.35}$$

i.e. neglecting the inter-cluster contributions of the self-energy, we can build a lattice Green function as:

$$\mathbf{G}(\tilde{\mathbf{k}}, \imath\omega_n) = \left[(\mu + \imath\omega_n)\mathbb{1} - \mathbf{t}(\tilde{\mathbf{k}}) - \mathbf{\Sigma_c}(\imath\omega_n)\right]^{-1}. \tag{3.36}$$

Where we have introduced the Fourier transform of the hopping matrix $\mathbf{t}(\mathbf{X})$ with respect to the superlattice vectors:

$$\mathbf{t}(\tilde{\mathbf{k}}) = \sum_i e^{-\imath \tilde{\mathbf{k}} \tilde{\mathbf{x}}_i} \mathbf{t}(\mathbf{X}) = \sum_i e^{-\imath \tilde{\mathbf{k}} \tilde{\mathbf{x}}_i} \begin{pmatrix} 0 & t & t' & t \\ t & 0 & t & t' \\ t' & t & 0 & t \\ t & t' & t & 0 \end{pmatrix}, \tag{3.37}$$

with t, t' the hopping constants for nearest and next-nearest neighbours respectively. In order to obtain the local Green function of the cluster, we have to integrate over the Brillouin zone Eq. (3.36):

$$\mathbf{G}(\imath\omega_n) = \frac{1}{4} \int \frac{d\tilde{\mathbf{k}}}{(\mu + \imath\omega_n)\mathbb{1} - \mathbf{t}(\tilde{\mathbf{k}}) - \mathbf{\Sigma_c}(\imath\omega_n)}. \tag{3.38}$$

Imposing that this last Green function of the cluster, calculated using the intra-cluster contributions of the self-energy, must reproduce the Green function of the effective problem (3.33), we obtain the self consistency equation of the Cellular Dynamical Mean-Field Theory:

$$\mathbf{G}(\imath\omega_n) = \mathbf{G}_c(\imath\omega_n). \tag{3.39}$$

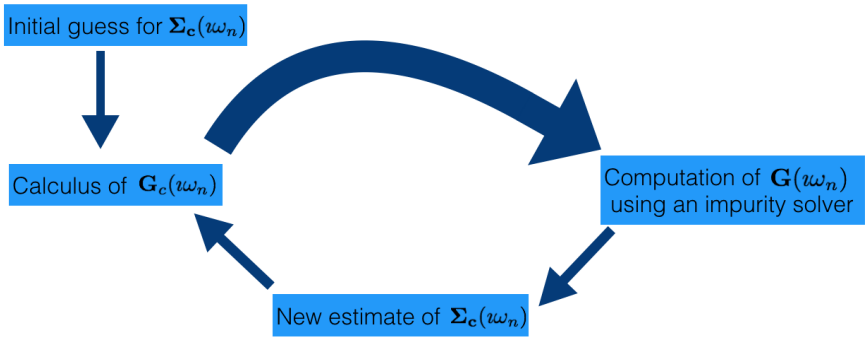

Figure 3.5: Sketch of the Cellular Dynamical Mean-Field Theory loop.

We can summarise this self consistency procedure, as shown in Fig. 3.5:

(i) the first step of this procedure is to choose a guess for the cluster self-energy $\mathbf{\Sigma_c}(\imath\omega_n)$;

(ii) the previous step is used to calculate $\mathbf{G}_c(\imath\omega_n)$ by means of Eq. (3.34);

(iii) an impurity solver is then used to calculate the Green function of the effective problem $\mathbf{G}(\imath\omega_n)$ of Eq. (3.38);

(iv) From the previous step a new estimate of the cluster self-energy is obtained $\mathbf{\Sigma_c}(\imath\omega_n)$, which is used to reiterate the loop until within the desired accuracy.

3.5 Continuous-Time Hybridisation Expansion Algorithm

As mentioned in the previous Sections, we need an impurity solver to calculate the Green function of the effective problem. In this section, we will briefly derive the Continuous-Time Hybridisation Expansion Algorithm (CT-HYB) [26, 27]. We will confine the discussion to the single site problem that is analogous to the cluster one. This approach was introduced as an impurity solver for the Anderson impurity problem [145, 146], so we will begin the discussion from the Hamiltonian (3.11) that can be re-expressed as:

$$H_{AIM} = H_{Loc} + H_{Bath} + H_{Hyb} \tag{3.40}$$

with:

$$H_{Loc} = \epsilon_d \sum_{\sigma} n_{d\sigma} + U n_{d\uparrow} n_{d\downarrow},$$

$$H_{Bath} = \sum_{i,\sigma}^{n} \epsilon_i c^{\dagger}_{i\sigma} c_{i\sigma},$$

$$H_{Hyb} = \sum_{i,\sigma}^{n} V_{i\sigma} (c^{\dagger}_{i\sigma} d_{\sigma} + d^{\dagger}_{\sigma} c_{i\sigma}).$$

In this context, it is convenient to switch to an interaction representation in which the time evolution of a generic operator $\mathcal{O}$ is:

$$\mathcal{O}(\tau) = e^{\tau(H_{Loc}+H_{Bath})} \mathcal{O} e^{-\tau(H_{Loc}+H_{Bath})}, \tag{3.41}$$

with imaginary time τ. The partition function of the system, performing a Taylor expansion of $e^{-\int_0^\beta d\tau H_{Hyb}(\tau)}$, can be written as:

$$Z = \operatorname*{Tr}_d \operatorname*{Tr}_c \left(e^{-\beta(H_{Loc}+H_{Bath})} T e^{-\int_0^\beta d\tau H_{Hyb}(\tau)} \right) =$$
$$= \underbrace{\sum_{n=0}^{\infty} \int_0^\beta \cdots \int_0^\beta}_{\sum_{\mathcal{C}}} \underbrace{d\tau_1 \dots d\tau_{2n} \operatorname*{Tr}_d \operatorname*{Tr}_c e^{-\beta(H_{Loc}+H_{Bath})} \frac{(-1)^n}{2n!} \left((H_{Hyb}(\tau_{2n}) + H^\dagger_{Hyb}(\tau_{2n})) \dots H_{Hyb}(\tau_1) \right)}_{w_{\mathcal{C}}},$$

where $\operatorname*{Tr}_d$, $\operatorname*{Tr}_c$ represent the trace of the impurity's and bath's operators respectively. $\sum_{\mathcal{C}}$ represents the summation over the possible configurations within the imaginary time interval and $w_{\mathcal{C}}$ is the weight for each configuration. It is now possible to construct a Monte Carlo procedure in order to estimate this expression by noticing that:

- In order to have equal number of creation and annihilation operators the only finite contribution comes from even order of expansion, $2n$.
- The previous fact also gives a contributions $\frac{2n!}{n!n!}$ for all possible configuration at each order.
- Due to the fact that the term $e^{-\beta(H_{Loc}+H_{Bath})}$ does not allow any spin flips, we have that each spin must also have the same number of creation and annihilation operators giving a contribution $\frac{n!}{n_\uparrow! n_\downarrow!}$ with $n! = n_\uparrow + n_\downarrow$.
- From time-ordering we also have a contribution $\frac{1}{2n!}$.

We make the simplification:

$$Z = \sum_{\{n_\sigma\}} \prod_\sigma \int_0^\beta d\tau_{1_\sigma} \cdots \int_{\tau_{n-1_\sigma}}^\beta d\tau_{n_\sigma} \int_0^\beta d\tau'_{1_\sigma} \cdots \int_{\tau'_{n-1_\sigma}}^\beta d\tau'_{n_\sigma} \operatorname*{Tr}_d \operatorname*{Tr}_c e^{-\beta(H_{Loc}+H_{Bath})} *$$
$$* \sum_{i_1 \dots i_n} \sum_{i'_1 \dots i'_n} V_{i_1\sigma} V^*_{i'_1\sigma} \dots V_{i_n\sigma} V^*_{i'_n\sigma} c^\dagger_{i_1\sigma}(\tau_{1\sigma}) d_{i_1\sigma}(\tau_{1\sigma}) d^\dagger_{i'_1\sigma}(\tau'_{1\sigma}) c_{i'_1\sigma}(\tau'_{1\sigma}) \dots$$
$$\dots c^\dagger_{i_n\sigma}(\tau_{n\sigma}) d_{i_n\sigma}(\tau_{1\sigma}) d^\dagger_{i'_n\sigma}(\tau'_{n\sigma}) c_{i'_n\sigma}(\tau'_{n\sigma}). \tag{3.42}$$

Due to the fact that the creation and the annihilation operators of the bath commute with those of the impurity, in this time dependent framework we calculate the traces of the impurity and the bath separately. For an arbitrary order, the part related to the bath can be computed

using the Wick theorem and we obtain:

$$\underset{c}{\mathrm{Tr}} \sum_{i_1 \dots i_n} \sum_{i'_1 \dots i'_n} \frac{V_{i_1\sigma} V^*_{i'_1\sigma} \dots V_{i_n\sigma} V^*_{i'_n\sigma} c^\dagger_{i_1\sigma}(\tau'_{1\sigma}) c_{i_1\sigma}(\tau_{1\sigma}) \dots c^\dagger_{i_n\sigma}(\tau'_{n\sigma}) c_{i_n\sigma}(\tau_{n\sigma})}{Z_{Bath}} = \prod_\sigma det \mathbf{M}^{-1}_\sigma, \tag{3.43}$$

where we have introduced the partition function for the bath $Z_{Bath} = \underset{c}{\mathrm{Tr}}\, e^{-\beta H_{Bath}}$ and the n X n matrix $\mathbf{M}$ defined as:

$$(M^{-1}_\sigma)_{ij} = \Delta(\tau'_i - \tau_j) \xrightarrow{Fourier\ transform} \Delta(\imath\omega_n) = \sum_i \frac{|V_i|^2}{\imath\omega_n - \epsilon_i}$$

where we introduced the Fourier transform of the hybridisation function of Eq. (3.12). Finally we obtain:

$$\begin{aligned} Z &= \sum_{\mathcal{C}} Z_{Bath} \prod_\sigma det \mathbf{M}^{-1}_\sigma \underset{d}{\mathrm{Tr}}\, e^{-\beta H_{Loc}} d_{i_1\sigma}(\tau_{1\sigma}) d^\dagger_{i_1\sigma}(\tau'_{1\sigma}) \dots d_{i_n\sigma}(\tau_{n\sigma}) d^\dagger_{i_n\sigma}(\tau'_{n\sigma}) = \\ &= \sum_{\mathcal{C}} w_{\mathcal{C}}. \end{aligned} \tag{3.44}$$

This expression can be evaluated through a Monte Carlo sampling, proceeding as follows: the integrands $w_{\mathcal{C}}$ define the weights of a distribution over the configuration space $\mathcal{C} = \{(i_1, \tau_1), \dots, (i'_n, \tau'_k)\}$ which is sampled with the Metropolis-Hastings algorithm [147]. Furthermore, this algorithm prescribes that at each step, beginning from a configuration $\mathcal{C}'$, a new configuration $\mathcal{C}$ is proposed with probability A and is accepted with probability:

$$p = \min\left(1, \frac{\mathrm{A}'|\mathrm{w}_{\mathcal{C}}|}{\mathrm{A}|\mathrm{w}'_{\mathcal{C}'}|}\right), \tag{3.45}$$

where $w_{\mathcal{C}}$ and $w'_{\mathcal{C}'}$ are respectively, the weights of the new and the old configuration, and A' is the proposed probability of the inverse update, i.e. to go from the configuration $\mathcal{C}$ to the configuration $\mathcal{C}'$. Once the weights and configurations are found, the next step is to calculate the Green function of Eq. (3.21) $G_{imp}(\imath\omega_n)$ of Eq. (3.21):

$$G_{imp}(\imath\omega_n) = \left\langle \sum_{ij} \frac{e^{\imath\omega_n(\tau_i - \tau_j)}}{\beta} M_{ij} \right\rangle_{MC} \tag{3.46}$$

where $\langle \dots \rangle_{MC}$ denotes the Monte Carlo average.

It is useful to mention that in DMFT, the average expansion order of the hybridisation expansion $\langle k \rangle$ is proportional to the kinetic energy per site [148]:

$$E_{kin} = -\frac{\langle k \rangle}{\beta}. \tag{3.47}$$

We can demonstrate this by explicitly calculating the expression for the kinetic energy per site:

$$\begin{aligned}
E_{kin} &= \frac{1}{2\pi^2} \sum_n e^{\imath\omega_n 0^+} \int dk \epsilon_k G(k, \imath\omega_n) \\
&= \frac{1}{2\pi^2} \sum_n e^{\imath\omega_n 0^+} \int dk [\imath\omega_n + G^{-1}(k, \imath\omega_n) - \Sigma(k, \imath\omega_n)] G(k, \imath\omega_n) \\
&= 2 \sum_n e^{\imath\omega_n 0^+} \left[(\imath\omega_n - \Sigma(k, \imath\omega_n)) G(k, \imath\omega_n) - 1 \right] \\
&= 2 \sum_n \Delta(\imath\omega_n) G_{imp}(\imath\omega_n) \\
&= -\frac{\langle k \rangle}{\beta}.
\end{aligned}$$

In the case of the Cellular Dynamical Mean-Field Theory we need some cluster corrections as discussed in detail in Chapters 5 and 4.

Our state of the art code includes optimisation with Lazy Skip-List [27]. This offers a fast way to perform the numerous products of matrices necessary in this algorithm via the use of Skip List [149] and a fast rejection of proposed configurations based on matrix bounds.

3.6 Emery Model

To perform a more realistic description of the cuprates, we need an extension of the simple Hubbard model of Eq. (3.1). The actual electronic configuration of the copper layers must take into account the presence of two oxygens and a copper atom per unit cell. As shown in Fig. 3.6, we have $3d_{x^2-y^2}$ orbitals for each copper ion and $2p_x$ or $2p_y$ orbitals for the oxygens. This leads to the three-band Hubbard Hamiltonian also known as the Emery model [3]:

$$H = \mathbf{h}_0 + U_d \sum_i n_{di\uparrow} n_{di\downarrow}, \tag{3.48}$$

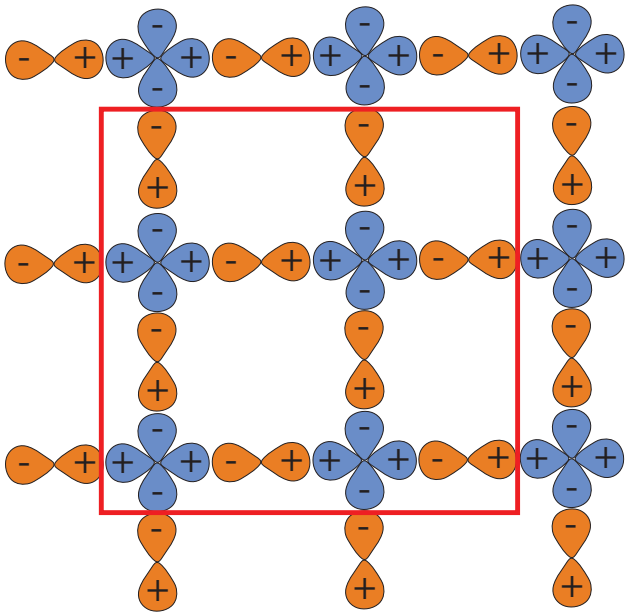

Figure 3.6: Sketch of the three-band model. The Cu $3d_{x^2-y^2}$ orbitals and the O $2p_x$, $2p_y$ orbitals are shown in blue and orange, respectively. We indicate our phase convention where, to apply the CDMFT, we use a cluster of 12 sites with $(N_d, N_p) = (4, 8)$, bounded by the red square in the figure, that is embedded in a self-consistent noninteracting bath.

where the electron correlations are introduced by the local Coulomb repulsion U_d on Cu sites and $\mathbf{h}_0$ is:

$$\mathbf{h}_0(\mathbf{k}) = \begin{pmatrix} \epsilon_d & V_{dp_x} & V_{dp_y} \\ V_{dp_x}^\dagger & \epsilon_p + W_{p_xp_x} & W_{p_xp_y} \\ V_{dp_y}^\dagger & W_{p_xp_y}^\dagger & \epsilon_p + W_{p_yp_y} \end{pmatrix}, \tag{3.49}$$

with $V_{dp_x} = t_{pd}(1-e^{ik_x})$, $V_{dp_y} = t_{pd}(1-e^{ik_y})$, $W_{p_xp_x} = 2t_{pp}(\cos k_x - 1)$, $W_{p_yp_y} = 2t_{pp}(\cos k_y - 1)$ and $W_{p_xp_y} = t_{pp}(1-e^{-ik_x})(1-e^{ik_y})$. Here t_{pd} (t_{pp}) is the oxygen-copper (oxygen-oxygen) hopping amplitude and ϵ_d (ϵ_p) is the copper (oxygen) on-site energy. The copper-copper distance and t_{pp} are taken as unity.

Similarly to the case of the Hubbard model, we solve the Emery model with Cellular Dynamical-Mean Field Theory [24, 25, 144], using a cluster of 12 lattice sites with $(N_d, N_p) = (4, 8)$, and replace the missing lattice environment by a non-interacting bath. We decided to consider no interaction on the oxygens, in order to integrate them out before applying CDMFT and, in this way, reduce the sign problem. This yields an effective lattice action involving only copper d-orbitals. The upper diagonal element of the matrix Green function for

the Hamiltonian of Eq. (3.48) corresponds to the non-interacting part of this action, namely $G_{0\text{eff}}(i\omega_n, \mathbf{k}) = ((i\omega_n + \mu - \mathbf{h}_0(\mathbf{k}))^{-1})_{dd}$, with $i\omega_n$ Matsubara frequencies and μ the chemical potential. The action of the corresponding impurity model for CDMFT then reads:

$$S_{\text{Imp}} = -\sum_{n\mathbf{R}\mathbf{R}'\sigma} d^{\dagger}_{\mathbf{R}\sigma}(i\omega_n)\mathbf{G}^{-1}_{0,\mathbf{R}\mathbf{R}'}(i\omega_n)d_{\mathbf{R}'\sigma}(i\omega_n) + U_d \sum_{\mathbf{R}} \int_0^{\beta} d^{\dagger}_{\mathbf{R}\uparrow}(\tau)d_{\mathbf{R}\uparrow}(\tau)d^{\dagger}_{\mathbf{R}\downarrow}(\tau)d_{\mathbf{R}\downarrow}(\tau)d\tau, \tag{3.50}$$

where $\mathbf{R}$ runs over the copper sites of the plaquette. The Weiss field $\mathbf{G}_0^{-1}$ is determined by the CDMFT self-consistency:

$$(\mathbf{G}_0^{-1}(i\omega_n) - \mathbf{\Sigma}(i\omega_n))^{-1} = \frac{N_d}{4\pi^2}\int (\mathbf{G}^{-1}_{0\text{eff}}(i\omega_n, \tilde{\mathbf{k}}) - \mathbf{\Sigma}(i\omega_n))^{-1} d\tilde{\mathbf{k}}, \tag{3.51}$$

where $\mathbf{\Sigma}$ is the self-energy of the impurity model and

$$G^{-1}_{0\text{eff},\mathbf{R}\mathbf{R}'}(i\omega_n, \tilde{\mathbf{k}}) = \frac{1}{N_d}\sum_{\mathbf{K}} e^{i(\mathbf{K}+\tilde{\mathbf{k}})(\mathbf{R}-\mathbf{R}')} G^{-1}_{0\text{eff}}(i\omega_n, \mathbf{K}+\tilde{\mathbf{k}}) \tag{3.52}$$

is the mixed representation in the real and momentum-space for the effective non-interacting lattice Green function $G_{0\text{eff}}(i\omega_n, \mathbf{k})$ defined above. The $\mathbf{K}$'s run over the momenta of the plaquette and the $\tilde{\mathbf{k}}$'s over the reduced Brillouin zone constrained to the partitioning of the lattice into clusters. Notice that here the self-energy is finite only on the copper orbitals and that the occupation and the interacting Green function of the oxygen orbitals can be computed with the lattice's Dyson equation of all orbitals. The impurity model Eq. 3.50 is solved with Continuous-Time Quantum Monte Carlo for the hybridisation expansion [26], where the Weiss field is written as:

$$\mathbf{G}_0^{-1}(i\omega_n) = i\omega + \mu - \mathbf{t}_{cl} - \mathbf{\Delta}(i\omega_n), \tag{3.53}$$

such that the hybridisation function $\mathbf{\Delta}(i\omega_n) \to 0$ for $n \to \infty$. Since the effective cluster hopping matrix $\mathbf{t}_{cl}$ is diagonal, as is clear from the high-frequency limit of the self-consistency equation, we can apply for the evaluation of the trace over the cluster, a segment algorithm similar to the one employed for the two dimensional Hubbard model.

3.7 Conclusion

In this chapter we have aimed to give an overview of the theoretical background adopted in the work presented in the next chapters, where we will analyse how the Mott transition characterises the phase diagram of the cuprates [2, 138, 150]. Indeed this metal to insulator transition, which appears in the undoped system, plays a significant role upon increasing doping. The Hubbard and Emery models, addressed in Sections 3.2 and 3.6 respectively, are the natural playground for such investigations. In Section 3.4 we discussed the numerical tool that we employ to solve them, that is the Cellular Dynamical Mean-Field Theory with the Continuous-Time Hybridisation Expansion Algorithm, outlined in Section 3.5.

Our examination thus far was confined to the study of the normal state for the sake of discussion. Indeed, the study of other phases can be performed by imposing their symmetries on the cluster. This we will do for the antiferromagnetic phase in Chapter 4, for the d-wave superconductivity in the Hubbard model in Chapter 5 and in the Emery model in Chapter 6. In these cases we will use, as a seed for the CDMFT loop of Fig. 3.5, a self-energy that respects the symmetries of the phase under consideration. Thus, the CDMFT loop will converge to a solution that still respects the symmetries of this phase or, otherwise, to a normal state solution, according to which of these two possible results is more stable under the parametric regime investigated. In other words, if the chosen parameters allow this phase in a particular region of the phase diagram, the converged solution will respect its symmetries.

Chapter 4

The Mott Transition at Half-Filling and its Interplay with the Antiferromagnetic Phase

4.1 Introduction

The work presented in this chapter is based on Ref. [28].

As discussed in Chapter 3, one of the most striking manifestations of strong interactions in quantum materials is the Mott transition [2, 138, 150], a first-order transition between a half-filled band metal and an insulator. Understanding the features of this transition is a fundamental problem in the study of cuprates, where the physics of the normal state is often hidden by broken symmetry states, such as the Néel antiferromagnetic state (AF) [138, 150]. Indeed, in the Mott insulator the electrons are localised, so local moments tend to order magnetically at low temperature via the super-exchange mechanism [151, 152].

In this chapter, we will begin our exploration of the phase diagram of cuprates by investigating the properties of their parent compounds and the interplay between the normal and antiferromagnetic states. Then we will be ready to discuss the implication for the $d-$wave superconductivity, introducing hole-doping in the next chapter.

Previous works for the half-filled model in 3D [153, 154] showed the existence of a single AF phase, which never disappears at $T = 0$. Nevertheless, the antiferromagnetism stems from

two different mechanisms. At weak interaction, AF emerges from cooling a metal, due to the nesting of the Fermi surface, whereas at strong interaction, AF originates from cooling a Mott insulator, due to the super-exchange between localised spins [153, 154]. These processes are referred to respectively as *Slater* and *Heisenberg* mechanisms. In the Slater regime, increasing the interaction leads to an increase in the Néel temperature T_N, the temperature below which an AF state is formed. In the Heisenberg regime, increasing the interaction leads to a decrease in T_N. The fate of this scenario for 2D systems is the topic of this chapter, where we are going to use the two-dimensional Hubbard Hamiltonian to explicitly investigate the Mott transition and its interplay with AF at half-filling.

The basic experimental phenomenology of 3D systems, as well as predictions (e.g. [21, 24, 155, 156]), have been obtained from the DMFT [21] solution of the Hubbard model. However, the strong momentum dependence of the self-energy in 2D makes DMFT inadequate in this case. This motivates the use of CDMFT, discussed in Chapter 3, as a way to include some of this momentum dependence. Although this and other methods have been used to study the AF phase [25, 157–164], the influence of the normal state Mott transition, if any, on the AF phase has been less investigated [165] and remains a challenge. Our goal is to decipher the interplay between the Mott transition and AF, showing that even if the Mott transition appears to be hidden, it originates the sharp crossovers responsible, to a large extent, for the properties of the antiferromagnetic phase.

It is worth to say that in 2D, as stated in the Bogoliubov-Hohenberg-Mermin-Wagner theorem [108–111], thermal fluctuations forbid any long-range order at finite temperature. Nevertheless, the onset temperature where the correlation length ξ has an exponential increase can be well defined. This temperature calculated with CDMFT and defined as the loci below which the staggered magnetisation m_z of Eq. 4.24 differs from zero, is a quantitative estimate at which short-range order antiferromagnetic correlations emerge in the system. We call it T_N^d, where the d stands for *dynamical* mean-field temperature.

This chapter is organised as follows: we will begin in Section 4.2 by introducing the methodology used in this chapter, then we will discuss the behaviour of the phase diagram at half-filling in the presence of antiferromagnetism, in Section 4.3. In Section 4.4, we provide benchmarks showing that despite our study being confined to short range correlations, due to the size of our cluster, they are close to those obtained for larger systems, where ξ can be larger. In Section

4.5, we show that our calculations reveal different features for the antiferromagnetic state in the weak or strong interaction regime. These differences are related to the normal state Mott transition, hidden beneath the antiferromagnetic dome. Furthermore, this transition regulates the driving mechanism that stabilises the AF state, leading to a sharp crossover between a potential and kinetic-energy driven antiferromagnetism, at small and large U respectively, also detectable in the local density of states, as discussed in Section 4.6.

4.2 Model and Method

As discussed in Chapter 3, we aim to study the local quantum fluctuations induced by the electron-electron interaction U on the same footing as the short-range correlations, solving the Hubbard model of Eq. 3.2 with Cellular Dynamical Mean-Field Theory [24, 25, 144]. CDMFT selects a cluster of the lattice, here a 2×2 plaquette, and embeds it in a self-consistent bath of non-interacting electrons, which approximates the missing lattice environment. We solve the impurity (plaquette in a bath) problem using the statistically exact Continuous-Time Quantum Monte Carlo method [26] based on the hybridisation expansion of the impurity action.

Differently from Chapter 3, where we considered just the normal state, here we also discuss what happens for the antiferromagnetic phase. In the latter case, we allow the symmetry breaking only in the bath and not in the cluster. To accelerate the calculation, we use the C_{2v} group symmetry with mirrors along the diagonals of the plaquette [166, 167]. We consider only the half-filled model.

As said, the effective action of the impurity (cluster in a bath) problem is given by:

$$S_{\text{eff}} = S_c(c, c^\dagger) + \int_0^\beta d\tau d\tau'\, c^\dagger(\tau)\mathbf{\Delta}(\tau - \tau')c(\tau'). \tag{4.1}$$

To solve the impurity problem, i.e. to find:

$$\mathbf{G}_c(\tau - \tau') = \mathbf{G}_c[\Delta(\tau - \tau')] = \langle Tc(\tau)c^\dagger(\tau')\rangle_{S_{\text{eff}}},$$

we use the Continuous-Time Quantum Monte Carlo method based on the expansion of S_{eff} in the hybridisation function (CT-HYB) Δ [26]. In this section, we shall show that the analysis of the symmetries of the problem has significant consequences on: the choice of the single-

particle basis for Eq. 4.1 in Section 4.2.1, the ergodicity of the CT-HYB impurity solver in Section 4.2.2, and the Monte Carlo sign problem in Section 4.2.3. For details on convergence and Monte Carlo error bars, see also Ref. [166].

4.2.1 Symmetries

In order to implement a version of the Cellular Dynamical Mean-Field Theory able to study the antiferromagnetic state we must note that:

1. The CDMFT procedure preserves the symmetries of the lattice accordingly with its partitioning (here the symmetries of a 2×2 square plaquette). The hybridisation function $\mathbf{\Delta}$ must respect all these symmetries in the normal state, but some of them are broken in the antiferromagnetic state.

2. In order to reach a faster convergence of the Continuous-Time Quantum Monte Carlo [148], we choose a single-particle basis for c (or $c^\dagger$) that transforms according to the irreducible representation of an Abelian point group that represents the spatial symmetries of the impurity Hamiltonian [148]. The Abelian group chosen must be a subgroup of the total point group of the impurity Hamiltonian. In this way, we can speed up the calculation of the trace of operators on the cluster.

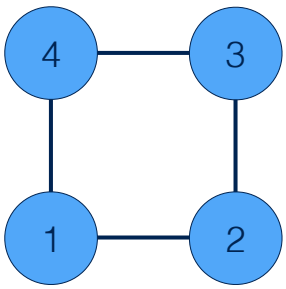

Figure 4.1: 2×2 plaquette for the CDMFT.

Taking into account the first remark, it is important to enumerate the symmetries of the normal state:

(i) charge conservation ($U(1)$) symmetry,

(ii) time-reversal symmetry,

(iii) spin rotational ($SU(2)$) symmetry,

(iv) translational symmetry,

(v) point group C_{4v} symmetry of the plaquette.

All these symmetries but the translational one are compatible with the lattice partitioning of the CDMFT. Following the second remark, we choose the point group C_{2v} with mirrors along horizontal and vertical axis of the plaquette. Using the convention for the indices of Fig. 4.1, the appropriate basis in the irreducible representations A_1, A_2, B_1, B_2 of C_{2v}, is:

$$c_{A_1\sigma} = \tfrac{1}{2}(c_{1\sigma} + c_{2\sigma} + c_{3\sigma} + c_{4\sigma}) \tag{4.2}$$

$$c_{A_2\sigma} = \tfrac{1}{2}(c_{1\sigma} - c_{2\sigma} + c_{3\sigma} - c_{4\sigma}) \tag{4.3}$$

$$c_{B_1\sigma} = \tfrac{1}{2}(c_{1\sigma} + c_{2\sigma} - c_{3\sigma} - c_{4\sigma}) \tag{4.4}$$

$$c_{B_2\sigma} = \tfrac{1}{2}(c_{1\sigma} - c_{2\sigma} - c_{3\sigma} + c_{4\sigma}). \tag{4.5}$$

In this way, the hybridisation function for each spin σ is a 4×4 diagonal matrix:

$$\mathbf{\Delta}_{\sigma,\sigma} = \begin{pmatrix} \Delta_{A_1\sigma,A_1\sigma} & 0 & 0 & 0 \\ 0 & \Delta_{A_2\sigma,A_2\sigma} & 0 & 0 \\ 0 & 0 & \Delta_{B_1\sigma,B_1\sigma} & 0 \\ 0 & 0 & 0 & \Delta_{B_2\sigma,B_2\sigma} \end{pmatrix}. \tag{4.6}$$

By imposing equal values for spin up and spin down, we automatically satisfy the time-reversal symmetry and the C_4 rotation symmetry is respected by imposing that:

$$\Delta_{B_1\sigma,B_1\sigma} = \Delta_{B_2\sigma,B_2\sigma}. \tag{4.7}$$

Consequently, the hybridisation function of Eq. (4.6) has only three independent elements.

By contrast, on the 2×2 plaquette, the antiferromagnetic phase breaks:

(i) time-reversal symmetry,

(ii) spin rotational symmetry,

(iii) C_4 ($\pi/2$) rotation.

However, time reversal combined with C_4 is still a symmetry of this system and, despite the lost of spin-rotational symmetry, the spin along the z direction is conserved in both phases. Since we are only interested in expectation values in the z direction, the breaking of spin-rotational symmetry has no consequences. Additionally, the Néel state breaks spatial C_{2v} symmetry with mirrors along the horizontal and vertical axis of the plaquette, but not with mirrors along the diagonals. Thus, following as before the indices convention of Fig. 4.1, our choice for the single-particle basis is:

$$c_{A_1\sigma} = \tfrac{1}{\sqrt{2}}(c_{1\sigma} + c_{3\sigma}) \tag{4.8}$$

$$c_{A_1'\sigma} = \tfrac{1}{\sqrt{2}}(c_{2\sigma} + c_{4\sigma}) \tag{4.9}$$

$$c_{B_1\sigma} = \tfrac{1}{\sqrt{2}}(c_{1\sigma} - c_{3\sigma}) \tag{4.10}$$

$$c_{B_2\sigma} = \tfrac{1}{\sqrt{2}}(c_{2\sigma} - c_{4\sigma}). \tag{4.11}$$

In this case, the hybridisation function for each spin is a 4×4 block-diagonal matrix, with one 2×2 block (A_1) and two 1×1 blocks (B_1 and B_2):

$$\mathbf{\Delta}_{\sigma,\sigma} = \begin{pmatrix} \Delta_{A_1\sigma,A_1\sigma} & \Delta_{A_1\sigma,A_1'\sigma} & 0 & 0 \\ \Delta_{A_1'\sigma,A_1\sigma} & \Delta_{A_1'\sigma,A_1'\sigma} & 0 & 0 \\ 0 & 0 & \Delta_{B_1\sigma,B_1\sigma} & 0 \\ 0 & 0 & 0 & \Delta_{B_2\sigma,B_2\sigma} \end{pmatrix} \tag{4.12}$$

since the imaginary-time hybridisation is a real function, we have:

$$\Delta_{A_1\sigma,A_1'\sigma} = \Delta_{A_1'\sigma,A_1\sigma}. \tag{4.13}$$

Moreover, the hybridisation function matrices for opposite spins are not independent, because

a spin flip followed by a rotation of $\pi/2$ transforms the operators as follows:

$$c_{A_1\sigma} \rightarrow c_{A_1'\bar{\sigma}} \tag{4.14}$$

$$c_{A_1'\sigma} \rightarrow c_{A_1\bar{\sigma}} \tag{4.15}$$

$$c_{B_1\sigma} \rightarrow c_{B_2\bar{\sigma}} \tag{4.16}$$

$$c_{B_2\sigma} \rightarrow -c_{B_1\bar{\sigma}}, \tag{4.17}$$

with $\bar{\sigma} = -\sigma$. The resulting hybridisation function, with opposite spin than Eq. (4.12), is:

$$\mathbf{\Delta}_{\bar{\sigma},\bar{\sigma}} = \begin{pmatrix} \Delta_{A_1'\sigma,A_1'\sigma} & \Delta_{A_1'\sigma,A_1\sigma} & 0 & 0 \\ \Delta_{A_1\sigma,A_1'\sigma} & \Delta_{A_1\sigma,A_1\sigma} & 0 & 0 \\ 0 & 0 & \Delta_{B_2\sigma,B_2\sigma} & 0 \\ 0 & 0 & 0 & \Delta_{B_1\sigma,B_1\sigma} \end{pmatrix} \tag{4.18}$$

Thus, in this basis the hybridisation function has 5 independent elements, that in case of a normal state solution are reduced to three, since in this case the additional equality for both spin species imposes:

$$\Delta_{A_1'\sigma,A_1'\sigma} = \Delta_{A_1\sigma,A_1\sigma} \tag{4.19}$$

$$\Delta_{B_1\sigma,B_1\sigma} = \Delta_{B_2\sigma,B_2\sigma}. \tag{4.20}$$

4.2.2 Ergodicity

It has been demonstrated in Ref. [167] that the Continuous-Time Hybridisation Expansion Algorithm, when applied to broken symmetry states, can be non-ergodic. In this case it can happen that the cluster has more symmetries than the bath, and we implement the Monte Carlo sampling, discussed in Section 3.5 adding or removing just a pair of creation-annihilation operators, i.e. a "2-operator update". To solve this issue, it may be necessary to make updates that involve a larger numbers of creation-annihilation operators, namely an "n-operator update". This is the case, for example, when we treat the d-wave superconductivity within 2×2 CDMFT, as in Chapters 5 and 6. In fact, by expanding the symmetry-breaking hybridisation function in a power series of single pairs of operators, the broken symmetry

can generate vanishing contributions to the trace. However, a "4-operator update", that corresponds, practically, to a power series expansion of the hybridisation function in couples of pairs, recovers the full symmetry and retrieves the ergodicity.

In the case of the antiferromagnetic state, the situation is different. The Hamiltonian of the cluster is invariant under the C_{2v} point group symmetry with mirrors along horizontal and vertical axes, whereas the Hamiltonian of the bath is not invariant. This suggests that a "2-operator update" is not sufficient to guarantee ergodicity. However, we used as a basis the irreducible representations of the C_{2v} symmetry, common to both the bath and the cluster. Therefore there is no coupling to point-group symmetries that exist only in the cluster and not in the bath and a "2-operator update" meets the requirements for ergodicity.

4.2.3 Sign Problem and Addendum on Ergodicity

One of the greatest problems using the CDMFT is that it is affected by a sign problem. This happens due to the Pauli principle and some coefficients of the Hamiltonian, the weights w_c of eq. 3.44 can have negative values. In order to interpret these as terms of a probability distribution, the standard way to treat this problem is to transfer the sign from the weight to the observable. Then we use the resulting partition function Z' with positive weights to sample instead of the original partition function Z. The partition function Z' corresponds to the one of the hardcore boson problem and the average sign is:

$$\langle sign \rangle = \frac{Z}{Z'} \tag{4.21}$$

This situation appears to influence the antiferromagnetic phase more than the normal state. Therefore, to reduce the sign problem in the Néel state, we can take advantage of the degeneracy in the A_1 subspace [166] by rotating with an angle θ the vectors of the basis, as follows:

$$c_{A_1\sigma} = \frac{\cos\theta}{\sqrt{2}}(c_{1\sigma} + c_{3\sigma}) + \frac{\sin\theta}{\sqrt{2}}(c_{2\sigma} + c_{4\sigma}) \tag{4.22}$$

$$c_{A_1'\sigma} = \frac{\sin\theta}{\sqrt{2}}(c_{1\sigma} + c_{3\sigma}) - \frac{\cos\theta}{\sqrt{2}}(c_{2\sigma} + c_{4\sigma}). \tag{4.23}$$

In Fig. 4.2 we plot several isothermal scans of the average sign (panel (a)) and angle θ (panel

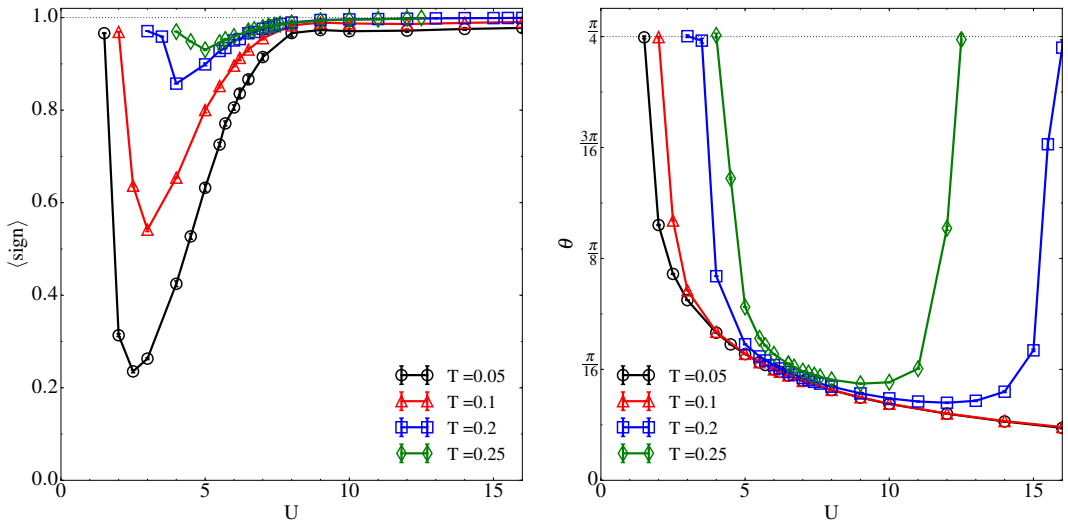

Figure 4.2: Panel (a): the average sign as a function of the interaction U. Panel (b): the average angle θ in Eqs. 4.22, 4.23 as a function of U. As indicated in the legend, the data is shown for temperatures $T = 1/20, 1/10, 1/5$ and $1/4$ and the angle $\pi/4$ never appears in the antiferromagnetic phase, i.e. when $m_z \neq 0$.

(b)) as a function of U. With an appropriate choice of θ, that must be optimised at each iteration of the CDMFT to minimise the off-diagonal component of the 2×2 block (A_1) of the hybridisation function matrix, we can minimise the sign problem. In any case, when $\theta = 0$ the basis of Eqs. 4.8-4.11 is restored. This procedure is implemented in the AF phase only. Indeed, the last rotation corresponds to change from the A_1 and A_1' basis to one that transforms like the A_1 and A_2 representations, Eqs. (4.2) and (4.3), of the C_{2v} symmetry with mirrors along the horizontal and vertical axis. The angle corresponding to this rotation causes the problem to become non-ergodic [167] when in an antiferromagnetic state. This is due to the fact that the hybridisation functions $\Delta_{A_1\sigma,A_2\sigma}$ and $\Delta_{A_2\sigma,A_1\sigma}$ are non-vanishing and therefore, so is their product in the power expansion of the hybridisation. Because the cluster itself does not break any symmetry but the product of A_1 and A_2 does, a product of an odd number of $\Delta_{A_1\sigma,A_2\sigma}$ or $\Delta_{A_2\sigma,A_1\sigma}$ can vanish. In this case a "2-operator update" does not suffice for ergodicity. This case never appears in our simulations, in the case of finite staggered magnetisation m_z, as demonstrated in Fig. 4.2 panel (b), 4.4 and Fig. 4.3.

4.3 Antiferromagnetic State at Half-Filling - Phase Diagram

After this excursus on the methodology, we are finally ready to discuss the phase diagram $T-U$ of the two-dimensional half-filled Hubbard model in presence of antiferromagnetism. In our calculations we use $t = 1$ for the nearest neighbour hopping and when referring to U and T, we tacitly assume their ratio with t, so they are pure numbers. We are in presence of an

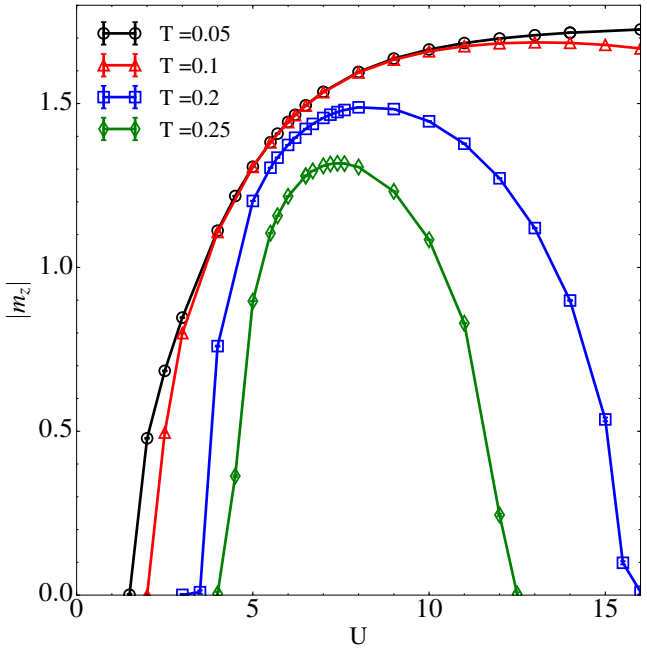

Figure 4.3: Staggered magnetisation m_z as a function of U for different values of T. T_N^d is drawn from the mean of the two temperatures where m_z is greater than a cut-off value to where it is smaller (here $m_z = 0.045$).

antiferromagnetic state when the staggered magnetisation m_z,

$$m_z = \frac{2}{N_c}\sum_{j}^{N_c}(-1)^j(n_{j\uparrow} - n_{j\downarrow}), \tag{4.24}$$

differs from zero. Fig. 4.3 shows the absolute value of the staggered magnetisation as a function of the interaction for different temperatures. The interpolation of these scans leads to the colormap in Fig. 4.4.

This latter figure shows T_N^d, i.e. the line below which $m_z \neq 0$, as a function of the interaction U. $T_N^d(U)$ has a dome shape. Similarly to the 3D case, this behaviour alone suggests that although there is a single AF phase, there are qualitative differences as a function of U: the initial rise of T_N^d occurs because of nesting of the Fermi surface whereas, at large U,

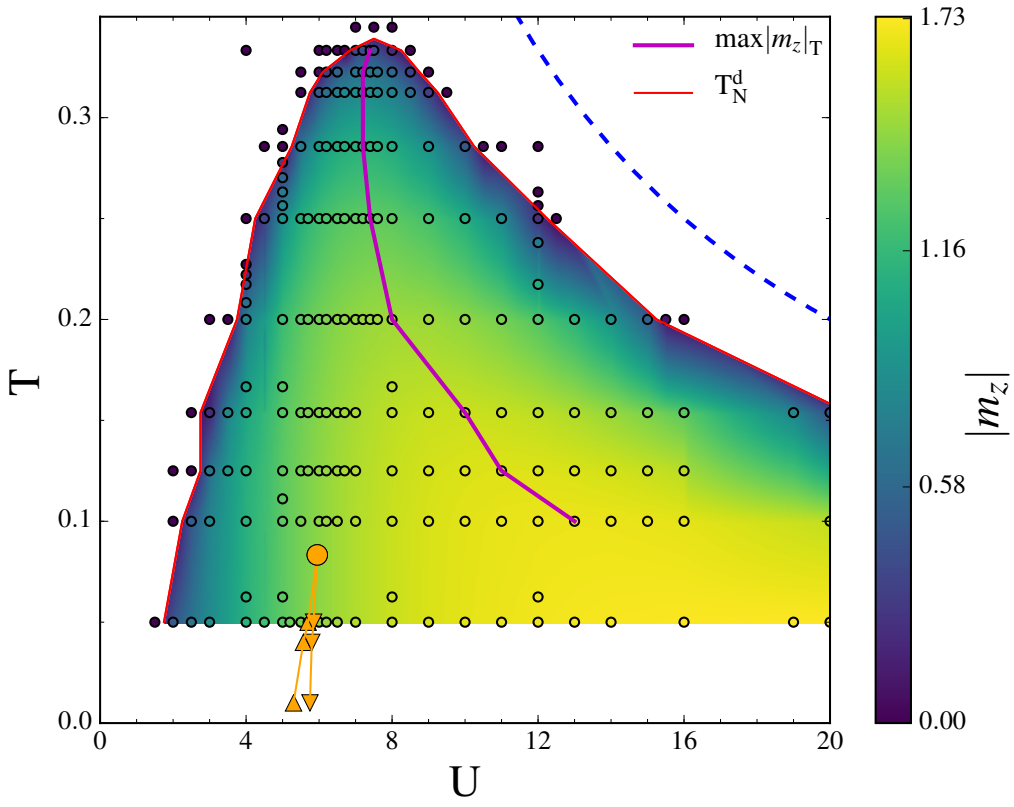

Figure 4.4: Néel temperature T_N^d versus U at $n = 1$. The AF phase is defined by the loci where $m_z \neq 0$ and is delimited by T_N^d. Colour corresponds to the magnitude of the staggered magnetisation m_z, shown in Fig. 4.3. The loci of the isothermal maxima of m_z are indicated with the magenta line. Between the lines of orange triangles, we draw the coexistence region of the Mott transition that culminates in second-order critical point, indicated here by an orange filled circle, at $(U_{\mathrm{MIT}}, T_{\mathrm{MIT}})$.

super-exchange $J = 4t^2/U$ leads to the decrease of T_N^d with U [153,161]. Our results for T_N^d are close to the onset of exponential behaviour [112,158,161,168,169] of ξ. The line connecting the maximum of m_z at fixed temperatures (magenta line) approximately follows J (blue dashed line), thereby indicating that super-exchange drives the Néel ordering at large U. As $T \to 0$, m_z saturates to its maximum value at large U. A different behaviour between weakly and strongly interacting antiferromagnetism is indicated by the normal state just above T_N^d. The Néel state can emerge by cooling a metal or a Mott insulator depending if we are in the weak or strong coupling regime, respectively, of the phase diagram [170]. This happens due to the underlying Mott insulator transition (MIT) that controls the physics of its supercritical region through a crossover line also above T_N^d. This transition, computed by isothermal hysteresis

loops in the double occupancy as a function of the interaction, is visible in 4.4 with orange triangles and it terminates in a full orange circle indicating a second-order critical point at $(U_{\mathrm{MIT}}, T_{\mathrm{MIT}})$. This transition, despite being hidden by the Néel phase, appears to determine the driving mechanism between antiferromagnetism at weak and strong coupling as well as the features of the local density of states (DOS). This is the central point of this Chapter, and we will discuss it in the following sections.

4.4 Some Benchmarks

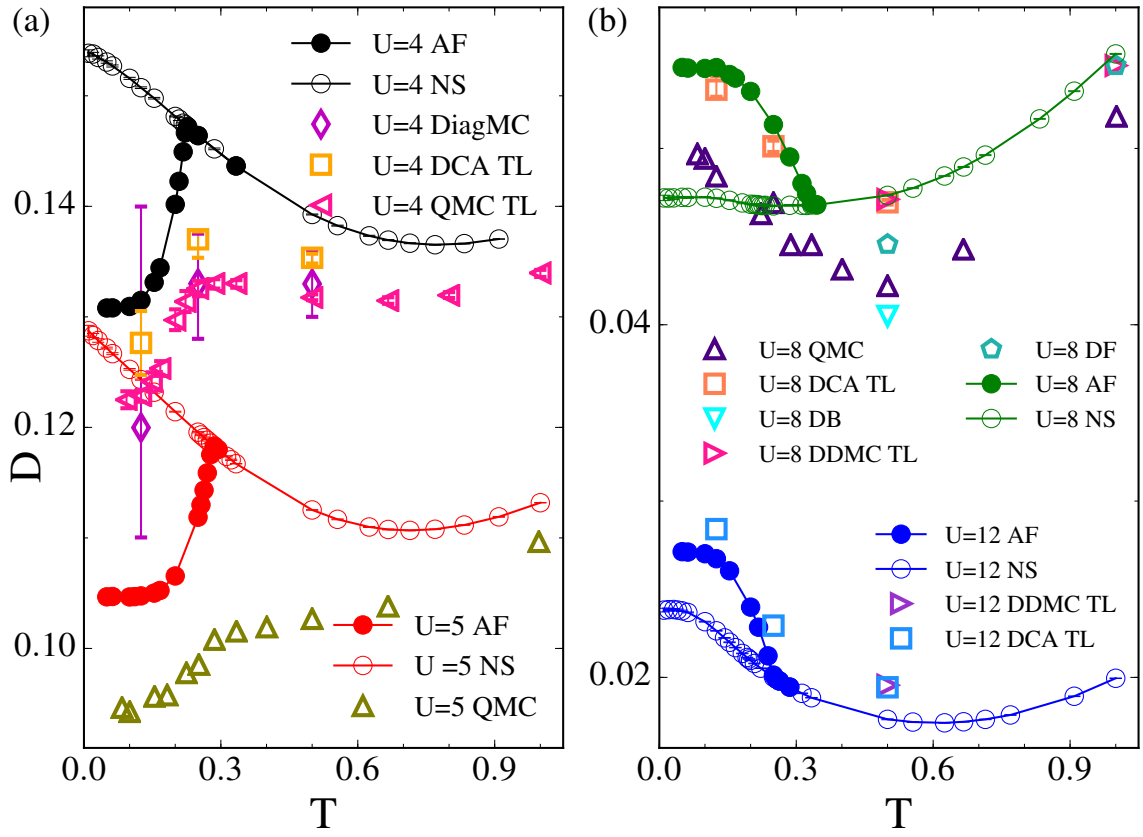

Figure 4.5: The double occupancy D as a function of the temperature T at $U = 4.5 < U_{\mathrm{MIT}}$ (panel (a)) and $U = 8, 12 > U_{\mathrm{MIT}}$ (panel (b)). The results for the AF state are indicated with filled circles whereas for the normal states with open circles. As benchmarks, we plot the results from alternative methods: diagrammatic Monte Carlo from Ref. [171] (diamonds), DCA extrapolated to infinite lattice from Ref. [171] (squares), determinantal QMC on 10^2 lattice from Ref. [163] (up triangles) and extrapolated to the thermodynamic limit [160] (left triangles), dual boson scheme from Ref. [172] (down triangle), diagrammatic determinant Monte Carlo extrapolated to the thermodynamic limit from Ref. [173] (right triangles) and dual fermion scheme from Ref. [173] (pentagons).

A direct measure for the degree of electronic correlations is given by the double occupancy $D = \langle n_{i\uparrow} n_{i\downarrow} \rangle$, displayed in Fig. 4.5 as a function of the temperature for several values of the interaction U. In panels (a) and (b) respectively, we display the results for interaction values below and above U_{MIT}. Also shown is the interaction where the Mott transition terminates in a second-order critical point at T_{MIT}, for both the AF and normal states (filled and open circles, respectively). As benchmarks, our results are plotted in comparison with the values of D obtained from alternative approaches [160,163,171–173]. As mentioned in Chapter 3, there are several methods to construct a cluster extension of DMFT, Dynamical Cluster Approximation (DCA) is an alternative to CDMFT. The difference between these two methodology is the way in which the cluster is built: in CDMFT the cluster is formulated in the real space, whereas in DCA it is formulated in the momentum space. The results of the DCA method here presented are the thermodynamic-limit data extrapolated from the infinite cluster size limit. Due to the computational cost of such a limit not many results are available.

We observe that for $T \ll T_N^d$, the antiferromagnetic results are closer to these benchmarks than those for the normal state. This was expected because, as far as local quantities are concerned, a state with a finite but exponentially large ξ is closer to an AF state than a normal state with ξ at most one lattice spacing. As a consequence, due to the phase transition at T_N^d our antiferromagnetic double occupancy data presents a kink, that is replaced in the benchmarks by a shallow crossover. The same would presumably be observed for the DCA data, if there had been more data points available. Such a crossover for methodologies like QMC is a consequence of the finite-size system, which cannot allow a phase transition due to the Bogoliubov-Hohenberg-Mermin-Wagner theorem [108–111]. Additionally, we observe a better agreement either by increasing the interaction, due to the localisation of the states, or by increasing temperature above T_N^d, because ξ is smaller. These benchmarks validate the reliability of CDMFT, that assures an exponentially fast convergence with cluster size [24,174] for any local quantity such as the double occupancy.

4.5 Energetics

From Fig. 4.5 we also notice that $D(T)$ of the normal state for all values of U presents a minimum. This minimum occurs due the competition of two mechanisms: increasing the local

moment, i.e. decreasing D, enhances the spin entropy upon heating from $T = 0$, whilst the non-interacting limit, where each lattice site has equal probability to be in any of the four possible states, must be reached at very large temperature [21, 175]. As T is reduced below T_N^d, the normal state becomes unstable with regard to AF, as also testified by the negative values of the total condensation energy of Fig. 4.8 that will be discussed in the following. We find a sharp difference between weak and strong interactions. For $U < U_{\mathrm{MIT}}$ in Fig. 4.5 panel (a), the D of the Néel state is suppressed compared with those of the normal state and the slope of $D(T)$ appears reversed in the two phases, i.e. for $T < T_N^d$: $dD/dT > 0$ in the AF state and $dD/dT < 0$ in the normal state. On the other hand, for $U > U_{\mathrm{MIT}}$ in Fig. 4.5 panel (b), D is larger in the AF state, and the slope of $D(T)$ has the same sign in the two phases. By definition of the potential energy

$$E_{\mathrm{pot}} = UD, \tag{4.25}$$

these results prove that the AF state leads to a potential energy decrease when $U < U_{\mathrm{MIT}}$ and to a potential energy increase when $U > U_{\mathrm{MIT}}$. This lies at the heart of the $T = 0$ stability of the AF state relative to the normal state.

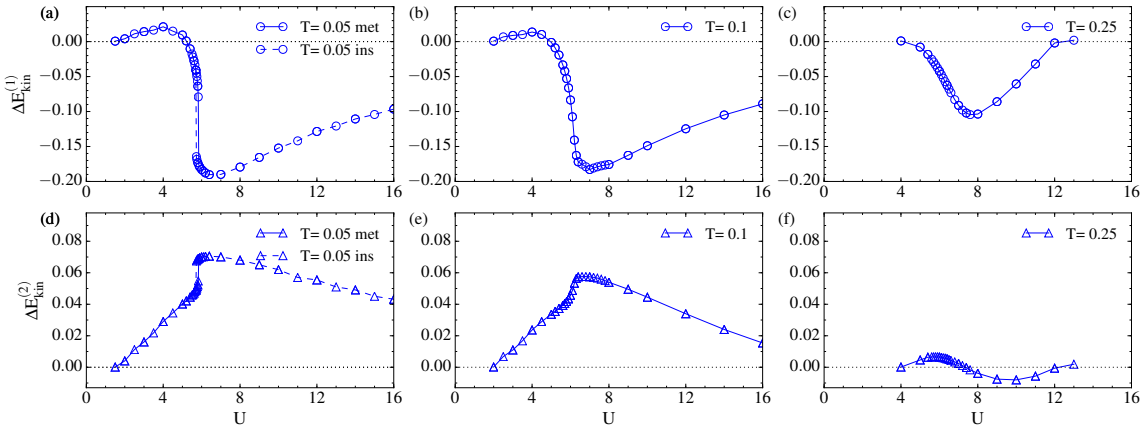

Figure 4.6: Contributions to the difference in kinetic energy between AF and normal state, as a function of U. Top (bottom) panels show $\Delta E_{\mathrm{kin}}^{(1)}$ ($\Delta E_{\mathrm{kin}}^{(2)}$). Data is shown for $T = 1/20 < T_{\mathrm{MIT}}$, $T = 1/10 > T_{\mathrm{MIT}}$, and $T = 1/4$ (left, central and right columns, respectively). For $T < T_{\mathrm{MIT}}$ two metastable solutions coexist at the Mott transition.

The kinetic energy, for CDMFT solved with CT-HYB Chapter 5, results from the summation of two contributions, $E_{kin} = E_{kin}^{(1)} + E_{kin}^{(2)}$, where $E_{kin}^{(1)}$ is a term related to the average

expansion order $\langle k \rangle$, as shown in Section 3.5:

$$E_{kin}^{(1)} = -\frac{\langle k \rangle}{N_c \beta} \tag{4.26}$$

and $E_{kin}^{(2)}$, as we will see in Section 5.7.1, is a term related to the cluster part:

$$E_{kin}^{(2)} = \frac{2T}{N_c} \sum_n e^{-i\omega_n 0^-} \sum_{ij} \left[t_{ij}^{imp} G_{ji}^{imp}(i\omega_n) \right], \tag{4.27}$$

where N_c is the cluster size (here $N_c = 4$), β is the inverse temperature, t_{ij}^{imp} and G_{ij}^{imp} are the hopping and the Green function of the impurity problem, respectively. Figure 4.6 shows these two contributions to the difference in the kinetic energy between antiferromagnetic and normal state, as a function of the interaction for $T = 1/20, 1/10, 1/4$, respectively on the left, central and right panels.

At low interaction, the behaviour of the energy agrees with the expectation of a Slater insulator and static mean-field theory, where the order parameter m_z corresponds to a larger local moment or decrease in D. In contrast, as shown in Fig. 4.7, at large U the ratio

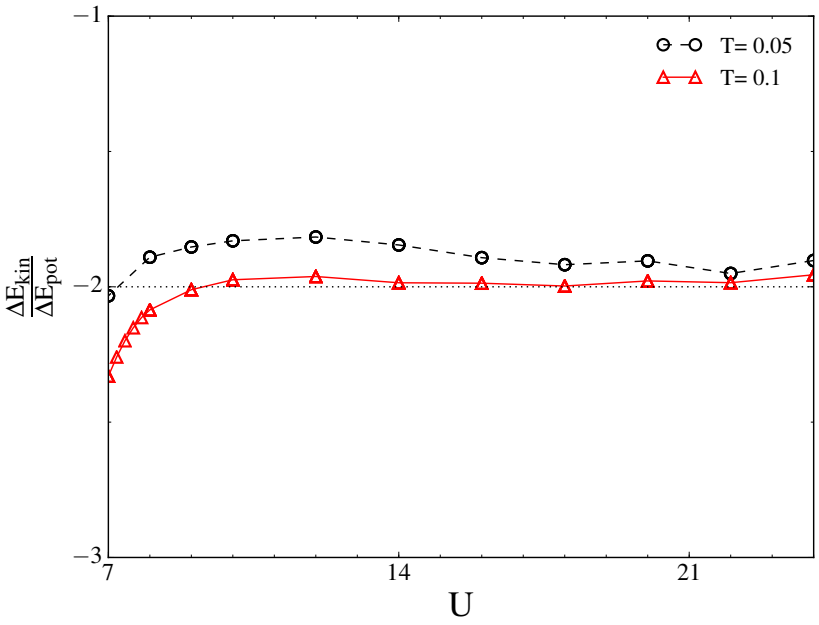

Figure 4.7: Ratio between kinetic energy and potential energy gain as a function of the interaction U. The red triangles and black circles are taken at $T = 1/10$ and at $T = 1/20$, respectively. At large U, $\Delta E_{\rm kin} \approx -2\Delta E_{\rm pot}$.

between the kinetic and potential energy gain approaches the expected energetic relation of

the Heisenberg limit [152]:

$$E_{\rm kin} \approx -2E_{\rm pot}. \tag{4.28}$$

Therefore, the AF state is stabilised by a kinetic-energy gain. This is illustrated in Fig. 4.8

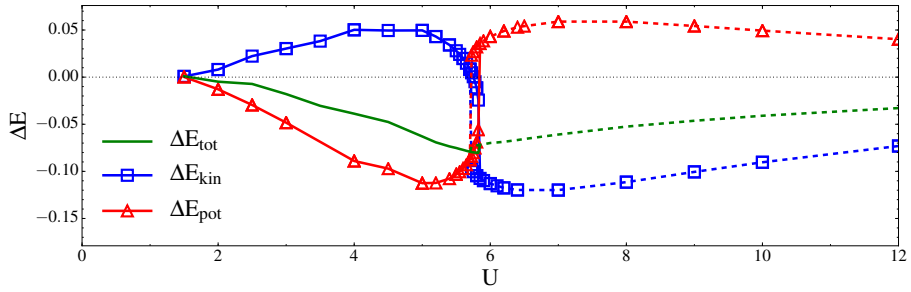

Figure 4.8: Difference in the potential, kinetic and total energies between the antiferromagnetic and normal state as a function of the interaction U at $T = 1/20$ respresented with the red, blue and green lines respectively.

where the difference in potential, kinetic, and total energies between the AF and the normal state, is plotted as a function of U for $T < T_{\rm MIT}$. Crucially, we find that the first-order Mott transition determined the critical U at which $\Delta E_{\rm pot}$ and $\Delta E_{\rm kin}$ cross zero, and where $\Delta E_{\rm tot}$ reaches its minimum. This is one of our main findings, as also shown for a broader set of parameters in Fig. 4.9, that displays the difference in kinetic, potential, and total energy between AF and the normal state as a function of U for $T = 1/20, 1/10, 1/4$ (left, central and right panels). As a benchmark, in Figs. 4.9 panels (a), (d) and (g) we also plot the $T = 0$ variational QMC calculation of Ref. [165].

These findings appear clearer from Fig.4.10, where $\Delta E_{\rm pot}$ is colour-coded for the entire AF region. The steep white region testifies to a change of sign in this quantity. This occurs at the Mott transition for $T < T_{\rm MIT}$ and, by increasing temperature $T > T_{\rm MIT}$, persists with a nontrivial crossover from the Mott endpoint to approximately $T_N^{d,\max}$. This crossover line is also in proximity to the minimum in the total condensation energy computed for isothermal scans and here indicated with the line of green diamonds. Furthermore, these results are in correlation with the Widom line [31–33] of the Mott transition (dashed line of open circles) that we computed as the isothermal maxima of the derivative of the double occupancy with respect to the interaction $dD/dU|_T$. Fig. 4.11 sums up our results in the $T-U$ phase diagram with the addition of the change in sign for $\Delta E_{\rm kin}$, marked with the blue line of squares. This latter quantity does not have the same behaviour as the previous crossover lines. It emerges

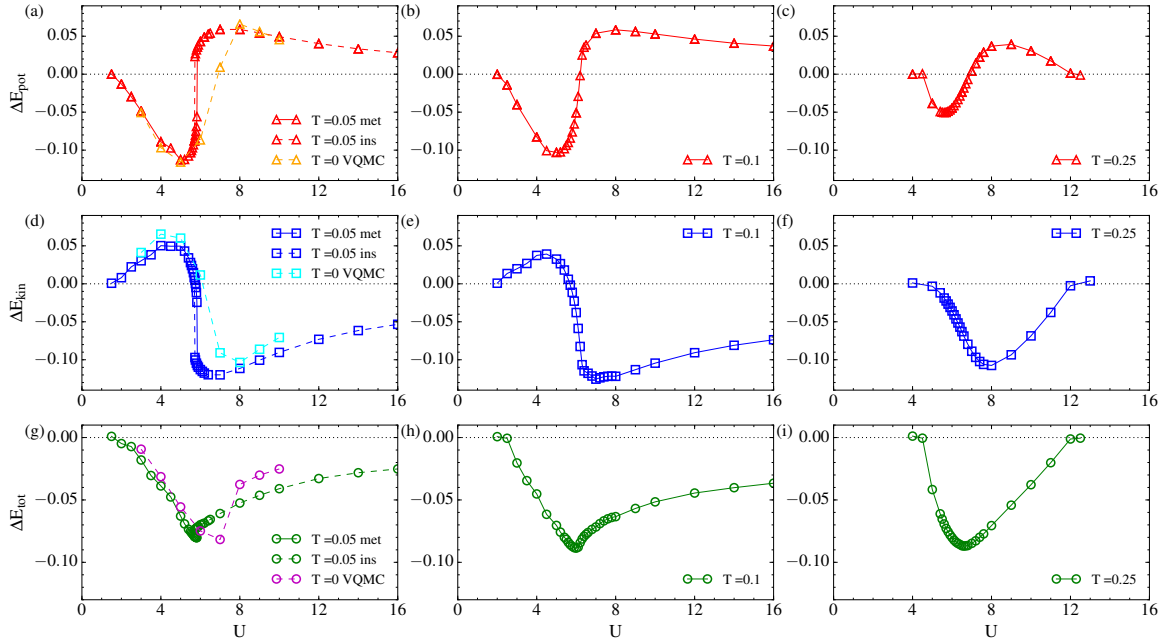

Figure 4.9: Difference in potential energy $\Delta E_{\rm pot} = E^{\rm AF}_{\rm pot} - E^{\rm NS}_{\rm pot}$ (top panels), in kinetic energy $\Delta E_{\rm kin}$ (central panels) and in total energy $\Delta E_{\rm tot}$ (bottom panels) as a function of U. As in Fig. 4.6, data is shown for $T = 1/20 < T_{\rm MIT}$, $T = 1/10 > T_{\rm MIT}$, and $T = 1/4$ (left, central and right columns, respectively). As a benchmark, at our lowest temperature (panels (a), (d) and (g)) we show the $T = 0$ variational QMC calculation of Ref. [165].

from the Mott transition, but extends down to $U \approx 5$ and up to $T \approx 1/5$.

This scenario extends, at finite temperature, the variational QMC calculations of Ref. [165], where they have found a change in sign for $\Delta E_{\rm pot}$ between $U = 6$ and $U = 7$, as indicated by the magenta circle at $T = 0$ in Fig. 4.10. This kind of change from a potential to a kinetic energy driven mechanism also appears in studies of the BCS-BEC crossover in the attractive Hubbard model [153, 156, 176–178].

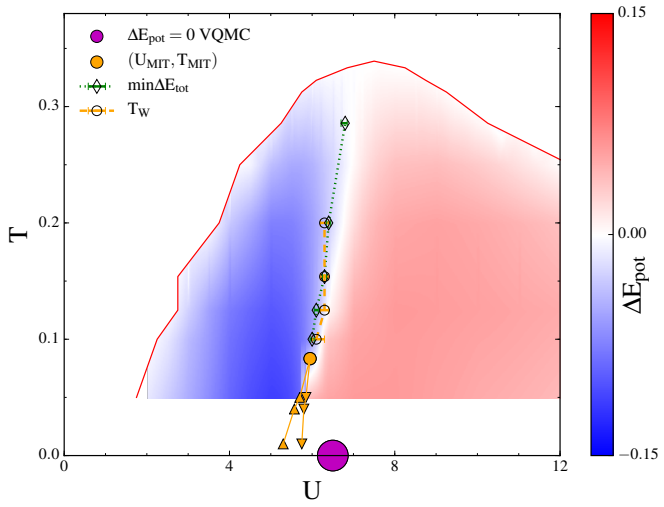

Figure 4.10: Phase diagram $T-U$ with $\Delta E_{\rm pot}$ colour-coded. The steep white region testifies to a change of sign in $\Delta E_{\rm pot}$ that connects $U_{\rm MIT}$ and $T_N^{d,\max}$. This crossover line correlates with the isothermal minimum of the condensation energy, indicated with the dashed line of green diamonds, and with the Widom line of the underlying Mott transition, calculated by by the max of $dD/dU|_T$ and indicated with the dashed line of open circles. The magenta circle at $T=0$ represent the variational QMC calculation of Ref. [165] for $\Delta E_{\rm pot}=0$.

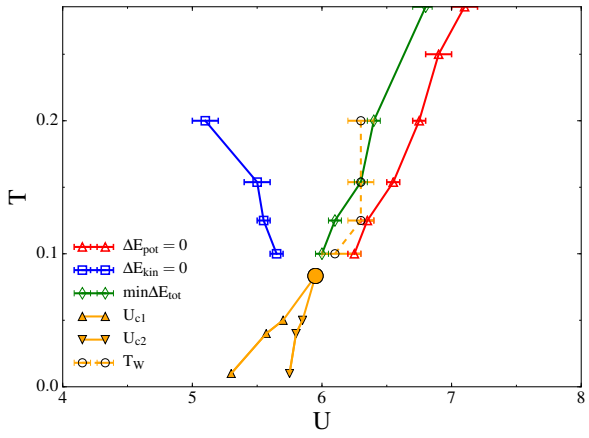

Figure 4.11: Temperature T versus interaction U phase diagram for the half-filled Hubbard model. As in Fig. 4.10 the first-order Mott metal-insulator transition is marked by the spinodal lines $U_{c1}(T)$ and $U_{c2}(T)$, with the up and down pointing triangles respectively, and its second-order critical endpoint with the full orange circle. We indicate, with the dashed orange line of open circles, the Widom line of this transition established by the isothermal local maximum of $dD/dU|_T$. The lines of red triangles blue square represent the isothermal loci for the change in sign for $\Delta E_{\rm pot}$ and $\Delta E_{\rm kin}$, respectively, and the line of green diamonds shows the minimum of the total condensation energy $\Delta E_{\rm tot}$.

4.6 Density of States

The difference bertween the weak and strong coupling regimes also emerges by looking to Figs. 4.12 and 4.13 at the local density of states defined as:

$$\mathcal{N}(\omega) = -\frac{1}{\pi}\mathrm{ImG}(\omega), \tag{4.29}$$

where $G(\omega)$ is the analytical continuation of the Green function in Matsubara frequencies $G(\imath\omega_n)$, obtained using the maximum-entropy approach based on Bayesian inference [179]. In both figures we plotted the total $\mathcal{N}(\omega)$ for the antiferromagnetic case with full colour coded lines and for the normal state with the dashed grey lines in the left panels, whereas in the right panel there are the two antiferromagnetic spin projections $\mathcal{N}_\uparrow(\omega)$, $\mathcal{N}_\downarrow(\omega)$. In Fig. 4.12, panels (a) and (b), is displayed the temperature evolution of the DOS across T_N^d. For $U = 4 < U_{\mathrm{MIT}}$ at low temperature, the structure of the AF DOS presents a narrow gap between two prominent peaks which are alike to the quasiparticles of the Bogoliubov theory, for this they are named after him. This gap, that in an infinite size-system is a pseudogap [112], establishes that we are in the presence of an antiferromagnetic insulator (AF-I). At higher energies we can appreciate small precursors of the Hubbard bands because the interaction is too strong to be treated in the static mean-field limit [112, 180, 181]. However the evolution of the DOS is similar to the one in this limit: the Bogoliubov peaks broaden upon decreasing the distance between each other as the temperature increases until they merge entirely above T_N^d, as shown in Fig. 4.12 panel (c). As expected from the mean-field approach, the spectral weight is reorganised mostly over a frequency range of the size of the gap. This is also visible on the spin-projected spectra in Fig. 4.12 panel (b): even though at low T, Bogoliubov peaks are relatively spin polarised, the distance between the two spin projections decreases at frequencies above the gap. As expected from a mean-field approach, the closure of the gap happens via a reorganisation of the spectral weight over a frequency range on the scale of the gap. This is also visible in the spin-projected spectra of Fig. 4.12 panel (b): despite at low T the Bogoliubov peaks appear to be spin polarised, the difference between the two spin projections decreases for frequencies above the gap. The DOS of the normal state is metallic with a marked peak at the Fermi level. This indicates that in the weak coupling regime the AF-I arises from a metallic normal state. These results differ from those at strong coupling regime as shown in Fig. 4.12 panels (d)

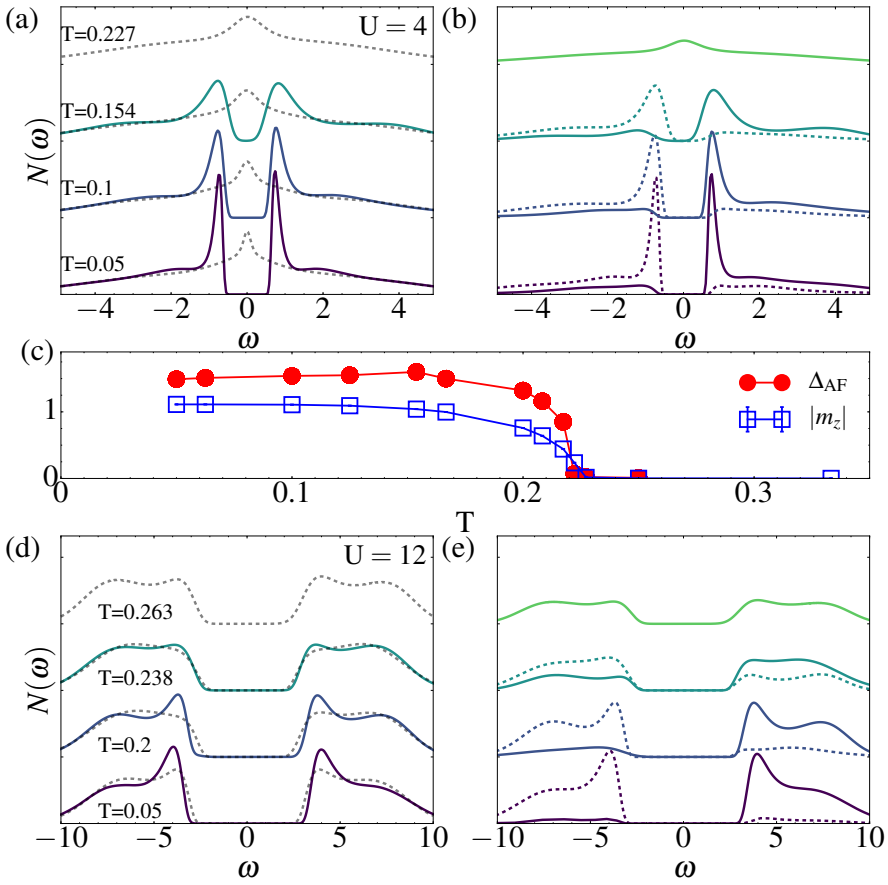

Figure 4.12: Panels (a) and (d) show the temperature evolution of $\mathcal{N}(\omega)$, calculated from analytically continued data [179], for $U = 4 < U_{\mathrm{MIT}}$ and $U = 12 > U_{\mathrm{MIT}}$, respectively. The normal state solutions are in dashed grey, whereas the antiferromagnetic case is displayed in colour. Panels (b) and (e) show the spin projections $\mathcal{N}_{\uparrow}(\omega)$ and $\mathcal{N}_{\downarrow}(\omega)$. Panel (c) displays the AF gap Δ_{AF}, calculated by the distance between the Bogoliubov peaks, and the staggered magnetisation m_z as a function of the temperature T for $U = 4$ with the lines of red dots and blue squares, respectively. The closure of Δ_{AF} follows the decrease of m_z.

and (e) for $U = 12 > U_{\mathrm{MIT}}$. In the AF case a four-peak structure characterises the shape of $\mathcal{N}(\omega)$: the two Hubbard bands are separated by a gap of the order of the interaction strength and at their lower edges are positioned two Bogoliubov peaks [112, 180, 181]. In this strong coupling regime the AF state is also insulating. However there is a different evolution once we increase the temperature, where the broadening of the Bogoliubov peaks is rearranged into the Hubbard bands. As commonly happens in strongly correlated systems, the difference between the two spin projections, particularly at low temperature, does not vanish at high frequencies as before for frequencies above the gap. The normal state in this interaction regime is a Mott insulator, and the gap of the AF states never merge approaching T_N^d. This indicates that in the strong coupling regime the AF-I arises from a Mott insulating state. It is worth to notice

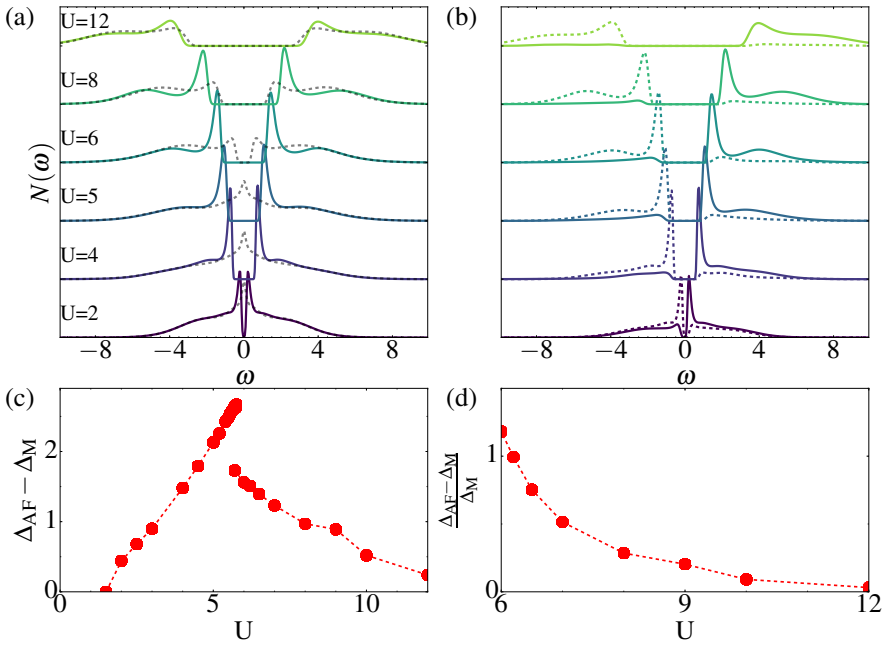

Figure 4.13: Panels (a) and (b) respectively show the interaction evolution of $\mathcal{N}(\omega)$ and their spin projections $\mathcal{N}_\uparrow(\omega)$ and $\mathcal{N}_\downarrow(\omega)$, calculated from analytically continued data [179]. The normal state solutions are in dashed grey, whereas the antiferromagnetic case is shown in colour. These DOS are also showed in an extended version, in Fig. 4.14. Panel (c): the difference between the AF gap Δ_{AF} and the normal state Mott gap Δ_{M}, measured by the distance between the two Hubbard bands, as a function of the interaction U for $T = 1/20$. Panel (d): $(\Delta_{\mathrm{AF}} - \Delta_{\mathrm{M}})/\Delta_{\mathrm{M}}$ as a function of the interaction U. All data are taken at the same temperature: $T = 1/20$.

that, as observed in previous works [170], even above T_N^d, the normal state $\mathcal{N}(\omega)$ presents a leftover signature of the Bogoliubov peaks at the Hubbard bands edges, this attests that the CDMFT solution allows the short-range AF.

Figs. 4.13, panels (a) and (b), and 4.14, exhibit the interaction evolution of $\mathcal{N}(\omega)$ at $T < T_{\mathrm{MIT}} < T_N^d$, in order to elucidate further the difference between weak and strong regimes. We can appreciate how the DOS, that at low interaction manifests two Bogoliubov peaks, evolves to one with only two featureless Hubbard bands at strong interaction. The intermediate cases, i.e. in proximity of $U = 6$ where the Mott transition is visible in the normal state $\mathcal{N}(\omega)$, are characterised by a four-peak structure: two Bogoliubov peaks next to the two Hubbard bands or their precursors [112,180,181]. These structures have a qualitative different evolution once we increase the interaction:

(i) The Bogoliubov peaks, that are narrow below U_{MIT}, first broaden to then disappear into the featureless Hubbard bands at $U \gg U_{\mathrm{MIT}}$. Interestingly, their maximum value occurs just below U_{MIT}.

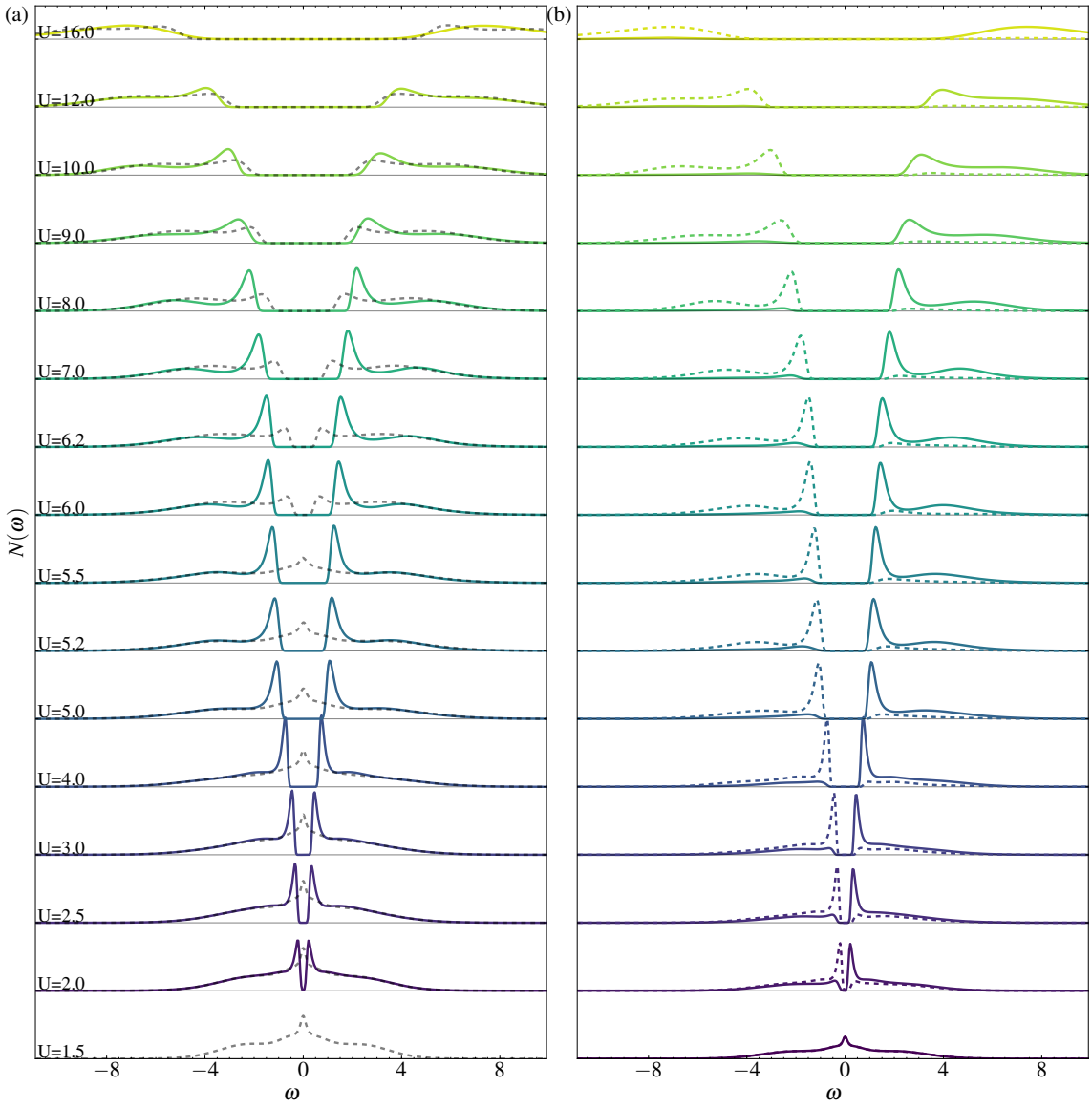

Figure 4.14: Panels (a) and (b) respectively show the interaction evolution of $\mathcal{N}(\omega)$ and their spin projections $\mathcal{N}_{\uparrow}(\omega)$ and $\mathcal{N}_{\downarrow}(\omega)$, calculated from analytically continued data [179]. The normal state solutions are in dashed grey, whereas the antiferromagnetic case is show in colour. This figure extends Fig. 4.13 panels (a) and (b), where fewer values of U are shown.

(ii) At $U \lessapprox U_{\mathrm{MIT}}$ we can observe the manifestation of the precursors of the Hubbard bands, that evolve into well defined Hubbard bands for $U \gtrapprox U_{\mathrm{MIT}}$.

By comparing the gap in the normal Δ_{M} and antiferromagnetic states Δ_{AF} in Fig. 4.13 panels (c) and (d), we can see that the antiferromagnetic gap is always larger than that of the normal state, as observed in the 3D case [182].

4.7 Conclusion

In this chapter, we have charted the phase diagram of the half-filled 2D Hubbard model for the normal and antiferromagnetic phases. This investigation aimed to explain some properties of the cuprates parent compounds. We have seen not only how the metal to Mott insulator transition and its associated Widom line characterises the normal state, but also its interplay with the antiferromagnetic phase that masks it. Indeed, by looking at the behaviour of the condensation energy, we established the presence of a sharp detectable crossover between two different regimes. At weak interaction, the antiferromagnetic phase is stabilised by a potential-energy driven mechanism, whereas at strong interaction the mechanism is kinetic-energy driven. We demonstrated that this crossover is correlated with the Widom line and that it is also visible in the different behaviours of the evolution of the density of states. Indeed, the frequency range over which the antiferromagnetism rearranges the spectral weight, the degree of spin polarisation in the spectra, and the relation between the size of the AF and Mott gaps are also controlled by the Mott transition.

The physics of Mott, so important in this chapter, leaves its signature also upon doping the system. In the next chapter, we will see how the normal and superconducting state are also intertwined phenomena, related to what happens at half-filling. The understanding of the properties of this case is then of primary importance, if we want to unveil the mysteries of the physics of the cuprates.

Chapter 5

Doping the System: an Organising Principle for Strongly Correlated Superconductivity

5.1 Introduction

The work presented in this chapter is based on Ref. [36].

After the analysis presented in the previous chapter, we are ready to explore the phase diagram of the hole-doped cuprates. Here we will focus our investigation on the normal and superconducting states when doping the two-dimensional Hubbard model of Eq. 3.2. Once again we will use the Cellular Dynamical Mean-Field Theory of Section 3.4 on a 2×2 plaquette. This is the minimal cluster size that encodes all two-dimensional short-range charge, spin, and superconducting dynamical correlations. In the previous chapter we charted the phase diagram of the normal state at half-filling, establishing the parametric regime in which the Mott transition emerges. Here we will investigate the fate of such a transition, upon hole-doping a Mott insulator. As found in other works [29–32], we will see that a new transition appears between two metallic states: the pseudogap and a highly correlated metal. Our analysis indicates that this emerging phase transition at finite doping shapes not only the normal-state phase diagram, as we outlined in Chapter 2, but also the complex structure of the superconducting condensate.

The competition at finite temperature with antiferromagnetism studied at T = 0 in previous works [183–185] is a subject we will pursue in future works.

This chapter is organised as follows: we will begin in Section 5.2 by introducing the methodology used in this chapter, then, in Section 5.3, we will consider the properties of the normal state, extending the results presented in Chapter 4 to finite doping. In Section 5.4, we will discuss the behaviour of the phase diagram for various regimes of the parameters, in the presence of superconductivity. Finally, we will demonstrate that the features of the physics of the superconducting state are an phenomenon intertwined with the physics of the normal state. To do this we will conduct an analysis of: the superconducting order parameter in Section 5.5, the scattering rate of the normal state in Section 5.6, and the condensation energy of the system in Section 5.7. To conclude, in Section 5.8, we will investigate how a finite next-nearest-neighbour hopping affects the system, revealing that the results of our analysis do not change in the presence of such a frustration.

5.2 Model and Method

For completeness, let us recall the basic notions on the method as examined in Chapter 3 with some additional information about the study of the d-wave superconductivity.

We consider the two-dimensional Hubbard model on a square lattice, Eq. 3.2, neglecting the second-neighbour hopping necessary to capture the correct Fermi surface, in order to minimise the Monte-Carlo sign-problem. This choice does not alter our main findings, as we will show in Section 5.8. The lattice spacing, Planck's constant, Boltzmann's constant and t are taken as unity. Antiferromagnetism is overemphasised because of the absence of frustration but since we do not allow this phase, by imposing that solution for both spins are the same, we expect that the qualitative results are robust. We solve this model using the Cellular Dynamical Mean-Field Theory covered in Section 3.4 on a 2×2 plaquette immersed in an infinite, self-consistent bath of non-interacting electrons. Since, in order to have a doped Mott insulator, we focus on large values of the interaction U, the best method to solve the impurity problem is the Hybridisation Expansion Continuous-Time Quantum Monte Carlo method of Section 3.5. Alternative quantum Monte Carlo methods [26] suffer a larger sign problem when studying the strong interaction regime. Improvements to speed up the calculations are

implemented by the use of two novel algorithms: a fast rejection algorithm with skip-list data structure [27] and, as discussed in Section 4.2.2, "4-operator updates" that are necessary to guarantee ergodicity [167].

Let us first consider the normal state. Then we will discuss the superconducting phase diagram and the features that determine its shape.

5.3 Pseudogap to Correlated Metal Transition in the Normal State

Fig. 5.1 summarises the principal findings of Refs. [29–32] that we confirm extensively, in unexplored parametric regimes, in the rest of the chapter.

The analysis of the normal state reveals the existence of a metal to metal transition upon doping a Mott insulator state, i.e.when the interaction $U > U_{\mathrm{MIT}}$ [29–32]. In this case, the average occupation n as a function of the chemical potential μ is characterised by a plateau before reaching finite doping $\delta = 1 - n$. When this happens the system becomes metallic, and it exhibits a metastable region of coexistence of two metallic solutions across a pseudogap to correlated metal first-order transition, as shown by the red shaded area in Fig. 5.1, panel (a) and discussed in Refs. [29–32]. This transition culminates in a second-order critical endpoint $(\delta_p, T_p) \approx (0.045, 1/65)$. In Fig. 5.1 panel (b) we plotted the doping as a function of the chemical potential μ at fixed values of the temperature. Here we can observe jumps in the doping for curves with $T < T_p$, these isothermal hysteresis loops define the boundaries of the coexistence region. On the other hand, for $T > T_p$ there is no discontinuity in the doping and only one normal-state phase exists. Despite this, there survives a supercritical behaviour detectable in many dynamical, thermodynamical, and transport quantities as displayed in Figs. 5.1, panels (b,c,e,g,i). The functions of the second-order, which are diverging at the critical endpoint, can present a local maximum for $T > T_p$. The loci of these maxima for each function eventually join forming a line, by asymptotically approaching the critical endpoint. This line, introduced to explain the properties of the phase diagram of the water, is called a Widom line T_W [33] and we determined it through study of the maxima of the charge

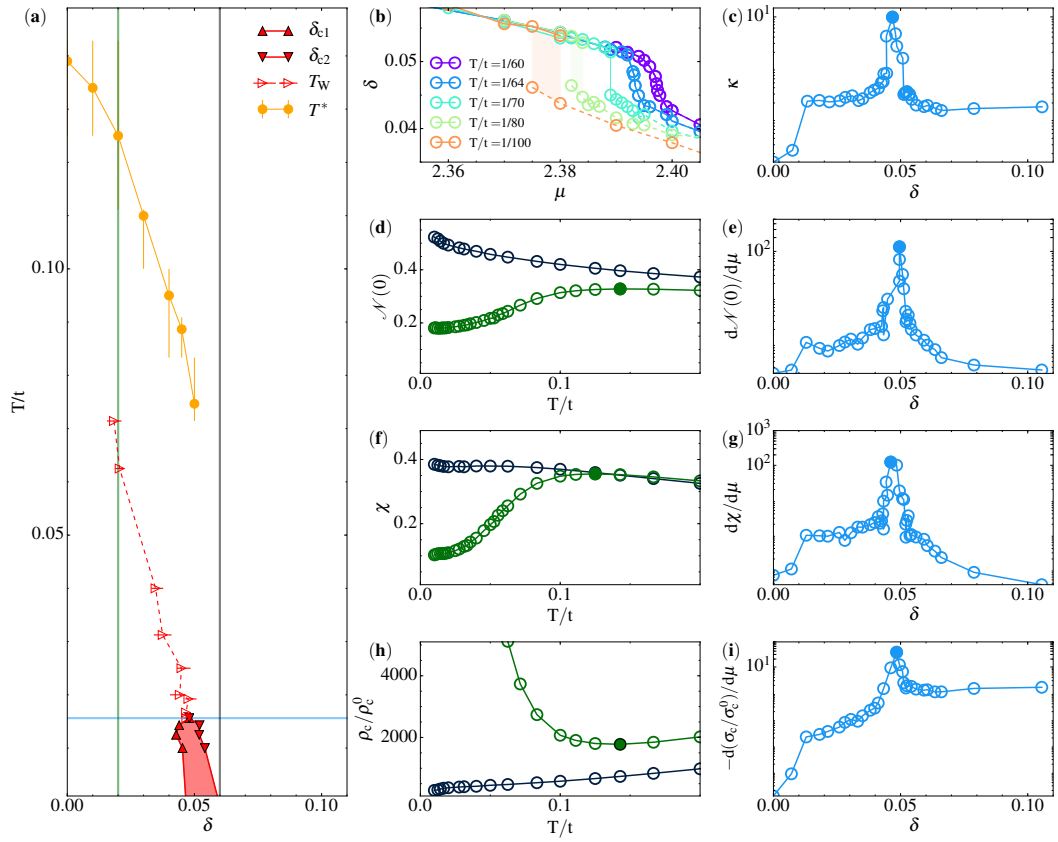

Figure 5.1: Panel (a): the temperature as a function of doping in the normal state phase diagram for $U/t = 6.2$ obtained by CDMFT. In the other panels, the horizontal and vertical shaded lines indicate the values of the temperature, and the doping of the observables, respectively. The extrapolations to $T = 0$ are provided just as a guide for the eye. Panel (b): the doping as a function of the chemical potential, for a range of temperatures as indicated in the legend. Panel (c): the charge compressibility as a function of the doping at $T/t = 1/60$. Panel (d): the density of states at the Fermi energy as a function of the temperature, at $\delta = 0.02$ in green and $\delta = 0.08$ in dark blue. Panel (e): the derivative of the density of states at the Fermi energy with respect to the chemical potential, plotted as a function of the doping at $T/t = 1/60$. Panel (f): the spin susceptibility at the Fermi energy as a function of the temperature, at $\delta = 0.02$ in green and $\delta = 0.08$ in dark blue. Panel (g): the derivative of the spin susceptibility at the Fermi energy with respect to the chemical potential, as a function of the doping at $T/t = 1/60$. Panel (h): c-axis resistivity at the Fermi energy as a function of temperature, at $\delta = 0.02$ in green and $\delta = 0.08$ in dark blue. Panel (i): derivative of the c-axis resistivity at the Fermi energy with respect to the chemical potential as a function of doping at $T/t = 1/60$. Data is taken from Refs. [29–32].

compressibility $\max|_\mu \kappa$ [31], with

$$\kappa = 1/n^2 (dn/d\mu)_T. \tag{5.1}$$

Fig. 5.1 panel (c) shows a semilogarithmic plot of κ as a function of the doping at $T/t = 1/60$ highlighting the position of the local maximum of κ with a filled dot. Charting this maximum for all isothermal maxima of the charge compressibility leads to the Widom line with red

triangles of Fig. 5.1 panel (a). The Widom line also rules the crossovers of other observables: the local density of states at the Fermi level $\mathcal{N}(\omega = 0)$ [31], the spin susceptibility χ [31], the c-axis DC conductivity σ_c [32], all show inflection points as a function of μ. Their derivative with respect to μ are shown in Fig. 5.1 panels (e,g,i) respectively. Furthermore, by considering the response functions at fixed doping as a function of the temperature, we see in Fig. 5.1 panels (d,f,h) different behaviour at low or high doping. ALthough for latter we observe monotonic behaviour for the temperature dependence of $\mathcal{N}(0)$, χ and the c-axis resistivity $\rho_c = 1/\sigma_c$, this changes for $\delta < \delta_p$. In this case we estimate the onset temperature of the pseudogap $T^*(\delta)$ by tracing the position of their maxima or minima. Now we are ready to analyse what happens to this scenario once we consider the superconducting phase.

5.4 Superconducting Dome

In order to study the superconducting state it is useful to introduce the cluster Nambu Green function [186] in the cluster momentum basis:

$$G_K(\tau) = \begin{pmatrix} G_{K\uparrow}(\tau) & F_K(\tau) \\ F_K^\dagger(\tau) & -G_{-K\downarrow}(-\tau) \end{pmatrix}, \tag{5.2}$$

where $F_K(\tau)$ is the anomalous Green function, which in presence of d-wave superconductivity has only a non-zero component: $F_{(0,\pi)}(\tau) = -F_{(\pi,0)}(-\tau) \equiv c_{(\pi,0)\uparrow}(\tau)c_{-(\pi,0)\downarrow}(\tau)$. This anomalous Green function defines the superconducting order parameter:

$$\Phi \equiv \langle T c_{(\pi,0)\uparrow}(\tau)c_{(-\pi,0)\downarrow}(\tau)\rangle, \tag{5.3}$$

namely the superconducting phase is defined by the loci where $|\Phi| \neq 0$ and is delimited by T_c^d, where the d reminds us that this is the *dynamical* mean-field temperature. The boundary, T_c^d, is drawn from the mean of the two temperatures where Φ is greater than a cut-off value to where it is smaller (here this value is $|\Phi|$=0.002).

Although, in agreement with the Bogoliubov-Hohenberg-Mermin-Wagner theorem [108–111], at a finite temperature, in two dimensions, no continuous symmetry breaking is allowed, T_c^d is the temperature below which we have Cooper pair formation within the cluster size [187].

In the interest of completeness, we are going to discuss the phase diagram at half-filling in order to extend the picture of the previous chapter once we allow d-wave superconductivity. Then we will enter into the core part of this chapter by exploring what happens upon doping a Mott insulator.

5.4.1 Half-Filling

The d-wave superconductivity emerges at half-filling and at finite doping in the metallic state near to the Mott insulator [159,183–185,187–195]. In Figure 5.2 we chart the superconducting state in the $U-T$ plane at half-filling.

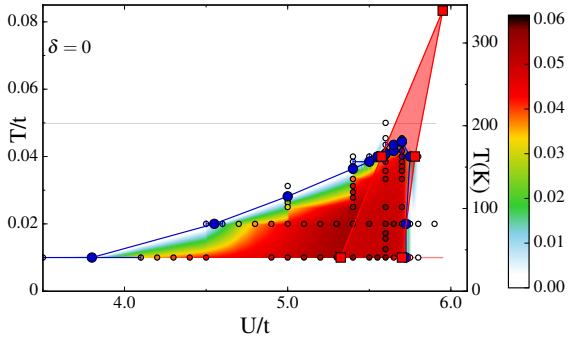

Figure 5.2: d-wave superconducting phase obtained by the plaquette CDMFT solution of the two-dimensional Hubbard model. We explore the $T-U$ space by taking cuts at half-filling as a function of U and T. The line with blue filled circles draws T_c^d, the loci below which we are in presence of superconductivity, i.e. the d-wave order parameter Φ is nonzero. Colour encodes the magnitude of $|\Phi|$ by interpolation of the data of Fig. 5.8. On the right vertical axis, we evaluated the temperature in Kelvin by using $t = 0.35$eV. The red shaded area shows the coexistence region across the first-order Mott metal-insulator transition, obtained from the hysteretic evolution of the double occupancy as a function of the interaction U [187].

Despite the fact that long wavelength thermal or quantum fluctuations [196] of competing long-range order [103] can diminish the actual T_c, the pairing mechanism through long wavelength antiferromagnetic fluctuations [197] can increase it. Nevertheless, T_c^d still has validity as a useful quantity for establishing the place where the Mott physics and short-range correlations produce pairing. At half-filling, T_c^d drops discontinuously to zero following, or in proximity to, the first-order Mott metal-insulator transition. This was shown in the red shaded region in Fig. 5.2 and also discussed in Chapter 4. At weak interaction, superconductivity rises in the metallic state and survives in the coexistence region to then disappear in the Mott insulator, as shown in Fig. 5.2.

5.4.2 Doping the System

In Fig. 5.3 we can observe the $T-\delta$ phase diagram when we dope a metallic solution $U = 5.6 < U_{\mathrm{MIT}}$. In this case, we observe that both the magnitude of the order parameter and T_c^d are decreasing with increasing doping. This behaviour completely differs from when we dope a state for $U > U_{\mathrm{MIT}}$. Indeed, as discussed in Chapter 2, the most interesting parametric

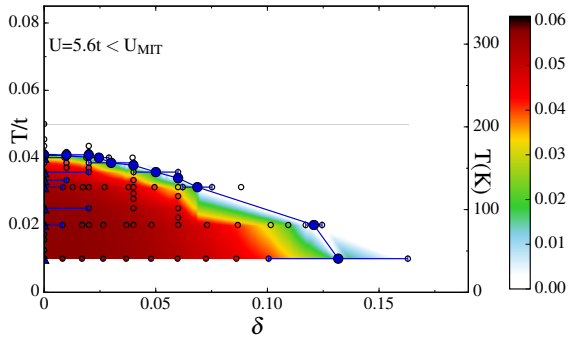

Figure 5.3: The $T-\delta$ phase diagram of the superconducting state for $U = 5.6 < U_{\mathrm{MIT}}$. The line with blue filled circles draws T_c^d, the loci below which we are in presence of superconductivity, i.e. the superconducting order parameter Φ is nonzero. Colour encodes the magnitude of $|\Phi|$ by interpolation of the data of Fig. 5.8. The loci of $\Phi_{\max}(\delta)$ are shown by the line of blue triangles. On the right vertical axis we convert temperature to Kelvin by using $t = 0.35$eV.

regime to describe the cuprates arises upon doping a Mott insulator state. This is the reason for which, in this Chapter, we will mainly focus our investigation on this regime.

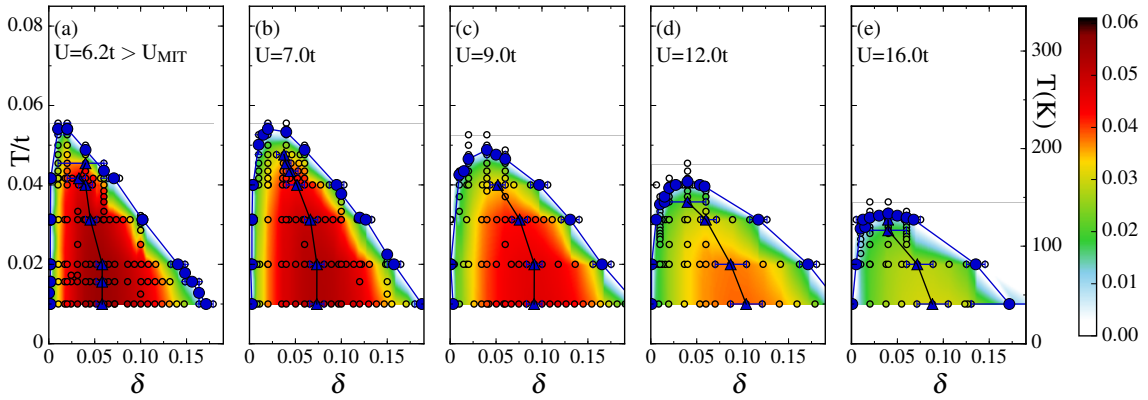

Figure 5.4: The $T-\delta$ phase diagram of the superconducting state for increasing values of the interaction $U = 6.2,\ 7.0,\ 9.0,\ 12.0,\ 16.0$ in panels (a), (b), (c), (d), and (e) respectively. The line of blue filled circles draws T_c^d, the loci below which we are in presence of Superconductivity, i.e. the superconducting order parameter Φ is nonzero. Colour encodes the magnitude of $|\Phi|$ (see Fig. 5.8 for $\Phi(U)$ and $\Phi(\delta)$ curves at different T). The loci of $\Phi_{\max}(\delta)$ are indicated with blue triangles. On the right vertical axis we convert temperature to Kelvin by using $t = 0.35$eV.

Upon doping a Mott insulator state, T_c^d forms a highly asymmetric dome-like shape. It

rises steeply at small doping, reaching its maximum at the optimal doping δ_{opt} and then it falls more gently with increasing doping, as exhibited by Fig. 5.4. In previous works [167,187] the question as to whether or not the insulating state was separated via a first-order transition from the superconducting phase was left open. Our results resolve this doubt. $T_c^d(\delta)$ drops near $\delta = 0$, so there is no trace of such a first-order transition. In the $U-\delta-T$ space, $T_c^{\max}$ of

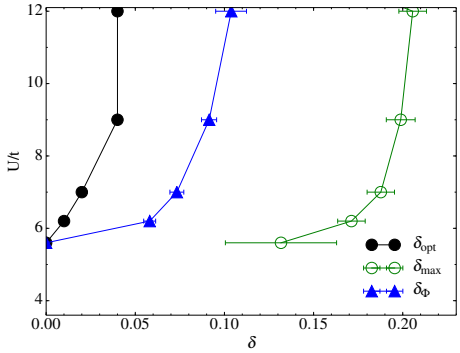

Figure 5.5: Characteristic dopings in the $U-T$ plane: black circles describe the optimal doping δ_{opt}, blue triangles the position of the maximum order parameter $\delta_{\Phi_{\max}}$ for $T/t = 1/100$, and green circles the largest doping at which superconductivity disappears for the lowest temperature studied $\delta_{\max}$, in this case $T/t = 1/100$.

T_c^d appears to be at finite optimal doping, just above U_{MIT}. By increasing the interaction U, we confirmed that $T_c^d(\delta)$ scales with the super-exchange energy $J = 4t^2/U$ for large enough U [185,198], thereby reducing $T_c^{\max}$. As shown in Fig. 5.5, we can observe that δ_{opt} is located at $\delta = 0$ for $U < U_{\text{MIT}}$ to then stabilise around $\delta \approx 0.04$ for large U.

As a benchmark, it is interesting to note that the range of doping in which we are in the presence of superconductivity at the lowest temperature [167] is consistent with that obtained with CDMFT at $T = 0$ [185], as displayed in the left side panels of Fig. 5.6. Nevertheless as illustrated in the right side panels of Fig. 5.6 in Fig. 5.7, Dynamical Cluster Approximation (DCA) results on larger clusters up to 16 sites [194] show an asymmetric superconducting dome with a sudden drop of T_c^d with decreasing δ, similarly to our case. However, the increased accuracy in the momentum space leads to a dome for T_c that begins at a higher doping than ours.

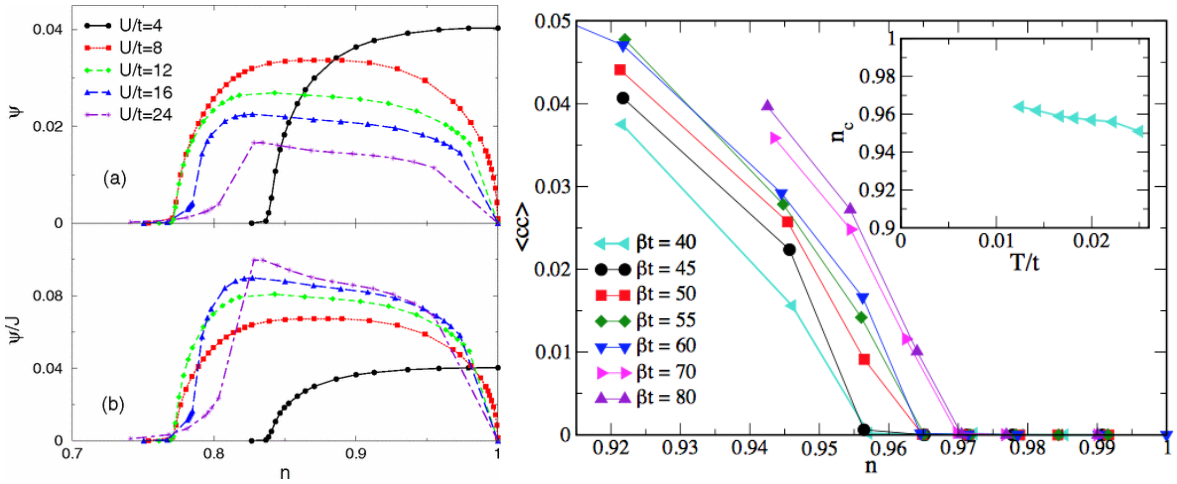

Figure 5.6: On the left: panel (a): d-wave order parameter ψ as a function of the filling $n = 1 - \delta$ for several values of the interaction U computed with CDMFT at $T = 0$ using Exact Diagonalization Technique as the impurity solver [199]. (b) As (a), but with the vertical axis divided by the super-exchange energy J. Figure taken from Ref. [185]. On the right: d-wave order parameter $\langle cc \rangle$ as a function of filling n for $U/t = 6.5$ for several values of the inverse temperature, computed with 8-site Dynamical Cluster Approximation using Continuous Time Auxiliary Field Quantum Monte Carlo as the impurity solver. Inset: scaling of the critical filling, i.e. the lowest value of the occupation that is superconducting for isothermal scans, computed for several temperatures. Figure taken from Ref. [194].

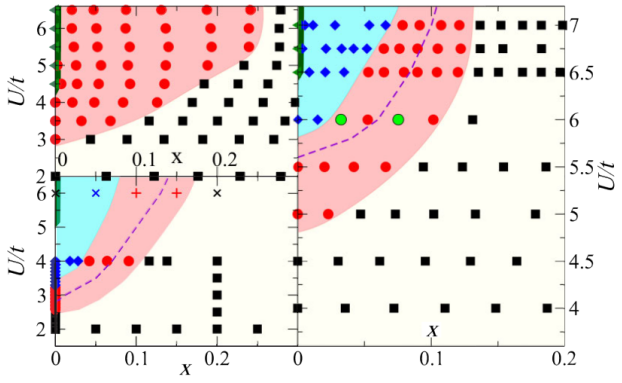

Figure 5.7: Phase diagram of the two-dimensional Hubbard model in the interaction U versus doping x plane, computed with 4-site (left upper panel), 16-site (left lower panel), and 8-site (right panel) Dynamical Cluster Approximation, using Continuous Time Auxiliary Field Quantum Monte Carlo as the impurity solver at temperature $T = 1/40$. The dashed line indicates the location of the normal state pseudogap onset. The circles in the red shaded area and the diamonds in the light blue shaded area display the superconducting region and the pseudogap respectively; whereas the black squares represent the Fermi liquid phase. The Mott insulator states of the undoped system are drawn with a heavy, dark green, solid line. Figure taken from Ref. [194].

5.5 Superconducting Order Parameter

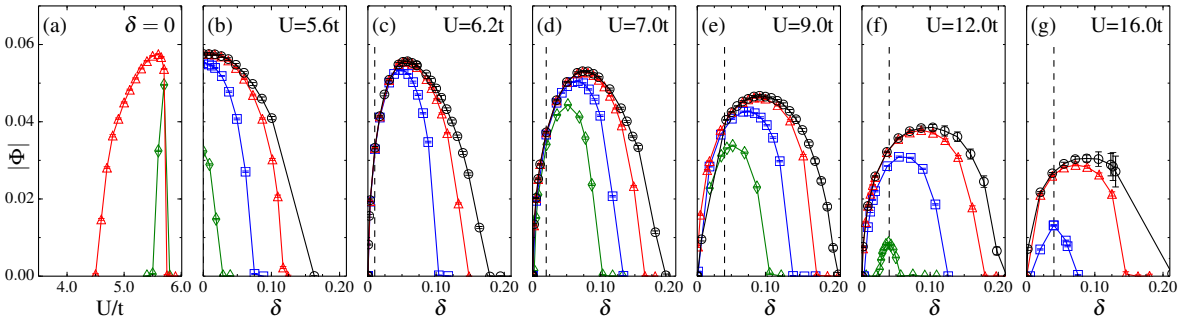

Figure 5.8: The superconducting order parameter $|\Phi|$ as a function of the interaction U in panel (a) and as a function of the doping δ for $U = 5.6,\ 6.2,\ 7.0,\ 9.0,\ 12.0,\ 16.0$ in panels (b) through to (g). The data is shown for isothermal scans of several different temperatures: with green diamonds for $T/t = 1/25$, with blue squares for $T/t = 1/32$, with red triangles for $T/t = 1/50$, and with black circles for $T/t = 1/100$. By interpolation of these curves we obtained the colour map in Figs. 5.2, 5.3, and 5.4. The optimal doping δ_{opt} is indicated with the dashed vertical black line in each panel.

The analysis of the superconducting order parameter Φ, whose magnitude is colour-coded in Fig. 5.4 (the raw data is in Fig. 5.8), helps in understanding the superconducting shape. While $T_c^{\max}$ occurs at finite doping, the overall maximum $\Phi_{\max}$ is found at half-filling close to the Mott insulator. However, as a function of doping, for $U > U_{\text{MIT}}$, Φ forms a dome-like shape with a maximum at $\delta_{\Phi_{\max}}$. At our lowest temperature, $\delta_{\Phi_{\max}}$ increases with incrementing U, until it saturates around $\delta \approx 0.11$ [185] for large values of U. It is interesting to notice the discrepancy of the value of $\delta_{\Phi_{\max}}$ at our lowest temperature with δ_{opt}, i.e. the doping that optimises T_c^d. This demonstrates a peculiar difference with the conventional s-wave superconductivity where $T_c(\delta)$ scales with $\Phi(\delta, T \to 0)$. Instead, the maximum of the order parameter as a function of doping at constant temperature in the $\delta - T$ plane $\Phi_{\max}(\delta)$ has a negatively sloped line that divides the superconducting dome into two regions. We can then argue that the sharp asymmetry of the superconducting dome is due to this negatively sloped line, which is intimately linked to the underlying first-order pseudogap to correlated metal transition of the normal state, as we will discuss below.

5.6 Superconductivity and Pseudogap

In this section, we will discuss how and to what extent the physics of the normal state influences that of high-temperature superconductivity. As examined in Section 5.3, for $U > U_{\text{MIT}}$, small

δ, and at low T a state with strong singlet correlations appears thanks to the strong interaction U and the emergent super-exchange J. The properties of this phase are those of the pseudogap phase [31].

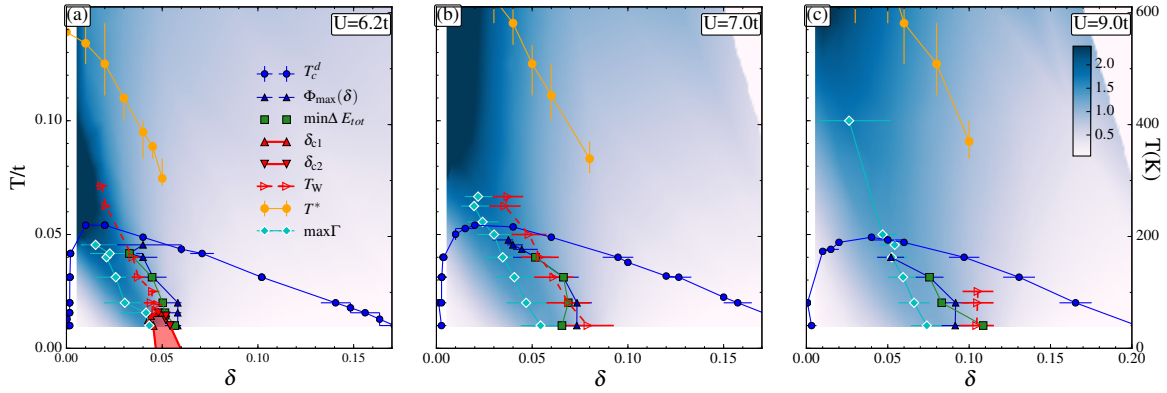

Figure 5.9: Temperature versus hole doping phase diagram for $U/t = 6.2, 7$, and 9, respectively. The line of blue filled circles outlines T_c^d. The red shaded area in (a) shows the hidden coexistence region across the first-order pseudogap to correlated metal transition obtained from the hysteretic evolution of the doping as a function of chemical potential μ. This region terminates in a second-order critical point at (T_p, δ_p) leaving a supercritical signature for $T > T_p$ encoded in the Widom line T_W (line of orange circles), the loci of the maxima of the charge compressibility as a function of δ at constant T [32]. The line of blue triangles outlines the maximum of the superconducting order parameter as a function of doping at constant temperature $\Phi_{\max}(\delta)$, and it is close to the values of T_W for the underlying normal state. The magnitude of the scattering rate Γ, estimated from the zero-frequency extrapolation of the imaginary part of the $(\pi, 0)$ component of the cluster self-energy [29,30], is colour-coded. Panels (d), (e), (f): the difference in the kinetic, potential and total energies between the superconducting and normal states are indicated with the blue, red and green lines respectively. The full and dashed lines represent $T/t = 1/50$ and $T/t = 1/100$ respectively. The shaded bands give the standard errors. The loci where the condensation energy reaches is minimum is shown with a line of green filled squares. It follows $T_W(\delta)$ and $\Phi_{\max}(\delta)$.

$T^*(\delta)$, the line of orange filled circles in Fig. 5.9, introduced in literature in Ref. [32] and here in Section 5.3, indicates the onset of the drop in the spin susceptibility. Equivalently, we can find a similar result using the onset for the fall in the density of states or in the minima of the c-axis resistivity [32]. $T^*(\delta)$ exists only up to a critical value of the doping $\delta < \delta_p$, which is the doping for the critical endpoint (δ_p, T_p) of the first-order transition that is visible in Fig. 5.9, panel (a). For larger values of U, this transition is no longer visible at accessible temperatures. However its supercritical signature survives, suggesting that it is still present [30]. In Fig. 5.9 we estimate this line as the loci of the maxima of the isothermal electronic compressibility [29–31]. This choice is vindicated by the fact that also other quantities, such as the local DOS at the Fermi energy, the spin susceptibility, and the c-axis DC conductivity, present an inflection point at $T_{\rm W}(\delta)$ [32], as shown in Section 5.3. Another important quantity to be linked with this transition is the anomalous scattering rate

that it generates [29, 30]. This is shown in Fig. 5.9 where we colour-coded the normal state scattering rate Γ and where we indicat,e with the blue open diamonds, its maximum $\Gamma_{\max}$. Our definition of Γ is:

$$\Gamma = -\mathrm{Im}\Sigma_{(\pi,0)}(\omega \to 0), \tag{5.4}$$

with $\Sigma_{(\pi,0)}$ the $(\pi, 0)$ component of the cluster self-energy. This quantity can be physically interpreted as the inverse of the lifetime of the quasiparticle excitations that in a Fermi liquid at the Fermi surface goes to infinity. We can observe in Fig. 5.9, panel (a) that the dark

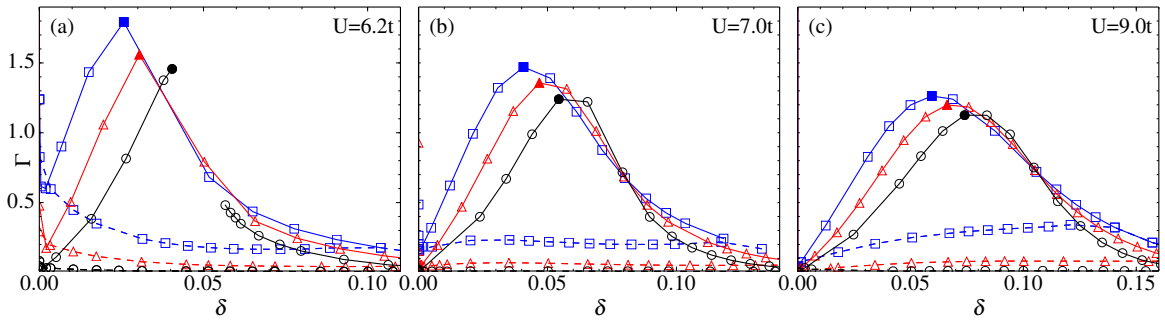

Figure 5.10: Scattering rate Γ for $U/t = 6.2, 7, 9$ in the normal and superconducting states (full and dashed lines, respectively). Data is presented as blue squares for temperature $T/t = 1/32$, red triangles for $T/t = 1/50$, and black circles for $T/t = 1/100$. By interpolation of this data we obtain the colour map of Fig. 5.9. The total maximum of the normal state scattering rate, $\Gamma(\delta)|_T$, is marked for each temperature by a solid symbol and their loci is displayed with the solid white diamond line in Fig. 5.9. For finite doping $\delta > 0$, there is a maximum in the normal state $\Gamma(\delta)|_T$, that is near to the first-order transition between the pseudogap and correlated metal for $T < T_p$ (cf. $U/t = 6.2$ and $T/t = 1/100$) and in the supercritical region for $T > T_p$ [29,30]. Upon increasing temperature, the value of $\Gamma(\delta)|_T$ at its maximum increases as does its width in doping.

blue region where the magnitude of Γ is larger, beginning at the transition approaches the Mott insulator well above T_c^d. Analysing the same quantity in the superconducting state, we see that the large scattering rate drops upon entering the superconducting dome, as already noticed in Refs [193, 200] and shown in Fig.5.10.

The superconducting state hides the first-order transition, but the properties of the latter shape the superconducting phase diagram:

(i) The isothermal maxima of the superconducting order parameter $\Phi_{\max}$ (line of blue filled triangles in Fig. 5.9) is parallel to T_W and $\Gamma_{\max}$. Hence the slope of the first-order transition and its supercritical crossovers in the $T - \delta$ plane relate mutually with the highly asymmetric shape of the superconducting dome.

(ii) The crossing of $\Gamma_{\max}$ and the superconducting dome at approximately δ_{opt} leaves a region

of anomalous scattering for $T > T_c^d$ around this doping.

(iii) The existence of T^* is limited to doping smaller than δ_p only. Therefore, superconductivity and pseudogap are intertwined phenomena: superconductivity can emerge at fixed temperature from a pseudogap phase below δ_p, or from a correlated metal above δ_p [187].

(iv) The source of condensation energy is also controlled by the normal state, as we are going to discuss in the next section.

5.7 Condensation Energy

The superconducting free energy is lower than that of the normal state. The difference in the energy of these two states at the ground state defines the condensation energy. The origin of this quantity is unambiguously defined just for a given model [201, 202]. The s-wave superconductivity in the BCS model emerges due to a reduction of the potential energy that overcomes the kinetic energy gain caused by particle-hole mixing. On the other hand, this picture is different in cuprates. Indeed, inelastic neutron scattering results suggest that the superconducting state is stabilised by an increment in the super-exchange energy [203]. Moreover, ARPES [7] and optical data [80, 82, 85, 87] have suggested that in the underdoped regime superconductivity is kinetic-energy driven [202–206].

We estimate the total condensation energy as:

$$\Delta E_{\text{tot}} = E_{\text{tot}}^{\text{SC}} - E_{\text{tot}}^{\text{NS}}, \tag{5.5}$$

the difference in the superconducting and normal state energies for our lowest temperatures, where we expect to be close to the ground state. Let us explicitly demonstrate the formulas used in order to evaluate the kinetic energy, then we will be able to comment on our findings.

5.7.1 Kinetic Energy in CDMFT within Hybridisation Expansion Impurity Solver

The kinetic energy per site in DMFT, using as the impurity solver the Continuous-Time Quantum Monte Carlo Hybridisation Expansion algorithm, is related to the average order of

expansion of the impurity partition function in the hybridisation function between the impurity and the bath $\langle k \rangle$, as demonstrated in Section 3.5:

$$E_{\text{kin}}^{(\text{DMFT})} = -\frac{\langle k \rangle}{\beta}, \tag{5.6}$$

with β the inverse temperature. The extension of this formula for the CDMFT case gives rise to an additional contribution coming from the cluster. This term can be calculated from the cluster density matrix. The kinetic energy per site reads

$$E_{\text{kin}} = \frac{2}{N} \sum_{i,j} \sum_{\mathbf{X},\mathbf{X}'} t_{ij} \left(\mathbf{X} - \mathbf{X}' \right) \left\langle c_i^\dagger \left(\mathbf{X} \right) c_j \left(\mathbf{X}' \right) \right\rangle, \tag{5.7}$$

where i, j label the position within the cluster, N is the number of sites, and $\mathbf{X}, \mathbf{X}'$ indicate the position of the cluster. Summing over all positions and observing that the hopping matrix $t_{ij} \left(\mathbf{X} - \mathbf{X}' \right)$ is symmetric, there is no need to add the Hermitian conjugate. Using the definition of the Green function we have:

$$E_{\text{kin}} = \frac{T}{N} \sum_n e^{-\imath\omega_n 0^-} \sum_{i,j} \sum_{\mathbf{X},\mathbf{X}'} t_{ij} \left(\mathbf{X} - \mathbf{X}' \right) G_{ji} \left(\mathbf{X}' - \mathbf{X}; \imath\omega_n \right). \tag{5.8}$$

By applying a Fourier transformation to this expression on the position of the clusters, we obtain:

$$E_{\text{kin}} = \frac{2T}{N} \sum_n e^{-\imath\omega_n 0^-} \sum_{i,j} \sum_{\widetilde{k}} t_{ij} \left(\widetilde{\mathbf{k}} \right) G_{ji} \left(\widetilde{\mathbf{k}}; \imath\omega_n \right). \tag{5.9}$$

By inserting the expression for the inverse of the lattice Green function, the hopping can be rearranged as:

$$\begin{aligned} E_{\text{kin}} &= \frac{2T}{N} \sum_n e^{-\imath\omega_n 0^-} \sum_{i,j} \sum_{\widetilde{\mathbf{k}}} \left[\imath\omega_n + \mu - \Sigma_{ij} \left(\imath\omega_n \right) - G_{ij} \left(\widetilde{\mathbf{k}}; \imath\omega_n \right)^{-1} \right] G_{ji} \left(\widetilde{\mathbf{k}}; \imath\omega_n \right) \\ &= \frac{2T}{N} \sum_n e^{-\imath\omega_n 0^-} \left[\sum_{i,j} \sum_{\widetilde{\mathbf{k}}} \left[(\imath\omega_n + \mu - \Sigma_{ij} \left(\imath\omega_n \right)) G_{ji} \left(\widetilde{\mathbf{k}}; \imath\omega_n \right) \right] - \sum_i \sum_{\widetilde{\mathbf{k}}} \mathbb{1} \right]. \end{aligned} \tag{5.10}$$

By recalling that the self-consistency condition is given by:

$$G_{ji}^{imp}\left(\imath\omega_n\right) = \frac{1}{N_{sr}} \sum_{\widetilde{\mathbf{k}}} G_{ji}\left(\widetilde{\mathbf{k}}; \imath\omega_n\right), \tag{5.11}$$

with $N_{sr} = N/N_c$, and N_c the cluster size (here $N_c = 4$), this last relation allows us to perform the sum over $\widetilde{\mathbf{k}}$ and to write E_{kin} as

$$E_{\text{kin}} = \frac{2T}{N_c} \sum_n e^{-\imath\omega_n 0^-} \left[\sum_{i,j} \left[(\imath\omega_n + \mu - \Sigma_{ij}\left(\imath\omega_n\right)) G_{ji}^{imp}\left(\imath\omega_n\right) \right] - \sum_i \mathbb{1} \right], \tag{5.12}$$

where we have used the relation: $\sum_{\widetilde{\mathbf{k}}} = N_{sr} = \frac{N}{N_c}$. Inserting the expression for $G_{ij}^{imp}\left(\imath\omega_n\right)^{-1}$, one obtains:

$$\begin{aligned} E_{\text{kin}} &= \frac{2T}{N_c} \sum_n e^{-\imath\omega_n 0^-} \left[\sum_{i,j} \left[(G_{ij}^{imp}\left(\imath\omega_n\right)^{-1} + t_{ij}^{imp} + \Delta_{ij}\left(\imath\omega_n\right)) G_{ji}^{imp}\left(\imath\omega_n\right) \right] - \sum_i \mathbb{1} \right] \\ &= \frac{2T}{N_c} \sum_n e^{-\imath\omega_n 0^-} \sum_{i,j} \left[(t_{ij}^{imp} + \Delta_{ij}\left(\imath\omega_n\right)) G_{ji}^{imp}\left(\imath\omega_n\right) \right] \\ &= \frac{2T}{N_c} \sum_n e^{-\imath\omega_n 0^-} \sum_{i,j} \left[\Delta_{ij}\left(\imath\omega_n\right) G_{ji}^{imp}\left(\imath\omega_n\right) \right] + \frac{2T}{N_c} \sum_n e^{-\imath\omega_n 0^-} \sum_{i,j} \left[t_{ij}^{imp} G_{ji}^{imp}\left(\imath\omega_n\right) \right]. \end{aligned}$$

The first term of this expression is linked to the expansion order, as demonstrated in Section 3.5, while the second contribution is:

$$\begin{aligned} \frac{2T}{N_c} \sum_n e^{-\imath\omega_n 0^-} \sum_{i,j} \left[t_{ij}^{imp} G_{ji}^{imp}\left(\imath\omega_n\right) \right] &= \frac{2T}{N_c} \sum_n e^{-\imath\omega_n 0^-} \sum_{\mathbf{K}} t_{\mathbf{K}}^{imp} G_{\mathbf{K}}^{imp}\left(\imath\omega_n\right) \\ &= \frac{1}{N_c} \sum_{\mathbf{K}} t_{\mathbf{K}}^{imp} n_{\mathbf{K}}^{imp}, \end{aligned} \tag{5.13}$$

where $n_{\mathbf{K}}^{imp}$ is the occupation of the cluster momentum $\mathbf{K}$. Finally, the total kinetic energy is given by:

$$E_{\text{kin}} = -\frac{\langle k \rangle}{N_c \beta} + \frac{1}{N_c} \sum_{\mathbf{K}} t_{\mathbf{K}}^{imp} n_{\mathbf{K}}^{imp}. \tag{5.14}$$

This last equation serves to define

$$E_{\text{kin}} = E_{\text{kin}}^{(1)} + E_{\text{kin}}^{(2)}. \tag{5.15}$$

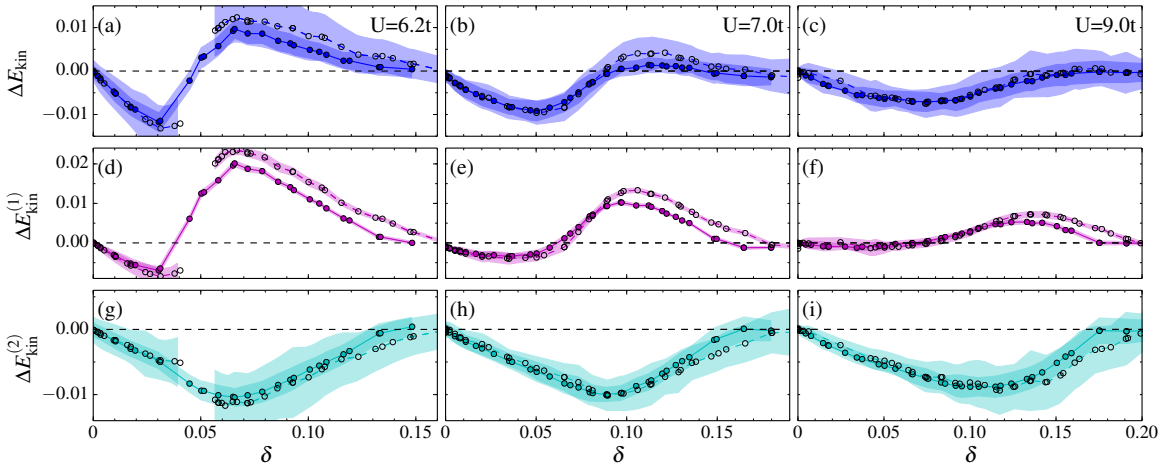

Figure 5.11: Contributions to the doping evolution for the spread of the kinetic energy between the superconducting and normal states at $U/t = 6.2, 7, 9$ on the left, central and right columns respectively. The full and dashed lines are for $T/t = 1/50$ and $T/t = 1/100$ respectively. Top panels: difference in the total kinetic energy $\Delta E_{\rm kin}$; Central panels: contribution from terms outside the cluster $\Delta E^{(1)}_{\rm kin}$; Bottom panels: contribution from terms within the cluster $\Delta E^{(2)}_{\rm kin}$. We relate the sign change in $\Delta E_{\rm kin}$ to the sign change in $\Delta E^{(1)}_{\rm kin}$. The definitions of the various contributions are given by Eqs. 5.14 and 5.15.

In Fig. 5.11 we plot the difference in the kinetic energy of the superconducting and normal states as a function of doping. It is interesting to note from the top panels of Fig. 5.11, that the contribution to the kinetic energy outside the cluster $E^{(1)}_{\rm kin}$ can change sign. On the other hand, from the bottom panels of Fig. 5.11 we observe that the cluster contribution to the kinetic energy $E^{(2)}_{\rm kin}$ decreases in the superconducting state for all dopings.

5.7.2 Results

Now that we have discussed how to evaluate the potential and kinetic energies, we can finally discuss the condensation energy of Eq. 5.5. Our results as a function of δ are plotted in Fig.

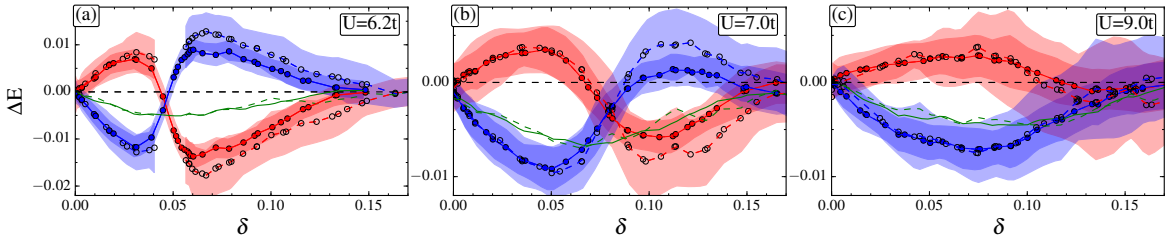

Figure 5.12: The difference in kinetic, potential and total energies between the superconducting and normal states are indicated with the blue, red and green lines respectively. The full and dashed lines are for $T/t = 1/50, 1/100$, respectively, and the shaded bands give the standard errors.

5.12 with the green line for the total energy, the blue line for the kinetic energy $\Delta E_{\rm kin}$, and the

red line for the potential energy $\Delta E_{\rm pot}$. The value of the net condensation energy is negative, as anticipated. Observing $\Delta E_{\rm kin}(\delta)$ and $\Delta E_{\rm pot}(\delta)$, we have two sharply distinguishable features:

(i) They have a non monotonic behaviour.

(ii) They can exhibit a sign change.

Furthermore, as shown for $U = 6.2, 7$, in Figs. 5.12, panel (a) and (b), the pairing mechanism changes from being kinetic-energy driven at small doping to being potential-energy driven, as in the BCS theory, at large doping. When $U \geq 9$, Fig. 5.12, panel (c), superconductivity is always driven by the kinetic energy, even though we can have a negative value of $\Delta E_{\rm pot}$. Although the change of sign of $\Delta E_{\rm kin}$, depending on T and U, has already been highlighted in other investigations [85, 195, 207], this behaviour remained a puzzle until now. To better

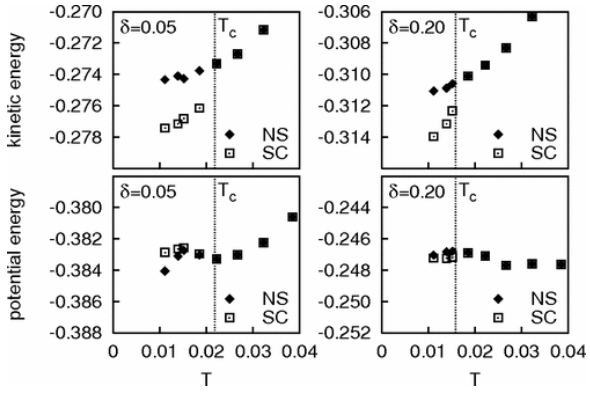

Figure 5.13: On the top the kinetic and on the bottom the potential energies of the normal (black diamonds) and superconducting (white squares) states as a function of temperature for low doping $\delta = 0.05$ and high doping $\delta = 0.20$ in the left and right panels respectively. The value of T_c is displayed with the vertical dotted lines. Figure taken from Ref. [207] where the Dynamical cluster approximation was employed, for a cluster of 4 sites, using Quantum Monte Carlo method as impurity solver.

understand this, we show the results from Ref. [207] in Fig 5.13. We can observe from these plots of the kinetic and potential energies at fixed doping as a function of the temperature that, contrary to the BCS theory, here the kinetic energy of the superconducting state is always lower than that of the normal state. On the other hand, the potential energy is almost the same in both phases. This indicates that the pairing mechanism is mediated by a loss in the kinetic energy. On the other hand, a different scenario is presented in Fig 5.14 where we show the results from Ref. [195]. Here we can see the difference in kinetic, potential and total energies as a function of doping. Here, similarly to what we saw in Fig. 5.12, panels (a)

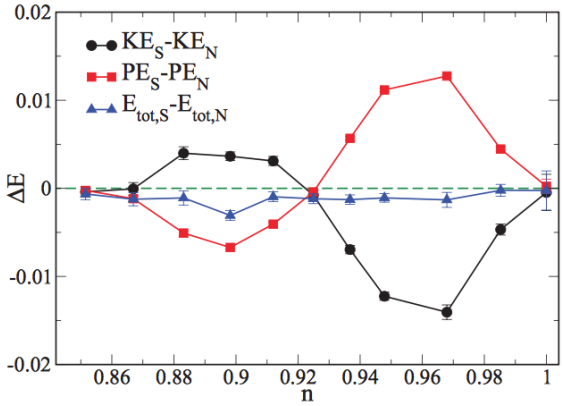

Figure 5.14: The difference between the superconducting and normal states in the kinetic, potential, and total energies indicated with the lines of black dots, red squares and blue triangles, respectively, at $T/t = 1/60$ as a function of the occupation $n = 1 - \delta$. The figure was taken from Ref. [195], where the Dynamical Cluster Approximation for a cluster of 8 sites was employed, using Continuous Time Auxiliary-Field Monte Carlo algorithm as impurity solver [208].

and (b), we can observe a change of the driving mechanism upon increasing doping. We move from a kinetic to a potential energy driven mechanism at small or large doping respectively.

Our comparative study for several values of the interaction produces a unified picture of these apparently paradoxical results. The locus of the maxima of the condensation energy for isothermal scans as a function of the doping, $\min\Delta E_{tot}$ (plotted with green squares in Fig. 5.9), lies on top of the isothermal maximum of the order parameter $\Phi(\delta)$. Consequently, this demonstrates that $\min\Delta E_{tot}$ correlates with the underlying phase transition in the normal state and its supercritical features. Since the sign change for the potential and kinetic components of the condensation energy takes place in proximity to $\min\Delta E_{tot}$ for all interactions that we have investigated, this sign change is also intertwined with the normal state properties.

5.7.3 Source of the Condensation Energy

In the strong interaction regime, the ratio between the potential energy and the kinetic energy gain approaches $-1/2$ in the underdoped region, as shown in Fig. 5.15, where we have plotted such a ratio for increasing values of the interaction. This term scales with the super-exchange energy J in the strong U limit [152]. The hopping of holes described by the term in the $t-J$ model, introduced in Eq. 3.4, does not appear to influence the energy gain significantly. Moreover, the divergences are the result of the zero crossings of either the kinetic or the potential energy differences. The value $-1/2$ for this ratio is expected when the super-exchange energy

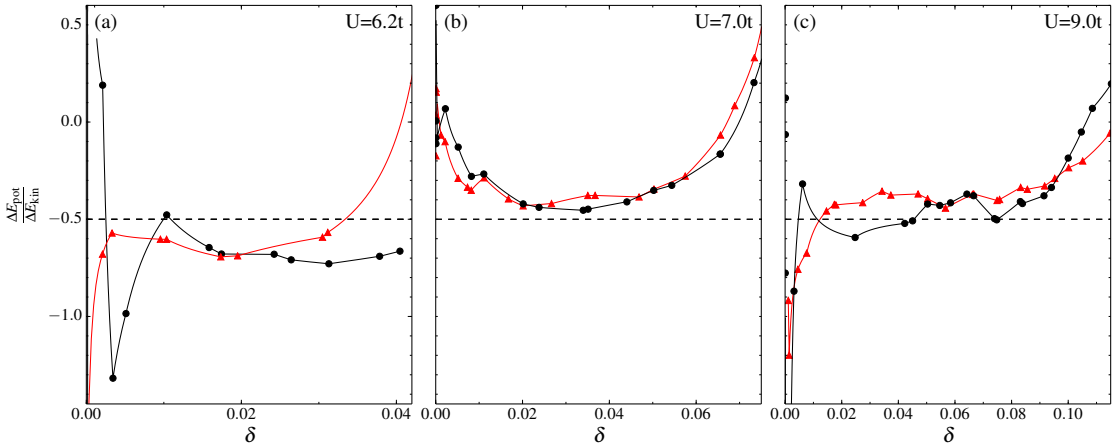

Figure 5.15: Ratio between the potential energy and the kinetic energy gain upon entering the superconducting state in the underdoped region. Red triangles are used for temperature $T/t = 1/50$ and black circles for $T/t = 1/100$. The horizontal dashed line shows the value $-1/2$ expected from the super-exchange energy proportional to J.

J [152] drives superconductivity [198]. Upon increasing the interaction U, the importance of J is also observed in:

(i) the reduction of the maximum T_c,

(ii) the magnitude of the individual kinetic and potential energy contributions to condensation energy,

(iii) the maximum value of the order parameter in the ground state [183–185, 190].

The BCS-like potential driving mechanism that characterises the over-doped regime for $U = 6.2, 7$ is most probably a consequence of the weak-coupling, long-wavelength, antiferromagnetic spin-wave pairing mechanism [209], but the result of the self-consistent rearrangement of the spin-fluctuation spectrum in the superconducting state needs further investigation.

5.8 Effect of the Frustration on the System

A system is frustrated when the geometric properties of a crystal lattice in the presence of conflicting atomic forces prevent simultaneous minimisation of all interaction energies at a given lattice point [210]. In the context of the 2 dimensional Hubbard model this situation can be studied by employing a finite next-nearest-neighbour hopping t'.

In this section, we will briefly discuss the effect of such a finite value of t' on our scenario. As previously stated our scenario does not seem to be affected by t', vindicating our choice to not take it into account in our calculations. The frustration of the system moves the value

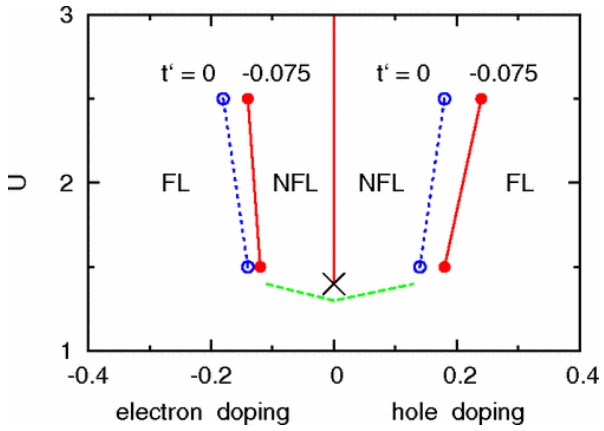

Figure 5.16: Phase diagram of 2D Hubbard model calculated within CDMFT solved using Exact Diagonalization algorithm for 2x2 clusters. At large hole or electron doping, there is a Fermi-liquid phase that becomes a non Fermi-liquid phase upon decreasing the doping. The symbols for $U = 1.5$ and $U = 2.5$ indicate the approximate critical doping δ_c for $t' = -0.075$ shown as solid red circles and for $t' = 0$ represented by empty blue circles. At $\delta = 0$, the vertical line represents the Mott insulating phase at half-filling. The critical U indicated by X is about 1.4 for $t' = 0$ and $t' = -0.075$. Finally, with the long-dashed green line, the approximate lower bound of the non Fermi-liquid domain is indicated. Figure taken from Ref. [211].

at which the first-order transition occurs to larger doping, as suggested by Ref. [211] (see Fig. 5.16). Moreover, at $U = 0$, the Van Hove singularity is moved to finite doping by frustration of the system via next-nearest-neighbour hopping t'. Such an effect should fade at very large U. Due to this, and the fact that the sign problem is less severe at $t' = 0$, the results presented here are mostly for $t' = 0$. We performed additional calculations for $t' = -0.1$ at $U = 6.0$, which, as shown in Fig. 5.17, is larger than the critical value of the interaction for the Mott transition at $n = 1$. Our qualitative conclusions concerning the organising principle of the phase diagram are unchanged. We still can observe a dome-like shape for T_c^d, with a maximum that correlates with maxΓ. The loci of the isothermal maxima of the order parameter is almost on top of the minima of the isothermal condensation energy, and they are in close proximity to the Widom line of the pseudogap-correlated metal transition.

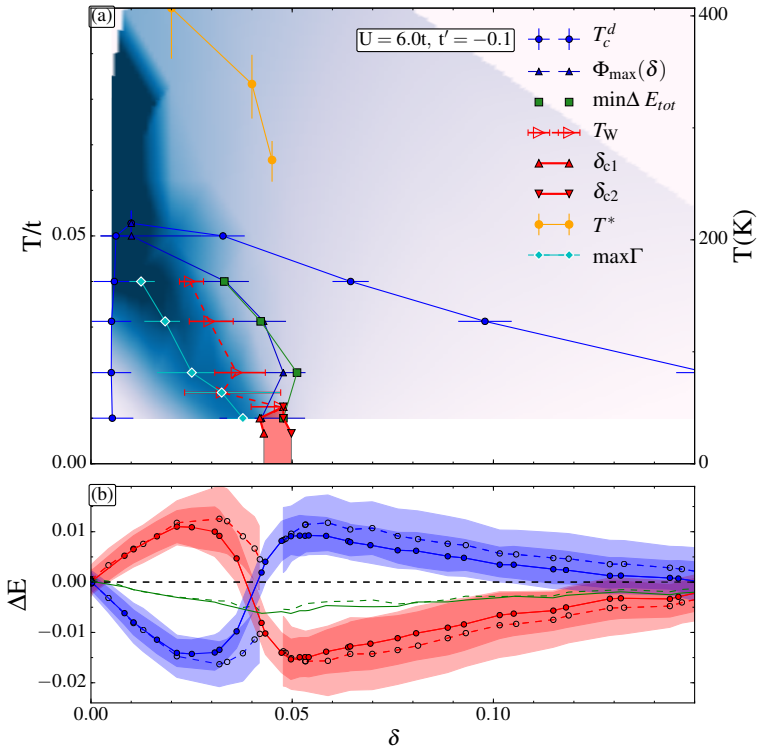

Figure 5.17: Same as Fig. 5.9, but for $U = 6.0t$ and $t' = -0.10$. All conclusions remain unchanged with a finite t'. T_c^d still has an asymmetric dome-like shape, with a maximum that is linked to maxΓ. $\Phi_{\max}(\delta)$, T_W, and minΔE_{tot} appear to be correlated with each other.

5.9 Conclusion

We have discussed a detailed analysis for the superconducting and normal state of the 2D Hubbard model in the doped Mott insulator regime using CDMFT. In the previous chapter we have seen that the physics of the normal state is governed by the Mott insulating transition at half-filling, here we have analysed the fate of such a transition upon doping a Mott insulator state. We confirm, for a broader parametric regime, the conclusion of previous investigations [29–32], upon doping a Mott insulator state the phase diagram is characterised by the occurrence of a pseudogap to correlated metal transition. Moreover, the supercritical behaviour of such a transition is determined by sharp crossovers in many response functions. By analysing the features of the d-wave superconductivity, we have demonstrated that these crossovers are acting as organising principle for the shape and the properties of this broken symmetry phase. Indeed, the maximum of T_c^d, and the loci of the isothermal minima of the condensation energy and maxima of the order parameter all correlate with the crossover lines

of the underlying normal state that is hidden under the superconducting dome [36]. Pseudogap and superconductivity are intertwined phenomena, governed by Mott physics and short-range correlations.

From an experimental perspective, a possible way to observe the normal state transition would be to simultaneously suppress the superconductivity via strong magnetic field and the charge density wave via high pressure. Alternatively, ultracold atoms in optical lattices provide a challenging but promising platform with which to test these results in a controlled enviroment [212–222]. In analogy with what is observed for the half-filled Mott transition in layered organics [35,36,223–227], we speculate that the large compressibility in the underlying normal state can produce sound anomalies in the supercritical regime.

Chapter 6

Pseudogap and Superconductivity in Two-Dimensional Doped Charge-Transfer Insulators

6.1 Introduction

The work presented in this chapter is based on Ref. [37].

In order to explain the cuprates, we have already argued in Chapter 3 that we must understand the physics of a square lattice made of CuO_2 unit cells where electrons on copper interact strongly. In Chapters 4 and 5 our strategy was to study the case of a single orbital per unit-cell with an on-site repulsion, i.e. the two-dimensional Hubbard model, the simplest model able to capture the essential phenomenology of these strongly correlated compounds [153,228]. We have seen how in this model the physics of the antiferromagnetic and superconducting states are both intertwined phenomena with the underlying normal state, organised by the Mott physics.

The Emery model that includes three orbitals per CuO_2 unit cell [3,4], appears to be more realistic, as discussed at the end of Chapter 3. The necessity of this model is demonstrated by numerous experiments that show that doped holes are found on oxygens [60]. Since electron-electron repulsion is strong only on the Cu site, one may think that electrons can travel to the weakly interacting oxygen sites, avoiding repulsion. This is not the case [10]. The ability

to delocalise on oxygen allows electrons to feel a much weaker effective interaction but, at one-hole per unit-cell and strong enough repulsion on copper, one obtains a charge-transfer insulator [10]. It is this kind of interaction-driven insulator of the three-orbital model that becomes a high-temperature superconductor upon doping. Hence this is the model that we are going to study in this chapter.

Previous single-site DMFT calculations [229–237] provided important insight into the phase diagram of this model. However, the inclusion of short-range correlations is still a formidable theoretical problem. Despite pioneering investigations using cluster methods [238–241], the precise form of the temperature-doping (T-δ) phase diagram is largely unexplored and several of its key aspects are uncertain. Notably, as we can see from the following summary of the results of Refs. [239–241], the finite temperature behaviour of the metal to charge-transfer insulator transition driven by hole doping is unknown.

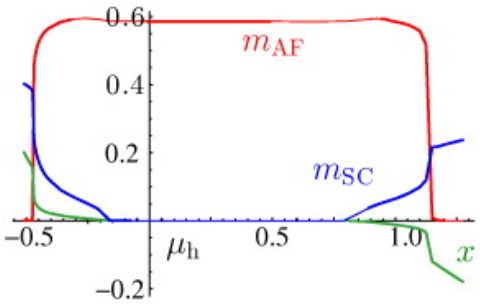

Figure 6.1: The electron doping x (green line) and the antiferromagnetic $m_{\rm AF}$, and superconducting $m_{\rm SC}$ order parameters (red and blue lines, respectively) as a function of the chemical potential μ_h of the Emery model at $T = 0$ solved using Variational Cluster Approach [242]. Figure taken from Ref. [239].

In Ref. [239], an analysis at $T = 0$ of the Emery model is carried out in the hole and the electron doped regime by using variational cluster method [242] and by comparing the order parameters of the antiferromagnetic and superconducting states in these two regimes. Their phase diagram reveals a mixed AF + SC phase at low doping that, upon increasing doping, evolves in a pure SC phase accompanied by phase separation. This result is displayed in Fig. 6.1, where the electron doping x (green line), and the order parameters for the superconducting and antiferromagnetic phases (blue and red lines respectively) are plotted as a function of the chemical potential μ_h. This is the first time that the d-wave superconducting phase was examined on the three band Hubbard model. A subject that we will also pursue in this chapter.

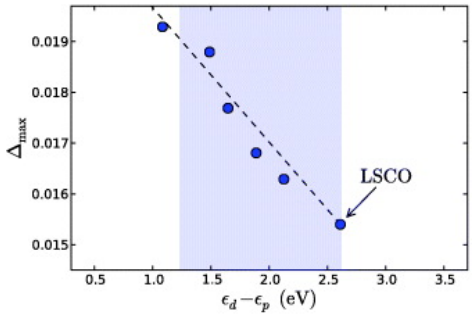

Figure 6.2: Optimal magnitude of the superconducting order parameter, $\Delta_{\max}$, as a function of the charge-transfer energy $\epsilon_d - \epsilon_p$ for the Emery model at $T = 0$ solved by using Exact Diagonalization [199]. The blue shaded area represents the parametric regime characteristic of the LSCO family. Figure taken from Ref. [240].

In Ref. [240], the Emery model is addressed with Cluster Dynamical Mean-Field Theory using finite temperature Exact Diagonalization as the impurity solver [199]. This work is mainly focused on the role of the variation in the charge-transfer energy that appears to largely account for the phenomenological trend of the optimal T_c. For example, a result is exhibited in Fig. 6.2 where the maximum value of the superconducting order parameter $\Delta_{\max}$ is plotted as a function of the charge-transfer energy $\epsilon_d - \epsilon_p$. The increase in this latter quantity results in a decrease of $\Delta_{\max}$.

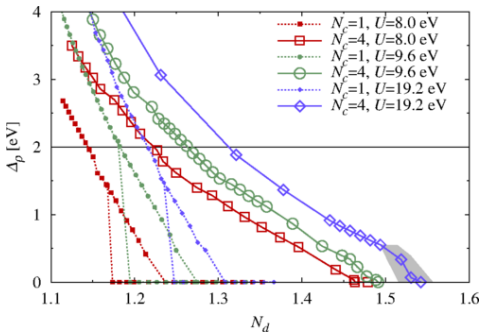

Figure 6.3: Charge transfer gap Δ_ρ as a function of copper occupancy N_d for various values of the interaction U, the number of bath states N_b=9,12, and the number of lattice sites $N_c = 1, 4$. The horizontal black line represents $\Delta_\rho = 2$ eV characteristic value of the parent compounds of cuprates. Here the Emery model at $T = 0$ is solved by single- and four-site versions of the Dynamical Cluster Approximation implementation of Dynamical Mean-Field Theory [25] with Configuration Interaction Approach as impurity solver [243]. Figure taken from Ref. [241].

In Ref. [241], single- and four-site versions of the Dynamical Cluster Approximation at $T = 0$ [25] have been employed. In Fig. 6.3 the charge transfer gap Δ_ρ is plotted as a function of the copper occupancy. Though the single-site calculations ($N_c = 1$) reveal the existence of single phase, this changes in the cluster analysis with $N_c = 4$. In this latter

case, by changing the copper occupation, two different slopes characterise the evolution of the spectral gap Δ_ρ. This reveals the existence of two distinct insulating states: the magnetically correlated insulator, driven by inter-site correlations, and the strongly correlated insulator, in which local physics suffices. By comparing the experimental feature of optical conductivity of the cuprates with their data, it is argued that these compounds are in the magnetically correlated Mott insulator regime.

These results are relevant for our analysis of the half-filled case at finite temperature.

In our work, in Section 6.3, using the methodology described in Section 6.2, we shall chart the CDMFT solution of the T-U_d phase diagram. We will then concentrate on a parametric regime able to highlight the features of a doped charge-transfer insulator in Section 6.4. In Section 6.5 we shall analyse four possible phases of the model- namely, the charge-transfer insulator, the pseudogap, the d-wave superconducting state, and the correlated metal, along with their phase boundaries. We aim to establish if the basic phenomenology of cuprates, discussed for the one-orbital model in Chapter 5, survives in the more realistic three-orbital model. Moreover, we shall determine the redistribution of spectral weight, the location of holes within the unit cell and which phenomena are independent of details such as the number of orbitals per unit cell.

6.2 Model and Method

For completeness let us recall the basic notions on the method as examined in Chapters 3 and 5, introducing the parametric regime that we used for our calculation. We consider the three-band Hamiltonian for copper $3d_{x^2-y^2}$ and oxygen $2p_x$,$2p_y$ orbitals. Ordering the corresponding annihilation operators as $(d_{\mathbf{k}\sigma}, p_{x,\mathbf{k}\sigma}, p_{y,\mathbf{k}\sigma})$, where $\mathbf{k}$ is the wave-vector and σ the spin, the non-interacting part of the Hamiltonian for the infinite lattice reads [244]:

$$\mathbf{h}_0(\mathbf{k}) = \begin{pmatrix} \epsilon_d & V_{dp_x} & V_{dp_y} \\ V_{dp_x}^\dagger & \epsilon_p + W_{p_xp_x} & W_{p_xp_y} \\ V_{dp_y}^\dagger & W_{p_xp_y}^\dagger & \epsilon_p + W_{p_yp_y} \end{pmatrix}, \tag{6.1}$$

with $V_{dp_x} = t_{pd}(1-e^{ik_x})$, $V_{dp_y} = t_{pd}(1-e^{ik_y})$, $W_{p_xp_x} = 2t_{pp}(\cos k_x - 1)$, $W_{p_yp_y} = 2t_{pp}(\cos k_y - 1)$ and $W_{p_xp_y} = t_{pp}(1-e^{-ik_x})(1-e^{ik_y})$. Here t_{pd} (t_{pp}) is the oxygen-copper (oxygen-oxygen)

hopping amplitude and ϵ_d (ϵ_p) is the copper (oxygen) on-site energy. The copper-copper distance and t_{pp} are taken as unity. The non-interacting Hamiltonian $\mathbf{h}_0$ leads to the Fermi

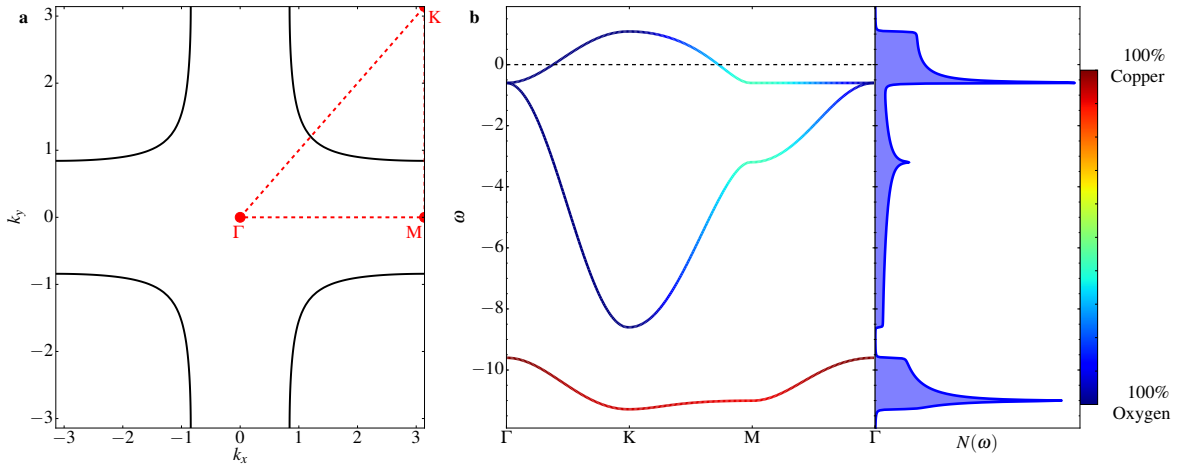

Figure 6.4: (a) Noninteracting Fermi surface for the model parameter : $\epsilon_p = 9$, $t_{pp} = 1$, $t_{pd} = 1.5$, which gives a total occupation n_{tot} equal to five. (b) Non-interacting band structure for the same model parameters along with the resulting total density of states. Colour corresponds to the d-character of the hybridised bands. The band crossing the Fermi level has mostly oxygen-character.

surface observed experimentally in the overdoped regime of the cuprates Fig. 6.4. For the interacting part, only the on-site repulsion on d-orbitals U_d is retained. Note that in doing the Fourier transform to obtain Eq. (6.1), we fixed the same phase for all atoms within a given unit cell.

Physically, band-structure calculations of Ref. [244] and previous DMFT works [229–241] suggest the following range of parameters in cuprates: $t_{pp} \approx 1.1$ eV, $t_{pd} \in (1.3 - 1.6)$ eV, $|\epsilon_p - \epsilon_d| \in (3 - 5)$ eV, $U_d \in (8 - 9)$ eV. Our choice of parameters ($t_{pp} = 1$, $t_{pd} = 1.5$) is compatible with those values for t_{pp} and t_{pd}. However, we selected a larger value for the charge-transfer energy $|\epsilon_p - \epsilon_d| = 9$, and, thus, a larger value of U_d to open a charge-transfer gap. Indeed with our specific choice of parameters, in the limit $U_d = 0$ and $t_{pd} = 0$, the d-levels are just below the oxygen bands. A finite t_{pd} then turns the d-levels into a band with mainly d-character, and the conduction band still keeps mostly a p-character (see Fig. 6.4 and red curves in Fig. 6.7). A smaller value of the charge-transfer energy $|\epsilon_p - \epsilon_d|$ will increase the mixed orbital character at the Fermi level.

We solve this model with Cellular Dynamical Mean-Field Theory, embedding a cluster of 12 lattice sites, with $(N_d, N_p) = (4, 8)$, in a self-consistent non-interacting bath, that acts as the

missing lattice environment. The cluster plus bath impurity model is solved with Continuous-Time Quantum Monte Carlo for the Hybridisation Expansion [26], as seen in Chapter 3.

6.3 Opening of the Charge Transfer Gap

The Zaanen-Sawatzky-Allen scheme [10] (ZSA), outlined in Fig. 6.5 shows the ground state phase diagram of the Emery model when the total occupation is $n_{\text{tot}} = n_d + 2n_p = 5$ (one hole per CuO_2 unit). At small on-site interaction and charge-transfer energy $\Delta = |\epsilon_p - \epsilon_d|$, we

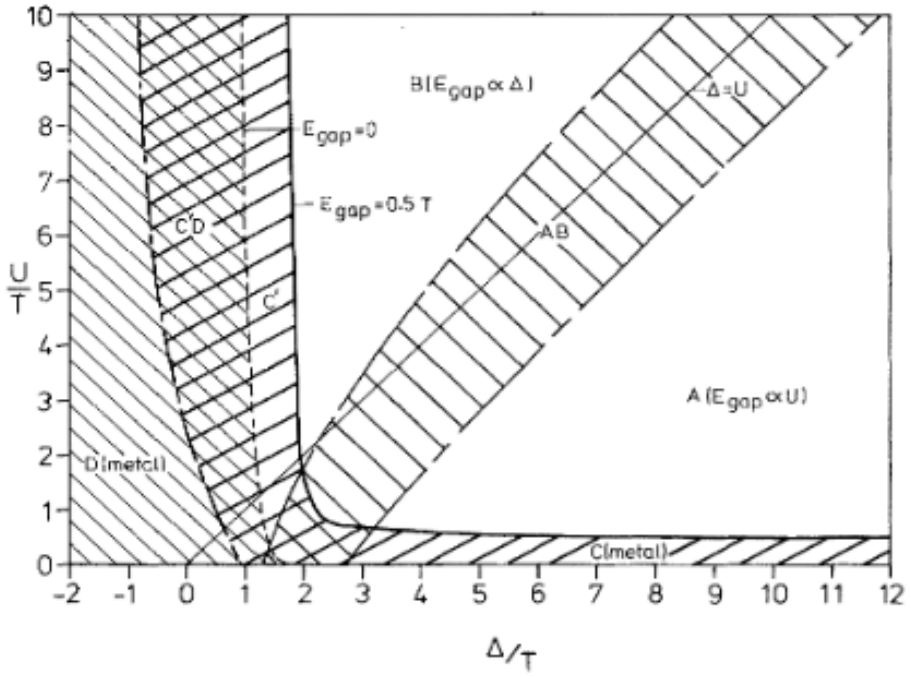

Figure 6.5: The Zaanen-Sawatzky-Allen scheme. This phase diagram shows how many possible phases are controlled by the value of the ratio of the local copper interaction to the hybridisation energy, $\frac{U}{T}$, as a function of the ratio of charge to hybridisation energy, $\frac{\Delta}{T}$ at zero temperature. Beginning from the top right side we are in the presence of a Mott-Hubbard insulator, here indicated by (A). The energy gap of this state is $E_{gap} \approx U$. By decreasing the magnitude of Δ, the state, after crossing an intermediate region of bound states (AB), becomes a charge transfer insulator (B) with an energy gap $E_{gap} \approx \Delta$. By lowering Δ further, we find a metallic state in the copper band, denoted (C), and a metallic state in the oxygen band, (D). Finally, with (CD) or (C'D) we have an intermediate region between these two metallic states. Figure taken from Ref. [10].

are in the presence of a metallic state where the conducting band has a p-character (D in Fig. 6.5). This state evolves into another metallic state by increasing charge-transfer energy, but this time the conducting band of the state has a d-character (C in Fig. 6.5). By increasing the on-site interaction, we find a Mott insulator state with an energy gap $E_{gap} \approx U$ (A in

Fig. 6.5). By increasing the interaction, this state becomes a charge transfer insulator with an energy gap $E_{gap} \approx \Delta$ (B in Fig. 6.5).

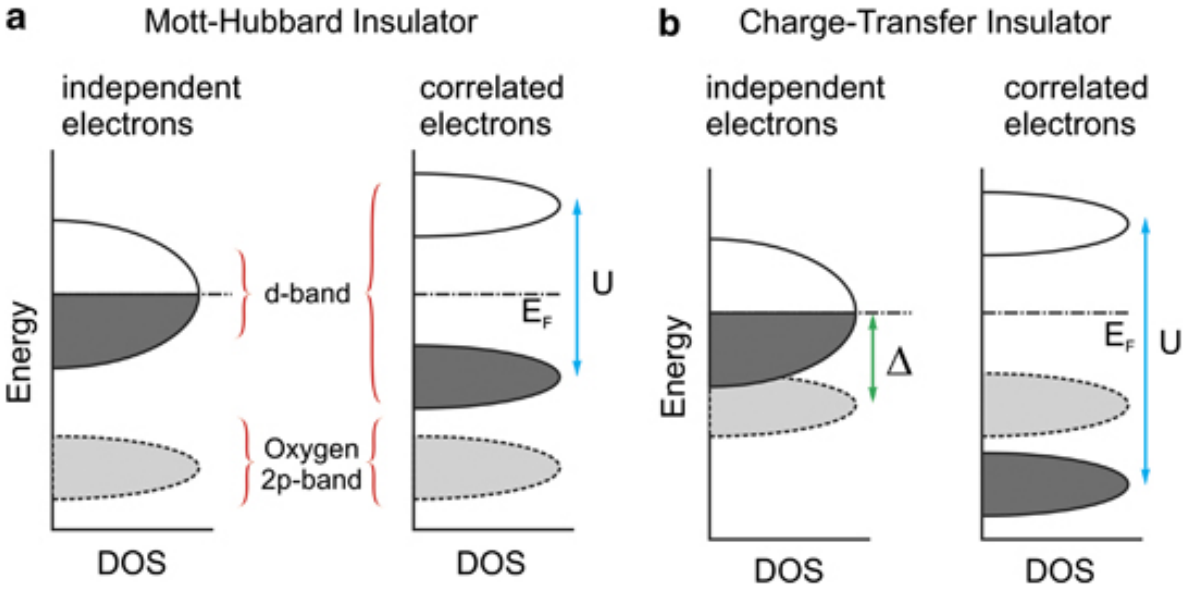

Figure 6.6: Cartoon of the local density of states as a function of the energy: in panel (a) for the Mott-Hubbard insulator and in panel (b) for the charge-transfer one, where the left side of each panel shows the independent electron case of the Emery model $U = 0$ and the right side the correlated electron case for $U > U_{\mathrm{MIT}}$. The DOS for the copper is displayed in dark grey and white, whereas that for the oxygen in light grey. Depending on the interaction U and the charge-transfer energy $\Delta = |\epsilon_p - \epsilon_d|$ we have two possible insulator states. Figure taken from Ref. [245].

The local density of states as a function of the energy for the charge-transfer and the Mott-Hubbard insulator is sketched in Fig. 6.6. When the interaction U_d is strong enough, the copper band is split into two Hubbard bands due to the Mott transition. In this case, the oxygen band can be located either between these two bands (charge-transfer insulator), if $\Delta < U_d$, or next to lower Hubbard band (Mott-Hubbard insulator), if $\Delta > U_d$. In this chapter we will focus on the former case, that is the one widely believed to better characterise the physics of the cuprates.

The local density of states (DOS), $\mathcal{N}(\omega) = -1/\pi \mathrm{ImG}(\omega)$, calculated for several values of U_d for $n_{tot} = 5$ (undoped system) and the inverse temperature $\beta = 50$, is plotted in Fig. 6.7 panel (a) (from left to right: total, projected DOS on the p- and d-orbitals). The upper red curve represents the non-interacting case where, thanks to the hybridisation term $t_{pd} = 1.5$, we can observe a finite dispersion for the DOS that forms a narrow band centred at $\omega \approx -11$. Here we choose $\epsilon_d = 0$ and $\epsilon_p = 9$ to set the system in the charge-transfer regime. Upon increasing

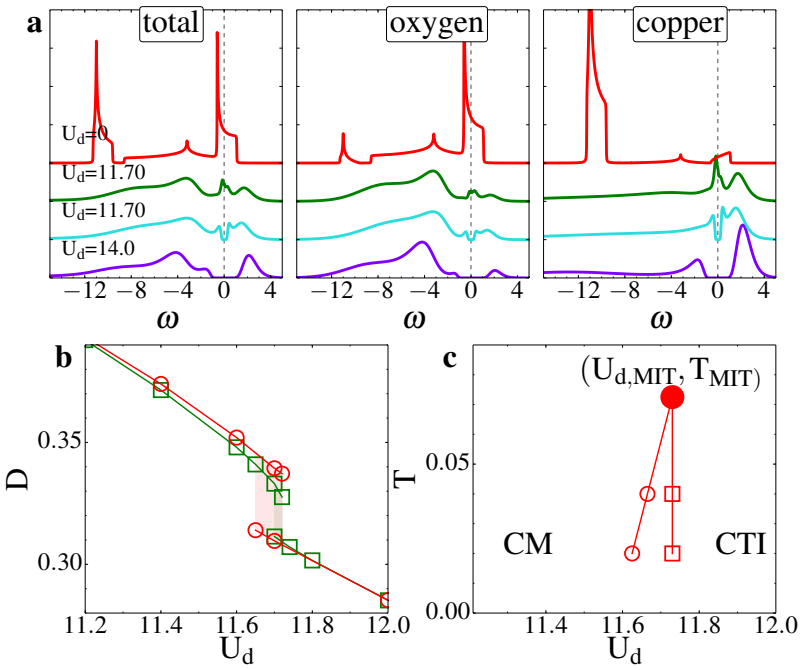

Figure 6.7: Panel (a): the local density of states $\mathcal{N}(\omega)$ at $n_{\rm tot} = 5$ and $\beta = 50$ for several values of U_d. From left to right: total, projected $\mathcal{N}(\omega)$ on the p- and d-orbitals. The zero of energy corresponds to the Fermi level. Other model parameters are $|\epsilon_p - \epsilon_d| = 9$, $t_{pp} = 1$ and $t_{pd} = 1.5$. Panel (b): the double occupancy D as a function of U_d at $n_{\rm tot} = 5$ for $\beta = 25$ (squares) and $\beta = 50$ (circles). Hysteresis region is shaded. Panel (c): the T versus U_d phase diagram at $n_{\rm tot} = 5$. The first-order transition at finite U_d between a charge-transfer insulator (CTI) and a correlated metal (CM) is computed by the jumps in the isothermal double occupancy and it terminates in a critical endpoint of the second-order.

the copper interactions, the lower violet curve shows the dramatic effect of the correlations: an interaction gap opens up, and the system becomes a charge-transfer insulator. In between these two cases, the green and blue lines computed for the same value of $U_d = 11.7$, demonstrate that the system can have coexistence of a metallic and an insulating solution, in analogy with the Mott transition of the single Hubbard band seen in Chapter 4. This interaction-driven transition between the metal and the charge-transfer insulator is first-order, as best shown in the double occupancy D of the d-orbitals as a function of U_d in Fig. 6.7 panel (b). Here we can appreciate that at low temperature D shows hysteresis loops between two solutions, with sudden jumps at $U_{d,c1}(T)$ and $U_{d,c2}(T)$ where the insulating and metallic solutions disappear, respectively. With further increasing temperature, these hysteresis loops stop at $T = T_{\rm MIT}$. Using this information we can chart the transition on a temperature versus U_d phase diagram in Fig. 6.7 panel (c). The correlated metal to charge-transfer insulator first-order transition occurs within the coexistence region, bounded by the critical values of the interaction $U_{d,c1}$

and $U_{d,c2}$ (open circles and squares, respectively), and terminates in a critical endpoint, where dD/dU_d diverges at $U_{d,\mathrm{MIT}}$ and T_{MIT}. Our results extend, to finite temperature, the ones previously obtained at $T = 0$ in Ref. [241].

6.4 Hole-Doping Driven Metal-Insulator Transition

After having seen that the effects of the interactions on the normal state of the undoped system are similar to those of the Hubbard model in Section 4.3, we are now ready to explore the hole-doping regime.

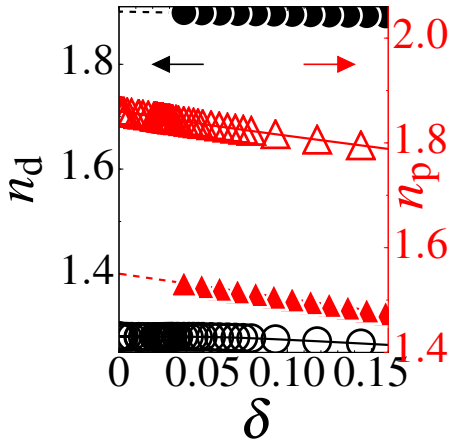

Figure 6.8: Partial occupation n_d (circles), n_p (triangles) versus $\delta = 5 - n_{\mathrm{tot}}$ at $\beta = 25$ and $U_d = 0, 12$ (full and open symbols, respectively). Model parameters are $|\epsilon_p - \epsilon_d| = 9$, $t_{pp} = 1$ and $t_{pd} = 1.5$.

In Fig. 6.8 the partial occupation of oxygen, in red, and copper, in black, is plotted as a function of the hole doping $\delta = 5 - n_{\mathrm{tot}}$ at $\beta = 25$ for independent electrons $U_d = 0$ with full symbols and for finite interaction $U_d = 12$ with open symbols. The comparison between interacting and non-interacting curves in the undoped regime, $\delta = 0$, establishes that the electrons are transferred from copper to oxygen bands. By increasing doping we can appreciate two different behaviours: the copper occupation n_d is essentially doping-independent, while that of the oxygens n_p decreases, this is expected and experimentally found in the charge-transfer regime [60], where the holes mainly enter the oxygens.

In Fig. 6.9 the isothermal doping variation is displayed as a function of the chemical potential for $U_d = 12$ and several temperatures. Also in this case $\delta(\mu)$ shows a plateau at $\delta(\mu) = 0$, revealing the onset of the incompressible charge-transfer insulator. By lowering

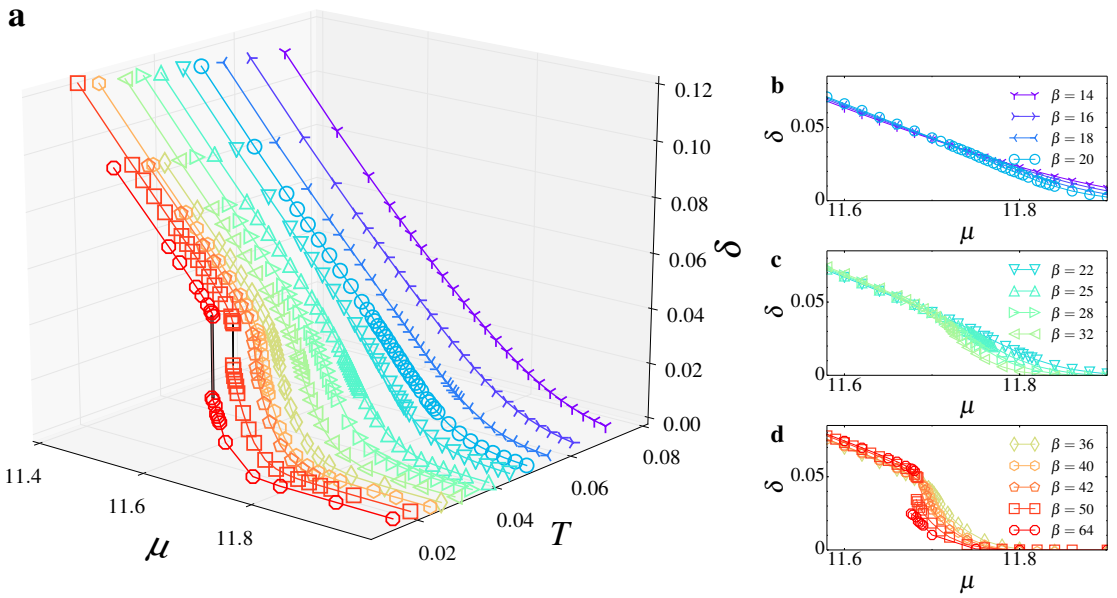

Figure 6.9: Panel (a): the isothermal doping δ as a function of the chemical potential μ for $U_d = 12$ is plotted for different temperatures. The plateau at $\delta(\mu) = 0$ is expected for the charge insulator state. As we decrease the chemical potential at our lowest temperature we can see the appearance of hysteresis, that evolves in a sigmoidal shape at higher temperature. Panel (b),(c) and (d): 2D projections of panel (a). Model parameters are $|\epsilon_p - \epsilon_d| = 9$, $t_{pp} = 1$ and $t_{pd} = 1.5$.

μ until we obtain a compressible state, the isotherms $\delta(\mu)$ evolve continuously, i.e. without hysteresis. This demonstrates that at our lowest temperature the charge-transfer insulator has a continuous transition in a compressible phase that, as we are going to discuss, has the features indicative of a pseudogap. At larger doping, the discontinuity of the $\delta(\mu)$ at low temperature that evolves into in a sigmoidal shape upon heating the system, testifies to the presence of a first-order transition between two compressible solutions: the pseudogap and a correlated metal. It is interesting to note that $(d\delta_{tot}/dT)_\mu$ changes sign, from positive to negative at small or large doping, respectively.

This transition culminates in a second-order critical endpoint (δ_p, T_p). Indeed some thermodynamic response functions such as the charge compressibility,

$$\kappa = 1/n_{tot}^2 (dn_{tot}/d\mu)_T, \tag{6.2}$$

at (δ_p, T_p) diverge. By increasing the temperature $T > T_p$, this divergence is replaced by a local maximum value, as shown for κ in Fig. 6.10, plotted as a function of the doping δ. This

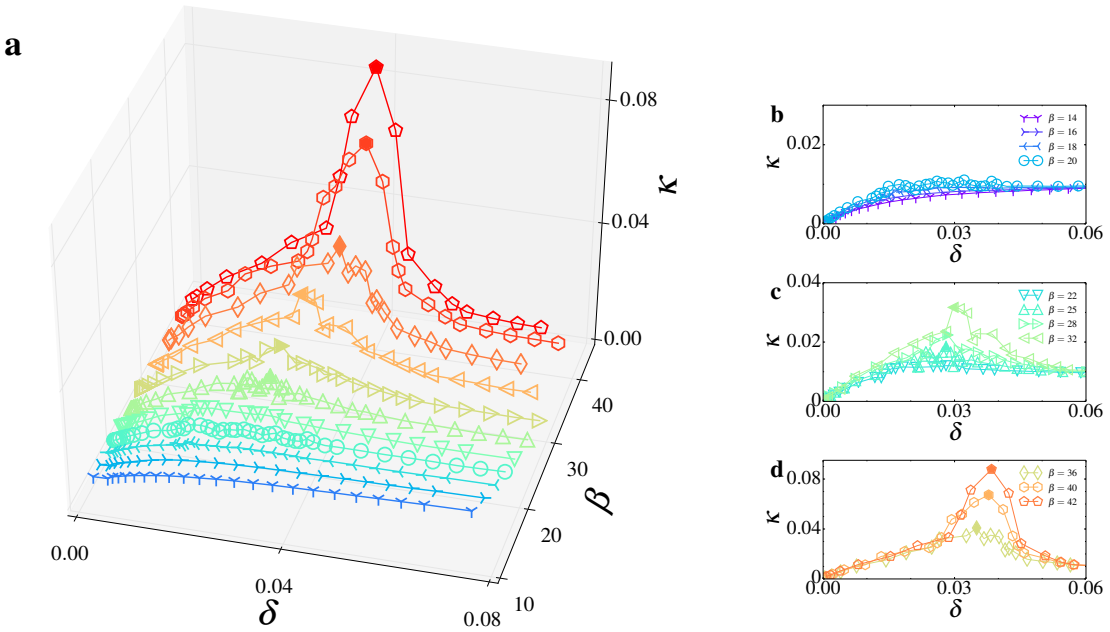

Figure 6.10: Panel (a): the isothermal charge compressibility κ as a function of the doping δ for $U_d = 12$ is plotted for different temperatures. κ diverges at the endpoint (δ_p, T_p) of the PG-CM first-order transition, here manifesting a supercritical behaviour given by its local maximum marked with fill markers. Panel (b),(c) and (d): 2D projections of panel (a). Model parameters are $|\epsilon_p - \epsilon_d| = 9$, $t_{pp} = 1$ and $t_{pd} = 1.5$.

is the same supercritical behaviour discussed in Section 5.3 for the 2D Hubbard model.

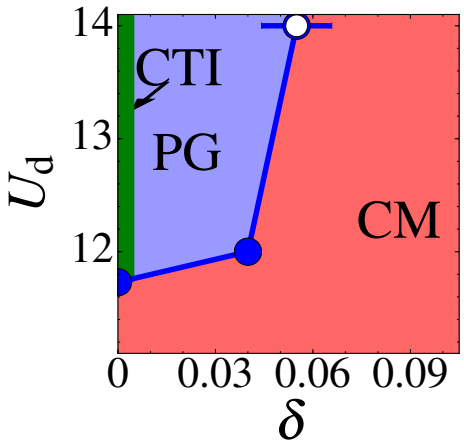

Figure 6.11: Phase diagram of the interaction U_d as a function of the doping δ. The charge transfer insulator, indicated by the green line, presents a continuous transition in the pseudogap, light blue shaded region. The boundary between the charge transfer insulator and the correlated metal, red shaded region, at zero doping is first-order. The first-order transition between the pseudogap and the correlated metal is drawn with the blue line. When possible, we show the position δ_p of the endpoints, with the solid blue circles, otherwise the doping of $\kappa_{\max}$ at our lowest temperature, is marked with the open blue circles. Model parameters are $|\epsilon_p - \epsilon_d| = 9$, $t_{pp} = 1$ and $t_{pd} = 1.5$.

In Fig. 6.11 we show the $U_d - \delta$ phase diagram of the model. By tracking the position of the critical endpoint δ_p as a function of U_d, we can see that the pseudogap to correlated metal transition at finite doping is connected to the charge-transfer insulator to correlated metal transition of the undoped case. Indeed, the position of the critical endpoint δ_p for $U_d \simeq 11.6$ begins at the metal to charge-transfer insulator transition at zero doping, and then moves to larger doping as we diminish U_d and the temperature T.

6.5 Phase Diagram

In this section we will consider the interplay between superconductivity and normal state. Before going into the features of the superconducting state, let us give a better characterisation of the pseudogap. The normal-state properties investigated so far are summarised in the temperature-doping phase diagram of Fig. 6.12 panel (a).

At zero doping, the thick green line represents the charge-transfer insulating phase separated from the pseudogap phase via a second-order transition. At low temperatures, upon increasing doping, a first-order transition between a pseudogap and a correlated metallic state is present. The red shaded region between the lines of red triangles represents a coexistence of metastable solutions for these two phases. By increasing temperature, this transition culminates in a second-order critical point at (T_p, δ_p), where the thermodynamic response functions, such as the charge compressibility κ of Eq. 6.2, diverge. The supercritical behaviour, for $T > T_p$, only presents one phase, but the first-order transition generates a crossover region, at which thermodynamic response functions show a maxima. The red line with circles tracks the loci of the maxima of κ, computed in Fig. 6.10, and it represents our definition of the Widom line T_W. As discussed in Section 5.3, quite generally T_W marks the border between different dynamic behaviours [31,33]: the local DOS, evaluated as a function of the temperature at fixed doping, goes through an inflexion point, the loci of such points is correlated with our T_W, as exhibited in Fig. 6.13. The onset of the drop in this quantity is the common definition for the onset of the pseudogap T^* and occurs at a higher precursor temperature (see the line with blue triangles and Fig. 6.13 panel (c)), in a qualitative agreement with the experiments [246].

The development of the pseudogap is characterised by the growth of inter-site self-energies, namely by a strong momentum differentiation of the electronic lifetimes, as shown in Figs.

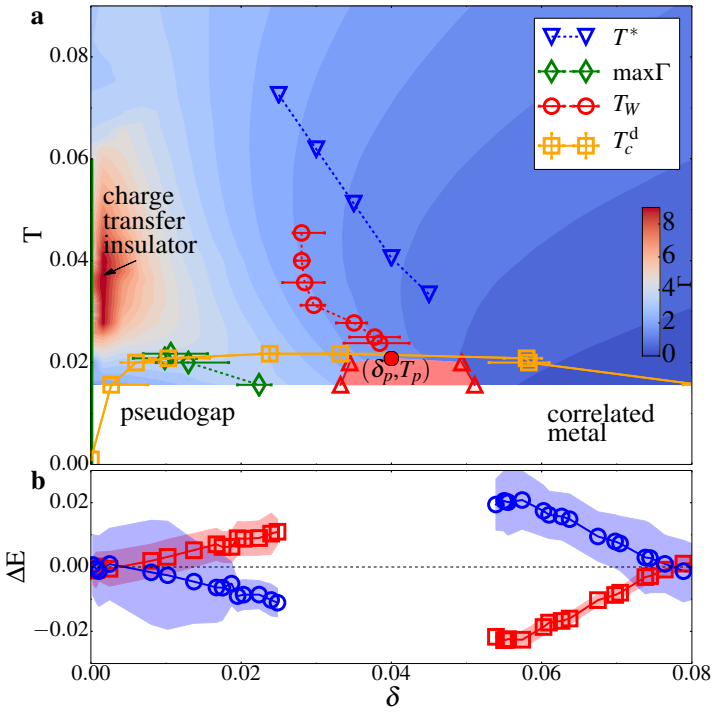

Figure 6.12: Panel (a): the temperature as a function of the hole doping phase diagram of the Emery model. Model parameters are $|\epsilon_p - \epsilon_d| = 9$, $t_{pp} = 1$, $t_{pd} = 1.5$ and $U_d = 12$. T_c^d, here the line of orange squares, is defined as the line below which the superconducting order parameter is non-zero. By analysing the behaviour of $\delta(\mu)$ we establish three normal-state phases: the charge transfer insulator for the undoped system, green line, that evolves into a pseudogap and then into a correlated metal at low temperature. Hidden by the superconducting dome, these two latter phases present a first-order transition, line of red triangles, that terminates in a second-order critical point at (δ_p, T_p), full circle. The loci of the isothermal maxima of the charge compressibility κ defines the Widom line of this transition T_W, open red circles. The line of blue triangles marks the onset temperature for the pseudogap T^*, computed as the drop of DOS at the Fermi evaluated at fixed doping and as a function of the temperature. The normal-state scattering rate Γ at cluster momentum $K = (\pi, 0)$ is colour-coded in the picture, and its isothermal maxima at finite doping are depicted with the line of green diamonds. Colour corresponds to the magnitude of the normal-state scattering rate Γ at cluster momentum $K = (\pi, 0)$. Green diamonds indicate the maximum of $\Gamma(\delta)|_T$ at low T and $\delta > 0$. Panel (b): we plot the difference of the kinetic and the potential energy, lines of blue dots and red squares respectively, between superconducting and normal state as a function of the doping δ at $T = 1/64$. The shaded area represents the standard errors of these quantities.

6.14 and 6.15. The first-order transition at finite doping between pseudogap and correlated metal, and its associated crossover, is the unifying feature of self-energy anisotropy. This can be seen by the ridge of large scattering rate $\Gamma_{K=(\pi,0)}$, shown as the colour plot in Fig. 6.12 panel (a), emerging from $\delta_{c1}(T \to 0)$ and bent toward the charge-transfer insulator (line with green diamonds).

The Mott physics is often intertwined with that of broken symmetry states. Here we confined our investigation to d-wave superconductivity, nevertheless we speculate on the possibility that a charge-density modulation can emerge along the charge-compressibility maxima

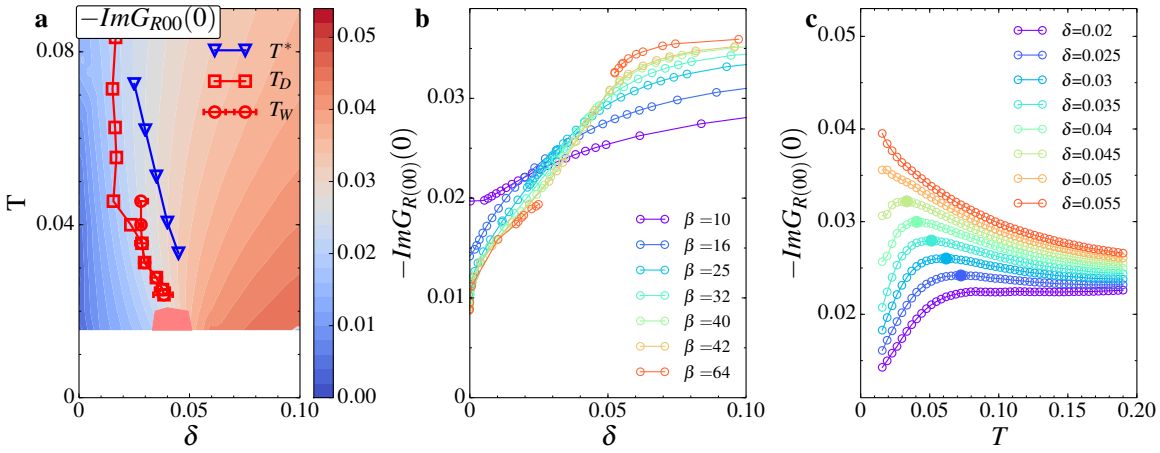

Figure 6.13: Panel (a): the extrapolated zero-frequency value of the imaginary part of the total cluster Green function -Im$G_{R=(0,0)}(\omega \to 0)$ is colour-coded as a function of the temperature and the hole doping. Line of red squares shows T_D, i.e. the locus of the inflection point of -Im$G_{R=(0,0)}(\omega \to 0)$ as a function of μ. For comparison, T_W, i.e. the locus of charge compressibility maxima, $\max_\mu \kappa$, is indicated by the line of red circles, see also Fig. 6.12. As the critical endpoint is approached, these lines become closer. Panel (b): the raw data at fixed temperature as a function of hole doping. At the lowest temperature ($\beta = 64$), a discontinuity is detectable at finite doping. Panel (c): the raw data at fixed doping as a function of temperature. The filled symbols indicate the onset of T^*.

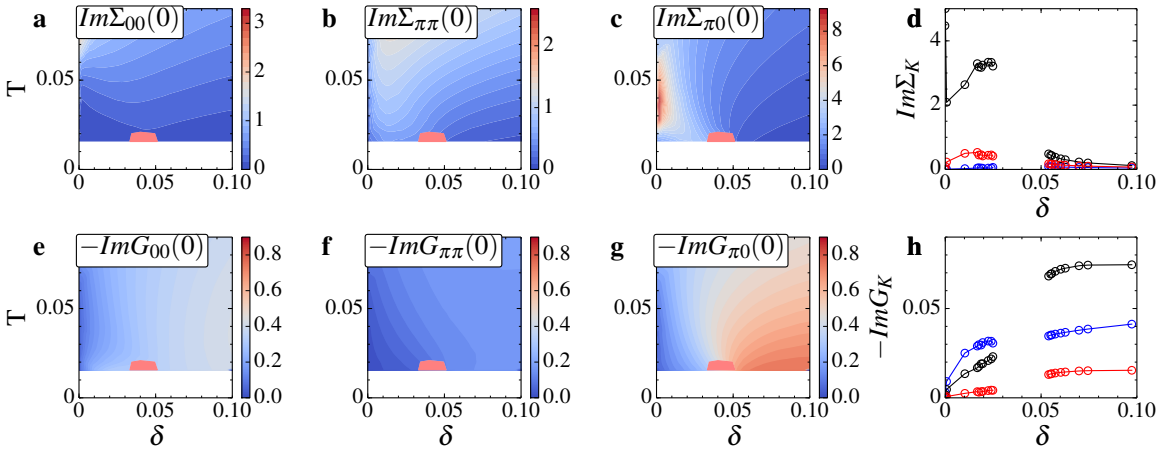

Figure 6.14: Panels (a), (b), (c): the extrapolated zero-frequency value of the imaginary part of the cluster self-energy -Im$\Sigma_K(\omega \to 0)$, with cluster momenta $(0,0)$, $(0,\pi)$ and (π,π), is colour-coded as a function of the temperature and the hole doping. (d) Raw data as a function of hole doping for $\beta = 50$. Panels (e), (f), (g), (h): as in the top panels, but for the extrapolated zero-frequency value of the imaginary part of the cluster Cu Green function -Im$G^d_K(\omega \to 0)$.

T_W. This is a subject that we will pursue in future works. The dynamical mean-field superconducting transition temperature T_c^d (orange line in Fig. 6.12 panel (a)) is defined as the temperature below which the superconducting order parameter $|\phi|$, defined in Eq. 5.3, is finite, as shown in Fig. 6.16. In fact, T_c^d corresponds to the temperature below which Cooper pairs

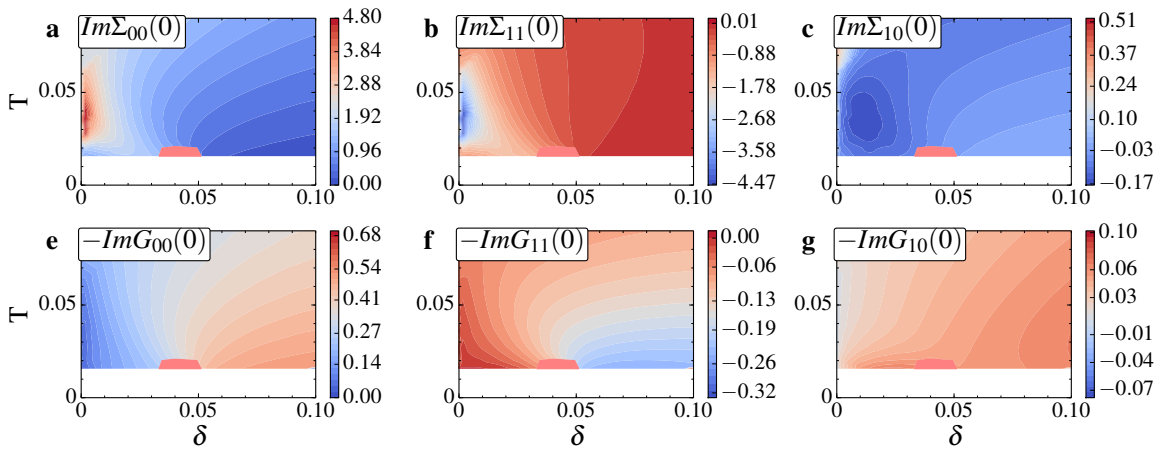

Figure 6.15: Same graphics as in Fig. 6.14, but in real space, where $R = (0,0)$, $(0,1)$ and $(1,1)$.

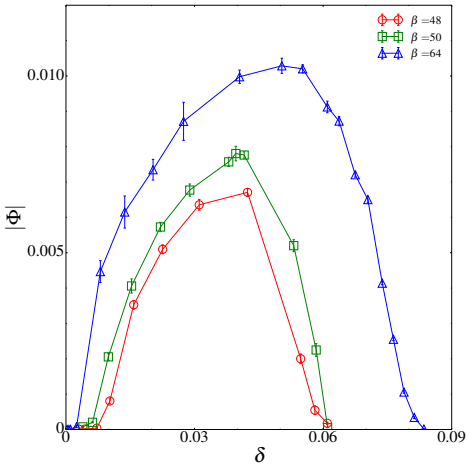

Figure 6.16: Superconducting order parameter $|\phi|$ as a function of the doping δ for different inverse temperatures β. The superconducting region in the T-δ phase diagram of Fig. 6.12 is defined as the region where Φ is nonzero.

develop within the cluster. The hidden pseudogap to correlated metal first-order transition results in complex features of the superconducting state:

(a) The superconducting dome bounded by T_c^d (line of orange squares) has a highly asymmetric dome-like shape in the $T-\delta$ phase diagram and its maximum is in close proximity to the intercept of the isothermal maximum of Γ (line of green diamonds).

(b) The crossing of T_W (line of red dots) and T_c^d indicates that the superconductivity and the pseudogap are distinct but intertwined phenomena, governed by the Mott physics.

(c) As illustrated in Fig. 6.12 panel (b), where we plotted the difference of the kinetic (line

of blue dots) and the potential energy (line of red squares) between the superconducting and normal states as a function of the doping, the pairing is driven by kinetic or potential energy respectively at $\delta < \delta_p$ or at $\delta > \delta_p$. This result is consistent with optical measurements [82, 87].

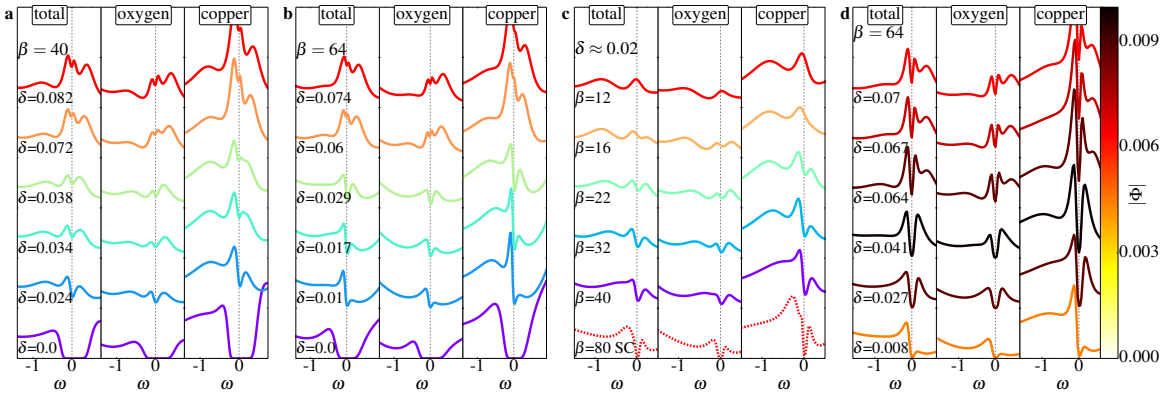

Figure 6.17: Low frequency part of the local DOS $\mathcal{N}(\omega)$. Each DOS is normalized to unity. $\mathcal{N}(\omega)_{tot} = \frac{2}{3}\mathcal{N}(\omega)_p + \frac{1}{3}\mathcal{N}(\omega)_d$. Panels (a,b): $\mathcal{N}(\omega)$ for different doping at constant inverse temperature (a) $\beta = 40 < 1/T_p$ and (b) $\beta = 64 > 1/T_p$. Panel (c): $\mathcal{N}(\omega)$ for different temperatures at constant doping $\delta \approx 0.02$. Panel (d): $\mathcal{N}(\omega)$ in the superconducting states at $\beta = 64$ for different doping. In this panel, colour corresponds to the magnitude of the superconducting order parameter.

In order to define all the phases encountered is useful to look at the local DOS in Fig. 6.17 or, alternatively, for the entire spectrum Figs. 6.18, 6.19, 6.20, and 6.21. Beginning from the

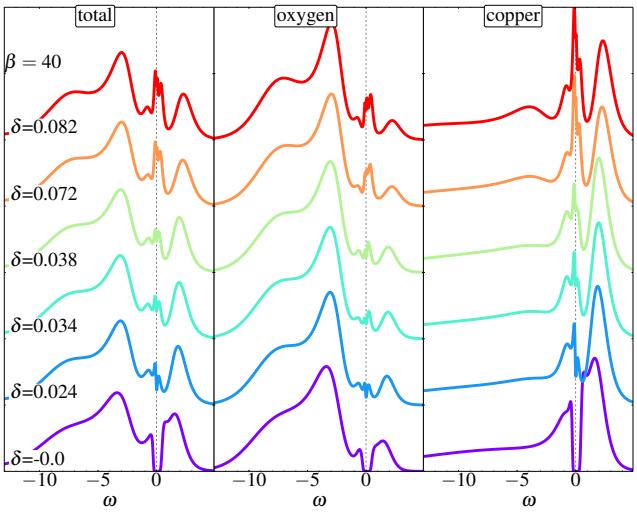

Figure 6.18: Full frequency spectrum of the DOS shown in 6.17 panel (a).

doping evolution of the $\mathcal{N}(\omega)$ for the normal state solution in Figs. 6.17 panels (a-b), 6.18 and 6.19 for several temperatures above and below T_p, we can note that:

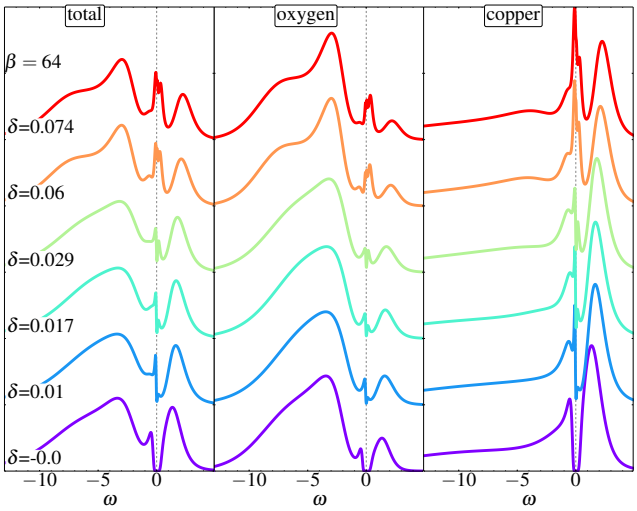

Figure 6.19: Full frequency spectrum of the DOS shown in Fig. 6.17 panel (b).

(i) The undoped, $\mathcal{N}(\omega)$ manifests a correlation gap typical of the charge-transfer type.

(ii) Upon increasing doping, as a consequence of electronic correlations, the spectral weight is rearranged to present a pseudogap, namely a finite depression of spectral weight around the Fermi level, $\omega = 0$. This phase presents a marked Cu-character, fairly hybridised with the O component [6, 238]. Moreover, $\mathcal{N}(\omega)$ reflects a large particle-hole asymmetry, that qualitatively corroborates the experimental results [247].

(iii) For larger doping, we observe a reduction of the particle-hole asymmetry and the pseudogap begins to fill up, eventually disappearing in favor of a broad peak at the Fermi level.

The temperature evolution of $\mathcal{N}(\omega)$ of the pseudogap, i.e. $\delta < \delta_p$, is displayed in Figs. 6.17 panel (c) and 6.20. These plots demonstrate that upon increasing the temperature the spectral weight at the Fermi energy gradually grows, as expected from the experimental results [248]. Finally, the doping evolution $\mathcal{N}(\omega)$ of the superconducting state is shown in Figs. 6.17 panel (d) and 6.21. The presence of coherence peaks in Cu and O partial DOS establishes that the Cooper pairs have a mixed $d-p$-character, reminiscent of "Zhang-Rice singlet" physics [6].

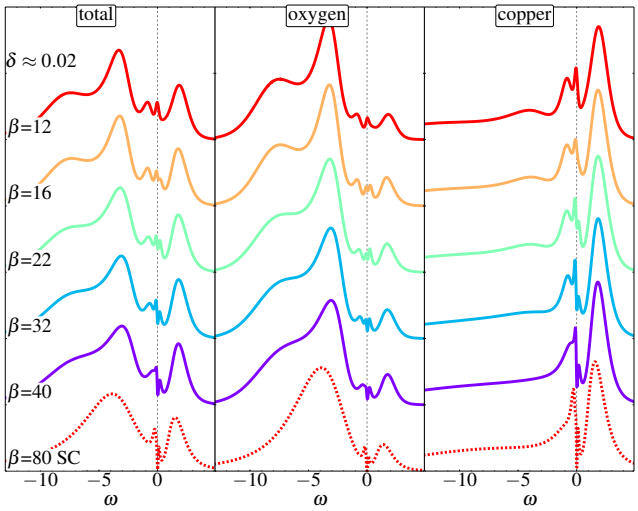

Figure 6.20: Full frequency spectrum of the DOS shown in Fig. 6.17 panel (c).

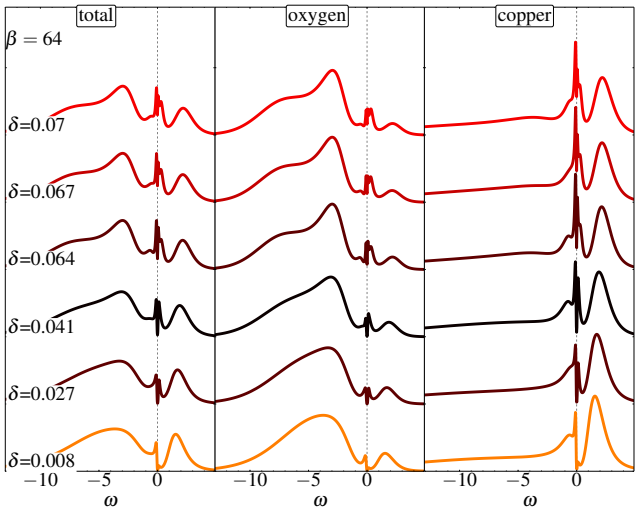

Figure 6.21: Full frequency spectrum of the DOS shown in Fig. 6.17 panel (d).

6.6 Conclusion and Discussion

In this chapter we have computed, by using the three-band Hubbard model solved with CDMFT, the phase diagram of a hole-doped charge-transfer insulator. We demonstrated that when doping the system the holes are mainly located on the oxygens, as expected in the charge-transfer regime and found experimentally [60]. Our study of dynamic and thermodynamic quantities also revealed the structure of both the normal and superconducting phases and fingerprinted their organising principle as a normal-state first-order transition below the

superconducting dome. Despite the many differences in the microscopic details, such as the presence of oxygen and the different band structure, this transition is an analogue to the one found in the single-band Hubbard model [29–32, 36, 187], analysed in Chapter 5.

This suggests that the emergent character of the phenomenon is caused by Mott physics and the short-range correlations. Thus, this leads to the following conjecture [37]: a first-order transition even when hidden by another phase, here superconductivity, can act as a general organising principle of strongly-coupled matter. This is the case also in other Hubbard-like models [35, 227, 249–252], and proves that the presence of the pseudogap and the $d-$wave superconductivity does not strictly require the existence of an antiferromagnetic quantum critical point [253].

In future investigations we shall also address the interplay of the normal state with other broken-symmetry phases, such as charge density waves [254–256], or loop currents [257–262].

Chapter 7

Conclusions and Perspectives

In this thesis we have performed a detailed analysis of the phase diagram of the two-dimensional Hubbard and Emery models, using Cellular Dynamical Mean-Field Theory with Continuous-Time Quantum Monte Carlo as the impurity solver. The physics of the normal state, governed at zero doping by the Mott transition, has significant consequences also in the features of other broken symmetry states, such as the antiferromagnetic and superconducting phases. In this thesis we explored by which extent the properties of the normal state, even when masked from the other phases, can organise the complex phase diagram of the cuprates.

In the initial study of the normal state in the half-filled Hubbard model, we have revealed the Mott transition that appears to be a first-order transition culminating in a second-order critical point between an insulating and a correlated metal phase. This transition at half-filling is hidden below the antiferromagnetic phase, but the physical properties of the latter strongly depend on it. There are, indeed, two mechanisms from which the antiferromagnetic phase emerges:

(i) In the weak interaction regime, we have the Slater mechanism, i.e. the nesting of the Fermi Energy causing the spins to antiferromagnetically order.

(ii) In the strong interaction regime, we have the Heisenberg mechanism, i.e. the antiferromagnetic state is stabilised by the super-exchange coupling.

In the first case, the Néel temperature grows as we increase the interaction, in the latter, it gets suppressed. We highlighted sharp differences between these two regimes that appear to be

organised by the underlying Mott transition and its supercritical behaviour. In particular, by analysing the condensation energy, we established a nontrivial crossover between a potential energy and a kinetic energy gain respectively in the Slater and Heisenberg regimes, contiguous to the Widom line of the normal state, as discussed in Chapter 4 and Ref. [28].

The Mott physics, also, controls the hole-dope phase diagram. By doping a Mott insulator dynamical, thermodynamical, and transport quantities show anomalous behaviour, demonstrating the existence of a pseudogap to correlated metal transition. Also this transition manifests a first-order line that culminates in a second-order critical point, leaving a new Widom line for higher temperatures [30–32]. The inspection of the properties of the d-wave superconductivity indicates that the physics of this phase is strongly intertwined with the normal state, as shown in a variety of parametric regimes in Chapter 5 and Ref. [36]. Upon doping a Mott insulator, the superconductivity arises from the pseudogap state reaching the maximum of T_c in concomitance with the maxima of the anomalous scattering rate of the pseudogap. Moreover, our analysis demonstrates that the Widom line is correlated with the maximum of the d-wave superconducting order parameter and the minimum of the condensation energy. A detailed analysis of the difference in the normal and superconducting potential and kinetic energies for different interaction values revealed that:

(i) for $U >> U_{\mathrm{MIT}}$ the super-exchange interaction drives superconductivity, with a gain in the kinetic energy,

(ii) for U larger but closer to U_{MIT} the over-doped regime has a potential energy growth, similar to what it is expected in the BCS case.

Although previous investigations highlight such a behaviour [85,195,207], it is our analysis that first unifies these scenarios linking them with the underlying physics of the normal state. Furthermore, these results stand also in the presence of antagonistic effects of nearest-neighbour repulsion, as shown in a recent collaboration, Ref. [252], which we did not include in this thesis.

The examination of the Emery model demonstrates that our results are also robust under inter-band interaction, as discussed in Chapter 6 and Ref. [37]. This work is the only one present in literature [238–241] that compares normal and superconducting phases at finite temperature in this model with CDMFT using Hybridisation expansion algorithm. At half-

filling we explicitly found a metal to charge transfer insulator transition, as expected in our parametric regime from the description of the Zaanen-Sawatzky-Allen scheme [10]. Upon doping the charge transfer insulator, we found a crossover transition with a pseudogap state. This state evolves, at low temperatures, in a correlated metal at higher doping via a first-order transition that culminates in a second-order critical point and continues as a Widom line for higher temperatures. Similarly to the Hubbard model case, the physics of the superconducting phase is intertwined with that of the pseudogap, corroborating in this way our scenario that the Mott physics acts as organising principle for the phase diagram of cuprates.

There are many perspectives to be developed in future studies. For instance, it will be interesting to explore a detailed analysis of the unusual aspects of the antiferromagnetic phase in juxtaposition with the superconducting and normal state.

In addition, further insight can be obtained analysing the antiferromagnetic phase in the Emery model. This model is a natural playground to study new parametric regimes, inaccessible with the Hubbard model, in the hope to gather a better understanding of the superconducting phase, so to maximise the value of T_c at optimal doping.

From an experimental perspective, it would be worth to directly observe the pseudogap to correlated metal transition, inhibited by the presence of the charge-order and the d-wave superconductivity. We speculated that, by exposing to a high magnetic field and a high pressure a sample of cuprate, we could directly observe the underlying normal state. Alternatively, some evidence can be gathered due to the recent progress in cold atom physics. Ultracold atoms in an optical lattice are starting to offer a new way to test the physics of the Hubbard model. The Mott transition and its interplay with the antiferromagnetic state are beginning to be tested [218–222]. Upon reaching a smaller temperature scale, than the ones currently accessible, it will be possible also to study the features of the superconducting state and the properties of the underlying normal state.

Appendix A

Convergence of the Algorithms

In this appendix, we will briefly discuss the convergence of the CDMFT solutions for the 5 algorithms employed in this thesis.

A.1 Normal State of the Hubbard Model

In the case of the normal state study, we have systematically performed from 4×10^7 to 10^8 Monte Carlo sweeps per processor; averaged over 72 processors. When necessary, for example close to phase transition boundaries, we may use up to 96 processors for each simulation. The quantities presented are the result of the average of the last $20 - 30$ iterations, but hundreds may be necessary close to phase boundaries. The total number of simulations computed and analysed with this algorithm is around 2000. We used the following procedure: First we verified the convergence of the double occupancy D, the average sign of Eq. 4.21, and the average expansion order k; as discussed in Section 3.5, and shown in Figs. A.1,A.2, and A.3 respectively, for three selected simulations.

In these simulations, taken at half filling, we can directly observe the coexistence of a metallic and an insulating solution (black and red curves respectively) for $U = 5.725$, $\beta = 20$, and $t' = 0$. Close to the phase boundaries, the convergence of the solution takes more loops. This is shown with the blue curve for $U = 5.7$; upon beginning the CDMFT loop with an insulating solution, we observe a "sudden jump" to a metallic one.

All of the independent response functions are then calculated as the result of the averaged functions, for the last 30 loops, and the error is the resulting standard deviation. In Fig.

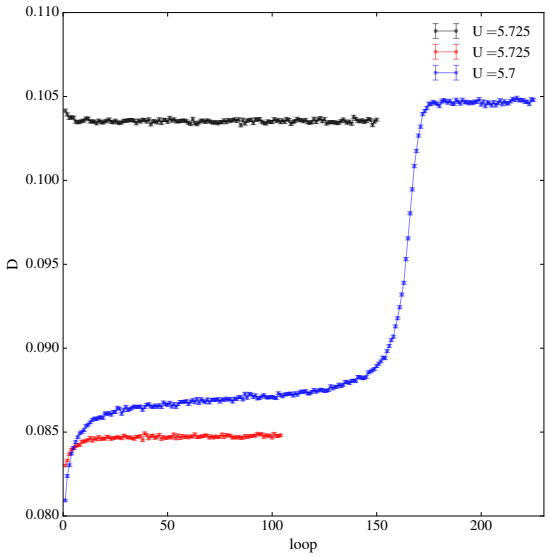

Figure A.1: The double occupancy as a function of the CDMFT iteration loops for: a metallic solution at $U = 5.725$, in black; an insulating solution at $U = 5.725$, in red; and another metallic solution at $U = 5.7$, in blue; for $\beta = 20$, $t' = 0$, at half-filling.

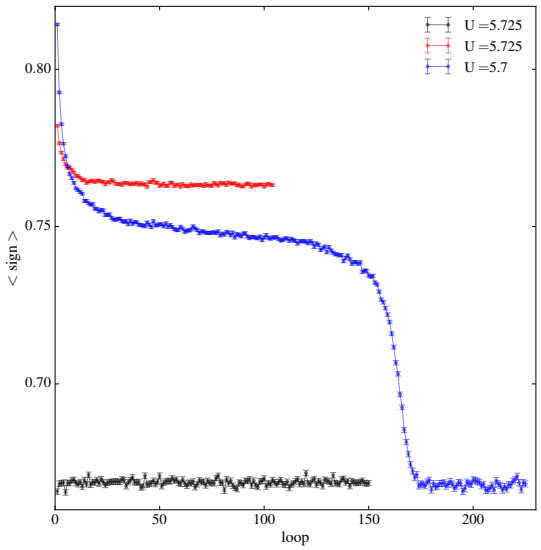

Figure A.2: The average sign as a function of the CDMFT iteration loops of isothermal simulations for: a metallic solution at $U = 5.725$, in black; an insulating solution at $U = 5.725$, in red; and another metallic solution at $U = 5.7$, in blue; for $\beta = 20$, $t' = 0$, at half-filling.

A.4, we show the Green function; in Fig. A.5, the self-energy functions; and in Fig. A.6, the hybridisation functions. The metallic solutions for $U = 5.725$, in red; and for $U = 5.725$, in blue; differ very little due to the parametric vicinity. The average error at low frequencies is of the order of 10^{-4}, demonstrating a well reached convergence for these results.

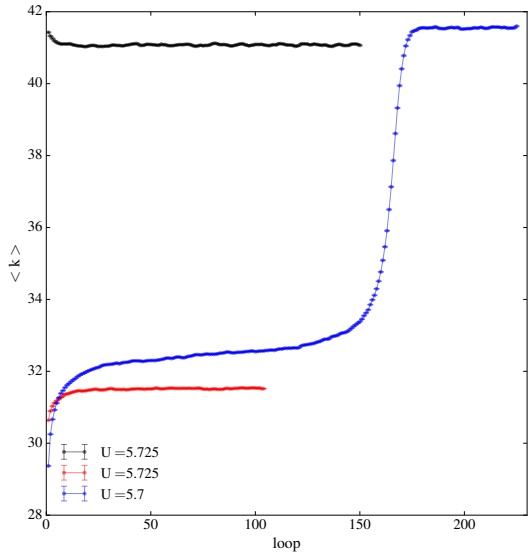

Figure A.3: The average expansion order as a function of the CDMFT iteration loops of isothermal simulations for: a metallic solution at $U = 5.725$, in black; an insulating solution at $U = 5.725$, in red; and another metallic solution at $U = 5.7$, in blue; for $\beta = 20$, $t' = 0$, at half-filling.

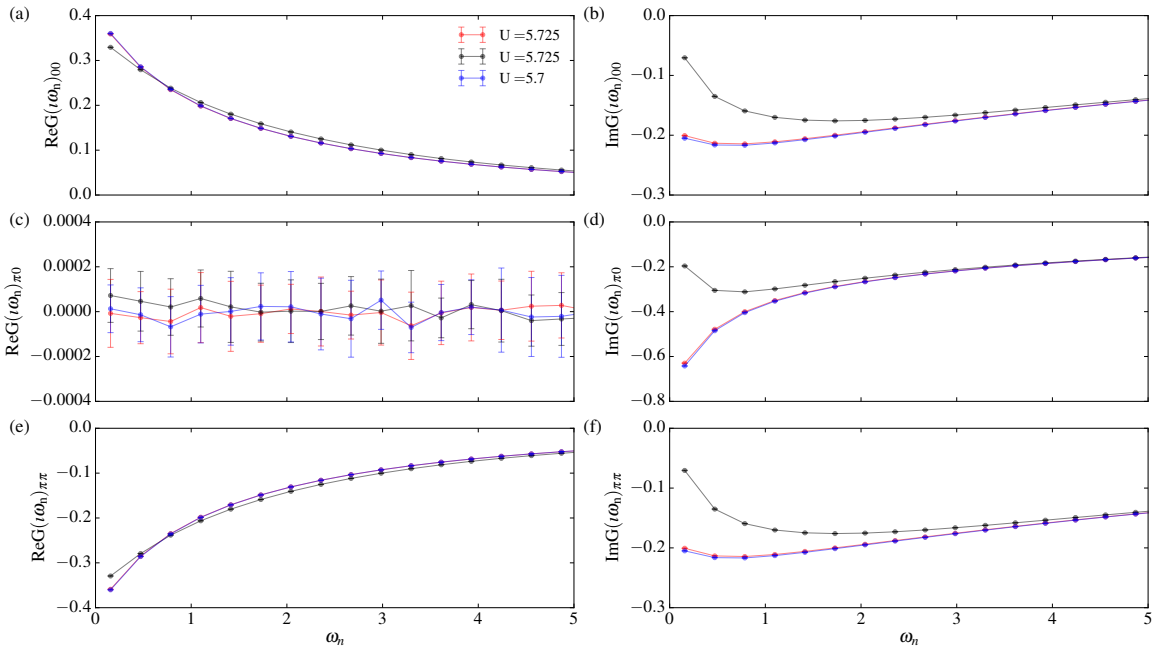

Figure A.4: All of the independent Green functions in the reciprocal space, as function of the Matsubara frequencies for: a metallic solution at $U = 5.725$, in black; an insulating solution at $U = 5.725$, in red; and another metallic solution at $U = 5.7$, in blue; for $\beta = 20$, $t' = 0$, at half-filling.

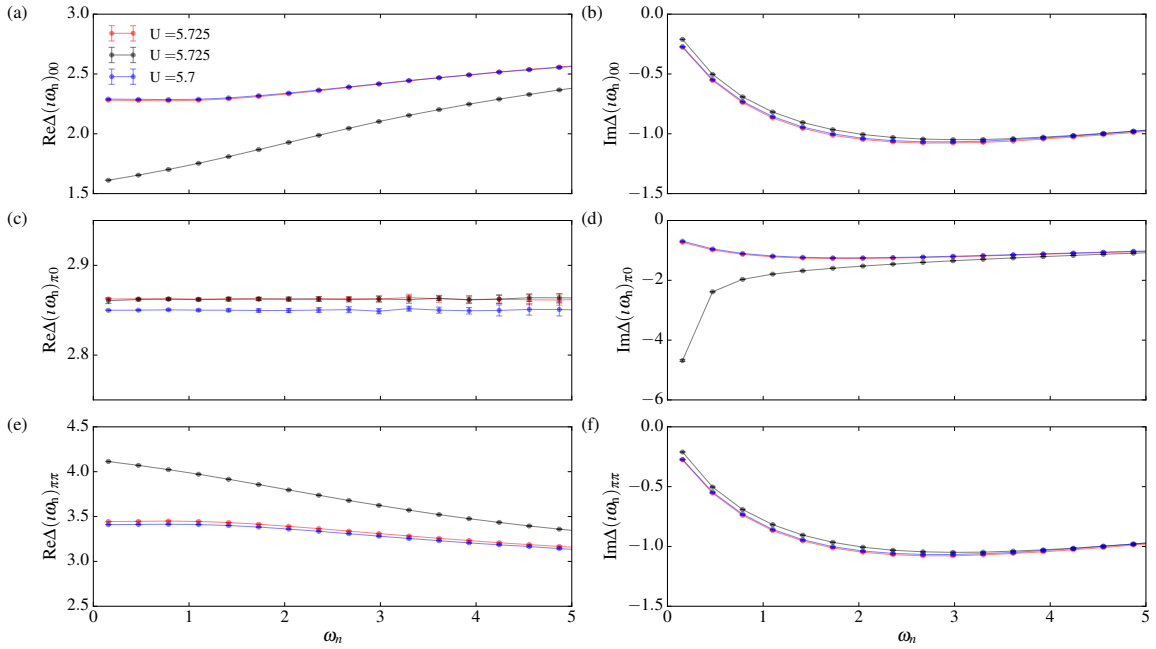

Figure A.5: All of the independent self-energy functions in the reciprocal space, as function of the Matsubara frequencies for: a metallic solution at $U = 5.725$, in black; an insulating solution at $U = 5.725$, in red; and another metallic solution at $U = 5.7$, in blue; for $\beta = 20$, $t' = 0$, at half-filling.

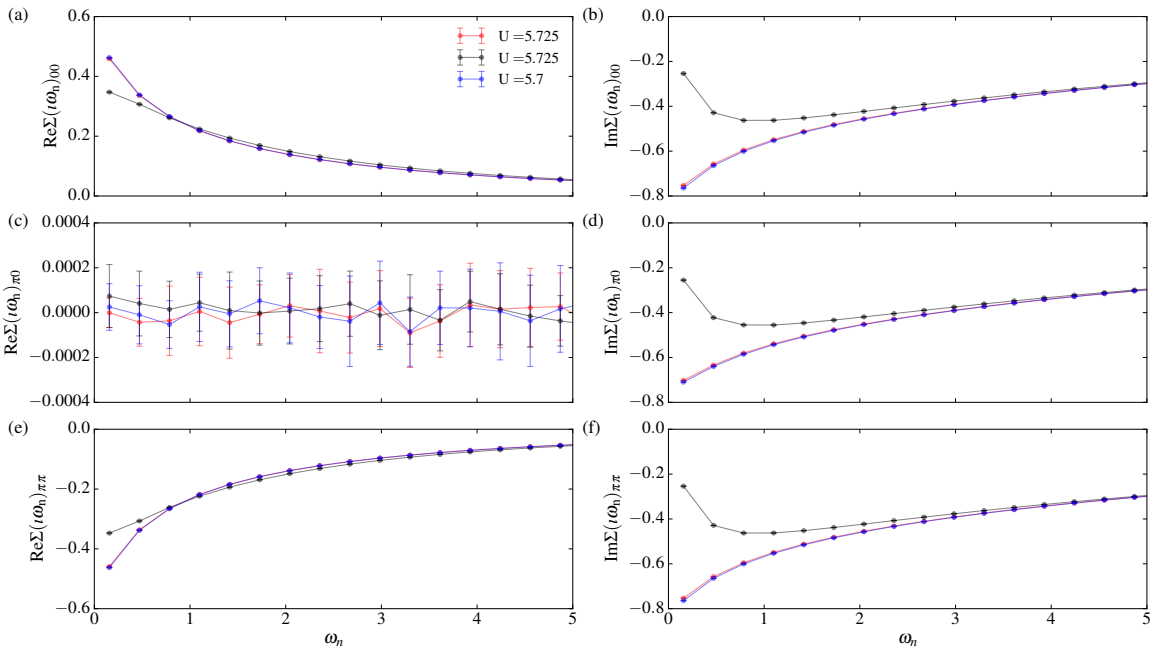

Figure A.6: All of the independent hybridisation functions in the reciprocal space, as function of the Matsubara frequencies for: a metallic solution at $U = 5.725$, in black; an insulating solution at $U = 5.725$, in red; and another metallic solution at $U = 5.7$, in blue; for $\beta = 20$, $t' = 0$, at half-filling.

A.2 Superconducting State of the Hubbard Model

Similarly to the normal state, in the case of the superconducting state study, we have systematically performed from 4×10^7 to 8×10^7 Monte Carlo sweeps per processor; averaged over 72 processors for each simulation. When necessary, for example close to phase transition boundaries, we may use up to 96 processors. The quantities presented are the result of the average of the last $20-30$ iterations, but hundreds may be necessary close to phase boundaries. The total number of simulations computed and analysed with this algorithm is around 1000. We used the following procedure: First we verified the convergence of the double occupancy D, the average sign of Eq. 4.21, the average expansion order k, discussed in Section 3.5, and the superconducting order parameter ϕ of eq. 5.3 as shown in Figs. A.7,A.8, A.9 and A.10 respectively, for three selected simulations.

These simulations were taken at fixed $U = 7.0$, $\beta = 50$, and $t' = 50$. For different values of the chemical potential μ, we can observe the convergence of the initially superconducting solution to either: a pseudogap solution as for $\mu = 2.74$, shown with the blue curve; or a superconducting one, as for $\mu = 2.15$ in black; and for $\mu = 1.95$, in red.

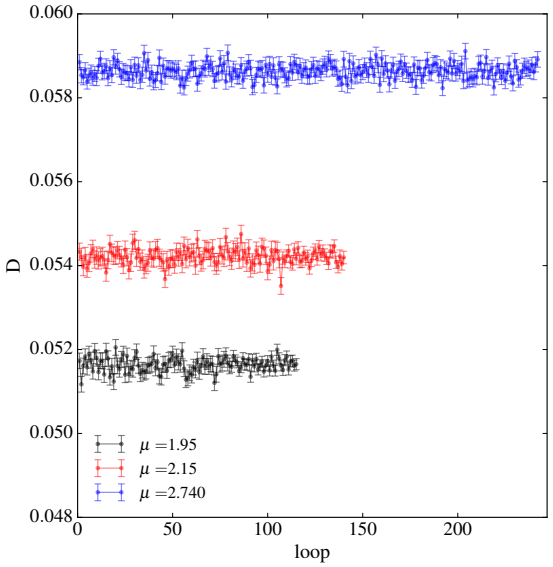

Figure A.7: The double occupancy as a function of the CDMFT iteration loops for: a superconducting solution at $\mu = 1.95$, in black; a superconducting solution at $\mu = 2.15$, in red; and a pseudogap solution at $\mu = 2.74$, in blue; for $\beta = 50$, $t' = 0$ and $U = 7.0$.

All of the independent response functions are then calculated as the result of the averaged functions, for the last 30 loops, and the error is the resulting standard deviation. In Fig. A.11,

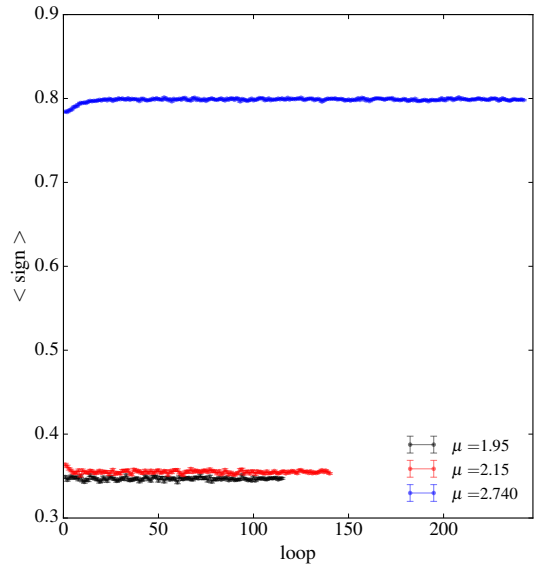

Figure A.8: The average sign as a function of the CDMFT iteration loops for: a superconducting solution at $\mu = 1.95$, in black; a superconducting solution at $\mu = 2.15$, in red; and a pseudogap solution at $\mu = 2.74$, in blue; for $\beta = 50$, $t' = 0$ and $U = 7.0$.

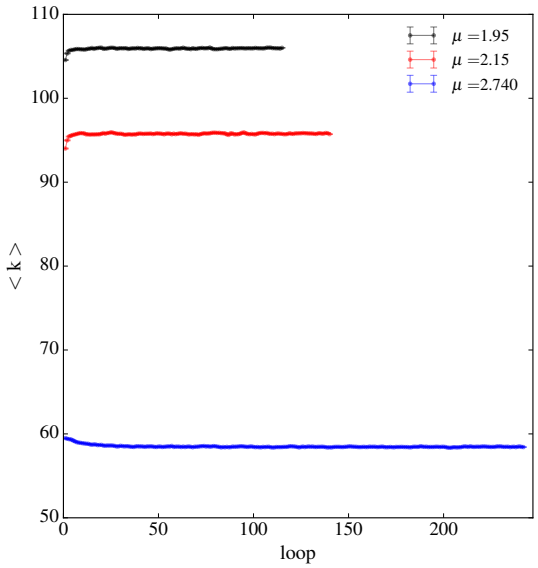

Figure A.9: The average expansion order as a function of the CDMFT iteration loops for: a superconducting solution at $\mu = 1.95$, in black; a superconducting solution at $\mu = 2.15$, in red; and a pseudogap solution at $\mu = 2.74$, in blue; for $\beta = 50$, $t' = 0$ and $U = 7.0$.

we show the Green function; in Fig. A.12, the self-energy functions; and in Fig. A.13, the hybridisation functions.

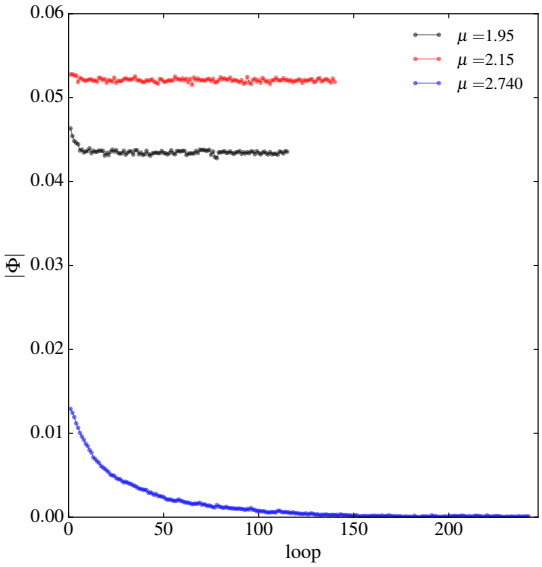

Figure A.10: The superconducting order parameter as a function of the CDMFT iteration loops for: a superconducting solution at $\mu = 1.95$, in black; a superconducting solution at $\mu = 2.15$, in red; and a pseudogap solution at $\mu = 2.74$, in blue; for $\beta = 50$, $t' = 0$ and $U = 7.0$.

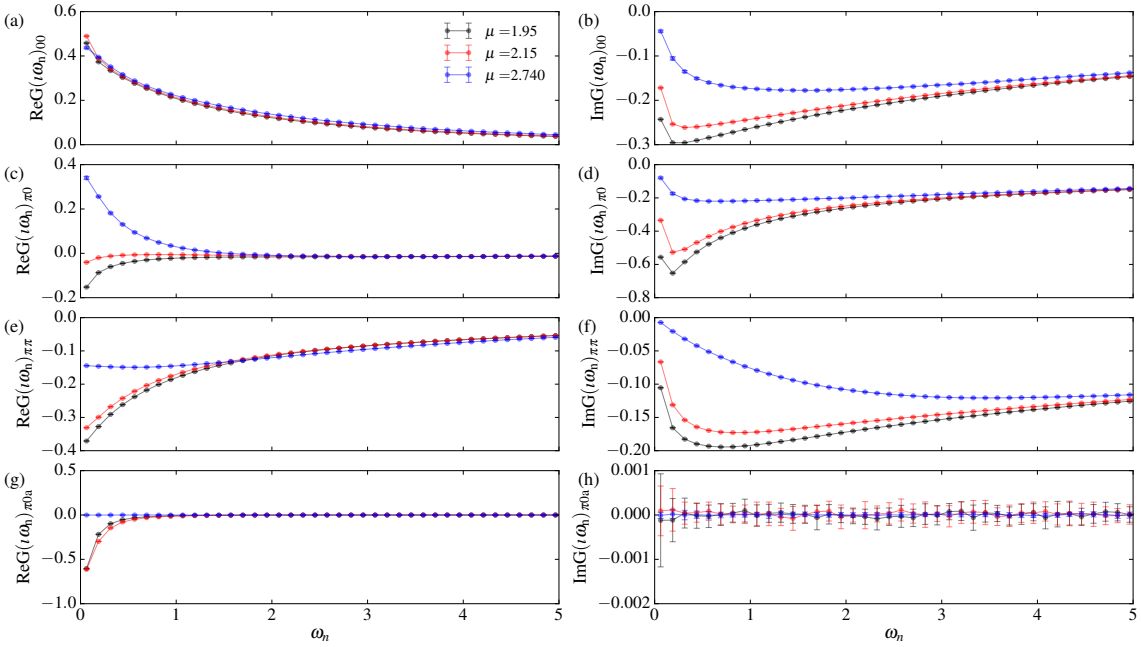

Figure A.11: All of the independent green functions in the reciprocal space, as function of the Matsubara frequencies for: a superconducting solution at $\mu = 1.95$, in black; a superconducting solution at $\mu = 2.15$, in red; and a pseudogap solution at $\mu = 2.74$, in blue; for $\beta = 50$, $t' = 0$ and $U = 7.0$.

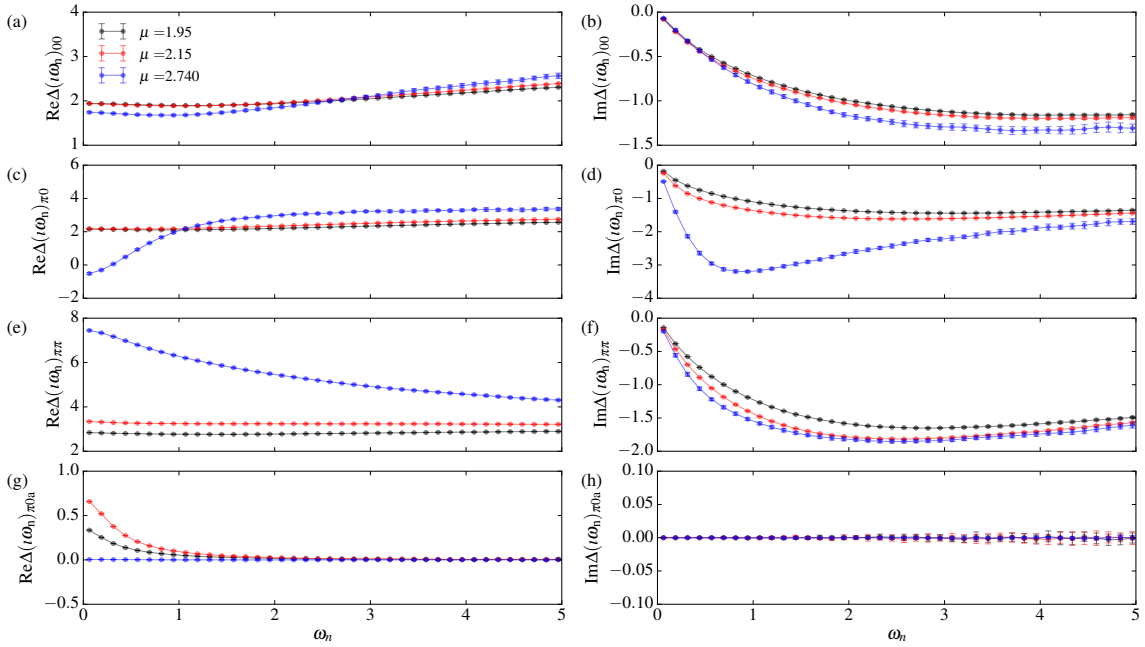

Figure A.12: All of the independent self-energies functions in the reciprocal space, as function of the Matsubara frequencies for: a superconducting solution at $\mu = 1.95$, in black; a superconducting solution at $\mu = 2.15$, in red; and a pseudogap solution at $\mu = 2.74$, in blue; for $\beta = 50$, $t' = 0$ and $U = 7.0$.

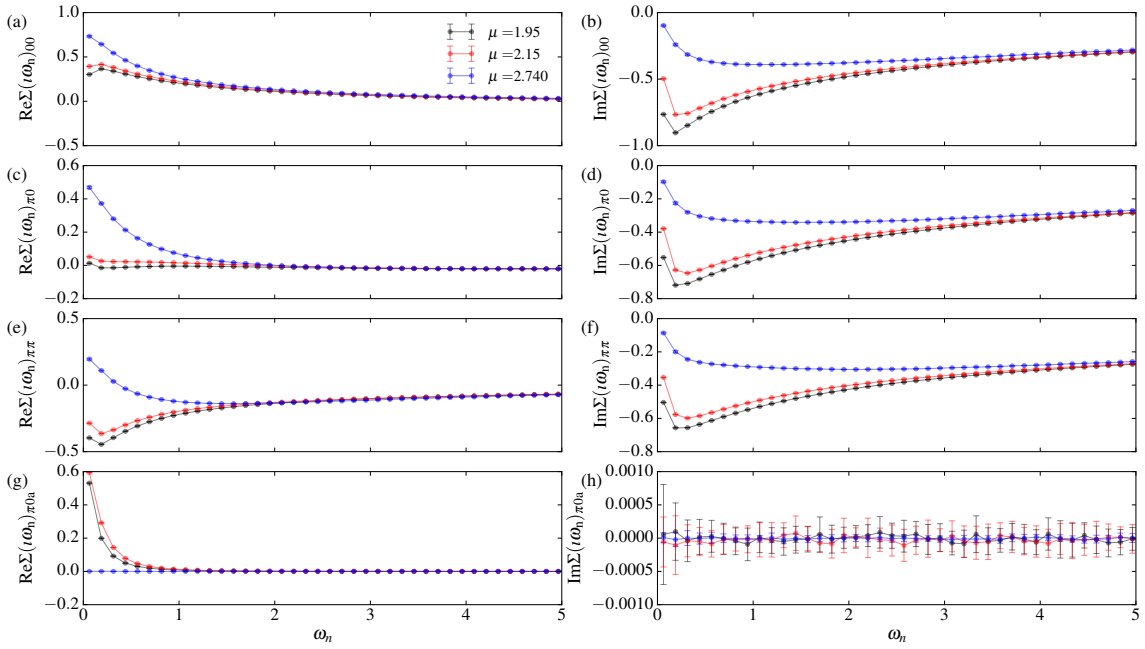

Figure A.13: All of the independent hybridisation functions in the reciprocal space, as function of the Matsubara frequencies for: a superconducting solution at $\mu = 1.95$, in black; a superconducting solution at $\mu = 2.15$, in red; and a pseudogap solution at $\mu = 2.74$, in blue; for $\beta = 50$, $t' = 0$ and $U = 7.0$.

A.3 Antiferromagnetic State of the Hubbard Model

In the antiferromagnetic state study, we have systematically performed from 4×10^7 to 1×10^8 Monte Carlo sweeps per processor; averaged over 72 processors for each simulation. When necessary, for example close to phase transition boundaries, we may use up to 96 processors. The quantities presented are the result of the average of the last $20-30$ iterations, but hundreds may be necessary close to phase boundaries. The total number of simulations computed and analysed with this algorithm is around 500. We used the following procedure: First we verified the convergence of the double occupancy D, the average sign of Eq. 4.21, the average expansion order k discussed in the Section 3.5, and the staggered magnetisation $m_z$of eq. 4.24 as shown respectively in Figs. A.14,A.15, A.16 and A.17 for three selected simulations.

These simulations were taken at $\beta = 10$, $t' = 0$, and at half-filling. For different values of the interaction U, we can observe the convergence of the initially antiferromagnetic solution to either: a metallic solution as for $U = 2.0$, black curve; or an antiferromagnetic one ,as for $U = 3.0$ in red; and $U = 9.0$, in blue.

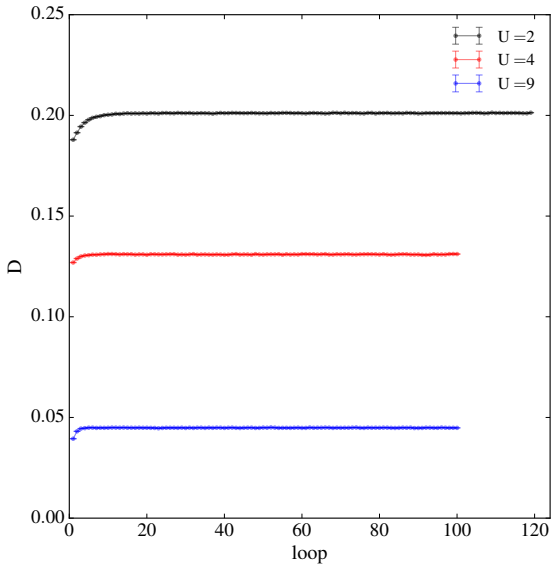

Figure A.14: The double occupancy as a function of the CDMFT iteration loops for: $U = 2$, in black; $U = 3.0$, in red; and $U = 9.0$, in blue. The first is a metallic solution; for the latter two we see convergence to two antiferromagnetic solutions in all simulations for $\beta = 10$, $t' = 0$, and at half-filling.

All of the independent response functions are then calculated as the result of the averaged functions, for the last 30 loops, and the error is the resulting standard deviation. In Fig. A.18, we show the Green functions; in Fig. A.19, the self-energy functions; and in Fig. A.20, the

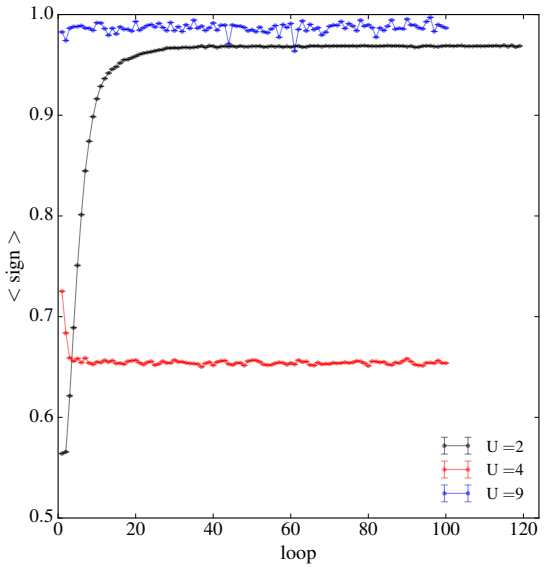

Figure A.15: The average sign as a function of the CDMFT iteration loops for a metallic solution for: $U = 2$, in black; $U = 3.0$, in red; and $U = 9.0$, in blue. The first is a metallic solution; for the latter two we see convergence to two antiferromagnetic solutions in all simulations for $\beta = 10$, $t' = 0$, and at half-filling.

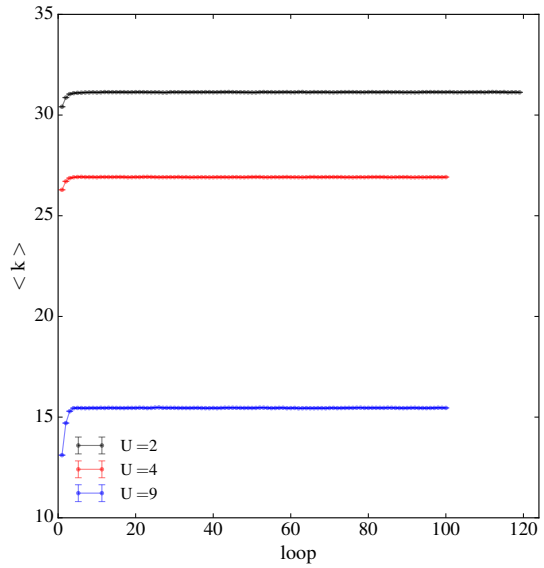

Figure A.16: The average expansion order as a function of the CDMFT iteration loops for: $U = 2$, in black; $U = 3.0$, in red; and $U = 9.0$, in blue. The first is a metallic solution; for the latter two we see convergence to two antiferromagnetic solutions in all simulations for $\beta = 10$, $t' = 0$, and at half-filling.

hybridisation functions.

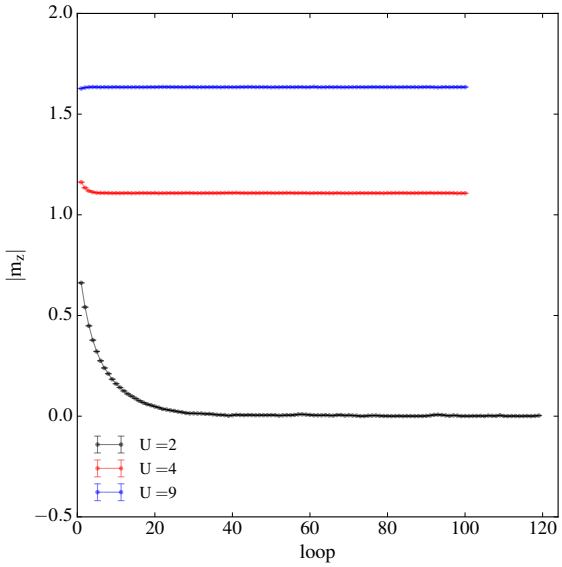

Figure A.17: The staggered magnetisation as a function of the CDMFT iteration loops for: $U = 2$, in black; $U = 3.0$, in red; and $U = 9.0$, in blue. The first is a metallic solution; for the latter two we see convergence to two antiferromagnetic solutions in all simulations for $\beta = 10$, $t' = 0$, and at half-filling.

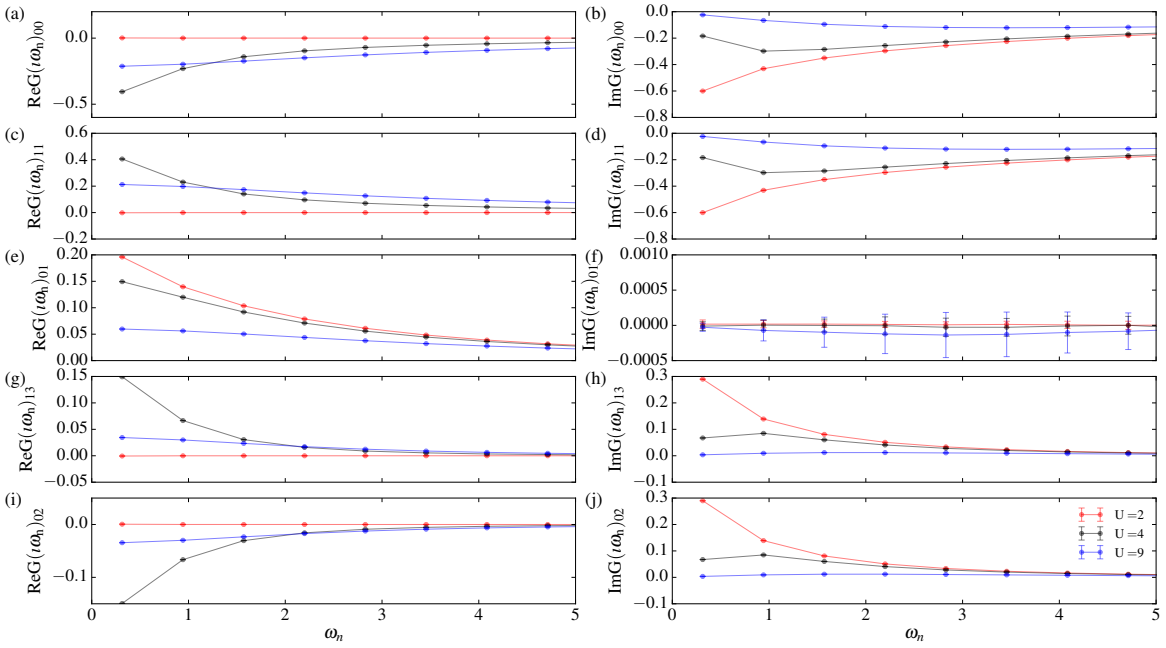

Figure A.18: All of the independent green functions in the irreducible representation base, as function of the Matsubara frequencies for: $U = 2$, in black; $U = 3.0$, in red; and $U = 9.0$, in blue. The first is a metallic solution; for the latter two we see convergence to two antiferromagnetic solutions in all simulations for $\beta = 10$, $t' = 0$, and at half-filling.

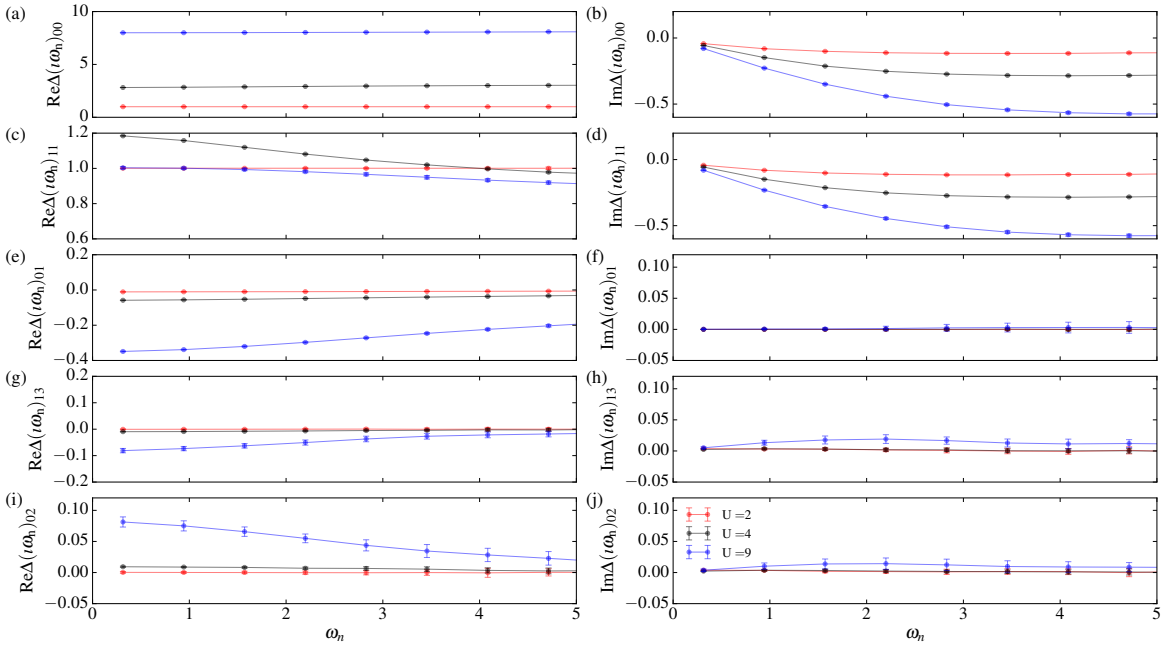

Figure A.19: All of the independent self-energy functions in the irreducible representation base, as function of the Matsubara frequencies for: $U = 2$, in black; $U = 3.0$, in red; and $U = 9.0$, in blue. The first is a metallic solution; for the latter two we see convergence to two antiferromagnetic solutions in all simulations for $\beta = 10$, $t' = 0$, and at half-filling.

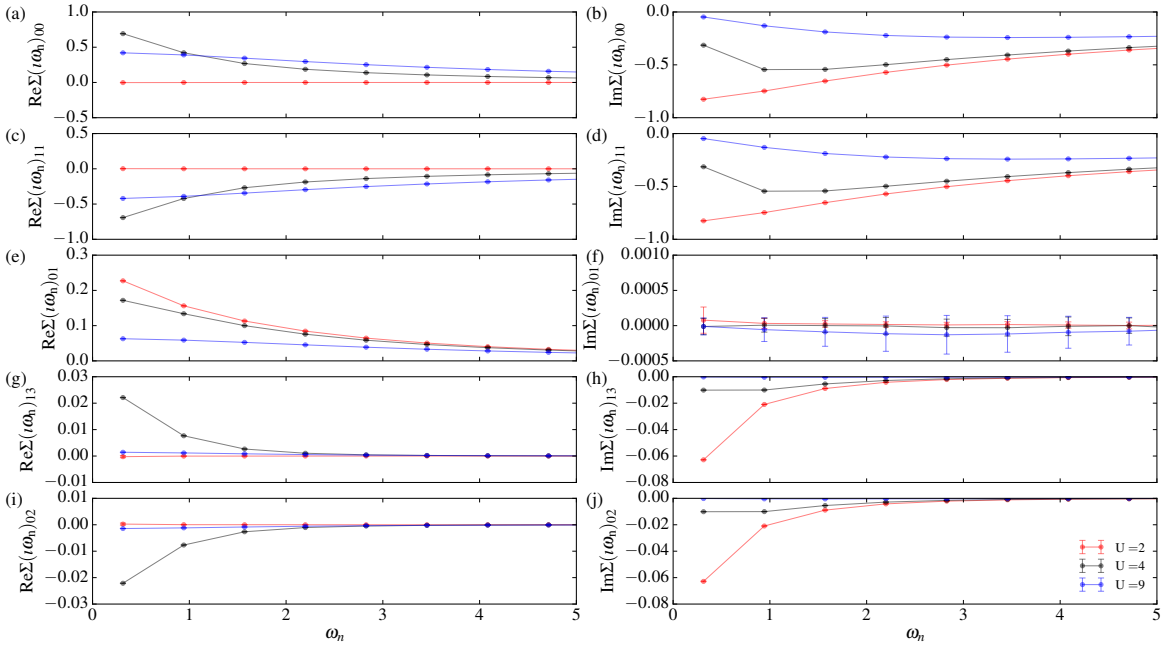

Figure A.20: All of the independent Hybridisation functions in the irreducible representation base, as function of the Matsubara frequencies for: $U = 2$, in black; $U = 3.0$, in red; and $U = 9.0$, in blue. The first is a metallic solution; for the latter two we see convergence to two antiferromagnetic solutions in all simulations for $\beta = 10$, $t' = 0$, and at half-filling.

A.4 Normal State of the Emery Model

In the case of the normal state study, we have systematically performed from 8×10^7 to 10^8 Monte Carlo sweeps per processor; averaged over 96 processors. When necessary, for example close to phase transition boundaries, we may use up to 110 processors for each simulation. The quantities presented are the result of the average of the last $10 - 30$ iterations, but hundreds may be necessary close to phase boundaries. The total number of simulations computed and analysed with this algorithm is more than 2000. We used the following procedure: First we verified the convergence of the double occupancy D, the average sign of Eq. 4.21 and the average expansion order k, discussed in Section 3.5, as shown respectively in Figs. A.21,A.22, and A.23; for three selected simulations.

In these simulations, taken at fixed copper interaction $U_d = 12.0$, we can directly observe the coexistence of a correlated metal and a pseudogap solution (blue and red curves respectively) for $\mu = 11.682$, $\beta = 50$.

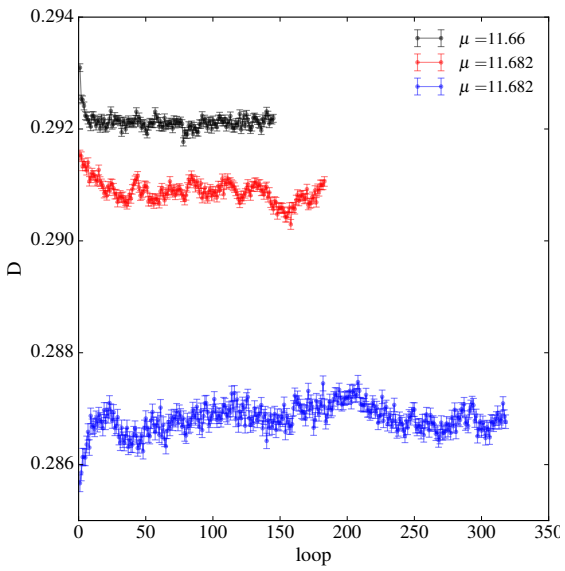

Figure A.21: The double occupancy as a function of the CDMFT iteration loops at $U_d = 12.0$, $\beta = 50$ for three metallic solutions: one at $\mu = 11.66$, in black; and two coexisting solutions at $\mu = 11.682$, a correlated metal and a pseudogap; the blue and red curves respectively.

All of the independent response functions are then calculated as the result of the averaged functions, for the last 10-30 loops, and the error is the resulting standard deviation. In Fig. A.24, we show the Green function; in Fig. A.25, the self-energy functions; and in Fig. A.26, the hybridisation functions. The average error at low frequencies is of the order of 10^{-3},

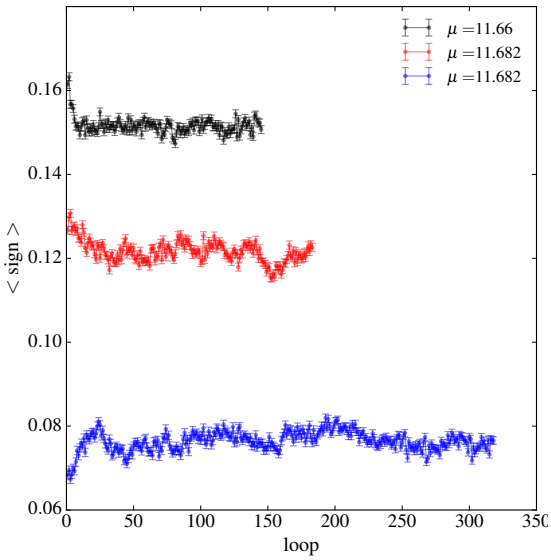

Figure A.22: The average sign as a function of the CDMFT iteration loops at $U_d = 12.0$, $\beta = 50$ for three metallic solutions: one at $\mu = 11.66$, in black; and two coexisting solutions at $\mu = 11.682$, a correlated metal and a pseudogap; the blue and red curves respectively.

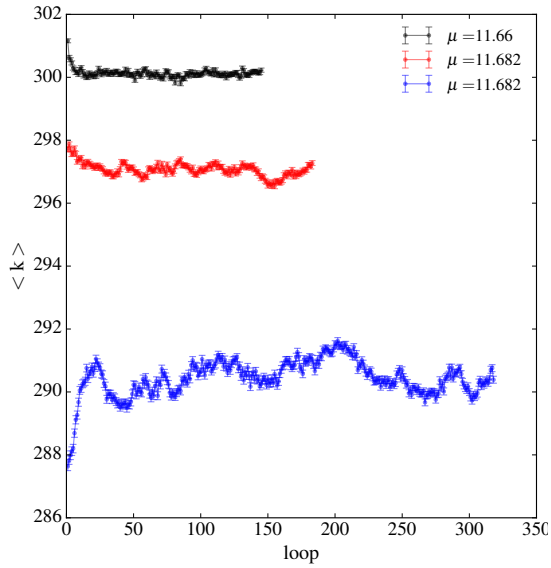

Figure A.23: The average expansion order as a function of the CDMFT iteration loops at $U_d = 12.0$, $\beta = 50$ for three metallic solutions: one at $\mu = 11.66$, in black; and two coexisting solutions at $\mu = 11.682$, a correlated metal and a pseudogap; the blue and red curves respectively.

demonstrating a well reached convergence for these results.

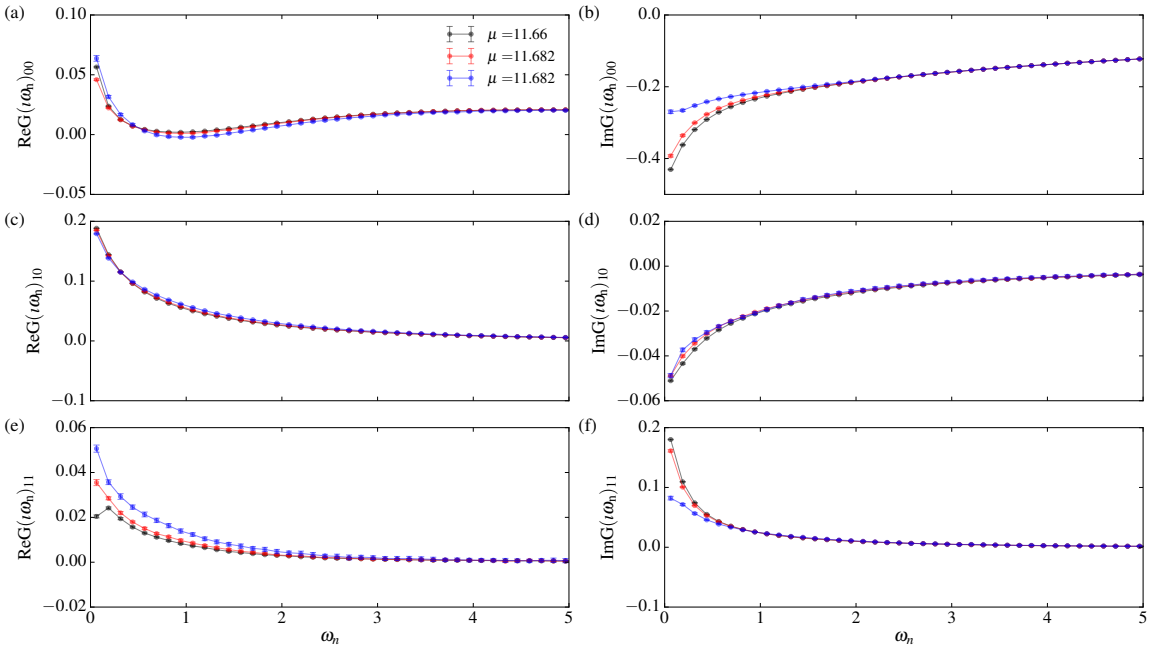

Figure A.24: All of the independent green functions in the real base, as a function of the Matsubara frequencies at $U_d = 12.0$, $\beta = 50$ for three metallic solutions: one at $\mu = 11.66$, in black; and two coexisting solutions at $\mu = 11.682$, a correlated metal and a pseudogap; the blue and red curves respectively.

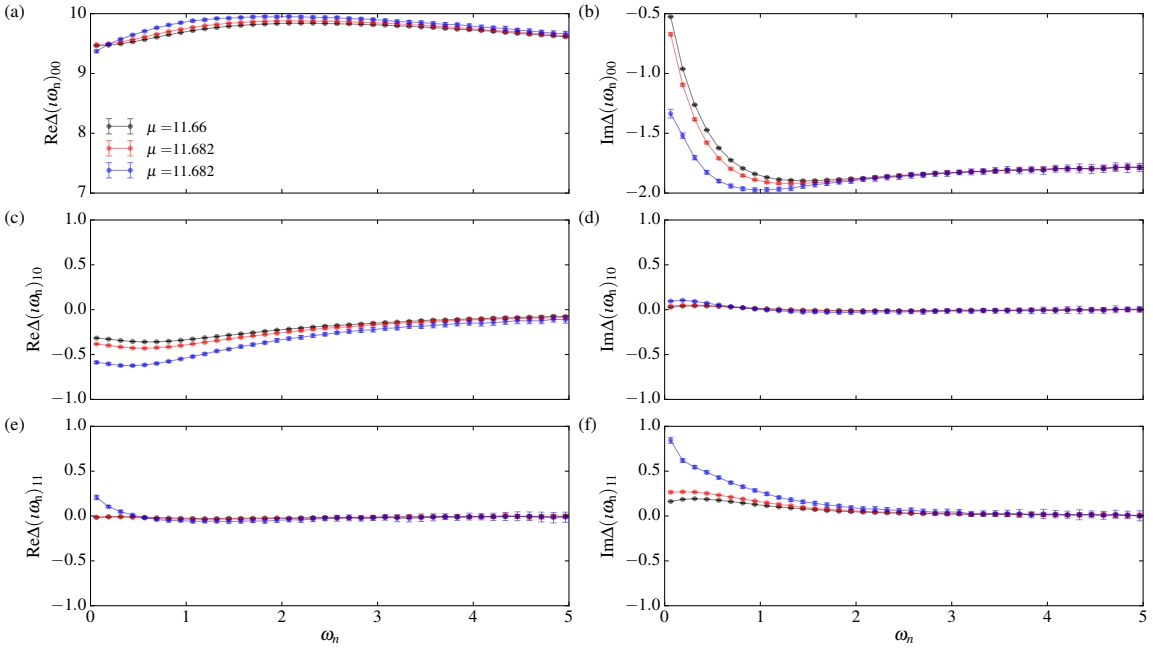

Figure A.25: All of the independent self-energy functions in the real base, as a function of the Matsubara frequencies at $U_d = 12.0$, $\beta = 50$ for three metallic solutions: one at $\mu = 11.66$, in black; and two coexisting solutions at $\mu = 11.682$, a correlated metal and a pseudogap; the blue and red curves respectively.

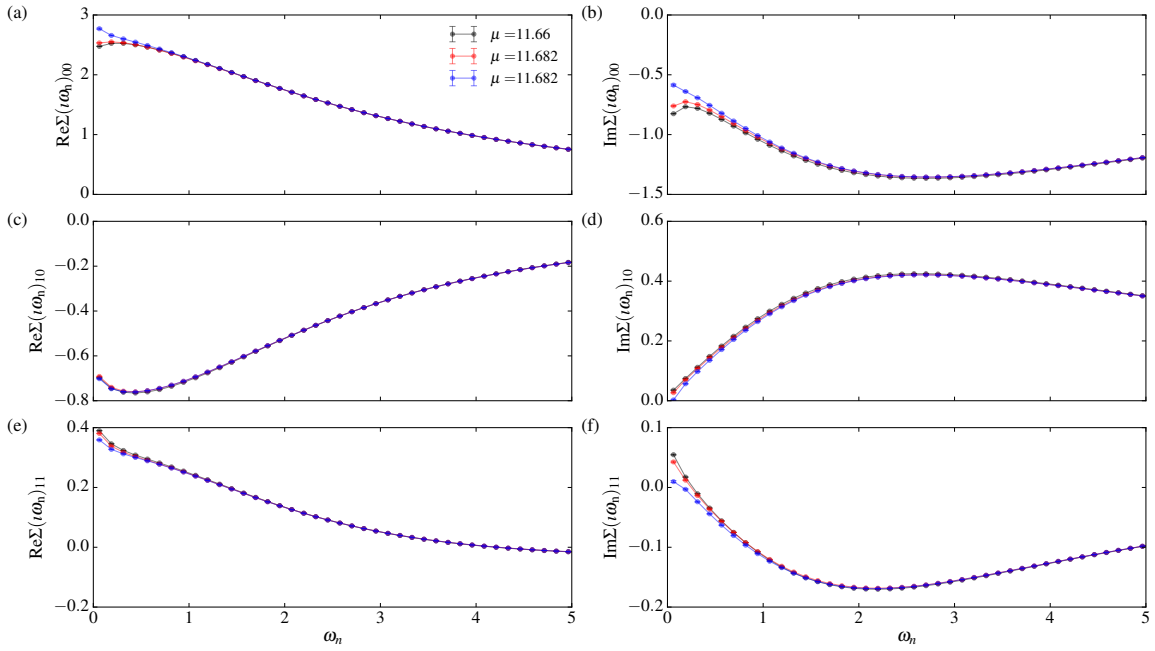

Figure A.26: All of the independent hybridisation functions in the real base, as a function of the Matsubara frequencies at $U_d = 12.0$, $\beta = 50$ for three metallic solutions: one at $\mu = 11.66$, in black; and two coexisting solutions at $\mu = 11.682$, a correlated metal and a pseudogap; the blue and red curves respectively.

A.5 Superconducting State of the Emery Model

In the superconducting state study, we have systematically performed from 8×10^7 to 10^8 Monte Carlo sweeps per processor; averaged over 96 processors. When necessary, for example close to phase transition boundaries, we may use up to 110 processors for each simulation. The quantities presented are the result of the average of the last $10 - 30$ iterations, but hundreds may be necessary close to phase boundaries. The total number of simulations computed and analysed with this algorithm is more than 200. We used the following procedure: First we verified the convergence of the double occupancy D, the average sign of Eq. 4.21, the average expansion order k discussed in the Section 3.5, and the superconducting order parameter ϕ of eq. 5.3 as shown respectively in Figs. A.27,A.28, A.29 and A.30 for three selected simulations.

These simulations were taken at fixed copper interaction $U_d = 12.0$, $\beta = 50$. For different values of the chemical potential μ; we can observe the convergence of the initially superconducting solution to either: a pseudogap solution as for $\mu = 11.73$, in black; or a superconducting one, as for $\mu = 11.65$ in blue; and for $\mu = 11.72$, in red.

All of the independent response functions are then calculated as the result of the averaged

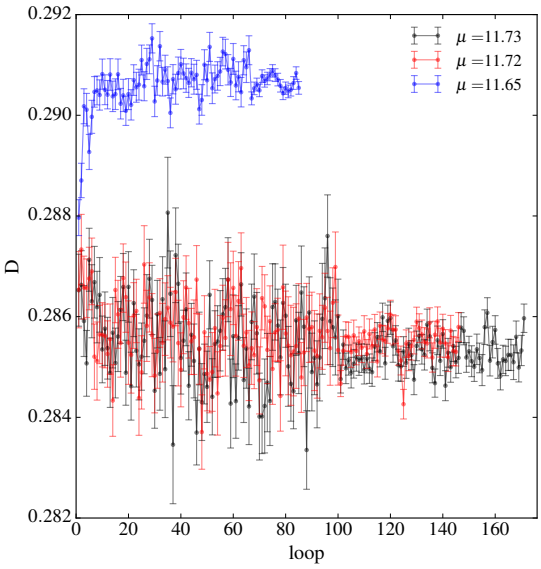

Figure A.27: The double occupancy as a function of the CDMFT iteration loops at $\beta = 50$ and $U = 12.0$ for two superconducting solutions: at $\mu = 11.73$, in red; and at $\mu = 11.65$, in blue; and for one pseudogap solution at $\mu = 11.65$, in black.

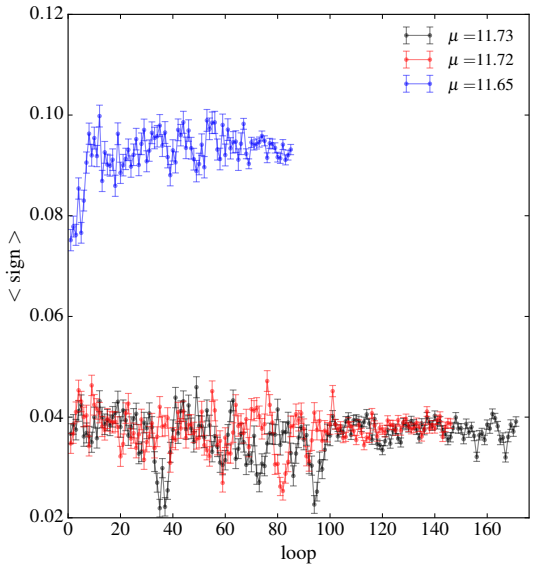

Figure A.28: The average sign as a function of the CDMFT iteration loops at $\beta = 50$ and $U = 12.0$ for two superconducting solutions at $\mu = 11.73$, in red; and at $\mu = 11.65$, in blue; and for one pseudogap solution at $\mu = 11.65$, in black.

functions, for the last 30 loops, and the error is the resulting standard deviation. In Fig. A.31, we show the Green function; in Fig. A.32, the self-energy functions; and in Fig. A.33, the hybridisation functions.

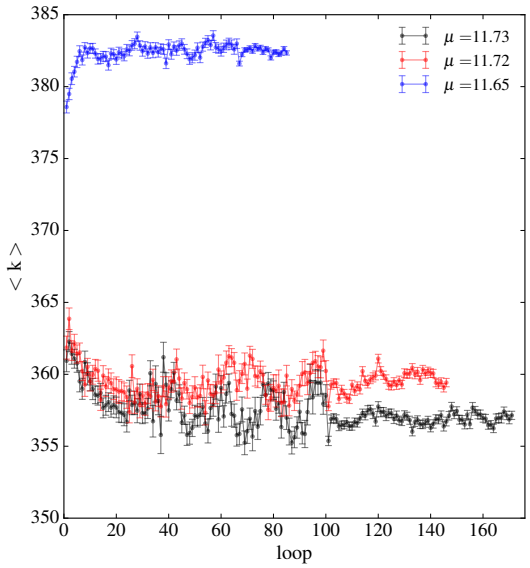

Figure A.29: The average expansion order as a function of the CDMFT iteration loops at $\beta = 50$ and $U = 12.0$ for two superconducting solutions: at $\mu = 11.73$, in red; and at $\mu = 11.65$, in blue; and for one pseudogap solution at $\mu = 11.65$, in black.

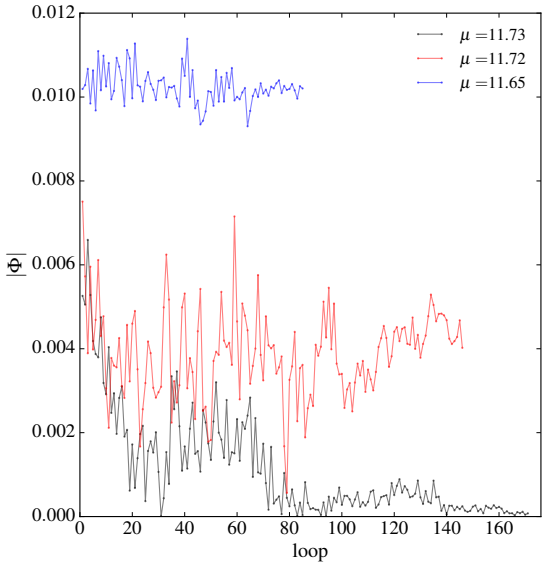

Figure A.30: The superconducting order parameter as a function of the CDMFT iteration loops at $\beta = 50$ and $U = 12.0$ for two superconducting solutions: at $\mu = 11.73$, in red; and at $\mu = 11.65$, in blue; and for one pseudogap solution at $\mu = 11.65$, in black.

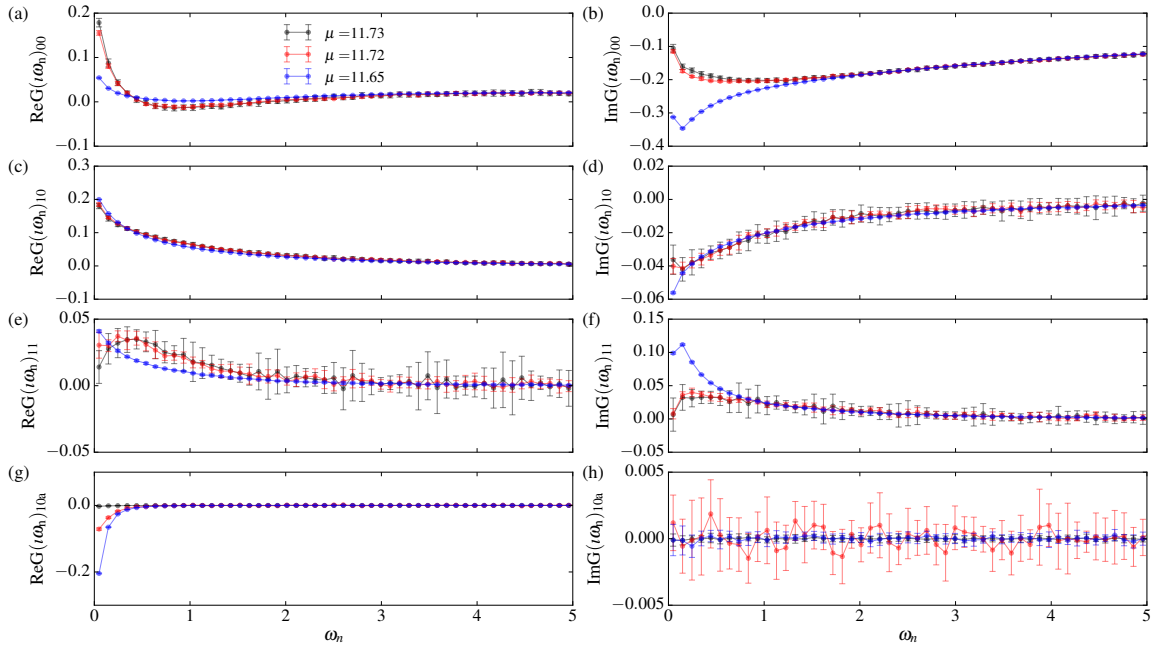

the real base

Figure A.31: Some of the independent green functions in the real base, as function of the Matsubara frequencies at $\beta = 50$ and $U = 12.0$, for two superconducting solutions: at $\mu = 11.73$, in red; and at $\mu = 11.65$, in blue; and for one pseudogap solution at $\mu = 11.65$, in black.

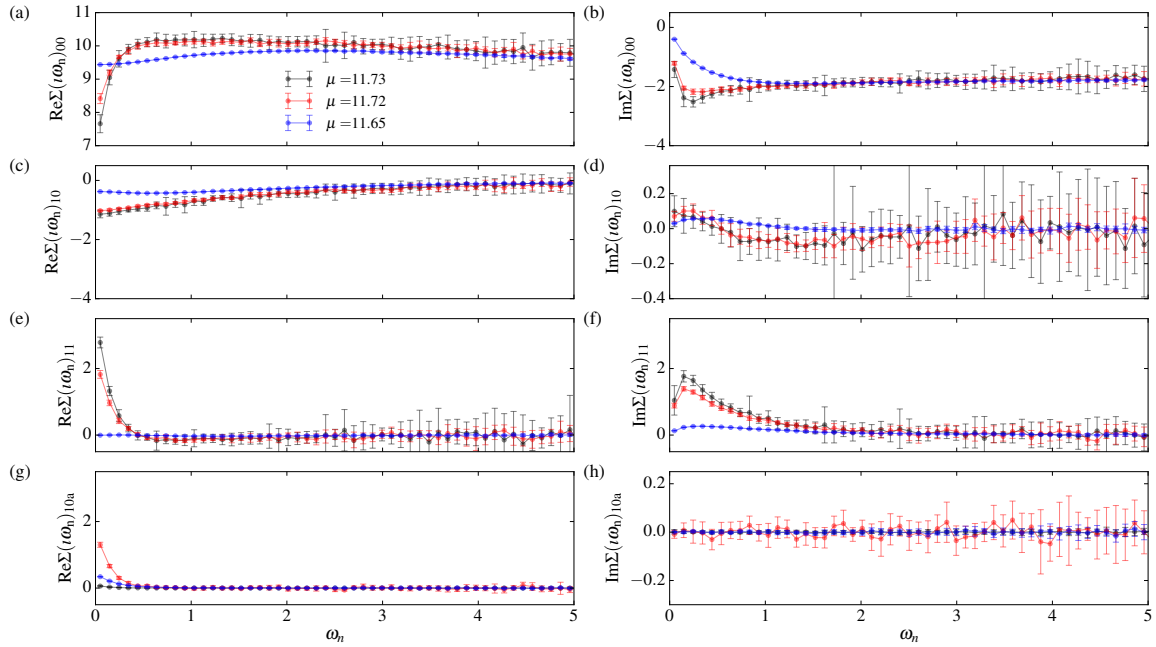

Figure A.32: Some of the independent self-energies functions in the real base, as function of the Matsubara frequencies at $\beta = 50$ and $U = 12.0$, for two superconducting solutions: at $\mu = 11.73$, in red; and at $\mu = 11.65$, in blue; and for one pseudogap solution at $\mu = 11.65$, in black.

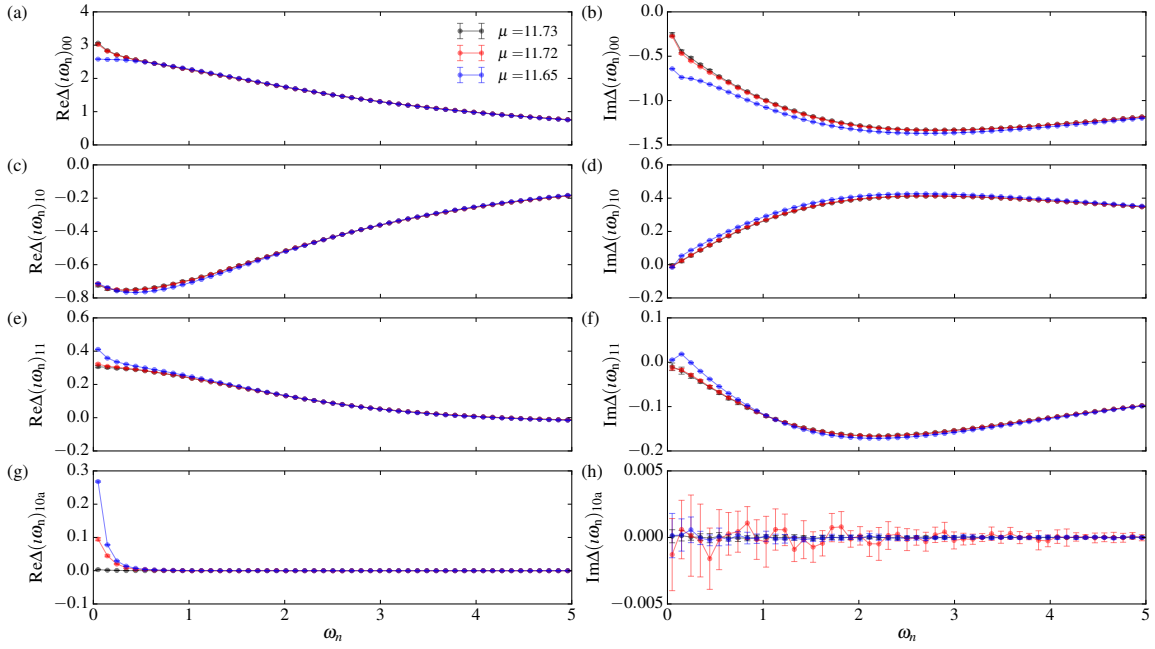

Figure A.33: Some of the independent hybridisation functions in the reciprocal space, as function of the Matsubara frequencies at $\beta = 50$ and $U = 12.0$, for two superconducting solutions: at $\mu = 11.73$, in red; and at $\mu = 11.65$, in blue; and for one pseudogap solution at $\mu = 11.65$, in black.

Bibliography

[1] J. G. Bednorz and K. A. Müller, "Possible highTc superconductivity in the Ba-La-Cu-O system," *Zeitschrift für Physik B Condensed Matter*, vol. 64, no. 2, pp. 189–193, 1986. http://dx.doi.org/10.1007/BF01303701

[2] P. W. Anderson, "The Resonating Valence Bond State in La_2CuO_4 and Superconductivity," *Science*, vol. 235, no. 4793, pp. 1196–1198, 1987. http://science.sciencemag.org/content/235/4793/1196

[3] V. J. Emery, " Theory of high-T_c superconductivity in oxides ," *Phys. Rev. Lett.*, vol. 58, pp. 2794–2797, Jun 1987. http://link.aps.org/doi/10.1103/PhysRevLett.58.2794

[4] C. Varma, S. Schmitt-Rink, and E. Abrahams, "Charge transfer excitations and superconductivity in "ionic" metals," *Solid State Communications*, vol. 62, no. 10, pp. 681 – 685, 1987. http://dx.doi.org/10.1016/0038-1098(87)90407-8

[5] N. Bickers, D. Scalapino, and R. Scalettar, "CDW and SDW mediated pairing interactions," *International Journal of Modern Physics B*, vol. 01, no. 03n04, pp. 687–695, 1987. http://www.worldscientific.com/doi/abs/10.1142/S0217979287001079

[6] F. C. Zhang and T. M. Rice, " Effective Hamiltonian for the superconducting Cu oxides ," *Phys. Rev. B*, vol. 37, pp. 3759–3761, Mar 1988. http://link.aps.org/doi/10.1103/PhysRevB.37.3759

[7] M. R. Norman, M. Randeria, B. Jankó, and J. C. Campuzano, "Condensation energy and spectral functions in high-temperature superconductors," *Phys. Rev. B*, vol. 61, pp. 14 742–14 750, Jun 2000. http://link.aps.org/doi/10.1103/PhysRevB.61.14742

[8] S. Hüfner, M. A. Hossain, A. Damascelli, and G. A. Sawatzky, "Two gaps make a high-temperature superconductor?" *Reports on Progress in Physics*, vol. 71, no. 6, p. 062501, 2008.

[9] L. Taillefer, "Scattering and Pairing in cuprate Superconductors," *Annual Review of Condensed Matter Physics*, vol. 1, no. 1, pp. 51–70, 2010.

[10] J. Zaanen, G. A. Sawatzky, and J. W. Allen, " Band gaps and electronic structure of transition-metal compounds ," *Phys. Rev. Lett.*, vol. 55, pp. 418–421, Jul 1985. http://link.aps.org/doi/10.1103/PhysRevLett.55.418

[11] M. Takigawa, P. C. Hammel, R. H. Heffner, and Z. Fisk, "Spin susceptibility in superconducting $YBa_2Cu_3O_7$ from ^{63}Cu Knight shift," *Phys. Rev. B*, vol. 39, pp. 7371–7374, Apr 1989. http://link.aps.org/doi/10.1103/PhysRevB.39.7371

[12] S. E. Barrett, D. J. Durand, C. H. Pennington, C. P. Slichter, T. A. Friedmann, J. P. Rice, and D. M. Ginsberg, "^{63}Cu Knight shifts in the superconducting state of $YBa_2Cu_3O_{7-\delta}$ (T_c=90 K)," *Phys. Rev. B*, vol. 41, pp. 6283–6296, Apr 1990. http://link.aps.org/doi/10.1103/PhysRevB.41.6283

[13] H. Ding, M. R. Norman, J. C. Campuzano, M. Randeria, A. F. Bellman, T. Yokoya, T. Takahashi, T. Mochiku, and K. Kadowaki, "Angle-resolved photoemission spectroscopy study of the superconducting gap anisotropy in $Bi_2Sr_2CaCu_2O_{8+x}$," *Phys. Rev. B*, vol. 54, pp. R9678–R9681, Oct 1996. http://link.aps.org/doi/10.1103/PhysRevB.54.R9678

[14] D. J. Van Harlingen, "Phase-sensitive tests of the symmetry of the pairing state in the high-temperature superconductors evidence for $d_{x^2-y^2}$ symmetry," *Rev. Mod. Phys.*, vol. 67, pp. 515–535, Apr 1995. https://link.aps.org/doi/10.1103/RevModPhys.67.515

[15] J. Annett, N. Goldenfeld, and S. R. Renn, "Interpretation of the temperature dependence of the electromagnetic penetration depth in $yba_2cu_3o_{7-\delta}$," *Phys. Rev. B*, vol. 43, pp. 2778–2782, Feb 1991. https://link.aps.org/doi/10.1103/PhysRevB.43.2778

[16] J. F. Annett, N. Goldenfeld, and A. J. Leggett, "Constraints on the pairing state of the cuprate superconductors," *Journal of Low Temperature Physics*, vol. 105, no. 3, pp. 473–482, 1996. https://doi.org/10.1007/BF00768431

[17] M. C. Gutzwiller, "Effect of correlation on the ferromagnetism of transition metals," *Phys. Rev. Lett.*, vol. 10, pp. 159–162, Mar 1963. http://link.aps.org/doi/10.1103/PhysRevLett.10.159

[18] J. Hubbard, "Electron correlations in narrow energy bands," in *Proceedings of the Royal Society of London A: Mathematical, Physical and Engineering Sciences*, vol. 276, no. 1365. The Royal Society, 1963, pp. 238–257. http://rspa.royalsocietypublishing.org/content/royprsa/276/1365/238.full.pdf

[19] J. Kanamori, "Electron correlation and ferromagnetism of transition metals," *Progress of Theoretical Physics*, vol. 30, no. 3, pp. 275–289, 1963. https://academic.oup.com/ptp/article/30/3/275/1865799/Electron-Correlation-and-Ferromagnetism-of

[20] A. Isidori, "Superconductivity in Strongly Correlated Electron Systems: Analytical Approaches Beyond Dynamical Mean Field Theory," Ph.D. thesis, Sapienza Universitá di Roma, Italy, 2008. http://padis.uniroma1.it/bitstream/10805/919/1/isidori_thesis.pdf

[21] A. Georges, G. Kotliar, W. Krauth, and M. J. Rozenberg, "Dynamical mean-field theory of strongly correlated fermion systems and the limit of infinite dimensions," *Rev. Mod. Phys.*, vol. 68, pp. 13–125, Jan 1996. http://link.aps.org/doi/10.1103/RevModPhys.68.13

[22] G. Kotliar, S. Y. Savrasov, G. Pálsson, and G. Biroli, "Cellular Dynamical Mean Field Approach to Strongly Correlated Systems," *Phys. Rev. Lett.*, vol. 87, p. 186401, Oct 2001. http://link.aps.org/doi/10.1103/PhysRevLett.87.186401

[23] O. Cyr-Choiniére, R. Daou, F. Laliberté, C. Collignon, S. Badoux, D. LeBoeuf, J. Chang, B. J. Ramshaw, D. A. Bonn, W. N. Hardy, R. Liang, J.-Q. Yan, J.-G. Cheng, J.-S. Zhou, J. B. Goodenough, S. Pyon, T. Takayama, H. Takagi, N. Doiron-Leyraud, and L. Taillefer, "Pseudogap temperature T* of cuprate superconductors from the Nernst effect," *arXiv preprint arXiv:1703.06927*, 2017. https://arxiv.org/abs/1703.06927

[24] G. Kotliar, S. Y. Savrasov, K. Haule, V. S. Oudovenko, O. Parcollet, and C. A. Marianetti, "Electronic structure calculations with dynamical mean-field theory," *Rev. Mod. Phys.*, vol. 78, no. 3, p. 865, 2006. http://link.aps.org/doi/10.1103/RevModPhys.78.865

[25] T. Maier, M. Jarrell, T. Pruschke, and M. H. Hettler, "Quantum cluster theories," *Rev. Mod. Phys.*, vol. 77, pp. 1027–1080, Oct 2005. http://link.aps.org/doi/10.1103/RevModPhys.77.1027

[26] E. Gull, A. J. Millis, A. I. Lichtenstein, A. N. Rubtsov, M. Troyer, and P. Werner, "Continuous-time Monte Carlo methods for quantum impurity models," *Rev. Mod. Phys.*, vol. 83, pp. 349–404, May 2011. http://link.aps.org/doi/10.1103/RevModPhys.83.349

[27] P. Sémon, C.-H. Yee, K. Haule, and A.-M. S. Tremblay, "Lazy skip-lists: An algorithm for fast hybridization-expansion quantum Monte Carlo," *Phys. Rev. B*, vol. 90, p. 075149, Aug 2014. http://link.aps.org/doi/10.1103/PhysRevB.90.075149

[28] L. Fratino, P. Sémon, M. Charlebois, G. Sordi, and A.-M. S. Tremblay, "Signatures of the Mott transition in the antiferromagnetic state of the two-dimensional Hubbard model," *Phys. Rev. B*, vol. 95, p. 235109, Jun 2017. https://link.aps.org/doi/10.1103/PhysRevB.95.235109

[29] G. Sordi, K. Haule, and A.-M. S. Tremblay, "Finite Doping Signatures of the Mott Transition in the Two-Dimensional Hubbard Model," *Phys. Rev. Lett.*, vol. 104, no. 22, p. 226402, Jun 2010. http://link.aps.org/doi/10.1103/PhysRevLett.104.226402

[30] G. Sordi, K. Haule, and A.-M. S. Tremblay, "Mott physics and first-order transition between two metals in the normal-state phase diagram of the two-dimensional Hubbard model," *Phys. Rev. B*, vol. 84, p. 075161, Aug 2011. http://link.aps.org/doi/10.1103/PhysRevB.84.075161

[31] G. Sordi, P. Sémon, K. Haule, and A.-M. S. Tremblay, "Pseudogap temperature as a Widom line in doped Mott insulators," *Sci. Rep.*, vol. 2, 2012. http://www.nature.com/articles/srep00547

[32] G. Sordi, P. Sémon, K. Haule, and A.-M. S. Tremblay, "C-axis resistivity, pseudogap, superconductivity, and Widom line in doped Mott insulators," *Phys. Rev. B*, vol. 87, p. 041101, Jan 2013. http://link.aps.org/doi/10.1103/PhysRevB.87.041101

[33] L. Xu, P. Kumar, S. V. Buldyrev, S.-H. Chen, P. H. Poole, F. Sciortino, and H. E. Stanley, "Relation between the Widom line and the dynamic crossover in systems with a liquid liquid phase transition," *Proc. Natl. Acad. Sci. USA*, vol. 102, no. 46, pp. 16 558–16 562, 2005. http://www.pnas.org/content/102/46/16558.short

[34] G. G. Simeoni, T. Bryk, F. A. Gorelli, M. Krisch, G. Ruocco, M. Santoro, and T. Scopigno, "The Widom line as the crossover between liquid-like and gas-like behaviour in supercritical fluids," *Nature Physics*, vol. 6, no. 7, pp. 503–507, Jul. 2010. http://dx.doi.org/10.1038/nphys1683

[35] T. Furukawa, K. Miyagawa, H. Taniguchi, R. Kato, and K. Kanoda, "Quantum criticality of Mott transition in organic materials," *Nature Physics*, vol. 11, pp. 221–224, Mar. 2015.

[36] L. Fratino, P. Sémon, G. Sordi, and A.-M. Tremblay, "An organizing principle for two-dimensional strongly correlated superconductivity," *Scientific reports*, vol. 6, 2016. http://www.nature.com/articles/srep22715

[37] L. Fratino, P. Sémon, G. Sordi, and A.-M. S. Tremblay, "Pseudogap and superconductivity in two-dimensional doped charge-transfer insulators," *Phys. Rev. B*, vol. 93, p. 245147, Jun 2016. http://link.aps.org/doi/10.1103/PhysRevB.93.245147

[38] H. Kamerlingh Onnes, "Commun. phys. lab," *Univ. Leiden*, vol. 1226, 1911.

[39] W. Meissner and R. Ochsenfeld, "Ein neuer effekt bei eintritt der supraleitfähigkeit," *Naturwissenschaften*, vol. 21, no. 44, pp. 787–788, 1933.

[40] P. J. Ray, "Structural investigation of $La_{(2-x)}Sr_xCuO_{(4+y)}$ - Following staging as a function of temperature," *Master's thesis*, 2016. https://figshare.com/articles/Structural_investigation_of_La_2_x_Sr_x_CuO_4_y_Following_staging_as_a_function_of_temperature/2075680

[41] F. London and H. London, "The electromagnetic equations of the supraconductor," in *Proceedings of the Royal Society of London A: Mathematical, Physical and Engineering Sciences*, vol. 149. The Royal Society, 1935, pp. 71–88.

[42] V. Ginzburg, "On the theory of superconductivity," *Zh. eksper. teor. Fiz.*, vol. 20, pp. 1064–1082, 1950.

[43] J. Bardeen, L. N. Cooper, and J. R. Schrieffer, "Theory of superconductivity," *Phys. Rev.*, vol. 108, pp. 1175–1204, Dec 1957. http://link.aps.org/doi/10.1103/PhysRev.108.1175

[44] B. Hyde, J. Thompson, R. Withers, J. Fitzgerald, A. Stewart, D. Bevan, J. S. Anderson, J. Bitmead, and M. Paterson, "The room-temperature structure of the 90-k superconducting phase $YBa_2Cu_3O_{7-\delta}$," *Nature*, vol. 327, no. 6121, pp. 402–403, 1987. http://www.nature.com/nature/journal/v327/n6121/full/327402a0.html

[45] A. Schilling, M. Cantoni, J. Guo, and H. Ott, "Superconductivity above 130 K in the HgBaCaCuO system," *Nature*, vol. 363, no. 6424, pp. 56–58, 1993. http://www.nature.com/nature/journal/v363/n6424/abs/363056a0.html

[46] P. Dai, B. Chakoumakos, G. Sun, K. Wong, Y. Xin, and D. Lu, "Synthesis and neutron powder diffraction study of the superconductor $HgBa_2Ca_2Cu_3O_{8-\delta}$ by tl substitution," *Physica C: Superconductivity*, vol. 243, pp. 201 – 206, 1995. http://www.sciencedirect.com/science/article/pii/0921453494024618

[47] http://www.toulouse.lncmi.cnrs.fr/spip.php?rubrique149&lang=en

[48] L. N. Cooper, "Bound electron pairs in a degenerate fermi gas," *Phys. Rev.*, vol. 104, pp. 1189–1190, Nov 1956. http://link.aps.org/doi/10.1103/PhysRev.104.1189

[49] M. R. Norman, "The challenge of unconventional superconductivity," *Science*, vol. 332, no. 6026, pp. 196–200, 2011. http://science.sciencemag.org/content/332/6026/196

[50] http://www.2physics.com/2013/08/visualizing-nodal-heavy-Fermion.html

[51] http://mrc.iisc.ernet.in/Research_Areas/01_Perovskite.htm

[52] K. Yvon and M. François, "Crystal structures of high-T_c oxides," *Zeitschrift für Physik B Condensed Matter*, vol. 76, no. 4, pp. 413–444, 1989. http://dx.doi.org/10.1007/BF01307892

[53] N. Barišić, M. K. Chan, Y. Li, G. Yu, X. Zhao, M. Dressel, A. Smontara, and M. Greven, "Universal sheet resistance and revised phase diagram of the cuprate high-temperature superconductors," *Proceedings of the National Academy of Sciences*, vol. 110, no. 30, pp. 12 235–12 240, 2013. http://www.pnas.org/content/110/30/12235

[54] X.-B. Chen, N. T. M. Hien, D. Lee, S.-Y. Jang, T. W. Noh, and I.-S. Yang, "Resonant A_1 phonon and four-magnon Raman scattering in hexagonal $HoMnO_3$ thin film," *New Journal of Physics*, vol. 12, no. 7, p. 073046, 2010. http://stacks.iop.org/1367-2630/12/i=7/a=073046

[55] D. Vaknin, S. K. Sinha, D. E. Moncton, D. C. Johnston, J. M. Newsam, C. R. Safinya, and H. E. King, "Antiferromagnetism in La_2CuO_{4-y}," *Phys. Rev. Lett.*, vol. 58, pp. 2802–2805, Jun 1987. http://link.aps.org/doi/10.1103/PhysRevLett.58.2802

[56] S. Chakravarty, B. I. Halperin, and D. R. Nelson, "Low-temperature behavior of two-dimensional quantum antiferromagnets," *Phys. Rev. Lett.*, vol. 60, pp. 1057–1060, Mar 1988. http://link.aps.org/doi/10.1103/PhysRevLett.60.1057

[57] M. A. Rahman, M. Z. Rahaman, and M. N. Samsuddoha, "A review on cuprate based superconducting materials including characteristics and applications," *American Journal of Physics and Applications.*, vol. 3, pp. 39–56, 2015. http://www.sciencepublishinggroup.com/journal/paperinfo.aspx?journalid=622&doi=10.11648/j.ajpa.20150302.15

[58] A. Fujimori, E. Takayama-Muromachi, Y. Uchida, and B. Okai, "Spectroscopic evidence for strongly correlated electronic states in La-Sr-Cu and Y-Ba-Cu oxides," *Phys. Rev. B*, vol. 35, pp. 8814–8817, Jun 1987. https://link.aps.org/doi/10.1103/PhysRevB.35.8814

[59] N. Nücker, J. Fink, B. Renker, D. Ewert, C. Politis, P. J. W. Weijs, and J. C. Fuggle, "Experimental electronic structure studies of $La_{2-x}Sr_xCuO_4$," *Zeitschrift für Physik B Condensed Matter*, vol. 67, no. 1, Mar 1987. https://doi.org/10.1007/BF01307300

[60] N. Gauquelin, D. Hawthorn, G. Sawatzky, R. Liang, D. Bonn, W. Hardy, and G. Botton, "Atomic scale real-space mapping of holes in $YBa_2Cu_3O_{6+\delta}$," *Nature Communications*, vol. 5, Jul. 2014. http://dx.doi.org/10.1038/ncomms5275

[61] N. P. Armitage, P. Fournier, and R. L. Greene, "Progress and perspectives on electron-doped cuprates," *Rev. Mod. Phys.*, vol. 82, pp. 2421–2487, Sep 2010. http://link.aps.org/doi/10.1103/RevModPhys.82.2421

[62] F. Kidwingira, J. D. Strand, D. J. Van Harlingen, and Y. Maeno, "Dynamical superconducting order parameter domains in Sr_2RuO_4," *Science*, vol. 314, no. 5803, pp. 1267–1271, 2006. http://science.sciencemag.org/content/314/5803/1267

[63] C. C. Tsuei and J. R. Kirtley, "Pairing symmetry in cuprate superconductors," *Rev. Mod. Phys.*, vol. 72, pp. 969–1016, Oct 2000. http://link.aps.org/doi/10.1103/RevModPhys.72.969

[64] K. M. Shen and J. Seamus Davis, "Cuprate high-T_c superconductors," *Materials Today*, vol. 11, no. 9, pp. 14 – 21, 2008. http://www.sciencedirect.com/science/article/pii/S1369702108701755

[65] S. E. Barrett, J. A. Martindale, D. J. Durand, C. H. Pennington, C. P. Slichter, T. A. Friedmann, J. P. Rice, and D. M. Ginsberg, "Anomalous behavior of nuclear spin-lattice relaxation rates in $YBa_2Cu_3O_7$ below T_c," *Phys. Rev. Lett.*, vol. 66, pp. 108–111, Jan 1991. https://link.aps.org/doi/10.1103/PhysRevLett.66.108

[66] L. Taillefer, B. Lussier, R. Gagnon, K. Behnia, and H. Aubin, "Universal Heat Conduction in $YBa_2Cu_3O_{6.9}$," *Phys. Rev. Lett.*, vol. 79, pp. 483–486, Jul 1997. http://link.aps.org/doi/10.1103/PhysRevLett.79.483

[67] W. N. Hardy, D. A. Bonn, D. C. Morgan, R. Liang, and K. Zhang, "Precision measurements of the temperature dependence of λ in $YBa_2Cu_3O_{6.95}$: Strong evidence for nodes in the gap function," *Phys. Rev. Lett.*, vol. 70, pp. 3999–4002, Jun 1993. http://link.aps.org/doi/10.1103/PhysRevLett.70.3999

[68] D. A. Wollman, D. J. Van Harlingen, W. C. Lee, D. M. Ginsberg, and A. J. Leggett, "Experimental determination of the superconducting pairing state in YBCO from the

phase coherence of YBCO-Pb dc SQUIDs," *Phys. Rev. Lett.*, vol. 71, pp. 2134–2137, Sep 1993. http://link.aps.org/doi/10.1103/PhysRevLett.71.2134

[69] D. A. Wollman, D. J. Van Harlingen, J. Giapintzakis, and D. M. Ginsberg, "Evidence for $d_{x^2-y^2}$ pairing from the magnetic field modulation of $YBa_2Cu_3O_7$-Pb josephson junctions," *Phys. Rev. Lett.*, vol. 74, pp. 797–800, Jan 1995. http://link.aps.org/doi/10.1103/PhysRevLett.74.797

[70] C. C. Tsuei, J. R. Kirtley, C. C. Chi, L. S. Yu-Jahnes, A. Gupta, T. Shaw, J. Z. Sun, and M. B. Ketchen, "Pairing Symmetry and Flux Quantization in a Tricrystal Superconducting Ring of $YBa_2Cu_3O_{7-\delta}$," *Phys. Rev. Lett.*, vol. 73, pp. 593–596, Jul 1994. http://link.aps.org/doi/10.1103/PhysRevLett.73.593

[71] J. Tersoff and D. R. Hamann, "Theory of the scanning tunneling microscope," *Phys. Rev. B*, vol. 31, pp. 805–813, Jan 1985. https://link.aps.org/doi/10.1103/PhysRevB.31.805

[72] N.-C. Yeh, C.-T. Chen, G. Hammerl, J. Mannhart, A. Schmehl, C. W. Schneider, R. R. Schulz, S. Tajima, K. Yoshida, D. Garrigus, and M. Strasik, "Evidence of doping-dependent pairing symmetry in cuprate superconductors," *Phys. Rev. Lett.*, vol. 87, p. 087003, Aug 2001. http://link.aps.org/doi/10.1103/PhysRevLett.87.087003

[73] D. H. Lu, D. L. Feng, N. P. Armitage, K. M. Shen, A. Damascelli, C. Kim, F. Ronning, Z.-X. Shen, D. A. Bonn, R. Liang, W. N. Hardy, A. I. Rykov, and S. Tajima, "Superconducting gap and strong in-plane anisotropy in untwinned $YBa_2Cu_3O_{7-\delta}$," *Phys. Rev. Lett.*, vol. 86, pp. 4370–4373, May 2001. http://link.aps.org/doi/10.1103/PhysRevLett.86.4370

[74] T. Masui, M. Limonov, H. Uchiyama, S. Lee, S. Tajima, and A. Yamanaka, "Raman study of carrier-overdoping effects on the gap in high-T_c superconducting cuprates," *Phys. Rev. B*, vol. 68, p. 060506, Aug 2003. http://link.aps.org/doi/10.1103/PhysRevB.68.060506

[75] L. V. Gasparov, P. Lemmens, N. N. Kolesnikov, and G. Güntherodt, "Electronic Raman scattering in $Tl_2Ba_2CuO_{6+\delta}$: Symmetry of the order parameter, oxygen doping

effects, and normal-state scattering," *Phys. Rev. B*, vol. 58, pp. 11 753–11 760, Nov 1998. http://link.aps.org/doi/10.1103/PhysRevB.58.11753

[76] M. B. Walker and J. Luettmer-Strathmann, "Josephson tunneling in high-T_c superconductors," *Phys. Rev. B*, vol. 54, pp. 588–601, Jul 1996. https://link.aps.org/doi/10.1103/PhysRevB.54.588

[77] A. G. Sun, D. A. Gajewski, M. B. Maple, and R. C. Dynes, "Observation of Josephson pair tunneling between a high-T_c cuprate ($YBa_2Cu_3O_{7-\delta}$) and a conventional superconductor (Pb)," *Phys. Rev. Lett.*, vol. 72, pp. 2267–2270, Apr 1994. https://link.aps.org/doi/10.1103/PhysRevLett.72.2267

[78] C. Tsuei, J. Kirtley, Z. Ren, J. Wang, H. Raffy, and Z. Li, "Pure $d_{x^2-y^2}$ order-parameter symmetry in the tetragonal superconductor $TI_2Ba_2CuO_{6+\mathrm{delta}}$," *Nature*, vol. 387, no. 6632, p. 481, 1997. http://www.nature.com/nature/journal/v387/n6632/abs/387481a0.html

[79] O. Cyr-Choinière, G. Grissonnanche, S. Badoux, J. Day, D. A. Bonn, W. N. Hardy, R. Liang, N. Doiron-Leyraud, and L. Taillefer, "Two types of nematicity in the phase diagram of the cuprate superconductor $YBa_2Cu_3O_y$," *Phys. Rev. B*, vol. 92, p. 224502, Dec 2015. http://link.aps.org/doi/10.1103/PhysRevB.92.224502

[80] G. Deutscher, A. F. Santander-Syro, and N. Bontemps, "Kinetic energy change with doping upon superfluid condensation in high-temperature superconductors," *Phys. Rev. B*, vol. 72, p. 092504, Sep 2005. http://link.aps.org/doi/10.1103/PhysRevB.72.092504

[81] A. F. Santander-Syro, R. P. S. M. Lobo, N. Bontemps, W. Lopera, D. Giratá, Z. Konstantinovic, Z. Z. Li, and H. Raffy, "In-plane electrodynamics of the superconductivity in $Bi_2Sr_2CaCu_2O_{8+\delta}$: Energy scales and spectral weight distribution," *Phys. Rev. B*, vol. 70, p. 134504, Oct 2004. https://link.aps.org/doi/10.1103/PhysRevB.70.134504

[82] H. J. A. Molegraaf, C. Presura, D. van der Marel, P. H. Kes, and M. Li, " Superconductivity-Induced Transfer of In-Plane Spectral Weight in $Bi_2Sr_2CaCu_2O_{8+\delta}$

," *Science*, vol. 295, no. 5563, pp. 2239–2241, 2002. http://www.sciencemag.org/content/295/5563/2239.abstract

[83] M. R. Norman and C. Pépin, "The electronic nature of high temperature cuprate superconductors," *Reports on Progress in Physics*, vol. 66, no. 10, p. 1547, 2003.

[84] K.-H. Bennemann and J. B. Ketterson, *The Physics of Superconductors: Vol II: Superconductivity in Nanostructures, High-T_c and Novel Superconductors, Organic Superconductors*. Springer Science & Business Media, 2011, vol. 2.

[85] F. Carbone, A. B. Kuzmenko, H. J. A. Molegraaf, E. van Heumen, V. Lukovac, F. Marsiglio, D. van der Marel, K. Haule, G. Kotliar, H. Berger, S. Courjault, P. H. Kes, and M. Li, "Doping dependence of the redistribution of optical spectral weight in $Bi_2Sr_2CaCu_2O_{8+\delta}$," *Phys. Rev. B*, vol. 74, p. 064510, Aug 2006. http://link.aps.org/doi/10.1103/PhysRevB.74.064510

[86] J. E. Hirsch, "The true colors of cuprates," *Science*, vol. 295, no. 5563, pp. 2226–2227, 2002. http://www.sciencemag.org/content/295/5563/2226

[87] C. Giannetti, F. Cilento, S. D. Conte, G. Coslovich, G. Ferrini, H. Molegraaf, M. Raichle, R. Liang, H. Eisaki, M. Greven, A. Damascelli, D. van der Marel, and F. Parmigiani, "Revealing the high-energy electronic excitations underlying the onset of high-temperature superconductivity in cuprates," *Nature Communications*, vol. 2, p. 353, Jun. 2011. http://www.nature.com/articles/ncomms1354

[88] D. C. Johnston, J. P. Stokes, D. P. Goshorn, and J. T. Lewandowski, "Influence of oxygen defects on the physical properties of La_2CuO_{4-y}," *Phys. Rev. B*, vol. 36, pp. 4007–4010, Sep 1987. http://link.aps.org/doi/10.1103/PhysRevB.36.4007

[89] D. Johnston, S. Sinha, A. Jacobson, and J. Newsam, "Superconductivity and magnetism in the high tc copper oxides," *Physica C: Superconductivity*, vol. 153, pp. 572–577, 1988. http://www.sciencedirect.com/science/article/pii/0921453488907204

[90] T. Freltoft, J. P. Remeika, D. E. Moncton, A. S. Cooper, J. E. Fischer, D. Harshman, G. Shirane, S. K. Sinha, and D. Vaknin, "Antiferromagnetism and oxygen deficiency

in single-crystal $La_2CuO_{4-\delta}$," *Phys. Rev. B*, vol. 36, pp. 826–828, Jul 1987. http://link.aps.org/doi/10.1103/PhysRevB.36.826

[91] S. Mitsuda, G. Shirane, S. K. Sinha, D. C. Johnston, M. S. Alvarez, D. Vaknin, and D. E. Moncton, "Confirmation of antiferromagnetism in La_2CuO_{4-y} with polarized neutrons," *Phys. Rev. B*, vol. 36, pp. 822–825, Jul 1987. http://link.aps.org/doi/10.1103/PhysRevB.36.822

[92] B. Keimer, A. Aharony, A. Auerbach, R. J. Birgeneau, A. Cassanho, Y. Endoh, R. W. Erwin, M. A. Kastner, and G. Shirane, "Néel transition and sublattice magnetization of pure and doped la_2cuo_4," *Phys. Rev. B*, vol. 45, pp. 7430–7435, Apr 1992. https://link.aps.org/doi/10.1103/PhysRevB.45.7430

[93] K. Ishida, K. Yoshida, T. Mito, Y. Tokunaga, Y. Kitaoka, K. Asayama, Y. Nakayama, J. Shimoyama, and K. Kishio, "Pseudogap behavior in single-crystal $Bi_2Sr_2CaCu_2O_{8+\delta}$ probed by Cu NMR," *Phys. Rev. B*, vol. 58, pp. R5960–R5963, Sep 1998. http://link.aps.org/doi/10.1103/PhysRevB.58.R5960

[94] W. W. Warren, R. E. Walstedt, G. F. Brennert, R. J. Cava, R. Tycko, R. F. Bell, and G. Dabbagh, "Cu spin dynamics and superconducting precursor effects in planes above T_c in $YBa_2Cu_3O_{6.7}$," *Phys. Rev. Lett.*, vol. 62, pp. 1193–1196, Mar 1989. http://link.aps.org/doi/10.1103/PhysRevLett.62.1193

[95] H. Alloul, T. Ohno, and P. Mendels, "^{89}Y NMR evidence for a fermi-liquid behavior in $YBa_2Cu_3O_{6+x}$," *Phys. Rev. Lett.*, vol. 63, pp. 1700–1703, Oct 1989. http://link.aps.org/doi/10.1103/PhysRevLett.63.1700

[96] S. Maekawa, T. Tohyama, S. E. Barnes, S. Ishihara, W. Koshibae, and G. Khaliullin, *Physics of transition metal oxides*. Springer Science & Business Media, 2013, vol. 144.

[97] J. W. Loram, K. A. Mirza, J. R. Cooper, and W. Y. Liang, "Electronic specific heat of $YBa_2Cu_3O_{6+x}$ from 1.8 to 300 K," *Phys. Rev. Lett.*, vol. 71, pp. 1740–1743, Sep 1993. http://link.aps.org/doi/10.1103/PhysRevLett.71.1740

[98] C. C. Homes, T. Timusk, R. Liang, D. A. Bonn, and W. N. Hardy, "Optical conductivity of c axis oriented $YBa_2Cu_3O_{6.70}$: Evidence for a pseudogap," *Phys. Rev. Lett.*, vol. 71, pp. 1645–1648, Sep 1993. http://link.aps.org/doi/10.1103/PhysRevLett.71.1645

[99] A. Loeser, Z. Shen, D. Dessau, D. Marshall *et al.*, "Excitation gap in the normal state of underdoped $Bi_2Sr_2CaCu_2O_{8+\delta}$," *Science*, vol. 273, no. 5273, p. 325, 1996. http://search.proquest.com/openview/38f121a657628239b54811c0fa541eaa/1?pq-origsite=gscholar&cbl=1256

[100] H. Ding, T. Yokoya, J. Campuzano, T. Takahashi *et al.*, "Spectroscopic evidence for a pseudogap in the normal state of underdoped high-T_c superconductors," *Nature*, vol. 382, no. 6586, p. 51, 1996. http://www.nature.com/nature/journal/v382/n6586/abs/382051a0.html

[101] C. Renner, B. Revaz, J.-Y. Genoud, K. Kadowaki, and O. Fischer, "Pseudogap Precursor of the Superconducting Gap in Under- and Overdoped $Bi_2Sr_2CaCu_2O_{8+\delta}$," *Phys. Rev. Lett.*, vol. 80, pp. 149–152, Jan 1998. http://link.aps.org/doi/10.1103/PhysRevLett.80.149

[102] E. Razzoli, Y. Sassa, G. Drachuck, M. Månsson, A. Keren, M. Shay, M. H. Berntsen, O. Tjernberg, M. Radovic, J. Chang *et al.*, "The fermi surface and band folding in $La_{2-x}Sr_xCuO_4$, probed by angle-resolved photoemission," *New Journal of Physics*, vol. 12, no. 12, p. 125003, 2010. http://iopscience.iop.org/article/10.1088/1367-2630/12/12/125003

[103] B. Keimer, S. A. Kivelson, M. R. Norman, S. Uchida, and J. Zaanen, "From quantum matter to high-temperature superconductivity in copper oxides," *Nature*, vol. 518, no. 204, pp. 179–186, 2015. http://dx.doi.org/10.1038/nature14165

[104] M. Norman, H. Ding, M. Randeria, J. Campuzano, T. Yokoya, T. Takeuchi, T. Takahashi, T. Mochiku, K. Kadowaki, P. Guptasarma *et al.*, "Destruction of the fermi surface in underdoped high-tc superconductors," *Nature*, vol. 392, no. 6672, pp. 157–160, 1998. http://www.nature.com/nature/journal/v392/n6672/full/392157a0.html

[105] Y. Nakamura and S. Uchida, "Anisotropic transport properties of single-crystal $La_{2-x}Sr_xCuO_4$: Evidence for the dimensional crossover," *Phys. Rev. B*, vol. 47, pp. 8369–8372, Apr 1993. https://link.aps.org/doi/10.1103/PhysRevB.47.8369

[106] R. Daou, N. Doiron-Leyraud, D. LeBoeuf, S. Li, F. Laliberté, O. Cyr-Choiniere, Y. Jo, L. Balicas, J.-Q. Yan, J.-S. Zhou *et al.*, "Linear temperature dependence of resistivity and change in the Fermi surface at the pseudogap critical point of a high-Tc superconductor," *Nature Physics*, vol. 5, no. 1, pp. 31–34, 2009. http://www.nature.com/nphys/journal/v5/n1/abs/nphys1109.html

[107] E. Fradkin, S. A. Kivelson, M. J. Lawler, J. P. Eisenstein, and A. P. Mackenzie, "Nematic Fermi fluids in condensed matter physics," *Annu. Rev. Condens. Matter Phys.*, vol. 1, no. 1, pp. 153–178, 2010. http://annualreviews.org/doi/abs/10.1146/annurev-conmatphys-070909-103925

[108] N. Bogoliubov, "Quasi-expectation values in problems of statistical mechanics," *New York: Gordon and Breach*, 1961.

[109] N. D. Mermin and H. Wagner, "Absence of Ferromagnetism or Antiferromagnetism in One- or Two-Dimensional Isotropic Heisenberg Models," *Phys. Rev. Lett.*, vol. 17, pp. 1133–1136, Nov 1966. http://link.aps.org/doi/10.1103/PhysRevLett.17.1133

[110] P. C. Hohenberg, "Existence of Long-Range Order in One and Two Dimensions," *Phys. Rev.*, vol. 158, pp. 383–386, Jun 1967. https://link.aps.org/doi/10.1103/PhysRev.158.383

[111] H. Wagner, "Long-wavelength excitations and the Goldstone theorem in many-particle systems with "Broken symmetries"," *Zeitschrift für Physik A Hadrons and Nuclei*, vol. 195, no. 3, pp. 273–299, 1966.

[112] Y. Vilk and A.-M. Tremblay, "Non-perturbative many-body approach to the Hubbard model and single-particle pseudogap," *Journal de Physique I*, vol. 7, no. 11, pp. 1309–1368, 1997. https://jp1.journaldephysique.org/en/articles/jp1/abs/1997/11/jp1v7p1309/jp1v7p1309.html

[113] E. Fradkin, S. A. Kivelson, and J. M. Tranquada, "Colloquium: Theory of intertwined orders in high temperature superconductors," *Rev. Mod. Phys.*, vol. 87, pp. 457–482, May 2015. http://link.aps.org/doi/10.1103/RevModPhys.87.457

[114] B. Lake, H. Rønnow, N. Christensen, G. Aeppli, K. Lefmann, D. McMorrow, P. Vorderwisch, P. Smeibidl, N. Mangkorntong, T. Sasagawa *et al.*, "Antiferromagnetic order induced by an applied magnetic field in a high-temperature superconductor," *Nature*, vol. 415, no. 6869, pp. 299–302, 2002. https://www.nature.com/nature/journal/v415/n6869/full/415299a.html

[115] G. Shirane, Y. Endoh, R. J. Birgeneau, M. A. Kastner, Y. Hidaka, M. Oda, M. Suzuki, and T. Murakami, "Two-dimensional antiferromagnetic quantum spin-fluid state in La_2CuO_4," *Phys. Rev. Lett.*, vol. 59, pp. 1613–1616, Oct 1987. http://link.aps.org/doi/10.1103/PhysRevLett.59.1613

[116] R. J. Birgeneau, Y. Endoh, K. Kakurai, Y. Hidaka, T. Murakami, M. A. Kastner, T. R. Thurston, G. Shirane, and K. Yamada, "Static and dynamic spin fluctuations in superconducting $La_{2-x}Sr_xCuO_4$," *Phys. Rev. B*, vol. 39, pp. 2868–2871, Feb 1989. http://link.aps.org/doi/10.1103/PhysRevB.39.2868

[117] J. Tranquada, B. Sternlieb, J. Axe, Y. Nakamura, and S. Uchida, "Evidence for stripe correlations of spins and holes in copper oxide superconductors," *Nature*, vol. 375, no. 6532, p. 561, 1995. http://www.nature.com/nature/journal/v375/n6532/abs/375561a0.html

[118] J. Zaanen and O. Gunnarsson, "Charged magnetic domain lines and the magnetism of high-T_c oxides," *Phys. Rev. B*, vol. 40, pp. 7391–7394, Oct 1989. http://link.aps.org/doi/10.1103/PhysRevB.40.7391

[119] N. Doiron-Leyraud, C. Proust, D. LeBoeuf, J. Levallois, J.-B. Bonnemaison, R. Liang, D. Bonn, W. Hardy, and L. Taillefer, "Quantum oscillations and the Fermi surface in an underdoped high-T_c superconductor," *Nature*, vol. 447, no. 7144, pp. 565–568, 2007. http://www.nature.com/nature/journal/v447/n7144/abs/nature05872.html

[120] S. E. Sebastian, N. Harrison, F. Balakirev, M. Altarawneh, P. Goddard, R. Liang, D. Bonn, W. Hardy, and G. Lonzarich, "Normal-state nodal electronic structure in underdoped high-Tc copper oxides," *Nature*, vol. 511, no. 7507, pp. 61–64, 2014. https://www.nature.com/nature/journal/v511/n7507/full/nature13326.html

[121] Y. Kamihara, H. Hiramatsu, M. Hirano, R. Kawamura, H. Yanagi, T. Kamiya, and H. Hosono, "Iron-based layered superconductor: Laofep," *Journal of the American Chemical Society*, vol. 128, no. 31, pp. 10 012–10 013, 2006. http://pubs.acs.org/doi/abs/10.1021/ja063355c

[122] Y. Kamihara, T. Watanabe, M. Hirano, and H. Hosono, "Iron-Based Layered Superconductor La[$O_{1-x}F_x$]FeAs (x = 0.05-0.12) with T_c = 26 K," *Journal of the American Chemical Society*, vol. 130, no. 11, pp. 3296–3297, 2008. http://dx.doi.org/10.1021/ja800073m

[123] D. N. Basov and A. V. Chubukov, "Manifesto for a higher T_c," *Nature Physics*, vol. 7, p. 272–276, 2011. http://www.nature.com/nphys/journal/v7/n4/full/nphys1975.html

[124] J. Zhao, Q. Huang, C. De La Cruz, S. Li, J. Lynn, Y. Chen, M. A. Green, G. Chen, G. Li, and Li, "Structural and magnetic phase diagram of $CeFeAsO_{1-x}F_x$ and its relation to high-temperature superconductivity," *Nature Materials*, vol. 7, pp. 953–959, 2008.

[125] D. C. Johnston, "The puzzle of high temperature superconductivity in layered iron pnictides and chalcogenides," *Advances in Physics*, vol. 59, no. 6, pp. 803–1061, 2010. http://www.tandfonline.com/doi/abs/10.1080/00018732.2010.513480

[126] C. Liu, A. D. Palczewski, R. S. Dhaka, T. Kondo, R. M. Fernandes, E. D. Mun, H. Hodovanets, A. N. Thaler, J. Schmalian, S. L. Bud'ko, P. C. Canfield, and A. Kaminski, "Importance of the Fermi-surface topology to the superconducting state of the electron-doped pnictide $Ba(Fe_{1-x}Co_x)_2As_2$," *Phys. Rev. B*, vol. 84, p. 020509, Jul 2011. https://link.aps.org/doi/10.1103/PhysRevB.84.020509

[127] R. Haddon, A. Hebard *et al.*, "Conducting Films of C_60 and C_70 by Alkali-Metal Doping," *Nature*, vol. 350, no. 6316, p. 320, 1991. https://www.nature.com/nature/journal/v350/n6316/abs/350320a0.html

[128] R. M. Fleming, A. P. Ramirez, M. J. Rosseinsky, D. W. Murphy, R. C. Haddon, S. M. Zahurak, and A. V. Makhija, "Superconductivity above 30 K in alkali-metal-doped hydrocarbon," *Scientific Reports*, vol. 2, 2012. http://dx.doi.org/10.1038/srep00389

[129] O. Gunnarsson, "Superconductivity in fullerides," *Rev. Mod. Phys.*, vol. 69, pp. 575–606, Apr 1997. https://link.aps.org/doi/10.1103/RevModPhys.69.575

[130] K. Tanigaki, T. Ebbesen, S. Saito, J. Mizuki, J. Tsai, Y. Kubo, and S. Kuroshima, "Superconductivity at 33 K in $Cs_xRb_yC_{60}$," *Nature*, vol. 352, no. 6332, pp. 222–223, 1991. https://www.nature.com/nature/journal/v352/n6332/abs/352222a0.html

[131] A. Y. Ganin, Y. Takabayashi, Y. Z. Khimyak, S. Margadonna, A. Tamai, M. J. Rosseinsky, and K. Prassides, "Bulk superconductivity at 38 k in a molecular system," *Nature materials*, vol. 7, no. 5, p. 367, 2008. https://www.nature.com/nmat/journal/v7/n5/full/nmat2179.html

[132] Y. Takabayashi, A. Y. Ganin, P. Jeglič, D. Arčon, T. Takano, Y. Iwasa, Y. Ohishi, M. Takata, N. Takeshita, K. Prassides, and M. J. Rosseinsky, "The Disorder-Free Non-BCS Superconductor Cs_3C_{60} Emerges from an Antiferromagnetic Insulator Parent State," *Science*, vol. 323, no. 5921, pp. 1585–1590, 2009. http://science.sciencemag.org/content/323/5921/1585

[133] Y. Ihara, H. Alloul, P. Wzietek, D. Pontiroli, M. Mazzani, and M. Riccò, "NMR Study of the Mott Transitions to Superconductivity in the Two Cs_3C_{60} Phases," *Phys. Rev. Lett.*, vol. 104, p. 256402, Jun 2010. http://link.aps.org/doi/10.1103/PhysRevLett.104.256402

[134] H. Alloul, P. Wzietek, T. Mito, D. Pontiroli, M. Aramini, M. Riccò, J. P. Itie, and E. Elkaim, "Mott Transition in the $A15$ Phase of Cs_3C_{60}: Absence of a Pseudogap and Charge Order," *Phys. Rev. Lett.*, vol. 118, p. 237601, Jun 2017. https://link.aps.org/doi/10.1103/PhysRevLett.118.237601

[135] Y. Nomura, S. Sakai, M. Capone, and R. Arita, "Unified understanding of superconductivity and Mott transition in alkali-doped fullerides from first principles," *Science Advances*, vol. 1, no. 7, 2015. http://advances.sciencemag.org/content/1/7/e1500568

[136] P. Fazekas, *Lecture Notes on Electron Correlation and Magnetism*, ser. Series in modern condensed matter physics. World Scientific, 1999. http://books.google.co.uk/books?id=j2F1uQAACAAJ

[137] N. F. Mott, "Metal-insulator transition," *Rev. Mod. Phys.*, vol. 40, pp. 677–683, Oct 1968. https://link.aps.org/doi/10.1103/RevModPhys.40.677

[138] N. F. Mott, *Metal-insulator transitions*. London: Taylor & Francis, 1974.

[139] C.-T. Chen, "Scanning tunneling spectroscopy studies of high-temperature cuprate superconductors," Ph.D. thesis, California Institute of Technology, 2006. http://thesis.library.caltech.edu/1943/

[140] W. Metzner and D. Vollhardt, "Correlated lattice fermions in $d = \infty$ dimensions," *Phys. Rev. Lett.*, vol. 62, pp. 1066–1066, Feb 1989. http://link.aps.org/doi/10.1103/PhysRevLett.62.1066.2

[141] A. Georges and G. Kotliar, "Hubbard model in infinite dimensions," *Phys. Rev. B*, vol. 45, pp. 6479–6483, Mar 1992. http://link.aps.org/doi/10.1103/PhysRevB.45.6479

[142] P. W. Anderson, "Localized magnetic states in metals," *Phys. Rev.*, vol. 124, pp. 41–53, Oct 1961. http://link.aps.org/doi/10.1103/PhysRev.124.41

[143] H. G. Grassmann, *Die lineare Ausdehnungslehre: ein neuer Zweig der Mathematik dargestellt und druch Anwendungen auf die übrigen Zweige der Mathematik, wie auch auf die Statik, Mechanik, der Lehre vom Magnetismus und der Krystallonomie erläutert von Hermann Grassmann*. Wigand, 1844.

[144] A.-M. S. Tremblay, B. Kyung, and D. Sénéchal, "Pseudogap and high-temperature superconductivity from weak to strong coupling. Towards a quantitative theory," *Low Temp. Phys.*, vol. 32, no. 9, p. 424, 2006. http://dx.doi.org/10.1063/1.2199446

[145] P. Werner, A. Comanac, L. de' Medici, M. Troyer, and A. J. Millis, "Continuous-time solver for quantum impurity models," *Phys. Rev. Lett.*, vol. 97, p. 076405, Aug 2006. http://link.aps.org/doi/10.1103/PhysRevLett.97.076405

[146] P. Werner and A. J. Millis, "Hybridization expansion impurity solver: General formulation and application to kondo lattice and two-orbital models," *Phys. Rev. B*, vol. 74, p. 155107, Oct 2006. http://link.aps.org/doi/10.1103/PhysRevB.74.155107

[147] W. K. Hastings, "Monte Carlo sampling methods using Markov chains and their applications," *Biometrika*, vol. 57, no. 1, pp. 97–109, 1970. https://academic.oup.com/biomet/article/57/1/97/2721936/Monte-Carlo-sampling-methods-using-Markov-chains

[148] K. Haule, "Quantum Monte Carlo impurity solver for cluster dynamical mean-field theory and electronic structure calculations with adjustable cluster base," *Phys. Rev. B*, vol. 75, no. 15, p. 155113, 2007. http://link.aps.org/doi/10.1103/PhysRevB.75.155113

[149] W. Pugh, "Skip Lists: A Probabilistic Alternative to Balanced Trees," *Commun. ACM*, vol. 33, no. 6, pp. 668–676, Jun. 1990. http://doi.acm.org/10.1145/78973.78977

[150] M. Imada, A. Fujimori, and Y. Tokura, "Metal-insulator transitions," *Rev. Mod. Phys.*, vol. 70, pp. 1039–1263, Oct 1998. http://link.aps.org/doi/10.1103/RevModPhys.70.1039

[151] P. W. Anderson, "Antiferromagnetism. Theory of Superexchange Interaction," *Phys. Rev.*, vol. 79, pp. 350–356, Jul 1950. http://link.aps.org/doi/10.1103/PhysRev.79.350

[152] P. Fazekas, *Lecture Notes on Electron Correlation and Magnetism*. World Scientific, Singapore, 1999.

[153] A.-M. S. Tremblay, "Strongly correlated superconductivity," in *Emergent Phenomena in Correlated Matter Modeling and Simulation*, E. Pavarini, E. Koch, and U. Schollwöck, Eds. Jülich: Verlag des Forschungszentrum, 2013, vol. 3, ch. 10. http://juser.fz-juelich.de/record/137827/files/FZJ-2013-04137.pdf?version=1

[154] A. Georges and T. Giamarchi, "Strongly correlated bosons and fermions in optical lattices," in *Many-body Physics with Ultracold Gases*, C. Salomon, G. Shlyapnikov, and L. Cugliandolo, Eds. Les Houches: Oxford University Press, 2010, vol. 94, ch. 1.

[155] F. Werner, O. Parcollet, A. Georges, and S. R. Hassan, "Interaction-induced adiabatic cooling and antiferromagnetism of cold fermions in optical lattices," *Phys. Rev. Lett.*, vol. 95, p. 056401, Jul 2005. http://link.aps.org/doi/10.1103/PhysRevLett.95.056401

[156] C. Taranto, G. Sangiovanni, K. Held, M. Capone, A. Georges, and A. Toschi, "Signature of antiferromagnetic long-range order in the optical spectrum of strongly correlated electron systems," *Phys. Rev. B*, vol. 85, p. 085124, Feb 2012. http://link.aps.org/doi/10.1103/PhysRevB.85.085124

[157] J. E. Hirsch, "Two-dimensional Hubbard model: Numerical simulation study," *Phys. Rev. B*, vol. 31, pp. 4403–4419, Apr 1985. http://link.aps.org/doi/10.1103/PhysRevB.31.4403

[158] S. R. White, D. J. Scalapino, R. L. Sugar, E. Y. Loh, J. E. Gubernatis, and R. T. Scalettar, "Numerical study of the two-dimensional Hubbard model," *Phys. Rev. B*, vol. 40, pp. 506–516, Jul 1989. http://link.aps.org/doi/10.1103/PhysRevB.40.506

[159] A. I. Lichtenstein and M. I. Katsnelson, "Antiferromagnetism and d-wave superconductivity in cuprates: A cluster dynamical mean-field theory," *Phys. Rev. B*, vol. 62, pp. R9283–R9286, Oct 2000. http://link.aps.org/doi/10.1103/PhysRevB.62.R9283

[160] T. Paiva, R. T. Scalettar, C. Huscroft, and A. K. McMahan, "Signatures of spin and charge energy scales in the local moment and specific heat of the half-filled two-dimensional hubbard model," *Phys. Rev. B*, vol. 63, p. 125116, Mar 2001. http://link.aps.org/doi/10.1103/PhysRevB.63.125116

[161] K. Borejsza and N. Dupuis, "Antiferromagnetism and single-particle properties in the two-dimensional half-filled Hubbard model: A nonlinear sigma model approach," *Phys. Rev. B*, vol. 69, p. 085119, Feb 2004. http://link.aps.org/doi/10.1103/PhysRevB.69.085119

[162] B. Kyung, S. S. Kancharla, D. Sénéchal, A.-M. S. Tremblay, M. Civelli, and G. Kotliar, "Pseudogap induced by short-range spin correlations in a doped Mott insulator," *Phys. Rev. B*, vol. 73, p. 165114, Apr 2006. https://link.aps.org/doi/10.1103/PhysRevB.73.165114

[163] T. Paiva, R. Scalettar, M. Randeria, and N. Trivedi, "Fermions in 2D Optical Lattices: Temperature and Entropy Scales for Observing Antiferromagnetism

and Superfluidity," *Phys. Rev. Lett.*, vol. 104, p. 066406, Feb 2010. http://link.aps.org/doi/10.1103/PhysRevLett.104.066406

[164] T. Schäfer, F. Geles, D. Rost, G. Rohringer, E. Arrigoni, K. Held, N. Blümer, M. Aichhorn, and A. Toschi, "Fate of the false Mott-Hubbard transition in two dimensions," *Phys. Rev. B*, vol. 91, p. 125109, Mar 2015. http://link.aps.org/doi/10.1103/PhysRevB.91.125109

[165] L. F. Tocchio, F. Becca, and S. Sorella, "Hidden Mott transition and large-U superconductivity in the two-dimensional Hubbard model," *Phys. Rev. B*, vol. 94, p. 195126, Nov 2016. http://link.aps.org/doi/10.1103/PhysRevB.94.195126

[166] P. Sémon and A.-M. S. Tremblay, "Importance of subleading corrections for the Mott critical point," *Phys. Rev. B*, vol. 85, p. 201101, May 2012. http://link.aps.org/doi/10.1103/PhysRevB.85.201101

[167] P. Sémon, G. Sordi, and A.-M. S. Tremblay, "Ergodicity of the hybridization-expansion monte carlo algorithm for broken-symmetry states," *Phys. Rev. B*, vol. 89, p. 165113, Apr 2014. http://link.aps.org/doi/10.1103/PhysRevB.89.165113

[168] T. Ayral and O. Parcollet, "Mott physics and spin fluctuations: A unified framework," *Phys. Rev. B*, vol. 92, p. 115109, Sep 2015. http://link.aps.org/doi/10.1103/PhysRevB.92.115109

[169] T. Ayral and O. Parcollet, "Mott physics and spin fluctuations: A functional viewpoint," *Phys. Rev. B*, vol. 93, p. 235124, Jun 2016. http://link.aps.org/doi/10.1103/PhysRevB.93.235124

[170] H. Park, K. Haule, and G. Kotliar, "Cluster Dynamical Mean Field Theory of the Mott Transition," *Phys. Rev. Lett.*, vol. 101, p. 186403, Oct 2008. http://link.aps.org/doi/10.1103/PhysRevLett.101.186403

[171] J. P. F. LeBlanc, A. E. Antipov, F. Becca, I. W. Bulik, G. K.-L. Chan, C.-M. Chung, Y. Deng, M. Ferrero, T. M. Henderson, C. A. Jiménez-Hoyos, E. Kozik, X.-W. Liu, A. J. Millis, N. V. Prokof'ev, M. Qin, G. E. Scuseria, H. Shi, B. V. Svistunov, L. F. Tocchio, I. S. Tupitsyn, S. R. White, S. Zhang, B.-X. Zheng, Z. Zhu, and E. Gull,

"Solutions of the Two-Dimensional Hubbard Model: Benchmarks and Results from a Wide Range of Numerical Algorithms," *Phys. Rev. X*, vol. 5, p. 041041, Dec 2015. http://link.aps.org/doi/10.1103/PhysRevX.5.041041

[172] E. G. C. P. van Loon, F. Krien, H. Hafermann, E. A. Stepanov, A. I. Lichtenstein, and M. I. Katsnelson, "Double occupancy in dynamical mean-field theory and the dual boson approach," *Phys. Rev. B*, vol. 93, p. 155162, Apr 2016. http://link.aps.org/doi/10.1103/PhysRevB.93.155162

[173] J. Gukelberger, E. Kozik, and H. Hafermann, "Diagrammatic Monte Carlo approach for diagrammatic extensions of dynamical mean-field theory – convergence analysis of the dual fermion technique," *ArXiv e-prints*, Nov. 2016. http://adsabs.harvard.edu/abs/2016arXiv161107523G

[174] G. Biroli and G. Kotliar, "Reply to "comment on 'cluster methods for strongly correlated electron systems'," *Phys. Rev. B*, vol. 71, p. 037102, Jan 2005. http://link.aps.org/doi/10.1103/PhysRevB.71.037102

[175] A. Georges and W. Krauth, "Physical properties of the half-filled Hubbard model in infinite dimensions," *Phys. Rev. B*, vol. 48, pp. 7167–7182, Sep 1993. http://link.aps.org/doi/10.1103/PhysRevB.48.7167

[176] B. Kyung, A. Georges, and A.-M. S. Tremblay, "Potential-energy-driven (bcs) to kinetic-energy-driven (bec) pairing in the two-dimensional attractive hubbard model: Cellular dynamical mean-field theory," *Phys. Rev. B*, vol. 74, p. 024501, Jul 2006. http://link.aps.org/doi/10.1103/PhysRevB.74.024501

[177] A. Garg, H. R. Krishnamurthy, and M. Randeria, "BCS-BEC crossover at $T = 0$: A dynamical mean-field theory approach," *Phys. Rev. B*, vol. 72, p. 024517, Jul 2005. http://link.aps.org/doi/10.1103/PhysRevB.72.024517

[178] A. Toschi, M. Capone, and C. Castellani, "Energetic balance of the superconducting transition across the BCS-Bose Einstein crossover in the attractive Hubbard model," *Phys. Rev. B*, vol. 72, p. 235118, Dec 2005. http://link.aps.org/doi/10.1103/PhysRevB.72.235118

[179] D. Bergeron and A.-M. S. Tremblay, "Algorithms for optimized maximum entropy and diagnostic tools for analytic continuation," *Phys. Rev. E*, vol. 94, p. 023303, Aug 2016. http://link.aps.org/doi/10.1103/PhysRevE.94.023303

[180] R. Preuss, W. Hanke, and W. von der Linden, "Quasiparticle Dispersion of the 2D Hubbard Model: From an Insulator to a Metal," *Phys. Rev. Lett.*, vol. 75, pp. 1344–1347, Aug 1995. http://link.aps.org/doi/10.1103/PhysRevLett.75.1344

[181] A. Moreo, S. Haas, A. W. Sandvik, and E. Dagotto, "Quasiparticle dispersion of the t - J and Hubbard models," *Phys. Rev. B*, vol. 51, pp. 12 045–12 048, May 1995. http://link.aps.org/doi/10.1103/PhysRevB.51.12045

[182] X. Wang, E. Gull, L. de' Medici, M. Capone, and A. J. Millis, "Antiferromagnetism and the gap of a Mott insulator: Results from analytic continuation of the self-energy," *Phys. Rev. B*, vol. 80, p. 045101, Jul 2009. http://link.aps.org/doi/10.1103/PhysRevB.80.045101

[183] D. Sénéchal, P.-L. Lavertu, M.-A. Marois, and A.-M. S. Tremblay, "Competition between Antiferromagnetism and Superconductivity in High-T_c Cuprates," *Phys. Rev. Lett.*, vol. 94, p. 156404, Apr 2005. http://link.aps.org/doi/10.1103/PhysRevLett.94.156404

[184] M. Capone and G. Kotliar, "Competition between d-wave superconductivity and antiferromagnetism in the two-dimensional Hubbard model," *Phys. Rev. B*, vol. 74, p. 054513, Aug 2006. http://link.aps.org/doi/10.1103/PhysRevB.74.054513

[185] S. S. Kancharla, B. Kyung, D. Sénéchal, M. Civelli, M. Capone, G. Kotliar, and A.-M. S. Tremblay, "Anomalous superconductivity and its competition with antiferromagnetism in doped mott insulators," *Phys. Rev. B*, vol. 77, p. 184516, May 2008. http://link.aps.org/doi/10.1103/PhysRevB.77.184516

[186] Y. Nambu, "Quasi-Particles and Gauge Invariance in the Theory of Superconductivity," *Phys. Rev.*, vol. 117, pp. 648–663, Feb 1960. https://link.aps.org/doi/10.1103/PhysRev.117.648

[187] G. Sordi, P. Sémon, K. Haule, and A.-M. S. Tremblay, "Strong Coupling Superconductivity, Pseudogap, and Mott Transition," *Phys. Rev. Lett.*, vol. 108, p. 216401, May 2012. http://link.aps.org/doi/10.1103/PhysRevLett.108.216401

[188] T. Maier, M. Jarrell, T. Pruschke, and J. Keller, "d-wave superconductivity in the hubbard model," *Phys. Rev. Lett.*, vol. 85, pp. 1524–1527, Aug 2000. http://link.aps.org/doi/10.1103/PhysRevLett.85.1524

[189] B. Kyung and A.-M. S. Tremblay, "Mott Transition, Antiferromagnetism, and d-Wave Superconductivity in Two-Dimensional Organic Conductors," *Phys. Rev. Lett.*, vol. 97, p. 046402, Jul 2006. http://link.aps.org/doi/10.1103/PhysRevLett.97.046402

[190] M. Aichhorn, E. Arrigoni, M. Potthoff, and W. Hanke, "Antiferromagnetic to superconducting phase transition in the hole- and electron-doped Hubbard model at zero temperature," *Phys. Rev. B*, vol. 74, p. 024508, Jul 2006. http://link.aps.org/doi/10.1103/PhysRevB.74.024508

[191] M. Balzer, W. Hanke, and M. Potthoff, "Importance of local correlations for the order parameter of high-T_c superconductors," *Phys. Rev. B*, vol. 81, p. 144516, Apr 2010. http://link.aps.org/doi/10.1103/PhysRevB.81.144516

[192] T. A. Maier, M. Jarrell, T. C. Schulthess, P. R. C. Kent, and J. B. White, "Systematic Study of d-Wave Superconductivity in the 2D Repulsive Hubbard Model," *Phys. Rev. Lett.*, vol. 95, p. 237001, Nov 2005. http://link.aps.org/doi/10.1103/PhysRevLett.95.237001

[193] K. Haule and G. Kotliar, "Strongly correlated superconductivity: A plaquette dynamical mean-field theory study," *Phys. Rev. B*, vol. 76, no. 10, p. 104509, 2007. http://link.aps.org/doi/10.1103/PhysRevB.76.104509

[194] E. Gull, O. Parcollet, and A. J. Millis, "Superconductivity and the pseudogap in the two-dimensional hubbard model," *Phys. Rev. Lett.*, vol. 110, p. 216405, May 2013. http://link.aps.org/doi/10.1103/PhysRevLett.110.216405

[195] E. Gull and A. J. Millis, "Energetics of superconductivity in the two-dimensional Hubbard model," *Phys. Rev. B*, vol. 86, p. 241106, Dec 2012. http://link.aps.org/doi/10.1103/PhysRevB.86.241106

[196] V. J. Emery and S. A. Kivelson, "Superconductivity in Bad Metals," *Phys. Rev. Lett.*, vol. 74, pp. 3253–3256, Apr 1995. http://link.aps.org/doi/10.1103/PhysRevLett.74.3253

[197] M. T. Béal-Monod, C. Bourbonnais, and V. J. Emery, "Possible superconductivity in nearly antiferromagnetic itinerant fermion systems," *Phys. Rev. B*, vol. 34, pp. 7716–7720, Dec 1986. http://link.aps.org/doi/10.1103/PhysRevB.34.7716

[198] G. Kotliar and J. Liu, "Superconducting instabilities in the large-U limit of a generalized hubbard model," *Phys. Rev. Lett.*, vol. 61, pp. 1784 – 7, 1988. http://link.aps.org/doi/10.1103/PhysRevLett.61.1784

[199] M. Caffarel and W. Krauth, "Exact diagonalization approach to correlated fermions in infinite dimensions: Mott transition and superconductivity," *Phys. Rev. Lett.*, vol. 72, pp. 1545–1548, Mar 1994. https://link.aps.org/doi/10.1103/PhysRevLett.72.1545

[200] K. Haule and G. Kotliar, "Avoided criticality in near-optimally doped high-temperature superconductors," *Phys. Rev. B*, vol. 76, no. 9, p. 092503, Sep 2007. http://link.aps.org/doi/10.1103/PhysRevB.76.092503

[201] G. V. Chester, "Difference between normal and superconducting states of a metal," *Phys. Rev.*, vol. 103, pp. 1693–1699, Sep 1956. http://link.aps.org/doi/10.1103/PhysRev.103.1693

[202] A. Leggett, "A midinfrared scenario for cuprate superconductivity," *Proceedings of the National Academy of Sciences*, vol. 96, no. 15, pp. 8365–8372, 1999. http://www.pnas.org/content/96/15/8365

[203] D. J. Scalapino and S. R. White, "Superconducting condensation energy and an antiferromagnetic exchange-based pairing mechanism," *Phys. Rev. B*, vol. 58, pp. 8222–8224, Oct 1998. http://link.aps.org/doi/10.1103/PhysRevB.58.8222

[204] P. W. Anderson, *The theory of Superconductivity in the High Tc cuprates.* Princeton: Princeton University Press, 1997.

[205] J. Hirsch and F. Marsiglio, "Where is 99% of the condensation energy of $Tl_2Ba_2CuO_y$ coming from? ," *Physica C: Superconductivity*, vol. 331, no. 2, pp. 150 – 156, 2000. http://www.sciencedirect.com/science/article/pii/S0921453499006693

[206] E. Demler and S.-C. Zhang, "Quantitative test of a microscopic mechanism of high-temperature superconductivity," *Nature*, vol. 396, no. 6713, pp. 733–735, 1998. http://www.nature.com/nature/journal/v396/n6713/abs/396733a0.html

[207] T. A. Maier, M. Jarrell, A. Macridin, and C. Slezak, "Kinetic energy driven pairing in cuprate superconductors," *Phys. Rev. Lett.*, vol. 92, p. 027005, Jan 2004. http://link.aps.org/doi/10.1103/PhysRevLett.92.027005

[208] E. Gull, P. Werner, O. Parcollet, and M. Troyer, "Continuous-time auxiliary-field Monte Carlo for quantum impurity models," *EPL (Europhysics Letters)*, vol. 82, no. 5, p. 57003, 2008. http://stacks.iop.org/0295-5075/82/i=5/a=57003

[209] D. Scalapino, "The case for $d_{x^2-y^2}$ pairing in the cuprate superconductors," *Physics Reports*, vol. 250, no. 6, pp. 329 – 365, 1995. http://www.sciencedirect.com/science/article/pii/037015739400086I

[210] J.-F. Sadoc and R. Mosseri, *Geometrical frustration*. Cambridge University Press, 2006.

[211] A. Liebsch and N.-H. Tong, "Finite-temperature exact diagonalization cluster dynamical mean-field study of the two-dimensional Hubbard model: Pseudogap, non-Fermi-liquid behavior, and particle-hole asymmetry," *Phys. Rev. B*, vol. 80, p. 165126, Oct 2009. http://link.aps.org/doi/10.1103/PhysRevB.80.165126

[212] I. Bloch, J. Dalibard, and W. Zwerger, "Many-body physics with ultracold gases," *Rev. Mod. Phys.*, vol. 80, pp. 885–964, Jul 2008. http://link.aps.org/doi/10.1103/RevModPhys.80.885

[213] T. Esslinger, "Fermi-Hubbard Physics with Atoms in an Optical Lattice," *Annual Review of Condensed Matter Physics*, vol. 1, no. 1, pp. 129–152, 2010. http://dx.doi.org/10.1146/annurev-conmatphys-070909-104059

[214] R. Jördens, N. Strohmaier, K. Günter, H. Moritz, and T. Esslinger, "A Mott insulator of fermionic atoms in an optical lattice," *Nature*, vol. 455, no. 204, pp. 204–207, 2008. http://www.nature.com/nature/journal/v455/n7210/abs/nature07244.html

[215] U. Schneider, L. Hackermüller, S. Will, T. Best, I. Bloch, T. A. Costi, R. W. Helmes, D. Rasch, and A. Rosch, "Metallic and Insulating Phases of Repulsively Interacting Fermions in a 3D Optical Lattice," *Science*, vol. 322, no. 5907, pp. 1520–1525, 2008. http://science.sciencemag.org/content/322/5907/1520

[216] C. Hofrichter, L. Riegger, F. Scazza, M. Höfer, D. R. Fernandes, I. Bloch, and S. Fölling, "Direct Probing of the Mott Crossover in the SU(N) Fermi-Hubbard Model," *Phys. Rev. X*, vol. 6, p. 021030, Jun 2016. http://link.aps.org/doi/10.1103/PhysRevX.6.021030

[217] E. Cocchi, L. A. Miller, J. H. Drewes, M. Koschorreck, D. Pertot, F. Brennecke, and M. Köhl, "Equation of State of the Two-Dimensional Hubbard Model," *Phys. Rev. Lett.*, vol. 116, p. 175301, Apr 2016. http://link.aps.org/doi/10.1103/PhysRevLett.116.175301

[218] D. Greif, T. Uehlinger, G. Jotzu, L. Tarruell, and T. Esslinger, "Short-Range Quantum Magnetism of Ultracold Fermions in an Optical Lattice," *Science*, vol. 340, no. 6138, pp. 1307–1310, 2013. http://science.sciencemag.org/content/340/6138/1307

[219] R. A. Hart, P. M. Duarte, T.-L. Yang, X. Liu, T. Paiva, E. Khatami, R. T. Scalettar, N. Trivedi, D. A. Huse, and R. G. Hulet, "Observation of antiferromagnetic correlations in the Hubbard model with ultracold atoms," *Nature*, vol. 519, pp. 211–214, 2015. http://dx.doi.org/10.1038/nature14223

[220] M. F. Parsons, A. Mazurenko, C. S. Chiu, G. Ji, D. Greif, and M. Greiner, "Site-resolved measurement of the spin-correlation function in the Fermi-Hubbard model," *Science*, vol. 353, no. 6305, pp. 1253–1256, 2016. http://science.sciencemag.org/content/353/6305/1253

[221] M. Boll, T. A. Hilker, G. Salomon, A. Omran, J. Nespolo, L. Pollet, I. Bloch, and C. Gross, "Spin- and density-resolved microscopy of antiferromagnetic correlations in Fermi-Hubbard chains," *Science*, vol. 353, no. 6305, pp. 1257–1260, 2016. http://science.sciencemag.org/content/353/6305/1257

[222] L. W. Cheuk, M. A. Nichols, K. R. Lawrence, M. Okan, H. Zhang, E. Khatami, N. Trivedi, T. Paiva, M. Rigol, and M. W. Zwierlein, "Observation of spatial charge and spin correlations in the 2D Fermi-Hubbard model," *Science*, vol. 353, no. 6305, pp. 1260–1264, 2016. http://science.sciencemag.org/content/353/6305/1260

[223] D. Fournier, M. Poirier, M. Castonguay, and K. D. Truong, "Mott transition, compressibility divergence, and the P-T phase diagram of layered organic superconductors: An ultrasonic investigation," *Phys. Rev. Lett.*, vol. 90, p. 127002, Mar 2003. http://link.aps.org/doi/10.1103/PhysRevLett.90.127002

[224] S. R. Hassan, A. Georges, and H. R. Krishnamurthy, "Sound velocity anomaly at the mott transition: Application to organic conductors and V_2O_3," *Phys. Rev. Lett.*, vol. 94, p. 036402, Jan 2005. http://link.aps.org/doi/10.1103/PhysRevLett.94.036402

[225] M. J. Rozenberg, R. Chitra, and G. Kotliar, "Finite temperature mott transition in the hubbard model in infinite dimensions," *Phys. Rev. Lett.*, vol. 83, no. 17, pp. 3498–3501, Oct 1999. http://link.aps.org/doi/10.1103/PhysRevLett.83.3498

[226] H. Terletska, J. Vučičević, D. Tanasković, and V. Dobrosavljević, "Quantum critical transport near the mott transition," *Phys. Rev. Lett.*, vol. 107, p. 026401, Jul 2011. http://link.aps.org/doi/10.1103/PhysRevLett.107.026401

[227] C.-D. Hébert, P. Sémon, and A.-M. S. Tremblay, "Superconducting dome in doped quasi-two-dimensional organic mott insulators: A paradigm for strongly correlated superconductivity," *Phys. Rev. B*, vol. 92, p. 195112, Nov 2015. http://link.aps.org/doi/10.1103/PhysRevB.92.195112

[228] E. Gull and A. J. Millis, "Ten years of nature physics: Numerical models come of age," *Nat Phys*, vol. 11, p. 808, 2015. http://dx.doi.org/10.1038/nphys3501

[229] A. Georges, G. Kotliar, and W. Krauth, " Superconductivity in the two-band Hubbard model in infinite dimensions ," *Zeitschrift für Physik B Condensed Matter*, vol. 92, no. 3, pp. 313–321, 1993. http://dx.doi.org/10.1007/BF01308748

[230] P. Lombardo, M. Avignon, J. Schmalian, and K.-H. Bennemann, "Dynamical mean-field theory for perovskites," *Phys. Rev. B*, vol. 54, pp. 5317–5325, Aug 1996. http://link.aps.org/doi/10.1103/PhysRevB.54.5317

[231] M. Zölfl, T. Maier, T. Pruschke, and J. Keller, " Electronic properties of CuO_2 planes: A DMFT study ," *The European Physical Journal B - Condensed Matter and Complex Systems*, vol. 13, no. 1, pp. 47–53, 2000. http://dx.doi.org/10.1007/s100510050009

[232] G. Sordi, A. Amaricci, and M. J. Rozenberg, " Metal-Insulator Transitions in the Periodic Anderson Model ," *Phys. Rev. Lett.*, vol. 99, p. 196403, Nov 2007. http://link.aps.org/doi/10.1103/PhysRevLett.99.196403

[233] C. Weber, K. Haule, and G. Kotliar, "Optical weights and waterfalls in doped charge-transfer insulators: A local density approximation and dynamical mean-field theory study of $La_{2-x}Sr_xCuO_4$," *Phys. Rev. B*, vol. 78, p. 134519, Oct 2008. http://link.aps.org/doi/10.1103/PhysRevB.78.134519

[234] C. Weber, K. Haule, and G. Kotliar, "Strength of correlations in electron- and hole-doped cuprates," *Nature Physics*, vol. 6, no. 8, pp. 574–578, 2010. http://www.nature.com/nphys/journal/v6/n8/full/nphys1706.html

[235] L. de' Medici, X. Wang, M. Capone, and A. J. Millis, " Correlation strength, gaps, and particle-hole asymmetry in high-T_c cuprates: A dynamical mean field study of the three-band copper-oxide model ," *Phys. Rev. B*, vol. 80, p. 054501, Aug 2009. http://link.aps.org/doi/10.1103/PhysRevB.80.054501

[236] X. Wang, L. de' Medici, and A. J. Millis, " Role of oxygen-oxygen hopping in the three-band copper-oxide model: Quasiparticle weight, metal insulator and magnetic phase boundaries, gap values, and optical conductivity ," *Phys. Rev. B*, vol. 83, p. 094501, Mar 2011. http://link.aps.org/doi/10.1103/PhysRevB.83.094501

[237] X. Wang, H. T. Dang, and A. J. Millis, " $d_{3z^2-r^2}$ orbital in high-T_c cuprates: Excitonic spectrum, metal-insulator phase diagram, optical conductivity, and orbital character of doped holes ," *Phys. Rev. B*, vol. 84, p. 014530, Jul 2011. http://link.aps.org/doi/10.1103/PhysRevB.84.014530

[238] A. Macridin, M. Jarrell, T. Maier, and G. A. Sawatzky, " Physics of cuprates with the two-band Hubbard model: The validity of the one-band Hubbard model ," *Phys. Rev. B*, vol. 71, p. 134527, Apr 2005. http://link.aps.org/doi/10.1103/PhysRevB.71.134527

[239] E. Arrigoni, M. Aichhorn, M. Daghofer, and W. Hanke, "Phase diagram and single-particle spectrum of CuO_2 high- T_c layers: variational cluster approach to the three-band hubbard model," *New Journal of Physics*, vol. 11, no. 5, p. 055066, 2009. http://stacks.iop.org/1367-2630/11/i=5/a=055066

[240] C. Weber, C. Yee, K. Haule, and G. Kotliar, "Scaling of the transition temperature of hole-doped cuprate superconductors with the charge-transfer energy," *EPL (Europhysics Letters)*, vol. 100, no. 3, p. 37001, 2012. http://stacks.iop.org/0295-5075/100/i=3/a=37001

[241] A. Go and A. J. Millis, "Spatial correlations and the insulating phase of the high-T_c cuprates: Insights from a configuration-interaction-based solver for dynamical mean field theory," *Phys. Rev. Lett.*, vol. 114, p. 016402, Jan 2015. http://link.aps.org/doi/10.1103/PhysRevLett.114.016402

[242] M. Potthoff, M. Aichhorn, and C. Dahnken, "Variational Cluster Approach to Correlated Electron Systems in Low Dimensions," *Phys. Rev. Lett.*, vol. 91, p. 206402, Nov 2003. https://link.aps.org/doi/10.1103/PhysRevLett.91.206402

[243] D. Zgid, E. Gull, and G. K.-L. Chan, "Truncated configuration interaction expansions as solvers for correlated quantum impurity models and dynamical mean-field theory," *Phys. Rev. B*, vol. 86, p. 165128, Oct 2012. https://link.aps.org/doi/10.1103/PhysRevB.86.165128

[244] O. Andersen, A. Liechtenstein, O. Jepsen, and F. Paulsen, "LDA energy bands, low energy hamiltonians, t',t", $t_\perp(k)$ and $J_\perp$," *J. Phys, Chem. Solids*, vol. 56, pp. 1573–1591, 1995. http://www.sciencedirect.com/science/article/pii/0022369795002693

[245] M. T. Greiner and Z.-H. Lu, "Thin-film metal oxides in organic semiconductor devices: their electronic structures, work functions and interfaces," *NPG Asia Materials*, vol. 5, no. 7, p. e55, 2013. http://www.nature.com/am/journal/v5/n7/abs/am201329a.html

[246] H. Alloul, "What is the simplest model that captures the basic experimental facts of the physics of underdoped cuprates?" *Comptes Rendus Physique*, vol. 15, no. 6, pp. 519 – 524, 2014. http://www.sciencedirect.com/science/article/pii/S1631070514000267

[247] Y. Kohsaka, C. Taylor, K. Fujita, A. Schmidt, C. Lupien, T. Hanaguri, M. Azuma, M. Takano, H. Eisaki, H. Takagi, S. Uchida, and J. C. Davis, "An intrinsic bond-centered electronic glass with unidirectional domains in underdoped cuprates," *Science*, vol. 315, no. 5817, pp. 1380–1385, MAR 9 2007. http://science.sciencemag.org/content/315/5817/1380

[248] T. Timusk and B. Statt, "The pseudogap in high-temperature superconductors: an experimental survey," *Reports on Progress in Physics*, vol. 62, no. 1, p. 61, 1999. http://iopscience.iop.org/article/10.1088/0034-4885/62/1/002/meta

[249] H. Terletska, J. Vučičević, D. Tanasković, and V. Dobrosavljević, " Quantum Critical Transport near the Mott Transition ," *Phys. Rev. Lett.*, vol. 107, p. 026401, Jul 2011. http://link.aps.org/doi/10.1103/PhysRevLett.107.026401

[250] J. Vučičević, H. Terletska, D. Tanasković, and V. Dobrosavljević, " Finite-temperature crossover and the quantum Widom line near the Mott transition ," *Phys. Rev. B*, vol. 88, p. 075143, Aug 2013. http://link.aps.org/doi/10.1103/PhysRevB.88.075143

[251] J. Vučičević, D. Tanasković, M. J. Rozenberg, and V. Dobrosavljević, " Bad-Metal Behavior Reveals Mott Quantum Criticality in Doped Hubbard Models ," *Phys. Rev. Lett.*, vol. 114, p. 246402, Jun 2015. http://link.aps.org/doi/10.1103/PhysRevLett.114.246402

[252] A. Reymbaut, M. Charlebois, M. F. Asiani, L. Fratino, P. Sémon, G. Sordi, and A.-M. S. Tremblay, "Antagonistic effects of nearest-neighbor repulsion on the superconducting pairing dynamics in the doped Mott insulator regime," *Phys. Rev. B*, vol. 94, p. 155146, Oct 2016. http://link.aps.org/doi/10.1103/PhysRevB.94.155146

[253] A. V. Chubukov, D. Pines, and J. Schmalian, *Superconductivity: Conventional and Unconventional Superconductors*. Berlin, Heidelberg: Springer Berlin Heidelberg,

2008, ch. A Spin Fluctuation Model for d-Wave Superconductivity, pp. 1349–1413. http://dx.doi.org/10.1007/978-3-540-73253-2_22

[254] K. B. Efetov, H. Meier, and C. Pepin, "Pseudogap state near a quantum critical point," *Nat Phys*, vol. 9, no. 7, pp. 442–446, Jul. 2013. http://dx.doi.org/10.1038/nphys2641

[255] S. Sachdev and R. La Placa, "Bond order in two-dimensional metals with antiferromagnetic exchange interactions," *Phys. Rev. Lett.*, vol. 111, p. 027202, Jul 2013. http://link.aps.org/doi/10.1103/PhysRevLett.111.027202

[256] Y. Wang and A. Chubukov, "Charge-density-wave order with momentum $(2q, 0)$ and $(0, 2q)$ within the spin-fermion model: Continuous and discrete symmetry breaking, preemptive composite order, and relation to pseudogap in hole-doped cuprates," *Phys. Rev. B*, vol. 90, p. 035149, Jul 2014. http://link.aps.org/doi/10.1103/PhysRevB.90.035149

[257] C. M. Varma, P. B. Littlewood, S. Schmitt-Rink, E. Abrahams, and A. E. Ruckenstein, "Phenomenology of the normal state of Cu-O high-temperature superconductors," *Phys. Rev. Lett.*, vol. 63, pp. 1996–1999, Oct 1989. http://link.aps.org/doi/10.1103/PhysRevLett.63.1996

[258] C. M. Varma, "Theory of the pseudogap state of the cuprates," *Phys. Rev. B*, vol. 73, p. 155113, Apr 2006. http://link.aps.org/doi/10.1103/PhysRevB.73.155113

[259] C. Weber, T. Giamarchi, and C. M. Varma, "Phase Diagram of a Three-Orbital Model for High-T_c Cuprate Superconductors," *Phys. Rev. Lett.*, vol. 112, p. 117001, Mar 2014. http://link.aps.org/doi/10.1103/PhysRevLett.112.117001

[260] S. Bulut, A. P. Kampf, and W. A. Atkinson, "Instability towards staggered loop currents in the three-orbital model for cuprate superconductors," *Phys. Rev. B*, vol. 92, p. 195140, Nov 2015. http://link.aps.org/doi/10.1103/PhysRevB.92.195140

[261] Y. F. Kung, C.-C. Chen, B. Moritz, S. Johnston, R. Thomale, and T. P. Devereaux, "Numerical exploration of spontaneous broken symmetries in multiorbital Hubbard models," *Phys. Rev. B*, vol. 90, p. 224507, Dec 2014. http://link.aps.org/doi/10.1103/PhysRevB.90.224507

[262] V. S. de Carvalho, C. Pépin, and H. Freire, "Coexistence of Θ_{II}-loop-current order with checkerboard d-wave CDW/PDW order in a hot-spot model for cuprate superconductors," *Phys. Rev. B*, vol. 93, p. 115144, Mar 2016. http://link.aps.org/doi/10.1103/PhysRevB.93.115144